THE SILVER INTERCALATED 2H-TaS_2 AND 1T-TiS_2 TRANSITION METAL DICHALCOGENIDES

by

Günter Adolf Scholz

B.Sc. (Hons.), Simon Fraser University, 1975

M.Sc., McMaster University, 1977

A THESIS SUBMITTED IN PARTIAL FULFILLMENT OF

THE REQUIREMENTS FOR THE DEGREE OF

DOCTOR OF PHILOSOPHY

in the Department

of

Physics

© GÜNTER ADOLF SCHOLZ 1982

Simon Fraser University

June 1982

All rights reserved. This thesis may not be reproduced in whole or part, by photocopy or other means, without permission of the author.

PARTIAL COPYRIGHT LICENSE

I hereby grant to Simon Fraser University the right to lend my thesis, project or extended essay (the title of which is shown below) to users of the Simon Fraser University Library, and to make partial or single copies only for such users or in response to a request from the library of any other university, or other educational institution, on its own behalf or for one of its users. I further agree that permission for multiple copying of this work for scholarly purposes may be granted by me or the Dean of Graduate Studies. It is understood that copying or publication of this work for financial gain shall not be allowed without my written permission.

Title of Thesis/Project/Extended Essay

"The silver intercalated 2H-TaS_2 and 1T-TiS_2 transition metal dichalcogenides"

Author: [signature]
(signature)

Guenter A. Scholz
(name)

Aug. 19, 1982
(date)

APPROVAL

Name: Guenter Adolf Scholz

Degree: Doctor of Philosophy

Title of Thesis: The Silver Intercalated 2H-TaS_2 and 1T-TiS_2 Transition Metal Dichalcogenides

Examining Committee:

Chairman:

Robert F. Frindt
Senior Supervisor

Michael [illegible]

Klaus E. Rieckhoff

Albert E. Curzon

Frank W. C. Boswell
External Examiner
Professor, Department of Physics
University of Waterloo, Waterloo, Ontario

Date Approved: July 8, 1982

ABSTRACT

2H-TaS_2 and 1T-TiS_2 are layer compounds that have a pseudo two-dimensional structure and are capable of intercalating atoms or molecules via an almost topotactic reaction and are useful, among other things, as electrodes in electrochemical intercalation cells. It is therefore of interest to study the detailed behaviour of these materials.

The effects of intercalation were studied in Ag_xTaS_2 and Ag_xTiS_2 with X-rays, voltammetry and optical transmission at room temperature, plus electron diffraction and electrical resistivity from 400K to 4.2K.

Electrochemical intercalation of silver into 2H-TaS_2 has been found to be very reversible, even though host stacking changes have been observed. However, in the Ag_xTiS_2 system where no stacking changes occur, intercalation appears to be irreversible for $x \lesssim 1/5$ but becomes reversible when cycling between $1/5 \lesssim x \lesssim 2/5$.

In both systems a progression of stages were observed for increasing x beginning with dilute stage 1, which changes to stage 2 and finally to stage 1.

Changes in the optical properties of Ag_xTaS_2 and

Ag_xTiS_2 were observed in the energy range 1.2 eV to 2.8 eV. The observations are consistent with a rigid band model where, with the filling of the "d_{z^2} orbitals", a decrease in the free carrier absorption and a shift in the inter-band transition edge occurs. These optical effects allowed staging along with intercalation and diffusion rates to be easely discernible and measurable. The intercalation rates are found to be thickness dependent and are considerably faster in 2H-TaS_2 as compared to 1T-TiS_2.

Using electron diffraction, an order-disorder transition to a $\sqrt{3}a_o$ superlattice is observed for Ag_xTiS_2 near 300K for stage 2 and stage 1.

For Ag_xTaS_2, complex silver superlattices that vary with x and temperature occur. For stage 2 ($x \sim 1/6$) a $\sqrt{3}a_o$ superlattice appears near 400K, for stage 2 ($x \sim 1/3$) near 300K a $2a_o$ superlattice coexists with randomly distributed ions, and below about 100K a $(5\sqrt{3} \times 2)a_o$ and $2a_o$ superlattice coexist. In stage 1 a $(\sqrt{3} \times 2)a_o$ superlattice coexists with randomly distributed ions near 300K, and below about 100K a $(2\sqrt{3} \times 5)a_o$ and $(\sqrt{3} \times 2)a_o$ superlattice coexist. In addition to these superlattices, when $0 \leq x \lesssim 1/4$, incommensurate side-band satellites due to a charge density wave with $q^* = (0.338 \pm 0.002)a_o^*$ ($x = 0$), and $q^* = (0.347 \pm 0.002)a_o^*$ ($x = 0.26$) were also observed.

The detailed study of these intercalation systems has given considerable insight into a variety of aspects governing intercalation, staging and changes in structure, much of which appears to be generally applicable to other intercalation systems.

für meine Mutter

Textbooks and Heaven only are ideal
Solidity is an imperfect state.
Within the cracked and dislocated Real
Nonstoichiometric crystals dominate.
Stray Atoms sully and precipitate;
Strange holes, exitons, wander loose; because
of Dangling Bonds, a chemical Substrate
Corrodes and catalyzes - surface Flaws
Help Epitaxial Growth to fix adsorptive claws.

John Updike

(The Dance of the Solids)

ACKNOWLEDGEMENTS

I wish to express my appreciation to my supervisor, Professor R.F. Frindt, for his enthusiasm, willing guidance and invaluable critical advice throughout the course of this very enjoyable research.

My thanks also go to, among others, Professor A.E. Curzon and his group for their co-operation in taking the many electron diffraction patterns; to Per Joensen whose technical assistance has been of great help, in particular by taking much of the data in Chapter 9; to Professor Michael Plischke for his comments and expert advice on many of the "intercalation topics"; and to the technical along with the secretarial staff of the Physics Department, in particular Marion Jaques for her expert typing of this manuscript.

The personal support provided by my supervisor and the Natural Sciences and Engineering Council of Canada who have made this research possible, along with the teaching assistantships and scholarships provided by Simon Fraser University, is also very gratefully acknowledged.

Finally, I will not forget the patience of my wife, Laura, and those many evenings and weekends she has been spending alone.

TABLE OF CONTENTS

Page

Page

LIST OF TABLES

LIST OF FIGURES

CHAPTER 1

INTRODUCTION

1.1 Structure of the Layer Compounds

Layer compounds like graphite and the transition metal dichalcogenides have attracted considerable interest in recent years from a number of viewpoints including:

(a) Superconductivity [1]

(b) Electronic instabilities [2]

(c) Order-Disorder transitions [3]

(d) Battery electrodes [4]

all of which results from essentially two properties that all of these materials have in common:

(i) their structure is pseudo two-dimensional;

(ii) they are capable of reversibly intercalating atoms or molecules via an almost topotactic reaction.

The MCh_2 (M = transition metal; Ch = chalcogen) layer materials are structurally quite similar in that they are all made up of Ch-M-Ch sandwiches which in turn consist of hexagonally packed planes of metal atoms, having hexagonally packed planes of chalcogen atoms on both sides (Fig. 1.1). The atoms within a Ch-M-Ch sandwich are covalently bonded into a relatively rigid framework, but the sandwiches in turn are only loosely bound to each other. The nature of this weak bond is not clearly understood but because it is so weak, it is thought by many to be of the van der Waals type and results

Fig. 1.1

The stacking of Ch-M-Ch sandwiches parallel to $\hat{c}$.

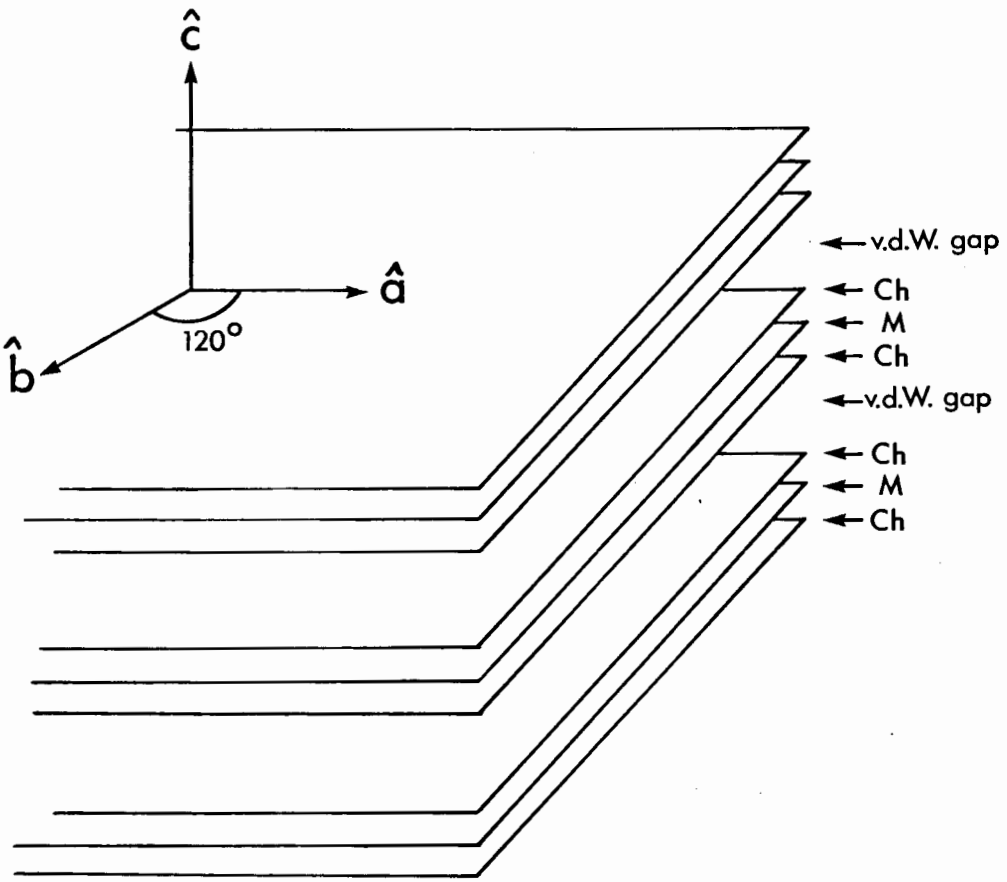
ĉ
â
b̂
120°
v.d.W. gap
Ch
M
Ch
v.d.W. gap
Ch
M
Ch

in the marked cleavage properties parallel to the basal planes in addition to the pronounced anisotropy, both mechanical and electrical, exhibited by the layer materials. For example, the ratio of the electrical resistivity perpendicular as compared to along the basal planes in 4Hb-TaS_2 is about 4 at room temperature and increases to about 500 at 4.2K [5].

The co-ordination of the chalcogen atoms will occur in only two ways within a Ch-M-Ch sandwich for all the transition metal dichalcogenides. They either form a trigonal-antiprism (distorted octahedron) as is the case for 1T-TiS_2, 1T-TaS_2, etc. or they arrange in a trigonal-prism as observed for 2H-TaS_2, 2H-$NbSe_2$, etc. (Fig. 1.2a). A $(11\bar{2}0)$ section of these two structures is shown in Fig. 1.2b and is a commonly used representation for illustration purposes because of its simplicity. By stacking and combining these two basic sandwich units in various ways one can generate the various polymorphs observed for a given transition metal and chalcogen (Fig. 1.3). However, the particular polymorph generated may be thermodynamically stable, metastable or may not occur at all at room temperature.

Electrically the MCh_2 layer materials vary widely from insulators like HfS_2 through semiconductors like MoS_2 and to metals like 2H-TaS_2. Dramatic electrical differences can also exist between the various polymorphs of a given dichalcogenide as, for example, between the 2H and 1T polymorphs

Fig. 1.2

(a) The two co-ordination symmetries that the chalcogen atoms will assume with respect to the transition metal atom.

(b) A $(11\bar{2}0)$ section of the co-ordination symmetries drawn in (a). The short hand notation for these structures is as indicated.

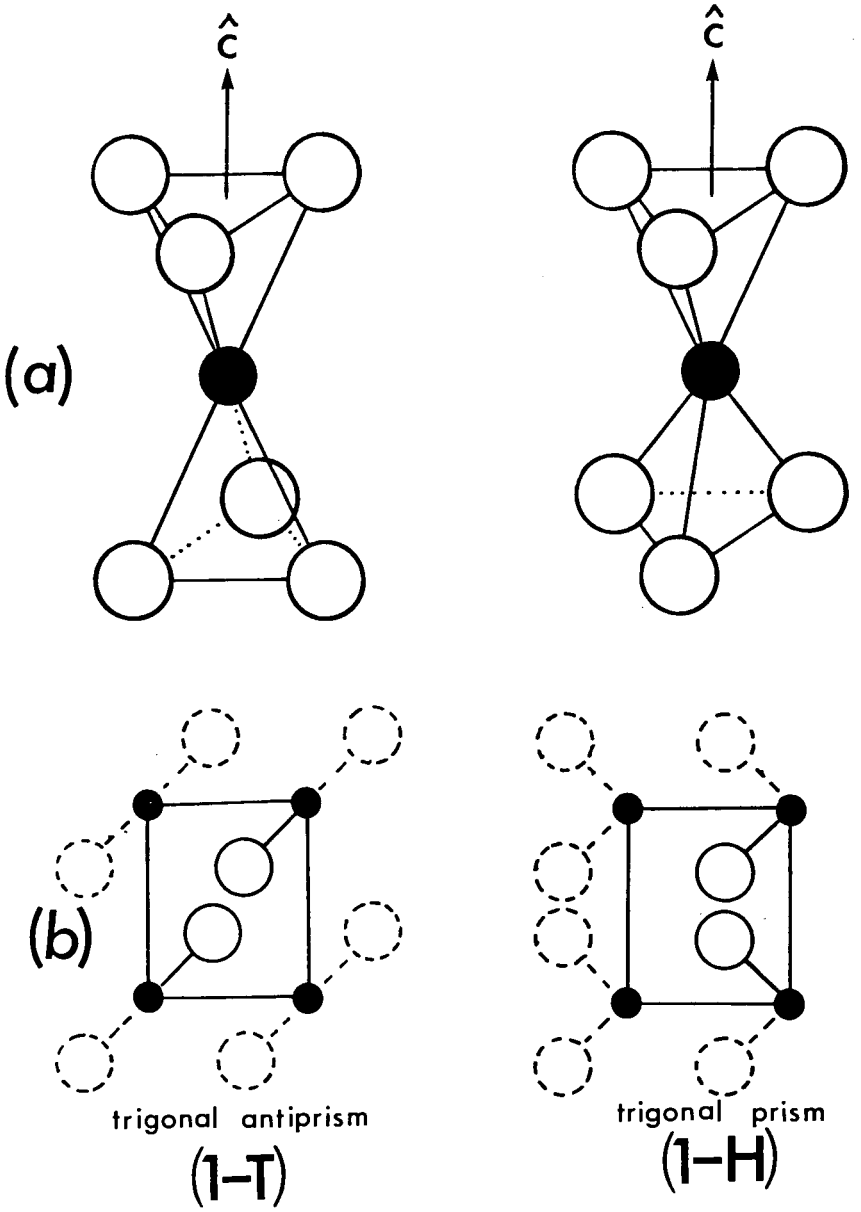
ĉ
ĉ
(a)
(b)
trigonal antiprism
(1-T)
trigonal prism
(1-H)

Fig. 1.3

An example of some of the polymorphs of a given transition metal dichalcogenide that can be generated from the basic building blocks indicated in Fig. 1.2.

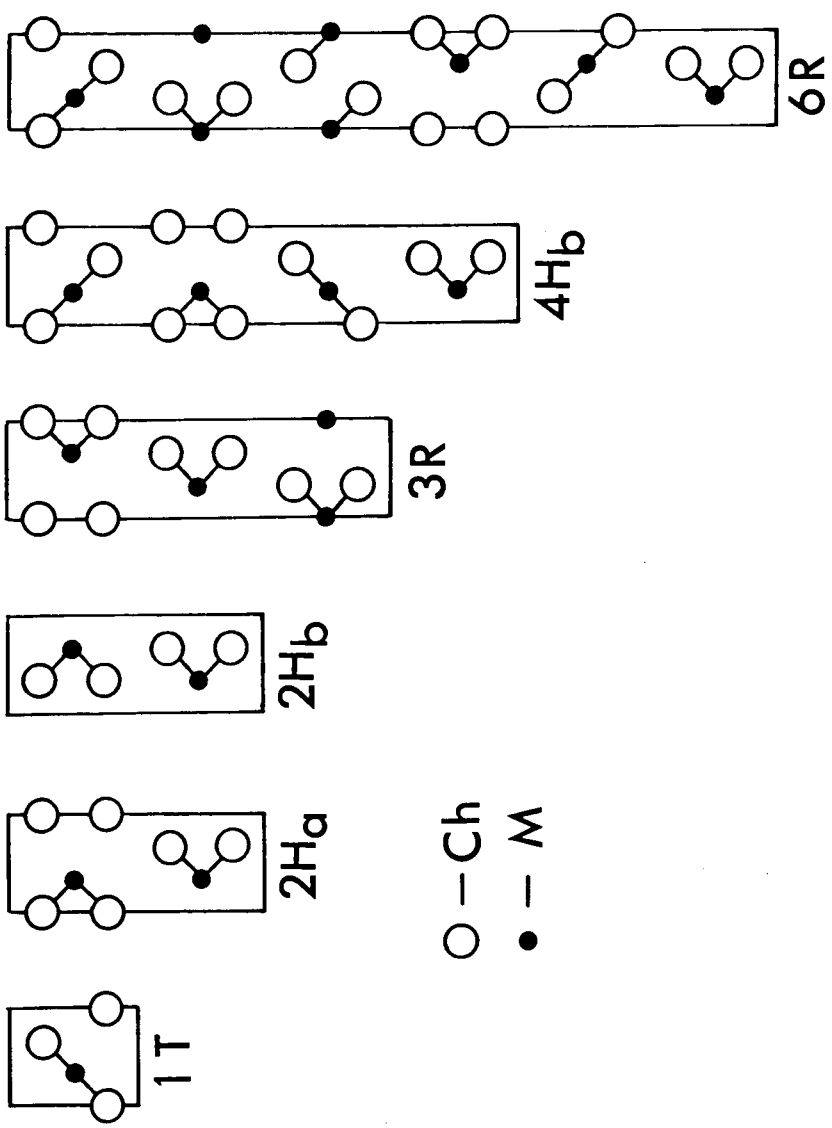
6R
4Hb
3R
2Hb
2Ha
1T
O — Ch
● — M

of TaS_2 (Fig. 1.3). At low temperatures the former polymorph undergoes a superconducting transition [1] while the latter undergoes a metal-insulator transition [6]. In order to understand this behaviour, it becomes essential to understand the band structures. To predict the band schemes of the various dichalcogenides, valence bond [7] along with ligand-field theory [8] is used and although both theories do present a very simplified picture, they can nevertheless give considerable insight into the varied electrical behaviour observed. As illustrated in Fig. 1.4, ligand-field splitting reduces the spherical symmetry of the five-fold degenerate d-orbitals by splitting them into e_g and t_{2g} levels in an octahedral field (Fig. 1.2) and if the field is trigonal-prismatic this separation can again be observed, but in addition the t_{2g} level will be further split into the doubly degenerate d_{x2-y2} and d_{xy} level and the singly degenerate d_{z2} level (Fig. 1.4). The doubly degenerate states d_{xz} and d_{yz}, because of their spatial orientations, will hybridize with the chalcogen p-states to form the covalent bonds which will generate the MCh_2 sandwiches. Therefore, it can be seen that it is the degree of filling of the non-bonding d-bands, composed of d_{x2-y2}, d_{xy} and d_{z2} orbitals, in conjunction with the co-ordination symmetry of the chalcogen atoms which determines to a large part the diversity in the electrical properties of the transition metal dichalcogenides.

Fig. 1.4

Lowering of the spherical symmetry of the five-fold degenerate d-orbitals produced by the trigonally prismatic and octahedral ligand fields, as proposed by Wilson and Yoffe [7].

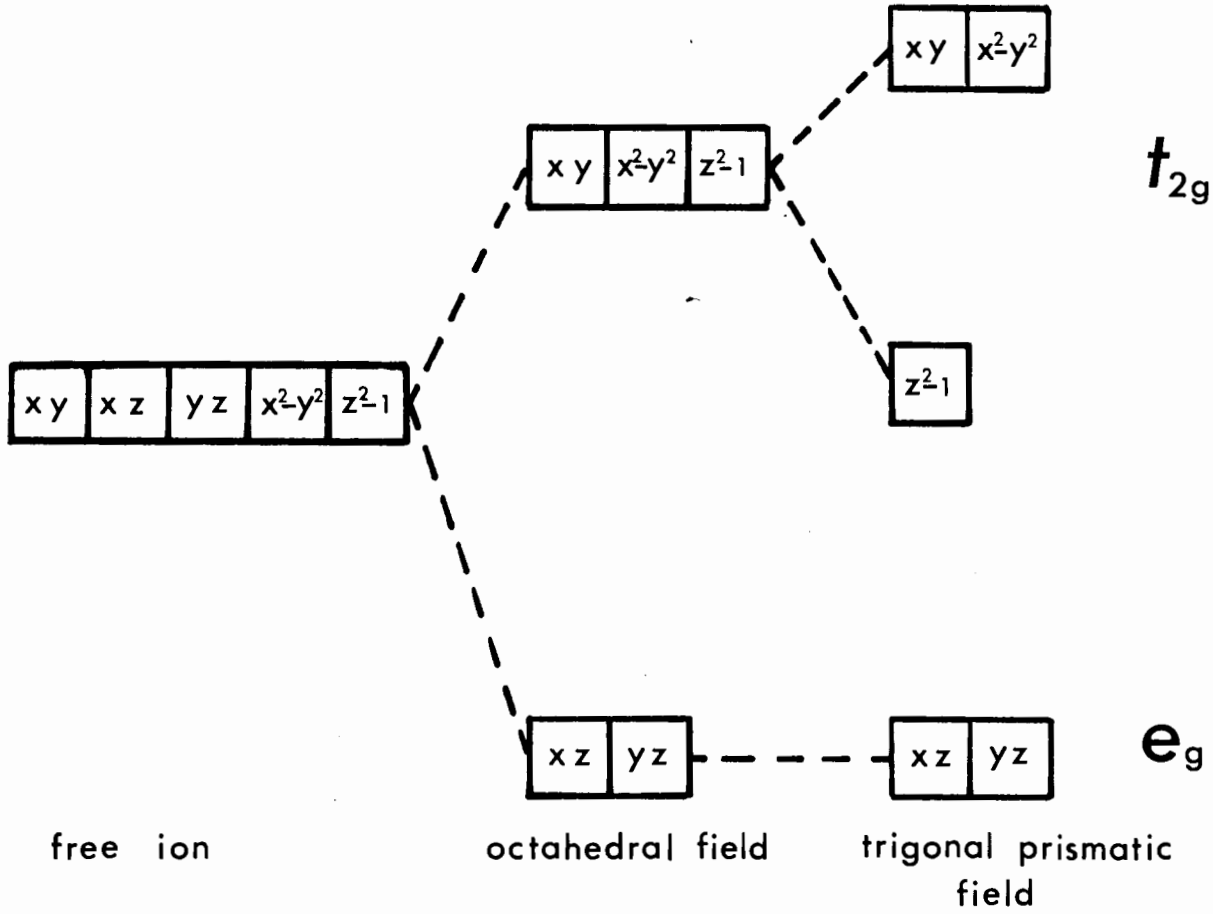
xy
xz
yz
x²-y²
z²-1
xy
x²-y²
z²-1
xy
x²-y²
z²-1
xz
yz
xz
yz
t2g
eg
free ion
octahedral field
trigonal prismatic field

1.2 Intercalation of the Layer Compounds

Intercalation refers to the insertion of extra calends of time into the calendar (ie. inter-calend) by the Romans. It has since also come to describe, among other processes, the insertion of a guest atom or molecule into the van der Waals gap of a layer material. In attempting to understand an intercalation system, the concepts and techniques of solid state physics, inorganic chemistry, electrochemistry, surface science, catalysis, thermodynamics and kinetics all come to bear.

Depending on the type of intercalated transition metal dichalcogenide (I_xMCh_2) it is possible to "tune", from subtle to extreme, the chemical, electronic and physical properties of the intercalated dichalcogenide by varying the mole fraction (x) of the intercalated guest species. Other interesting aspects of intercalated layer compounds are due to the consequences of restricting the intercalate to an essentially two-dimensional motion within the van der Waals gap, and the effects this has on order-disorder transitions (observed on cooling) of the intercalate as the mole fraction is varied.

Whether or not intercalation occurs is determined by the energetics and interplay of several factors, of which three of the most important are:

(a) the oxidation potential of the intercalate

e.g. $Li \rightarrow Li^+ + e^-$ +2.8V

$xLi^+ + xe^- + TiS_2 \rightarrow Li_xTiS_2$ -0.4V

resulting in the net reaction

$xLi + TiS_2 \rightarrow Li_xTiS_2$ +2.4V

The intercalation reaction of lithium into 1T-TiS_2 has a positive free energy with respect to H^+/H_2 and thus requires energy to proceed. The oxidation of lithium metal on the other hand, with its very large negative free energy, can supply ample driving potential to allow the intercalation reaction to proceed spontaneously. Consequently, intercalation compounds like Li_xTiS_2 should be viewed as being largely ionic in character (e.g. $Li^+TiS_2^-$) with the dichalcogenide acting as a macro-anion. In any case, it is obvious that a anode having a large positive oxidation potential is always desirable for intercalation to occur.

(b) the enhanced delocalization of the intercalate's electrons, provided by the host

e.g. $\times NH_3 + TaS_2 \rightarrow (NH_3)_xTaS_2$

This type of reaction illustrates the overall decrease in the free energy of a system achieved by partially transferring a localized charge, the lone pair on NH_3, to the 2H-TaS_2 host where it can subsequently delocalize throughout the non-bonding conduction band. The net effect is again the creation of an ionic compound (e.g. $NH_3+TaS_2^-$) where the dichalcogen acts as a macro-anion.

(c) the work required to separate and bend the MCH_2 sandwiches along with the Coulomb interaction of the intercalated ions are some of the penalties of intercalation in contrast to (a) and (b) which were both examples of factors enhancing, or even causing intercalation.

If intercalation does occur, one might at first assume that the van der Waals regions will all fill uniformly with the intercalates species up to some maximum mole fraction. However, this is not always observed and instead, the phenomenon of staging [9] often occurs and corresponds to the systematic dispersal of intercalated and unintercalated layers. Thus a stage n compound is one where n MCh_2 sandwiches are interposed between a pair of intercalated layers (Fig. 1.5). Therefore n expresses the periodicity, in terms of MCh_2 sandwiches, of the intercalated regions perpendicular to the basal plane (Fig. 1.5).

1.3 Motivation and Outline of the Research

A considerable amount of fundamental research has been carried out on the intercalation compounds of graphite [10]. However, although they do behave similarly to the transition metal dichalcogenides in certain repects, they differ considerably in a number of important fundamental aspects such as bonding, electron distribution, structure, their ability to intercalate both Lewis acids and bases, etc., and it is dubious that meaningful parallels can be drawn between these

Fig. 1.5

Examples of stage n = 1, 2, and 3 stacking sequences.

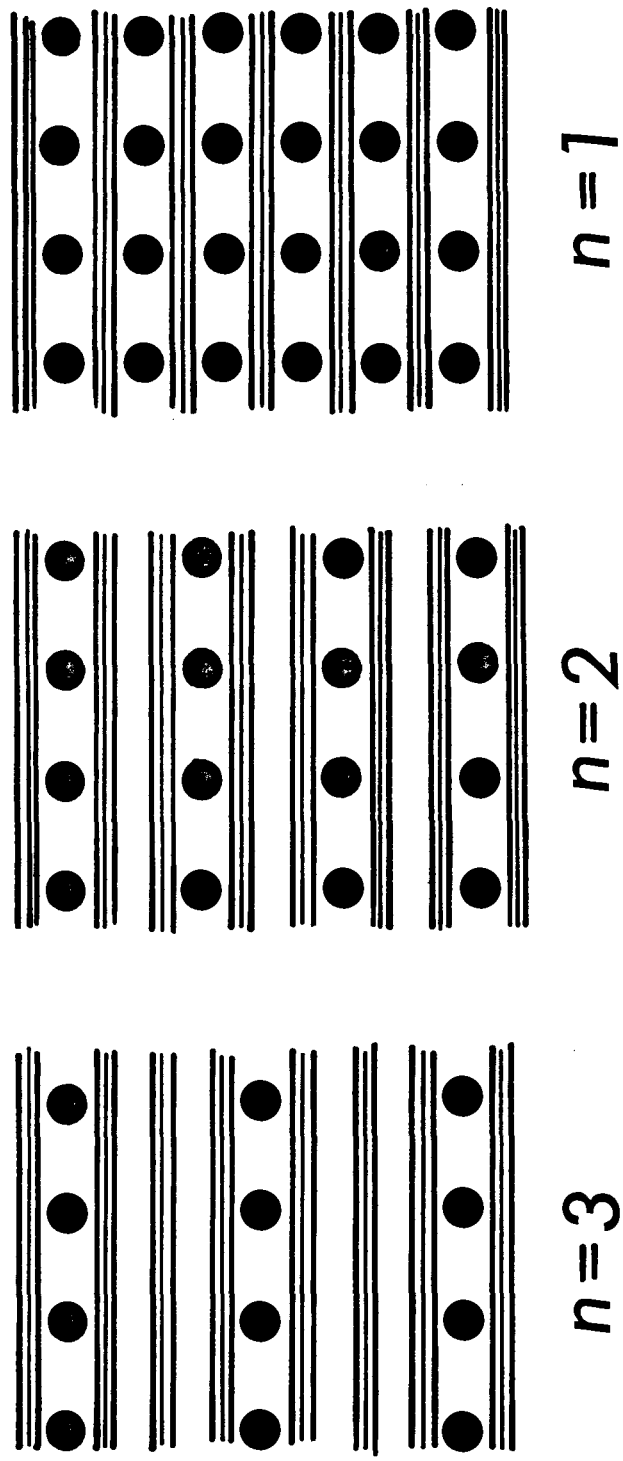
n=1
n=2
n=3

systems. Of the MCh_2 intercalation compounds, Li_xTiS_2 has become the most studied and the prime motivation behind this is its inherent potential excellence as an anode in a secondary high energy density battery [11]. However, a systematic study of Li_xTiS_2 is not without problems, if routine experimental procedures are to be used, because of lithium's highly reactive nature and its small scattering cross-section to X-rays.

To avoid these problems I have decided to use silver as the intercalate because, along with being chemically relatively inert and possessing a larger scattering cross-section, it can have the electronic simplicity of a pseudo-alkali metal. Silver's large scattering cross-section makes it easily observable with X-rays or electrons when structure determinations are performed. Furthermore, I have decided to use 2H-TaS_2 and 1T-TiS_2 as representative dichalcogenides having the trigonal-prismatic and trigonal-antiprismatic symmetry respectively. The reason for choosing 2H-TaS_2 is the great ease with which it can be intercalated and cleaved, and on the other hand 1T-TiS_2 was chosen because of its potential commercial use as a secondary battery electrode.

In order to obtain a microscopic picture of the intercalation process and, in particular, to be able to suggest mechanisms which govern processes like staging, intercalation rates and structural changes among others, it is important to carry out a systematic study, as complete as

possible, of a given intercalation system. Therefore, in this thesis, detailed results are presented in six areas that are considered to be of fundamental importance to intercalation systems. In Chapter 2 sample preparation is discussed, using both thermal and electrolytic techniques; Chapters 3, 4, 5 and 6 discuss structural changes in the host and the superstructures observed with the silver ions and/or host; Chapter 7 presents results of the open circuit potential variation of the intercalation compounds as a function of the number of mole fractions of silver intercalated; in Chapter 8 the optical transmission is investigated as the silver content varies; Chapter 9 presents observations on the intercalation and diffusion rates of silver; and, finally, in Chapter 10 an attempt is made to explain and generalize the observations on structural changes and staging. In addition, a number of structural and staging changes of the host, not yet observed, are predicted.

CHAPTER 2

SAMPLE PREPARATION

The silver intercalation compounds of 2H-TaS_2 and 1T-TiS_2 can be prepared via thermal or electrochemical methods. Thermal intercalation can have the advantage over electrolytic intercalation, if some care is exercised, of yielding a uniformly intercalated sample with the intercalate dispersed in accordance with the lowest free energy state of that particular intercalation compound. There is the drawback, however, that intercalation and deintercalation cannot be performed at will, so that, for example, the electronic or optical properties cannot be monitored continuously and reversibly as can be done if electrochemical intercalation is used. The electrochemical intercalation method is an obvious necessity for some investigations such as, for example, the study of intercalation rates. Throughout this thesis either method of sample preparation was utilized, according to whichever method was more appropriate to the situation, and at times both methods were used and a comparative study made.

2.1 Thermal Method of Sample Preparation

Some samples of Ag_xTaS_2 were prepared in a similar way as the pure dichalcogenides. Therefore, appropriate amounts of the elements, including about 1 mg. of iodine, which facilitates crystal growth, was placed in a well cleaned and

evacuated 750 cc quartz transport tube. This tube was then placed in a three zone furnace and a temperature gradient of about 50K established along its length as illustrated in Fig. 2.1 [12].

However, most of the Ag_xTaS_2 and Ag_xTiS_2 samples, having $0 < x \lesssim 2/3$ and $0 < x \lesssim 0.42$ respectively, were prepared by heating the appropriate amounts of pre-reacted dichalcogenide, either 2H-TaS_2 or 1T-TiS_2, and silver powder in a well cleaned and evacuated quartz tube at 750 C and 800 C respectively. There is no particular significance to the use of different growth temperatures for the dichalcogenides. After reacting for approximately 100 hours, the furnace was shut off and the sample allowed to cool very slowly overnight. It was found that the intercalation process will be severely impeded if small amounts of water vapour are present in the reaction tube and particular care in this regard was therefore exercised.

2.2 Electrolytic Method of Sample Preparation

Uniformity in the distribution of the intercalate throughout the sample is an area of concern when the dichalcogenides are electrochemically intercalated. Therefore, the use of small crystallites is a prerequisite for achieving uniformity of intercalation and it was found that crystals up to about 100μg (ρ_{TaS_2} = 7.1 g/cm^3; ρ_{TiS_2} = 3.2 g/cm^3)in weight intercalate quite uniformly.

Fig. 2.1

Schematic of a three-zone furnace used for thermal crystal growth. Generally the temperatures used are in the range $1000 \lesssim K \lesssim 1500$ depending on the type of crystal grown.

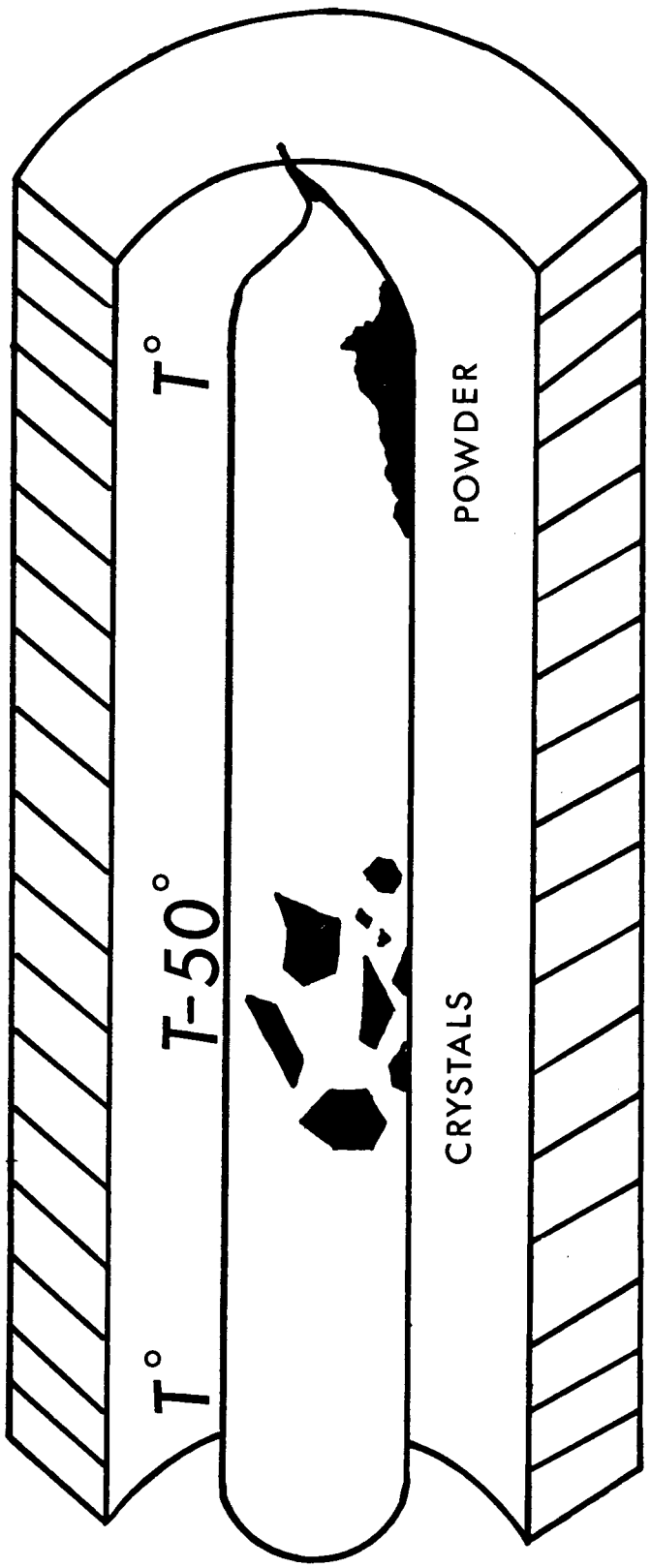
T°
T-50°
T°
POWDER
CRYSTALS

The electrochemical intercalation cell is straightforward (Fig. 2.2), consisting of a silver anode in conjunction with either 2H-TaS_2 or 1T-TiS_2 as the cathode. By completing the external circuit the cathodic and anodic half-cells

$$Ag \rightarrow Ag^+ + e^- \qquad (2.1)$$

$$MCh_2 + xAg^+ + xe^- \rightarrow Ag_xMCh_2 \qquad (2.2)$$

are able to proceed, resulting in the net reaction

$$MCh_2 + xAg \rightarrow Ag_xMCh_2 \qquad (2.3)$$

The open circuit voltages for the Ag/$AgNO_3$(0.1N)/2H-TaS_2 and Ag/$AgNO_3$(0.1N)/1T-TiS_2 electrochemical cells are about +215 mV and +150 mV respectively. Because the free energy change for both reactions is negative, they can proceed spontaneously. The choice of salt used for the electrolyte fell naturally on $AgNO_3$ since it is one of the few soluble silver salts which is readily available.

One way to determine the mole fraction of silver intercalated into the dichalcogenides is to weigh the samples before and after intercalation. This method gave the mole fractions of silver to about 5%. The weighing was done on a Cahn model G-2 electrobalance. Another method is to use X-ray fluorescence, where the intensity of the Ag L_α line is compared with the intensity of the Ta M_α or Ti K_α line.

Fig. 2.2

Galvanic cell, using $AgNO_3$ electrolyte, for preparing silver intercalated crystals.

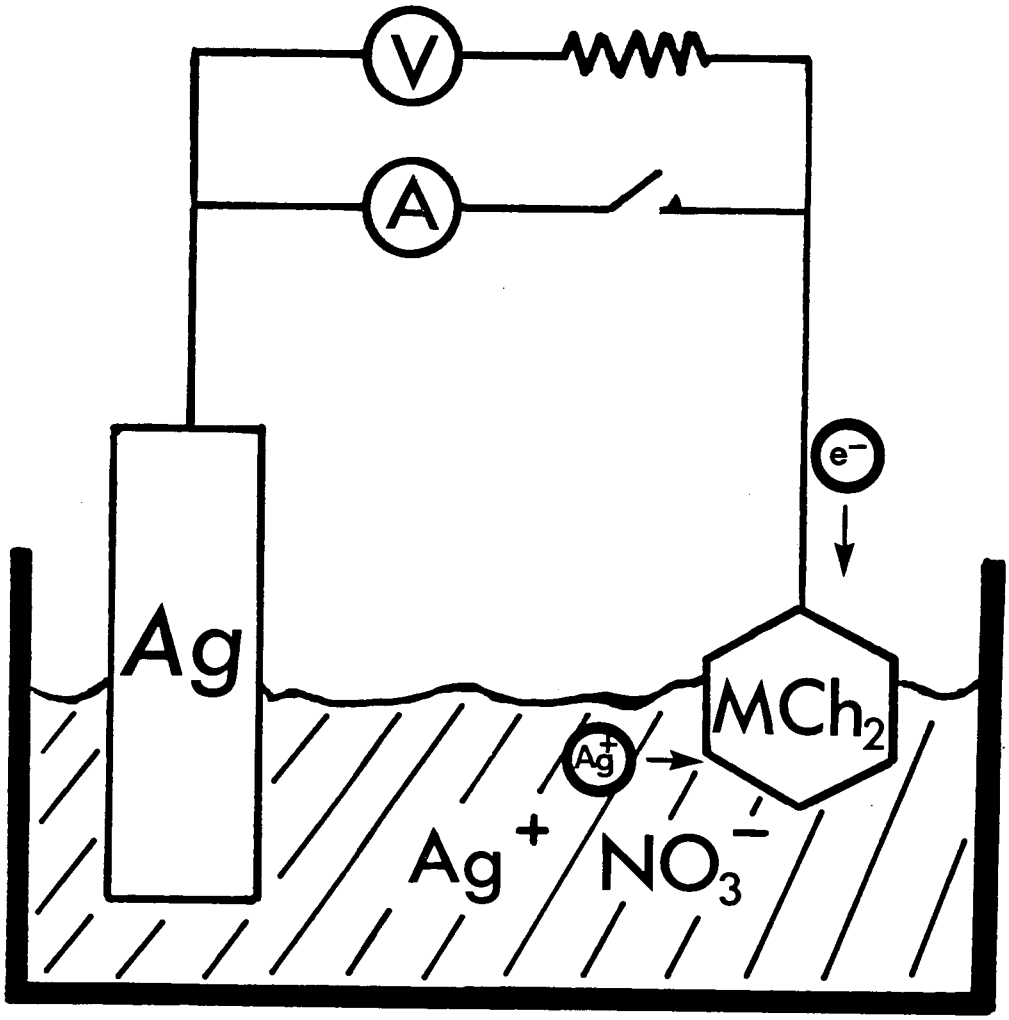
V
A
e⁻
Ag
MCh₂
Ag⁺
Ag⁺
NO₃⁻

This method will easily yield accurate information on the relative concentrations of silver present throughout, say, a single crystal but is not that accurate for determining the absolute concentration. Yet another way of determining silver concentrations in the dichalcogenide crystals is via coulometry. However, coulometry is completely inappropriate and should never be used when aqueous $AgNO_3$ solutions are used as electrolyte. The reason is that if an aqueous solvent is used to prepare the electrolyte, both 2H-TaS_2 and 1T-TiS_2 will react with the electrolyte and/or intercalate silver spontaneously, to a degree determined by the $AgNO_3$ concentration and it turns out (Chapter 9), the crystal thickness.

For lower $AgNO_3$ concentrations, in an aqueous solution, the predominant reaction becomes the intercalation of silver into the dichalcogenides and the hydrolysis of the dichalcogenides is not observed anymore. Since the only source of electrons is from the decomposition of water, that is

$$TaS_2 + H_2O \rightarrow (TaS_2OH)^- + H^+ \qquad (2.4)$$

the intercalation reaction must proceed as written in Eqn. 2.6. For example, in a 0.1N aqueous $AgNO_3$ electrolyte

intercalation into 2H-TaS_2 will proceed to a maximum mole fraction of x about 0.30 (i.e. $Ag_{0.30}TaS_2$), as determined by weighing. Of course, it is then possible to increase the silver content further by completing the external circuit (Fig. 2.2) which will enable the intercalation reaction (Eqn. 2.2) to proceed until $x \simeq 2/3$ mole fraction of silver has intercalated. Once the degree of intercalation for a given $AgNO_3$ concentration was determined via weighing and/or X-ray fluorescence, it became particularly simple to repeatedly prepare identical samples, with a given mole fraction of intercalated silver up to about 0.30, simply by placing 2H-TaS_2 powder into an aqueous $AgNO_3$ solution having the appropriate concentration.

For 1T-TiS_2, on the other hand, reducing the $AgNO_3$ concentration to 0.1N causes the cessation of any observable chemical reactions and of any appreciable intercalation, except maybe right at the crystals edges where some intercalation can still be observed for a few of the optically transparent crystallites.

The problems with spontaneous intercalation (i.e Equations (2.6) or (2.5)) can be avoided altogether if a non-aqueous electrolyte is used. This requirement can be met to a large part by dissolving $AgNO_3$ in glycerol. Although other non-aqueous solvents for $AgNO_3$ exist, such as ethanol, glycerol appears to be the best in preventing spontaneous

intercalation judging from experience. However, even with glycerol there are problems when trying to restrict the intercalant to mole fractions of about 1/10 or less unless special precautions are taken such as preparing the electrolyte in a dry box and, because of the photochemical nature of $AgNO_3$, shielding it from intense light. Of course the electrochemical cell also has to be scrupulously clean so that reducing substances, causing silver to precipitate, are not present because this would again cause spontaneous intercalation if the silver precipitate were to come into contact with the dichalcogenide. As a consequence of using the $AgNO_3$/glycerol electrolyte, coulometry has become feasible and was repeatedly used to verify the mole fraction of silver intercalated as determined via weighing.

If a saturated aqueous $AgNO_3$ solution is mixed with 2H-TaS_2 or 1T-TiS_2 powder, a chemical reaction ensues which is overall very similar for both dichalcogenides. During the reaction the crystallites alter their appearance and change from metallic looking platelets, having respectively a steel-blue and gold luster, to a material which is green-yellow in colour and disintegrates completely when touched. Furthermore, it was also possible to observe the formation of some elemental sulphur and silver, however, no sulphide odours were ever noticeable. In the case of 2H-TaS_2, one could in addition to the above also observe the formation of a gelatinous substance which is slightly milky in colour

and undoubtedly is tantalic acid, that is, $Ta_2O_5 \cdot xH_2O$. The origin of this hydrous pentoxide must be from the hydrolysis of 2H-TaS_2 and if this is correct, hydrogen ions should be produced by the hydrolysis reaction. If the pH of the electrolyte is monitored during the chemical reaction of either dichalcogenide with the aqueous $AgNO_3$ electrolyte, one does indeed observe that the pH changes from an initial value of about 5 to a final value, after the reaction, which is less than 1 so that hydrogen ions definitely are produced. This observation confirms the hydrolysis reaction in 2H-TaS_2, and therefore suggests that in addition to 2H-TaS_2, 1T-TiS_2 also undergoes a hydrolysis reaction.

After washing either of the green-yellow substances in distilled water, they again change their colour and in both cases become black. X-ray diffraction powder patterns reveal some weak lines, a number of which are quite fuzzy, but they do not correspond to any of the known diffraction patterns, or simple variations thereof, reported in Chapter 3. X-ray fluorescence results on the black powders were quite variable, but do indicate the presence of a large silver to tantalum or titanium ratio, on the order of 4 to 1, for both dichalcogenides [13]. This large ratio must be caused, at least in part, by the elemental silver which has formed and by other silver compounds, such as Ag_2S, which may well form. Therefore this ratio can not be used as a guide in identifying the black powders. Consequently, the bulk of the new material

appears to be 'amorphous' and, in view of the chemical reactions which occur, has a detailed composition which is fairly uncertain. However, I would suggest that one of the major chemical half-cell reactions, for 2H-TaS_2 in concentrated aqueous $AgNO_3$ for example, is as written in Equation 2.5 below because it satisfies all observations. In addition, one might also expect partial hydrolysis of 2H-TaS_2 to occur along with an intercalation half-cell reaction as written in Equation 2.6.

$$TaS_2 + 1/2(5+x)H_2O+5Ag^+ \rightarrow 1/2(Ta_2O_5 \cdot xH_2O) + 2Ag_2S+Ag+5H^+ \qquad (2.5)$$

$$TaS_2 + xAg^+ + xH_2O \rightarrow Ag_xTaS_2(OH)_x + xH^+ \qquad (2.6)$$

1T-TiS_2 likely undergoes similar reactions, except that the hydrated oxide is probably a dioxide instead of a pentoxide. Therefore, it is very likely that the end products obtained by reacting the dichalcogenides with a concentrated aqueous silver nitrate solution consist in large part of the dichalcogenides which are hydrolyzed to various degrees, along with silver sulphide and some elemental silver. For further observations and comments on this reaction see Chapter 9.

CHAPTER 3

STRUCTURE AND STAGING IN Ag_xTaS_2 AND Ag_xTiS_2

3.1 Experimental Arrangement and Procedure for X-ray Studies

Samples of Ag_xTaS_2 and Ag_xTiS_2 were predominantly prepared thermally with $0 < x \lesssim 2/3$ and $0 < x \lesssim 0.42$ mole fraction of silver respectively, by heating the appropriate amount of pre-reacted dichalcogenide powder (2H-TaS_2 or 1T-TiS_2) and silver powder in an evacuated quartz tube at 750 C and 800 C respectively for approximately 100 hours and then letting it cool slowly overnight (see Chapter 2).

Single intercalated crystals of Ag_xTaS_2 and Ag_xTiS_2 were also prepared by using the crystals as an cathode in an electrochemical cell having a silver anode (see Chapter 2).

Powder patterns of these samples were recorded using CuK_α radiation and a Debye-Scherrer camera. A Geiger-counter spectrometer was used occasionally to verify the intensity estimates for the powder patterns. Samples were affixed to glass fibers with nail polish and because the powder consists of tiny platelets, some preferred orientation occurs such that the (00.ℓ) lines have a much stronger intensity than others and appear as fairly short arcs, rather than circles, on the film. Both of these characteristics allow an unambiguous identification of the (00.ℓ) lines. A consideration of the relative intensities and systematic

absences of certain lines then allows the determination of the stacking sequence of the TaS_2 and TiS_2 sandwiches and the site occupancy of the silver intercalant. It should be noted that because of the preferred orientation of the crystallites, no comparison can be made between the intensities for, say, (00.ℓ) and (hk.0) lines.

3.2 Results of X-ray Diffraction Studies on Ag_xTaS_2 and Ag_xTiS_2 at Room Temperature

Diffraction powder photographs were first taken of the pure dichalcogenides 2H-TaS_2 and 1T-TiS_2 to verify their quality (Fig. 3.2c, Fig. 3.6c). The unit cells and the lattice constants are shown in Fig. 3.1 and agree with those found by others [14,15].

When determining the structures for the intercalated dichalcogenides, it is assumed that to a first approximation the S-M-S sandwiches will remain intact and unchanged. This seems reasonable considering the strong covalent intralayer bonding. In particular, when calculating structure factors for the intercalated systems, it is assumed that the separation of the neighbouring tantalum and sulphur planes remains constant at 1.57Å [16] and those of the titanium and sulphur planes at 1.48Å [17]. Furthermore, no attempts were made to apply any corrections to the square of the structure factor, $|F(hk.\ell)|^2$ so that it might more closely resemble the

Fig. 3.1

The $(11\bar{2}0)$ diagonal cross section of the unit cells.

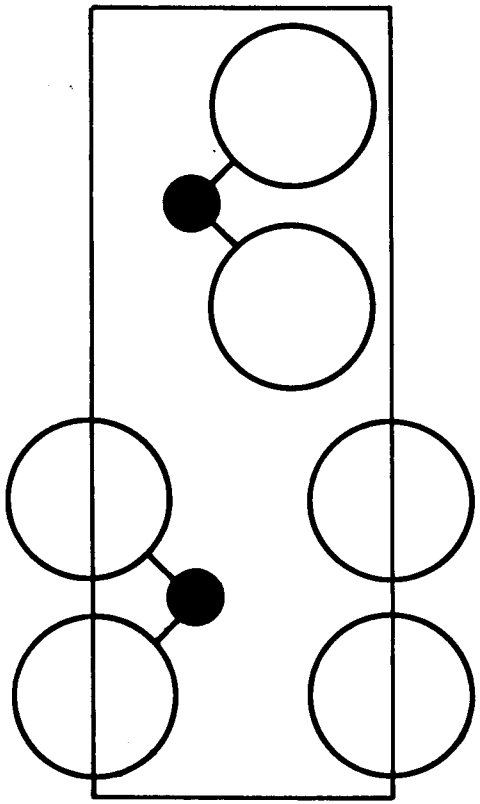

$2H_b - TaS_2$

$a_o = 3.315 \pm 0.001$ Å

$c_o = 12.08 \pm 0.02$ Å

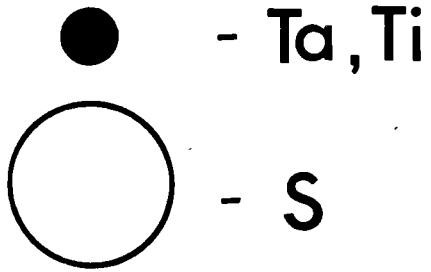

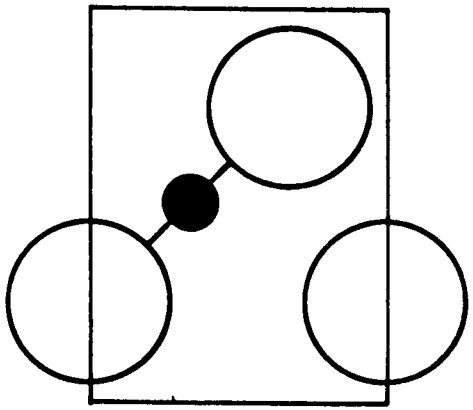

$1T - TiS_2$

$a_o = 3.404 \pm 0.001$ Å

$c_o = 5.696 \pm 0.003$ Å

actual intensity scattered from the lattice plane (hk.ℓ). Therefore, in particular, since the observed intensities of the diffracted lines decrease as the scattering angle increases, useful comparisons of $|F(hk.\ell)|^2$ should only be made for adjacent lines.

A. The Ag_xTaS_2 Intercalation Compounds

(a) $Ag_{2/3}TaS_2$

It is found that $x \simeq 2/3$ corresponds to the maximum mole fraction of silver which can be intercalated into 2H-TaS_2 both thermally and electrolytically. The powder pattern of $Ag_{2/3}TaS_2$ is shown in Fig. 3.2(a). This pattern allows the determination of the unit cell parameters $a_o = 3.335 \pm 0.001$Å and $c_o = 14.42 \pm 0.02$Å corresponding to 2 layers per unit cell. These lattice parameters are obtained from indexing all lines (i.e. ~50 lines up to $2\theta \sim 150°$), with a fit which is better than 0.2% in all cases.

It can be seen in Fig. 3.2(a) that there are no systematic absences among the (10.ℓ) reflections. However, the (00.ℓ) reflections are absent for ℓ odd. In fact, absences for ℓ odd are observed in (hk.ℓ) whenever $h-k = 3n$ ($n = 0,1,2,...$) and therefore the structure can be referred to the same space group as 2H-TaS_2, namely $P6_3/mmc$ (i.e. D_{6h}^4). The layer stacking sequence of pure 2H-TaS_2 is given by

Fig. 3.2

X-ray powder pattern lines for: (a) $Ag_{2/3}TaS_2$; (b) $Ag_{1/3}TaS_2$. and (c) 2H-TaS_2. The length of the lines qualitatively indicates the blackness of the film.

(a)
002
004
100
101
102
103
006
104
105
008
110
112
108
114
200
109
203
116
205
(b)
006
009
0012
101
104
105
0015
107
108
0018
1013
1014
0021
110
0024
116
119
1022
1112
0027
201
205
207
208
1026
2013
2014
(c)
002
004
100
101
102
103
104
006
105
110
112
008
114
200
202
204
116
10
20
30
40
50
60
70
2θ

AcA/BcB. With this arrangement, intensity calculations predict that reflections with ℓ even (except those for which h-k = 3n) are always stronger than with ℓ odd, as is seen in Fig.3.2(c). However, for $Ag_{2/3}TaS_2$ it can be seen that reflections with ℓ odd are always stronger than those with ℓ even. In fact, for the (20.ℓ), (21.ℓ) and (31.ℓ) lines, only ℓ odd is observable. Such intensity changes mean that the tantalum stacking sequence in $Ag_{2/3}TaS_2$ is not the same as in pure 2H-TaS_2.

A systematic displacement of TaS_2 sandwiches allows the generation of the remaining two stacking sequences AcA/AbA and AcA/CaC. The line intensities $|F(hk.\ell)|^2$ are then determined for both stacking sequences and all possible intercalant positions, where the silver ions are assumed to occupy the intercalation sites symetrically on either ordered or random positions. On comparing these to the oberved intensities it becomes immediately clear that the correct stacking sequence is AcA/CaC, known as the MoS_2 structure, with the silver ions occupying tetrahedral sites (Fig. 3.3, Table 3.1). One cannot, however, conclude anything about the possible ordering of the silver ions on these tetrahedral sites because an ordered and disordered arrangement produces very similar intensities. It should be pointed out though that the qualitative (00.ℓ) intensity pattern observed agree well with that calculated, justifying the assumption that the TaS_2 sandwich height is not significantly changed after

Fig. 3.3

$(11\bar{2}0)$ section of the $Ag_{2/3}TaS_2$ unit cell. One-third of the tetrahedral sites are occupied with silver ions.

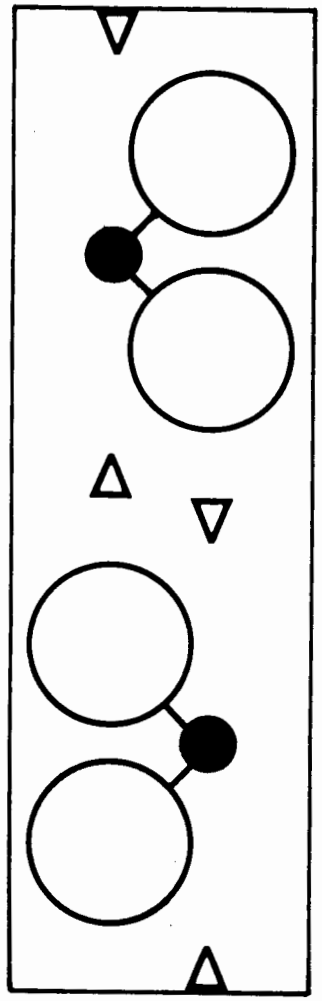

● – Ta

○ – S

Δ – Ag

$a_o = 3.335 \pm 0.001$ Å

$c_o = 14.42 \pm 0.02$ Å

Table 3.1

The structure factor squared, $|F|^2$ (calc.), is calculated for silver ions in octahedral (oct.) and tetrahedral (tet.) sites for the structure in Fig. 3.3, and compared to the estimated blackness, F (obs.), of the film. The silver ions are preferred in tetrahedral sites.

TABLE 3.1

(10.ℓ)	F(obs.)	$\|F\|^2$(calc.)	
		Oct.	Tet.
0	vst	3	32
1	vst(-)	16	20
2	w	36	5
3	st	41	25
4	w	3	9
5	vst	54	90
6	--	27	5
7	--	28	9
8	vw	2	14
9	m	12	31

intercalation.

By short-circuiting several single crystal Ag/TaS_2 electrochemical cells for several weeks, the change in weight of the crystals corresponds to an uptake of 0.69 ± 0.06 mole fraction of silver. The X-ray powder photograph of the crystals cut into several small pieces, showed the identical pattern to that obtained from thermally intercalated $Ag_{2/3}TaS_2$ powder. There was, however, no indication of any spottiness in the diffraction pattern thus indicating that electrochemical intercalation breaks up the single crystals into small microcrystals with random orientation.

(b) $Ag_{1/3}TaS_2$

For $Ag_{1/3}TaS_2$ there are no systematic absences observed for ℓ odd and h-k = 3n, if a two layer unit cell is assumed. In fact, all ℓ's are observed. By indexing the 60 reflections, again to within 0.2%, it appears that there are six TaS_2 layers per unit cell (Fig. 3.2b). The unit cell parameters are a_o = 3.329 ± 0.001Å and c_o = 39.66 ± 0.06Å. If, for the moment, the increase in unit cell due to the stacking arrangement is ignored, then the simplest way to account for the presence of all (00.ℓ) lines is by assuming that there are two different interlayer spacings which will prevent the destructive interference for ℓ odd that occurs when the layers are evenly spaced. Therefore, it would not be unreasonable to assume that there are full and empty layers

alternating, i.e., a stage 2 compound. Since there are 1/3 mole fraction of silver ions present, the full layers will have to fill to x = 2/3 as in $Ag_{2/3}TaS_2$. Therefore, by assuming that the empty layers retain their c spacing of 6.04Å, as in pure 2H-TaS_2, then the full layers must expand to 7.18Å to account for the observed c_o spacing in $Ag_{1/3}TaS_2$ (i.e. [6.04 + 7.18] x 3). It is gratifying that this lattice spacing is also is quite comparable to the 7.21Å interlayer spacing observed for $Ag_{2/3}TaS_2$.

To determine the stacking sequence of the TaS_2 layers, the structure factor of the mixed reflections again needs to be calculated. In order to do this it is assumed that to a first approximation only 3 of the six van der Waals gaps will expand by 7.18Å to accommodate the silver ions. After calculating $|F(hk.\ell)|^2$ for all reasonable stacking sequences, including non-alternating empty/intercalated layers, good agreement is only obtained with the stacking arrangement shown in Fig. 3.4. The important reflections and calculated structure factors are given in Table 3.2 and are in good qualitative agreement. The silver ions again occupy tetrahedral sites but it is again impossible to ascertain whether or not they are ordered.

Soaking 2H-TaS_2 single crystals in an aqueous 0.1N $AgNO_3$ electrolyte produces a stage 2 diffraction pattern identical to that obtained for thermally prepared $Ag_{1/3}TaS_2$. The quality of the powder pattern again indicates that the crystal

Fig. 3.4

($11\bar{2}0$) section of the $Ag_{1/3}TaS_2$ unit cell. The silver ions are occupying 1/6 of the available tetrahedral sites. Note that the Ta's are staggered wherever silver intercalates.

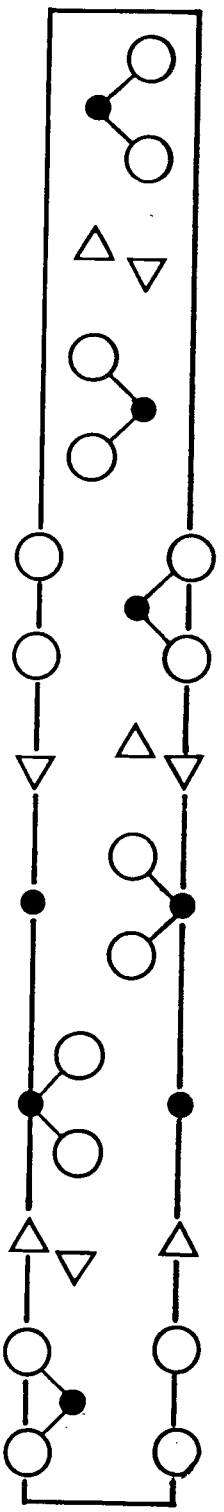

● - Ta

○ - S

△ - Ag

$a_o = 3.329 \pm 0.001$ Å

$c_o = 39.66 \pm 0.06$ Å

Table 3.2

Comparison of the important diffraction lines for the $Ag_{1/3}TaS_2$ structure, as in Table 3.1.

TABLE 3.2

(10.ℓ)	F(obs.)	$\|F\|^2$(calc.)	
		Oct.	Tet.
0	--	0	0
1	vst	16	35
2	--	8	1
3	--	0	0
4	w	0	3
5	m/st	33	19
6	--	0	0
7	st	53	24
8	st(+)	18	30
9	--	0	0
10	--	10	0
11	--	1	2
12	--	0	0
13	vst	36	72
14	vst(-)	71	60
15	--	0	0
16	--	3	1
17	--	4	3
18	--	0	0

has broken up into small microcrystals having random orientations.

(c) Mixed Phases of Ag_xTaS_2

For silver concentrations within about $0.40 \lesssim x \lesssim 0.55$ in Ag_xTaS_2 a composite of stage 2 and 1 diffraction patterns is found. At $x = 7/12$ the powder pattern shows that the sample is completely stage 1 with essentially the same lattice parameters as those for $x = 2/3$. There are small differences in some of the diffraction line intensities as is to be expected from the lower silver content. For $x = 5/12$, all (00.ℓ) lines for both stage 2 and 1 structures are found. However, the line corresponding to the mixed indices with large ℓ values of the stage 2 structure are quite diffuse.

By analogy with the graphite intercalation compounds, a stage 3 structure should exist when $x = 0.22$. This was definitely not observed. In fact, no higher stage structure was observed for any value of $x < 1/3$. It was found that up to $x \simeq 0.08$ no significant change occurred in the crystal structure, and above this concentration the stage 2 structure starts developing. However for concentrations of $0.08 \lesssim x \lesssim 0.30$ the mixed reflections, especially for larger ℓ values, are again broad and diffuse but become sharper as $x = 1/3$ is approached. It should be pointed out explicitly that even though the mixed reflections become diffuse, all the (00.ℓ) and (hk.0) reflections remain sharp. This indicates that the

Fig. 3.5

The lattice parameters and stage (n) of Ag_xTaS_2 as a function of the mole fraction of silver intercalated. Note that c_o' refers to the average separation between layers.

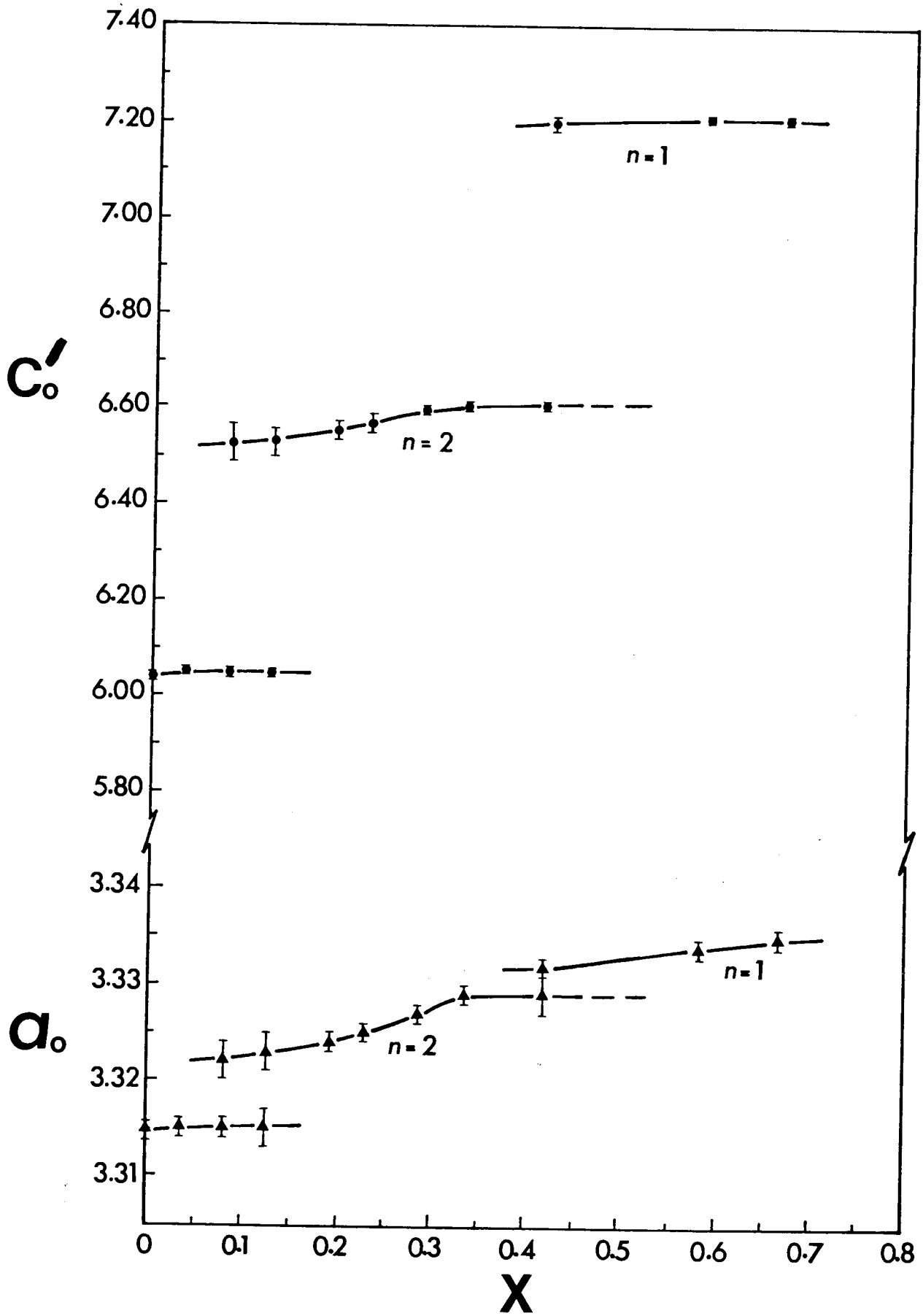
7.40
7.20
7.00
6.80
6.60
6.40
6.20
6.00
5.80
c_o'
n = 1
n = 2
3.34
3.33
3.32
3.31
a_o
n = 1
n = 2
0
0.1
0.2
0.3
0.4
0.5
0.6
0.7
0.8
X

staging of the silver intercalate and the integrity of the TaS_2 layers is in no way compromised. Therefore, the diffuse lines for the mixed reflections are caused by an incomplete stacking sequence of the TaS_2 layers and indicates that the relatively long range 3-dimensional correlation of the TaS_2 layers, for stage 2, is relatively quickly destroyed unless the silver concentration is within about ±0.05 of x = 1/3.

In Fig. 3.5 the lattice parameters and the stage (n) of Ag_xTaS_2 is shown as a function of the silver content. All the samples were thermally prepared to guarantee a uniform silver distribution.

B.) The Ag_xTiS_2 Intercalation Compounds

(a) $Ag_{0.42}TiS_2$

The maximum mole fraction of silver which could be electrochemically intercalated into TiS_2 via a short-circuited Ag/TiS_2 electrochemical cell, having a 0.1N aqueous electrolyte, was determined by weighing five samples and was consistently found to be within 0.42 ± 0.02 mole fraction. When attempting thermal intercalation with larger mole fractions, pure silver diffraction lines were observed. Both the thermal and electrochemical methods of preparation yielded identical powder patterns.

The X-ray diffraction pattern for $Ag_{0.42}TiS_2$ (Fig. 3.6a)

Fig. 3.6

X-ray powder pattern lines for: (a) $Ag_{0.42}TiS_2$; (b) $Ag_{0.20}TiS_2$ and (c) 1T-TiS_2. The length of the lines qualitatively indicates the blackness of the film.

(a)
001
100
002
101
102
003
103
110
004
201
104
202
005
(b)
002
003
100
101
102
103
005
104
007
110
106
112
113
107
008
203
202
009, 108
204
(c)
001
002
101
003
102
110
111
103
113
202
201, 004
10
20
30
40
50
60
70
2θ

shows no systematic absences and can be referred to the space group P3ml (ie. $D_{3d}2$), the same as that of 1T-TiS_2. The unit cell parameters are $a_o = 3.437 \pm 0.001$Å and $c_o = 6.445 \pm 0.003$Å again determined by indexing to within 0.2% the 30 diffraction lines observed. The best fit of $|F(hk.\ell)|^2$ to the observed intensities (Table 3.3) is obtained when placing the silver ions in octahedral sites (Fig. 3.7). Raman scattering results for $Ag_{1/3}TiS_2$ [68] are also best explained if the silver ions are placed into octahedral sites.

Electron diffraction by single crystals of $Ag_{0.42}TiS_2$, electrochemically prepared, showed a very fuzzy $\sqrt{3}a_o$ superlattice along $\langle 11.0 \rangle$ at room temperature. When the sample was cooled to about -150C, these superlattice satellites slowly sharpened and eventually became more intense than the main diffraction spots. This shows that the silver ions are ordering on a $\sqrt{3}a_o$ superlattice within the van der Waals gap [7]. It seemed likely that this ordering of the silver ions might also be observable in powder patterns. In Fig.3.8c a powder pattern of $Ag_{0.30}TiS_2$ (mostly stage 1) cooled to -80C indeed shows an extra diffracted line. At higher temperatures (Fig.3.8) the extra diffraction line becomes progressively more diffuse. Notice that the line terminates sharply on the low-angle side but falls off gradually in intensity on the high-angle side. This is scattering characteristic of a random two-dimensional layer lattice. Therefore, since the host

Fig. 3.7

$(11\bar{2}0)$ section of the $Ag_{0.42}TiS_2$ unit cell. 0.42 of the octahedral sites are occupied with silver ions.

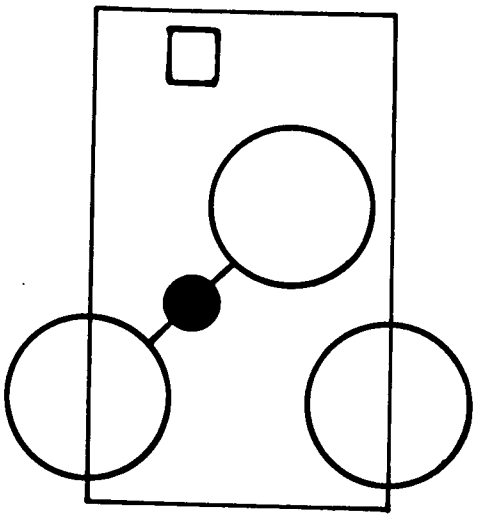

● – Ti

○ – S

□ – Ag

$a_o = 3.437 \pm 0.001$ Å

$c_o = 6.445 \pm 0.003$ Å

Table 3.3

Comparison of the important lines for the $Ag_{0.42}TiS_2$ structure, as in Table 3.1. The silver ions are preferred in octahedral sites.

TABLE 3.3

(10.ℓ)	F(obs.)	$\|F\|^2$(calc.)	
		Oct.	Tet.
0	m/st	4	2
1	vst	15	31
2	vst(+)	56	22
3	st	15	26
4	st	14	8
5	m/w	10	10
6	vst	55	43
7	vw	10	22
8	st(+)	27	15

TiS_2 unit cell is not changing and the silver ions are ordering in the basal planes at low temperatures as determined from the electron diffraction results in Ch. 6, this extra line most likely corresponds to the silver ions ordering in the basal planes. When indexing the extra line as a (10.0) line of a $\sqrt{3}a_o$ superlattice, a_o is calculated to be 3.20 ± 0.04Å. However, this value of a_o is in considerable disagreement with the value of a_o = 3.42 ± 0.04Å as determined from the (10.0) line of the host lattice. Very surprisingly this line can be indexed very well as a (00.4/3) line, suggesting that the new low temperature unit cell is $3c_o$ perpendicular to the basal planes. However, this agreement is thought to be fortuitous since the line shape suggests very strongly that a superlattice in the basal planes, which is randomly stacked, is causing it. Therefore, in order to obtain agreement with the known host lattice cell parameters, this line likely corresponds to a (10.1) reflection from a $\sqrt{3}a_o$ x c_o unit cell.

(b) $Ag_{0.20}TiS_2$

By analogy with the 2H-TaS_2 intercalation compounds, $Ag_{0.20}TiS_2$ might also be expected to have a stage 2 structure. The X-ray diffraction pattern of a thermally prepared sample, shown in Fig. 3.6b, confirms this. Again, all the observed diffraction lines (~40) can be indexed with

Fig. 3.8

Powder pattern photographs of $Ag_{0.30}TiS_2$ for various temperatures; (a) about 70C; (b) room temperature; (c) about -80C.

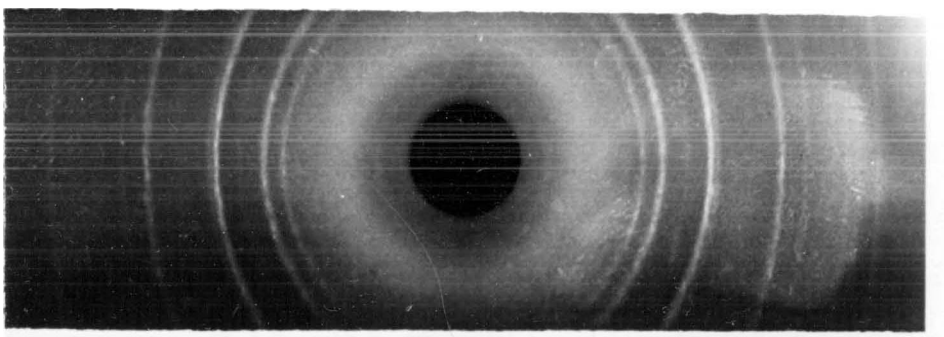

(a)

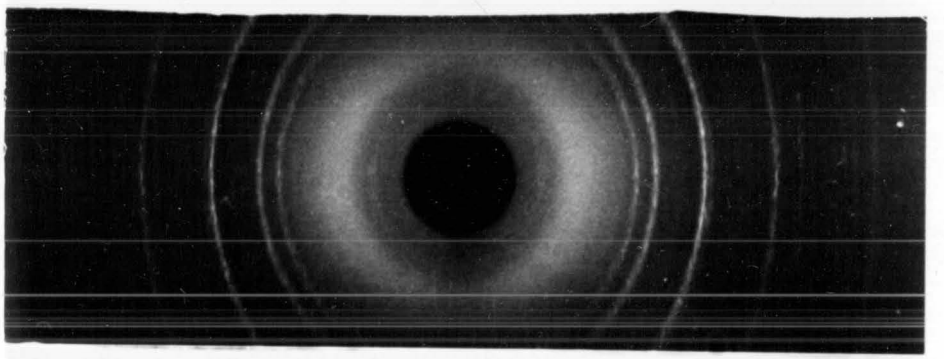

(b)

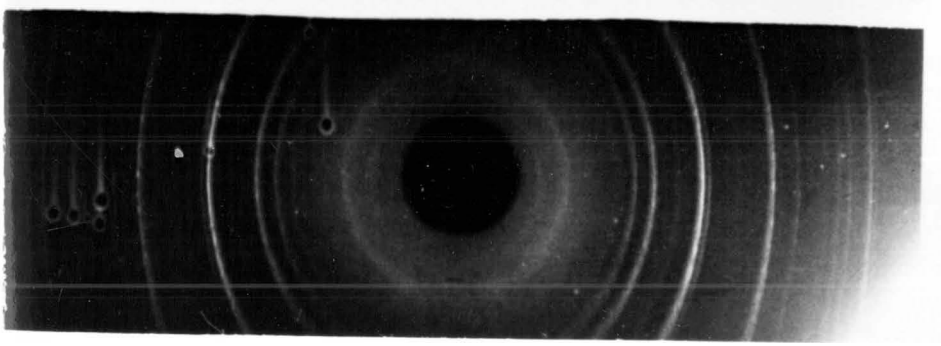

(c)

an accuracy of better than 0.2%. There are no systematic absences for ℓ when h-k = 3n. Indexing the mixed reflections shows that there are two layers per unit cell. So, $Ag_{0.20}TiS_2$ is a stage 2 compound with a_o = 3.416 ± 0.001Å and c_o = 12.145 ± 0.005Å. $|F(hk.\ell)|^2$ (Table 3.4) for the diffracted lines was calculated by assuming that in unintercalated regions the c spacing remains at 5.70Å, which implies that the intercalated regions (where x = 0.40) expand to 6.445Å which is in perfect agreement with c_o found for $Ag_{0.42}TiS_2$. The structure deduced is shown in Fig. 3.9, where the silver ions are in octahedral sites and again it is impossible to ascertain whether or not they are ordered.

(c) Mixed Phases of Ag_xTiS_2

For concentrations of silver between about $0.25 \lesssim x \lesssim 0.35$, a composite of stage 2 and 1 diffraction patterns is found. For lower concentrations, pure stage 2 exists down to below x = 0.15 with only slight variations in the lattice parameters. For lower mole fractions of silver no higher stages are observed. There was, however, some question about stage 4 developing when x = 0.10, since the c_o parameter of 5.91 ± 0.03 Å is very similar to that expected for a stage 4 compound, namely (3 x 5.70 + 6.45)/4 = 5.89Å. However, the structure factor calculation for such a stage 4 compound predicts some strong lines which are not observed.

Fig. 3.9

($11\bar{2}0$) section of $Ag_{0.20}TiS_2$. 0.20 of the octahedral sites are occupied by silver ions.

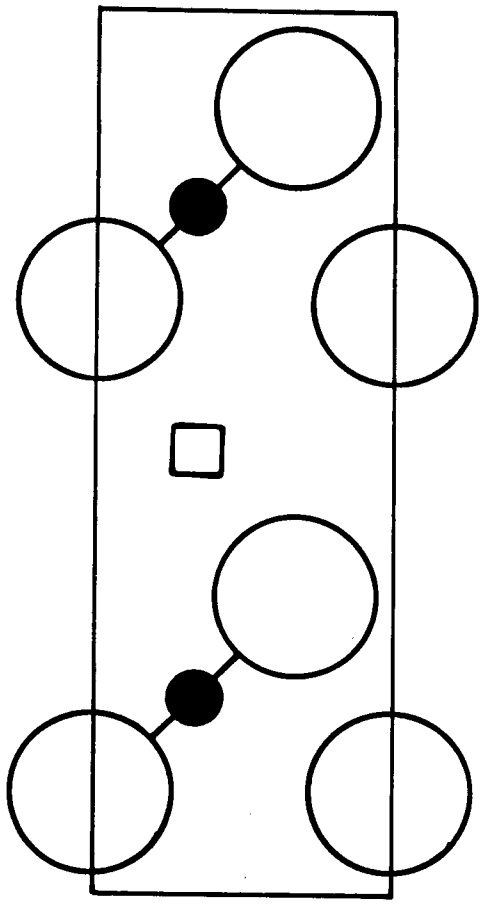

● - Ti

○ - S

□ - Ag

$a_o = 3.416 \pm 0.001$ Å

$c_o = 12.145 \pm 0.005$ Å

TABLE 3.4

Comparison of the important lines for the $Ag_{0.20}TiS_2$ structure, as in Table 3.1. Again, the silver ions are preferred in octahedral sites.

TABLE 3.4

(10.ℓ)	F(obs.)	$\|F\|^2$(calc.)	
		Oct.	Tet.
0	m(+)	4	0
1	m(-)	3	2
2	vst(+)	42	74
3	st	16	2
4	vst(+)	87	51
5	w	5	12
6	m	31	28
7	m(-)	20	24

For $x \lesssim 0.08$ the structure is essentially the same as that of pure TiS_2. The small lattice expansion which does take place is very similar to that observed in the $Ti_{1+a}S_2$ system for $a \lesssim 0.08$ [19]. When $0.08 \lesssim x \lesssim 0.15$ the diffraction patterns showed very few lines. In particular, they did not show lines, like (00.3), characteristic of the stage 2 structure. All lines could be indexed as (hk.1) and (hk.2) reflections. However, since $c \simeq \sqrt{3}\, a_o$, those reflections having large ℓ values superimpose on those having lower ℓ values and higher h and k values. It would therefore seem that in this concentration region stage 2 has not formed and the TiS_2 lattice is simply expanding to accommodate the silver ions. It is interesting to note though that the lattice expansion is very much greater than that observed in the $Ti_{1+a}S_2$ system [19].

In Fig. 3.10 a summary of the lattice parameters and the stage (n) of Ag_xTiS_2 is shown as a function of the mole fraction of silver intercalated. Again all the samples, except for x = 0.37 and 0.42, were thermally prepared while the two others were electrochemically prepared.

3.3 Discussion of the Ag_xTaS_2 and Ag_xTiS_2 X-Ray Diffraction Results

Using silver as the intercalant has shown that, respectively, octahedral and tetrahedral sites will be predominantly filled in the 1T-TiS_2 and 2H-TaS_2 hosts.

Fig. 3.10

The lattice parameters and stage (n) of Ag_xTiS_2 as a function of the mole fraction of silver intercalated.

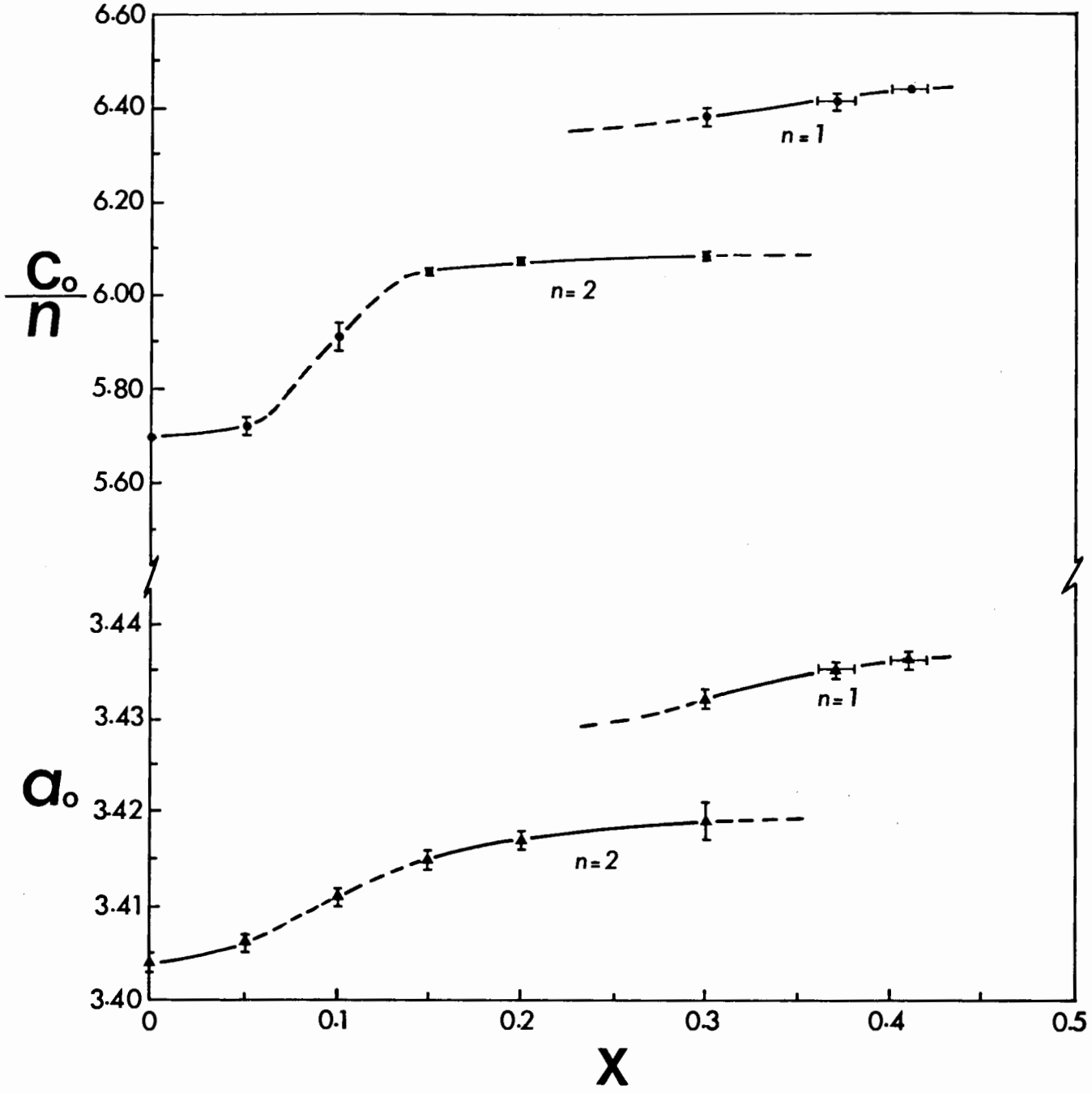
6.60
6.40
6.20
$\frac{c_o}{n}$
6.00
5.80
5.60
n = 1
n = 2
3.44
3.43
a_o
3.42
3.41
3.40
n = 1
n = 2
0
0.1
0.2
0.3
0.4
0.5
X

However, this does not mean that the other site is never occupied, but it is difficult, due to lack of absolute intensity measurements, to quote a fractional occupancy of a given site.

In almost all intercalation compounds the intercalate resides in octahedral (trigonally distorted) or trigonal prismatic sites. Silver and copper [20] are quite unique in that they reside in tetrahedral sites in the Ta and Nb dichalcogenides. Furthermore, for these intercalates it is also true that the layers slip with respect to each other wherever silver (or copper) intercalates. In TiS_2, where the silver ions occupy octahedral sites, the layers do not slip. The cause of this might well be that in TaS_2 the charge transferred to the tantalum "$d_{z}2$ orbitals" (which are ideally already 1/2 full) when the silver intercalates, will increase the Coulomb repulsion to the point where the TaS_2 layers slide so that the Ta's are staggered in the $\hat{c}$ direction (Figs. 3.3, 3.4). However, in TiS_2 the charge transferred to the titanium "$d_{z}2$ orbitals" (which are ideally unoccupied) will increase the overlap integral for metal-metal bonding and this may in fact be the reason why the silver ions are found in octahedral sites. More support for this idea will be found in Chapter 5 and a more detailed discussion for the "slippage" of layers and the site occupancy of the silver ions is presented in Chapter 10.

For both Ag_xTaS_2 and Ag_xTiS_2 prepared either thermally

or electrochemically, only stages n = 2 and 1 are observed. Furthermore, both methods of sample preparation gave identical lattice parameters, which is also the case for $Cu_{2/3}TaS_2$ [21]. This is in contrast to alkali metal intercalates [22] where the c spacings are greater for samples prepared in aqueous electrolytes and indicates that co-intercalation of water does not occur when Ag_xTaS_2 and Ag_xTiS_2 are electrochemically prepared.

The lattice parameters suggest that if either dichalcogenide is thermally intercalated at low concentrations, the intercalate will be uniformly distributed throughout the host structure forming a dilute stage 1 compound. As the mole fraction of intercalate is increased to $x \sim 0.08$ in Ag_xTaS_2, stage 2 regions begin to form and will coexist with dilute stage 1 regions (Fig. 3.5). Therefore, presumably to relieve the crystal strain but at the expense of Coulomb interactions and the need to separate layers, the intercalate will coalesce into islands which will stage with n = 2, thereby reducing the overall crystal free energy (see Chapter 10 for more detail). As x is further increased, stage 2 will grow at the expense of the dilute stage 1. Pure stage 2 is observed for $0.17 \lesssim x \lesssim 0.38$ and for higher concentrations, regions of stage 1 begin to form. These again will grow at the expense of stage 2 if x is further increased until finally, for $x \gtrsim 0.55$ only stage 1 is

observed. These observations agree with Safran's phase diagram for staging [23].

For Ag_xTiS_2 essentially the same sequence of events is observed, except that the coexistence of the dilute stage 1 and stage 2 phases is not observed when $0.08 \lesssim x \lesssim 0.15$ (Fig. 3.10). Instead, the dilute stage 1 structure persists for these concentrations until stage 2 forms at $x \simeq 0.15$. This suggests that T/U_o in Safran's staging model [23] (U_o is the average in-plane interaction and T is the temperature) is large enough to allow a second order transition from dilute stage 1 (i.e. "gas") to stage 2.

To check a prediction of Safran's staging phase diagram [23], a $Ag_{5/12}TaS_2$ sample (normally prepared at 750 C and cooled slowly) was prepared at 850C and quenched to room temperature in an attempt to lock in the phase existing at this higher temperature. The X-ray powder pattern showed that it had completely converted to stage 2 from that of a mix of stage 1 and 2, in agreement with the change expected from the phase diagram.

CHAPTER 4

SUPERLATTICES AND ELECTRICAL RESISTIVITY IN $Ag_{1/3}TaS_2$ AND $Ag_{2/3}TaS_2$

4.1 Experimental Arrangement and Procedure

Electron diffraction patterns and the electrical resistivity were both obtained as a function of temperature for stage 1 and stage 2 single crystals of $Ag_{2/3}TaS_2$ and $Ag_{1/3}TaS_2$ respectively. The samples were electrochemically prepared as described in Chapter 2. The amount of intercalated silver was determined via weighing and because there are variations in the quality of intercalation, X-ray powder patterns were taken to identify and eliminate those samples containing mixed phases and to give assurance that the host crystal structure is properly developed.

The resistivity measurements were made in the basal plane using a four-probe technique down to liquid helium temperature. The electron diffraction patterns were obtained with crystallites peeled from the same samples, using a Phillips E.M. 300 electron microscope at 100kV with a cooling stage that cooled samples to about 25K [24]. The electron beam size was typically about 1μm.

4.2 Results of Low Temperature Superlattice Formation and Electrical Resistivity in $Ag_{2/3}TaS_2$ and $Ag_{1/3}TaS_2$

(a) $Ag_{2/3}TaS_2$ Superlattices and Electrical Resistivity

In this stage 1 intercalation compound the silver ions reside in tetrahedral sites as determined in Chapter 3, and the room temperature electron diffraction pattern is shown in Fig. 4.1a. The diffraction spots correspond to a (00.ℓ) section of the TaS_2 reciprocal lattice basal plane and the very much weaker spots, half-way between the main spots, correspond to an apparent "$2a_o$" superlattice. In addition to these satellites, diffuse scattering is observed. When cooling to about 25K the formation of two further superlattices is always observed. The second superlattice (Fig. 4.1b) appears below about 200K and has satellites, less intense than the "$2a_o$" satellites, half-way again between the "$2a_o$" satellites, but none between the "$2a_o$" and the main lattice spots. These satellites are referred to as "$4a_o$" satellites. Below about 90K a third, rather complex pattern (Fig. 4.1c), is observed.

The "$2a_o$" satellites (Fig. 4.1a) exhibit a history, with temperature cycling, and also show a sample dependent behaviour. They are typically observed at room temperature, but deviations of about ±20K in their occurrence are not uncommon. The history dependence is related to the rate at

Fig. 4.1

Diffraction patterns of stage 1 $Ag_{2/3}TaS_2$ with the beam perpendicular to the basal plane. (a) At about 250K; the apparent "$2a_o$" superlattice and the diffuse hexagons around the main spots developed near room temperature. Stage 2 $Ag_{1/3}TaS_2$ has a virtually identical pattern for these temperatures. (b) At about 150K; below about 200K additional "$4a_o$" superlattice satellites appear and the diffuse scattering is beginning to coalesce into further satellites. (c) At about 25K; below about 90K the diffuse scattering is replaced by these new satellites.

(Photographs kindly taken by Mr. M. Smith and Dr. A.E. Curzon.)

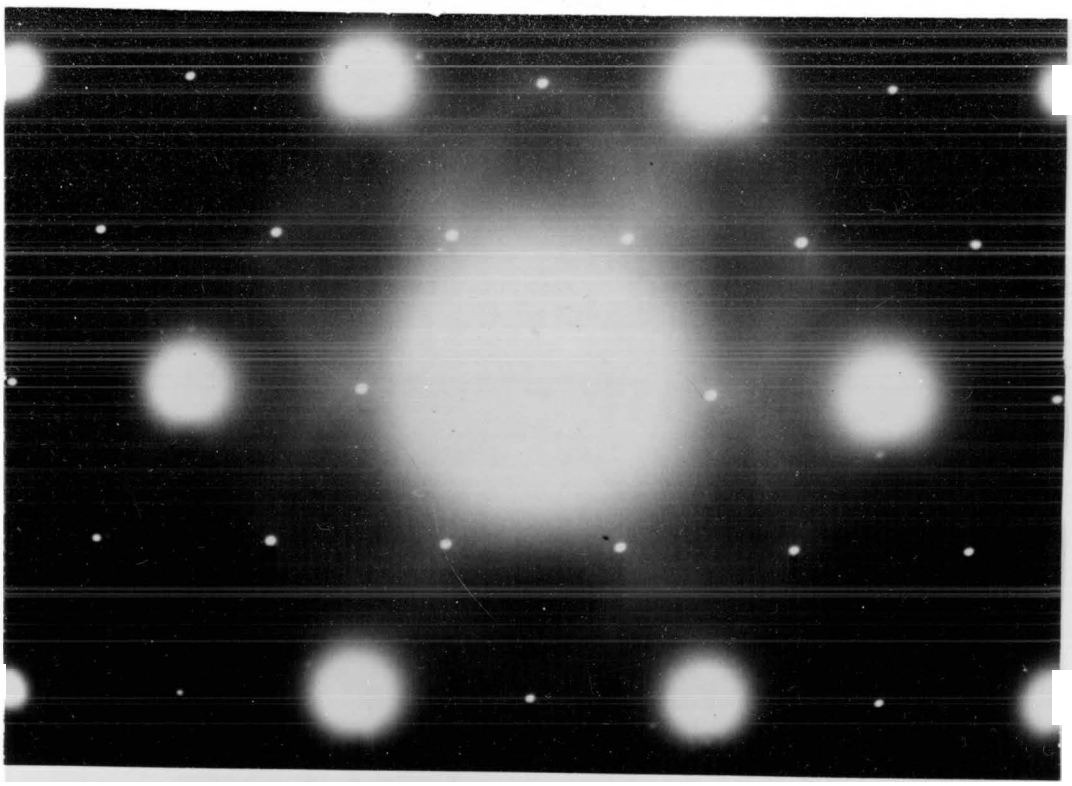

(a)

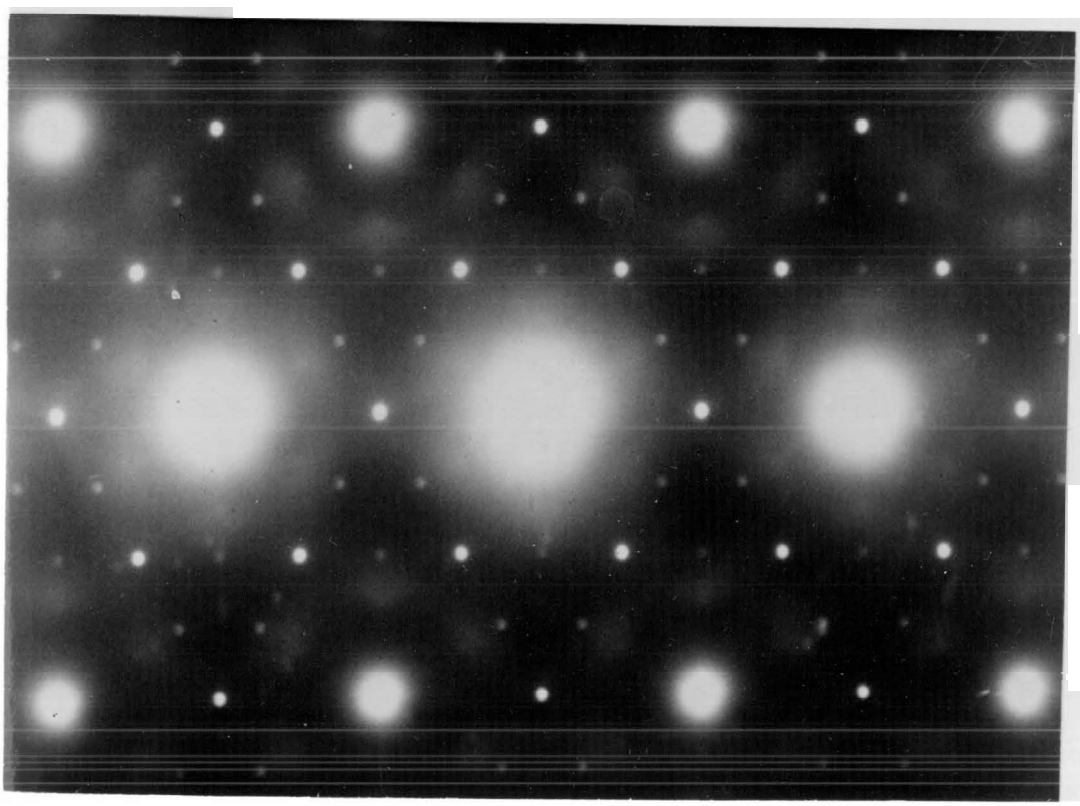

(b)

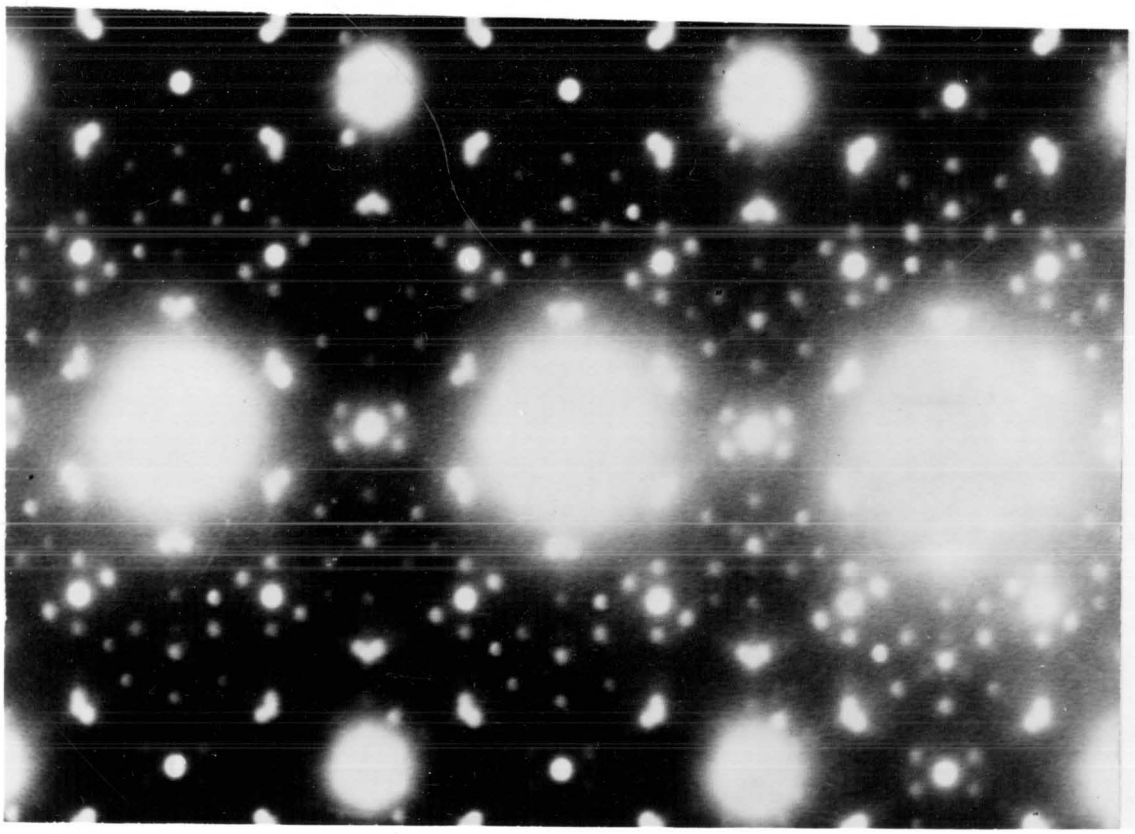

(c)

which the sample is cycled, with the spots remaining until higher temperatures when the sample is warmed quickly. Diffuse scattering is also observed which hexagonally surrounds the main spots. The corners of the diffuse hexagons point in the <10.0> directions and have a distance between opposing corners of less than a_o^* (about $0.85a_o^*$). Further diffuse scattering joins the corners of adjacent hexagons and passes through the "$2a_o$" satellites. This diffuse scattering intensifies, along with the "$2a_o$" satellites, when cooling to about 200K. When the sample is heated above room temperature, the "$2a_o$" satellites become fuzzy and gradually disappear above about 330K.

The "$4a_o$" satellites (Fig. 4.1b) are also somewhat sample dependent in their behavior. When cooling they become noticeable anywhere from about 190K to about 130K. On heating, they tend to disappear in the range of about 170K to about 220K and this again depends on the rate of heating. Their appearance and disappearance is in marked contrast to "usual" satellite spots, in that they do not condense from a diffuse background. Instead, they initially appear fairly sharp, but very weak, on a clear background and rapidly increase in intensity as the temperature is lowered, reaching saturation by about 110K. Simultaneously, in this same temperature range, the hexagons of diffuse scattering have disappeared along with the diffuse scattering through the "$2a_o$" satellites. They are replaced by relatively intense,

but very diffuse spots where the straight segments of the diffuse hexagons had previously been. These spots, on further cooling, resolve into the low temperature superlattice described below.

Below about 90K, the seemingly complicated pattern in Fig. 4.1c is suddenly observed ($\Delta T \lesssim 5K$). It is highly reversible with temperature cycling and without any apparent hysteresis. These new satellites, except for those close to the main lattice reflections, are very much weaker than the "$2a_o$" satellites and their appearance coincides with the disappearance of the diffuse scattering. These additional satellites can readily be accounted for by assuming orientational variants. For this choice of superlattice no absences are required, which otherwise would be considerable if a hexagonal superlattice were chosen. In Fig. 4.2a only the low temperature superlattice satellites are drawn and it is clear that the indicated orientational variants incorporate all of the new satellites. Therefore it is concluded that the superlattice is $(1/4 \times \sqrt{3}/10)a_o^*$ or $(2\sqrt{3} \times 5)a_o$ in real space. For some samples an additional $\sqrt{3}a_o^*/6$, that is, $2\sqrt{3}a_o$ hexagonal superlattice is observed, but because it is not always observed, further discussion of this superlattice will be delayed until the results for the mixed phases have been considered in the next chapter to avoid unnecessary complications. In Fig. 4.2b, one of the orientational variants of the $(2\sqrt{3} \times 5)a_o$ superlattice is shown for

Fig. 4.2

The superlattice satellites in Figs. 4.1 (a),(b) and (c) are best explained by three orientation variants of a $(1/4 \times \sqrt{3}/10)a_o^*$ superlattice and a hexagonal $\sqrt{3}a_o^*/6$ superlattice. (a) Diagram of the three orientational variants of the $(1/4 \times \sqrt{3}/10)a_o^*$ superlattice appearing below about 90K as in Fig. 4.1(c). (b) Diagram of one variant of the $(1/4 \times \sqrt{3}/10)a_o^*$, that is $(2\sqrt{3} \times 5)a_o$ superlattice.

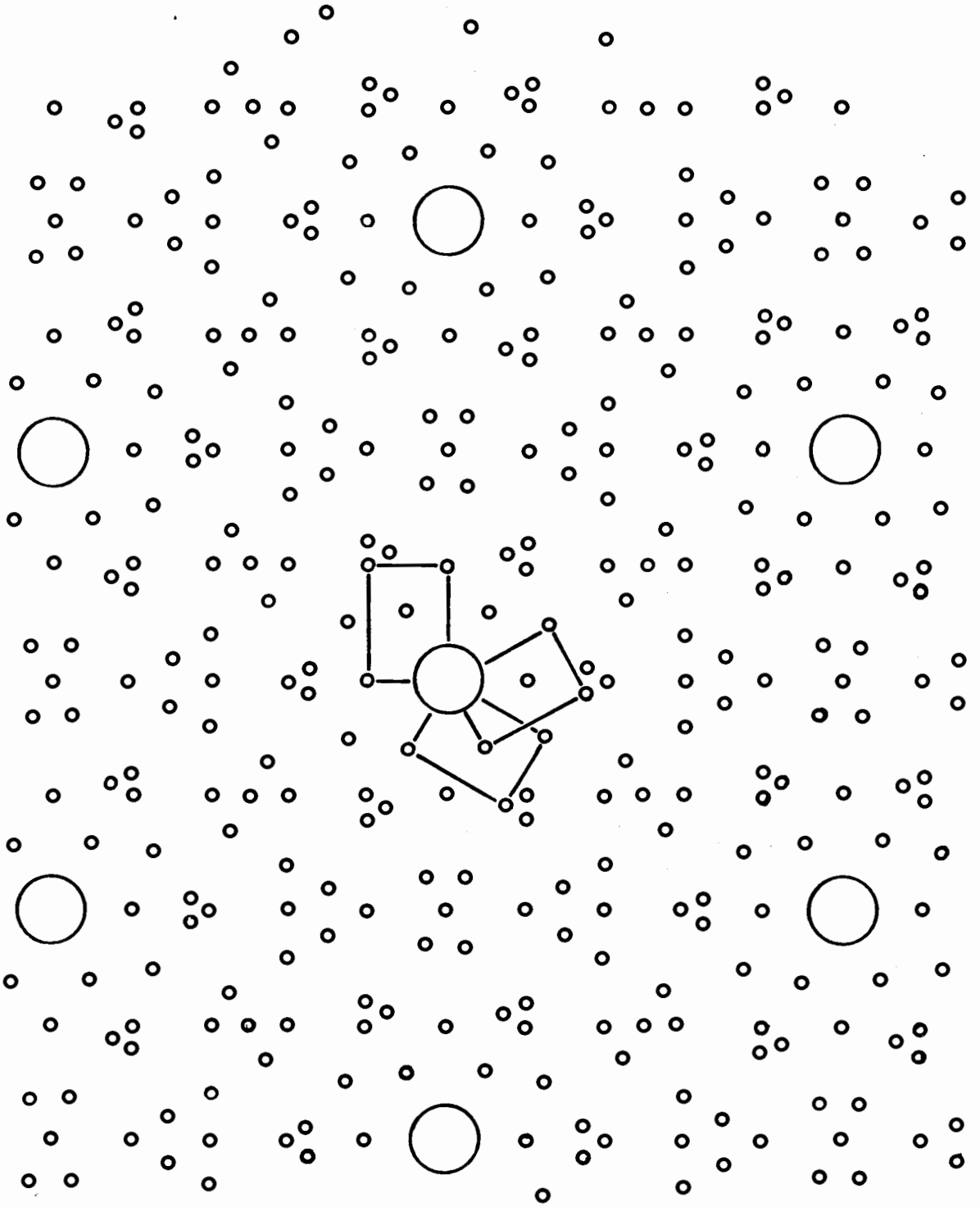

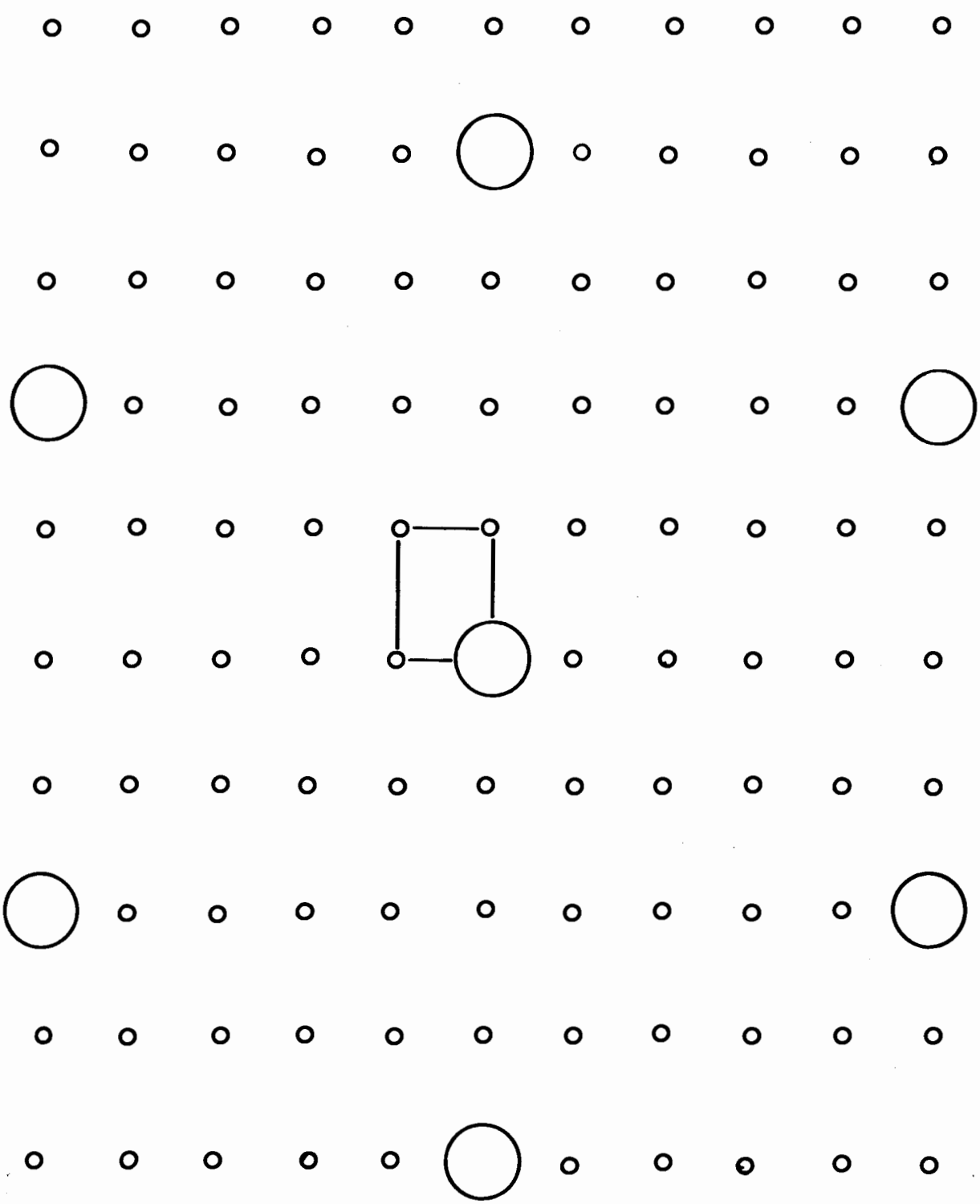

clarity. Confirming evidence for the existence of orientational variants was provided by one sample in which the absence of a set of satellites belonging to a particular variant was observed.

The room temperature electrical resistivity of $Ag_{2/3}TaS_2$ is found to be $200 \times 10^{-6} \pm 30\%$ $\Omega \cdot cm$, while that of the unintercalated 2H-TaS_2 used here is found to be $150 \times 10^{-6} \pm 15\%$ $\Omega \cdot cm$ in agreement with other results [25]. The $\rho(T)$ behavior for $Ag_{2/3}TaS_2$ is shown in Fig. 4.3, $S_1(a,b)$. No cycle dependent behavior is observed for $\rho(T)$ and in all cases the resistance ratio ($R_{300}/R_{4.2}$) was very close to about 4, a decrease from about 60 for the unintercalated 2H-TaS_2 used here.

When cycling through the transition at about 200K, little or no hysteresis is observed and the small knee just below 210K is real since it is observed for all samples. There is a small hysteresis below 90K which is similar in all samples. Above 90K there is some sample to sample variability (compare $S_1(a)$ and $S_1(b)$ in Fig. 4.3), but the overall similarity of $\rho(T)$ is clear. Above about 320K the resistivity is observed to increase very sharply, and then always becomes erratic. When subsequently cooled, $\rho(T)$ always becomes nonreproducible and therefore indicates sample modification or degradation. Therefore, this behavior was not further pursued.

There is good correlation between the appearance

Fig. 4.3

Electrical resistivity versus temperature for stage 1 $Ag_{2/3}TaS_2$ (S_1(a) and S_1(b)) and stage 2 $Ag_{1/3}TaS_2$ (S_2). S_1(a) and S_1(b) illustrate the maximum deviations in ρ(T) found for various samples. Curve S_2 is observed for all x = 1/3 samples. For comparison ρ(T) for pure 2H-TaS_2 [4] is also shown.

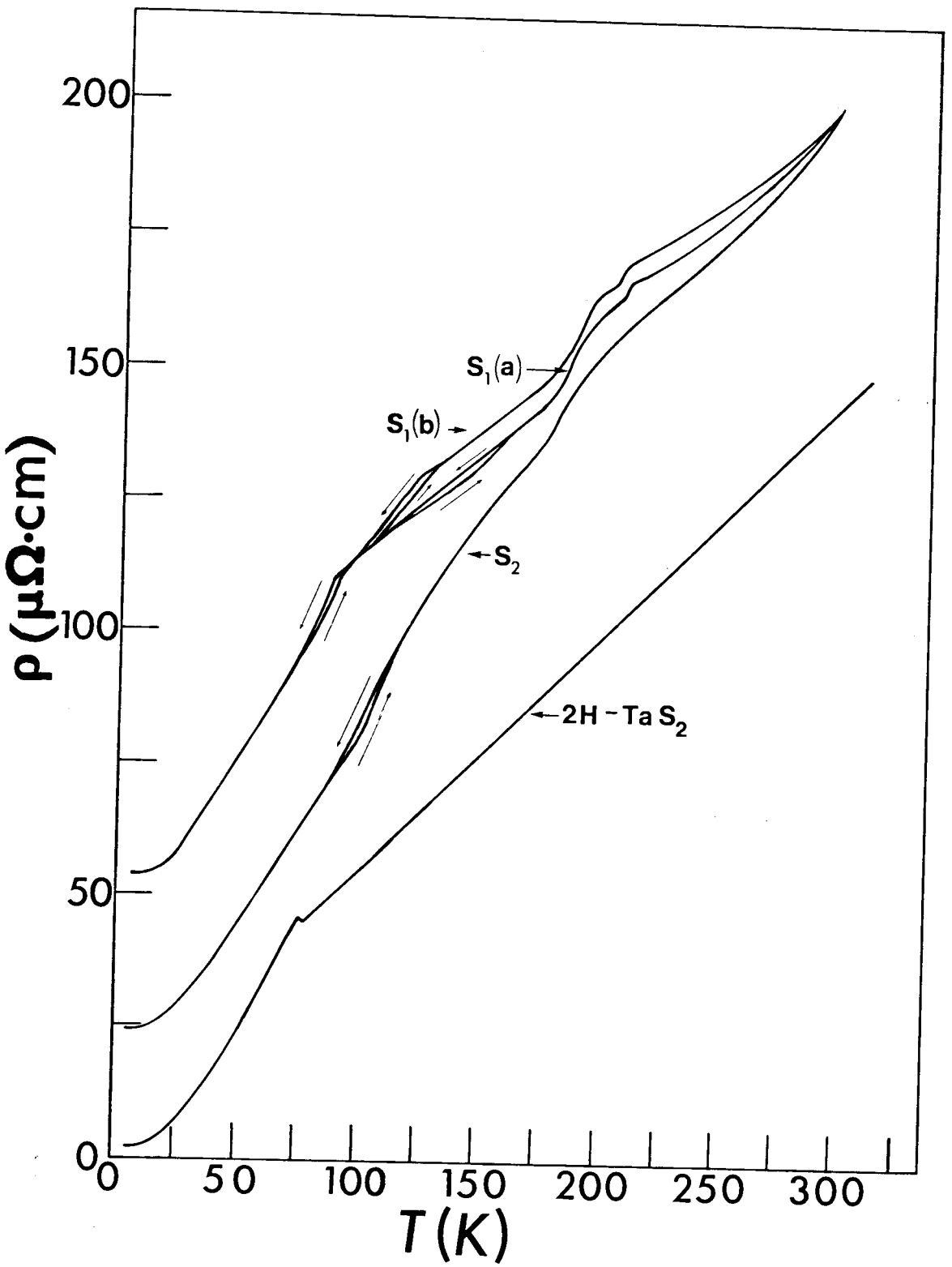
200
150
100
50
0
ρ (μΩ·cm)
S1(a)
S1(b)
S2
2H - Ta S2
0
50
100
150
200
250
300
T (K)

of additional satellite spots and/or the changes in diffuse scattering which occur below about 200K and 90K and the breaks in the slope observed in $\rho(T)$ at essentially the same temperatures.

(B) $Ag_{1/3}TaS_2$ Superlattice and Electrical Resistivity

This is a stage 2 intercalation compound and the silver ions again reside in tetrahedral sites as determined in Chapter 3. The room temperature electron diffraction pattern is essentially the same as that of stage 1 $Ag_{2/3}TaS_2$ at room temperature (see Fig. 4.1a). The "$2a_o$" satellites and the diffuse intensity contours are, however, somewhat weaker, as might be expected because of the lower silver ion content. Again there is some sample to sample variations in the appearance of the "$2a_o$" satellites, but as for stage 1, they are always observable within about ± 20K of room temperature.

When cooling below about 200K, $Ag_{1/3}TaS_2$ and $Ag_{2/3}TaS_2$ samples behave differently, aside from the general intensification of their superlattice features. In particular, no "$4a_o$" satellites are observed with $Ag_{1/3}TaS_2$ and the diffuse intensity contours, instead of changing into diffuse spots hexagonally surrounding all the main spots, as in stage 1, appear as diffuse streaks through the "$2a_o$" satellites (Fig. 4.4a). These diffuse streaks show some sample to sample variation in their sharpness, but

Fig. 4.4

Diffraction patterns of stage 2 $Ag_{1/3}TaS_2$ with the beam perpendicular to the basal plane (a) At about 150K; the apparent "$2a_o$" superlattice developed near room temperature and the diffuse streaking through the "$2a_o$" satellites develops below about 200K from the diffuse hexagons (Fig. 4.1a). (b) At about 25K; below about 100K the diffuse streaking is replaced by these new satellites.

(Photographs kindly taken by Mr. M. Smith and Dr. A.E. Curzon.)

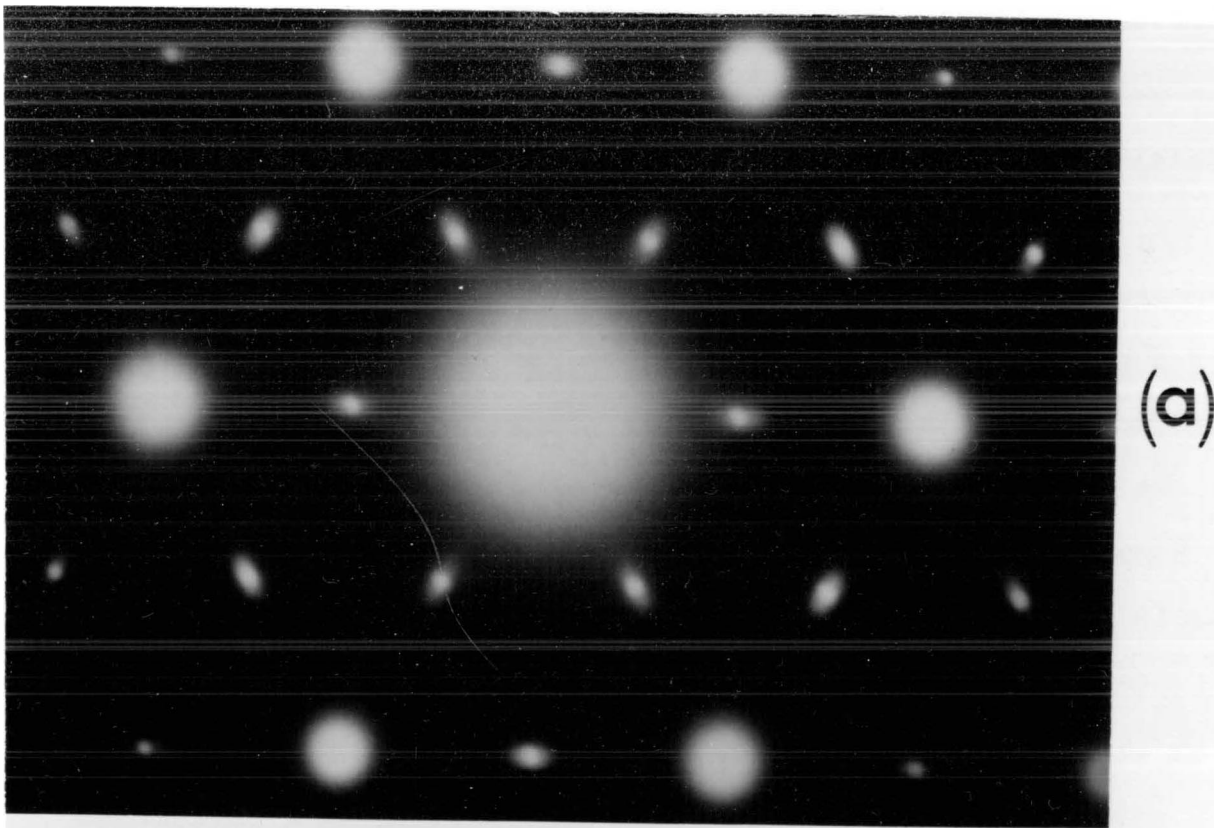

(a)

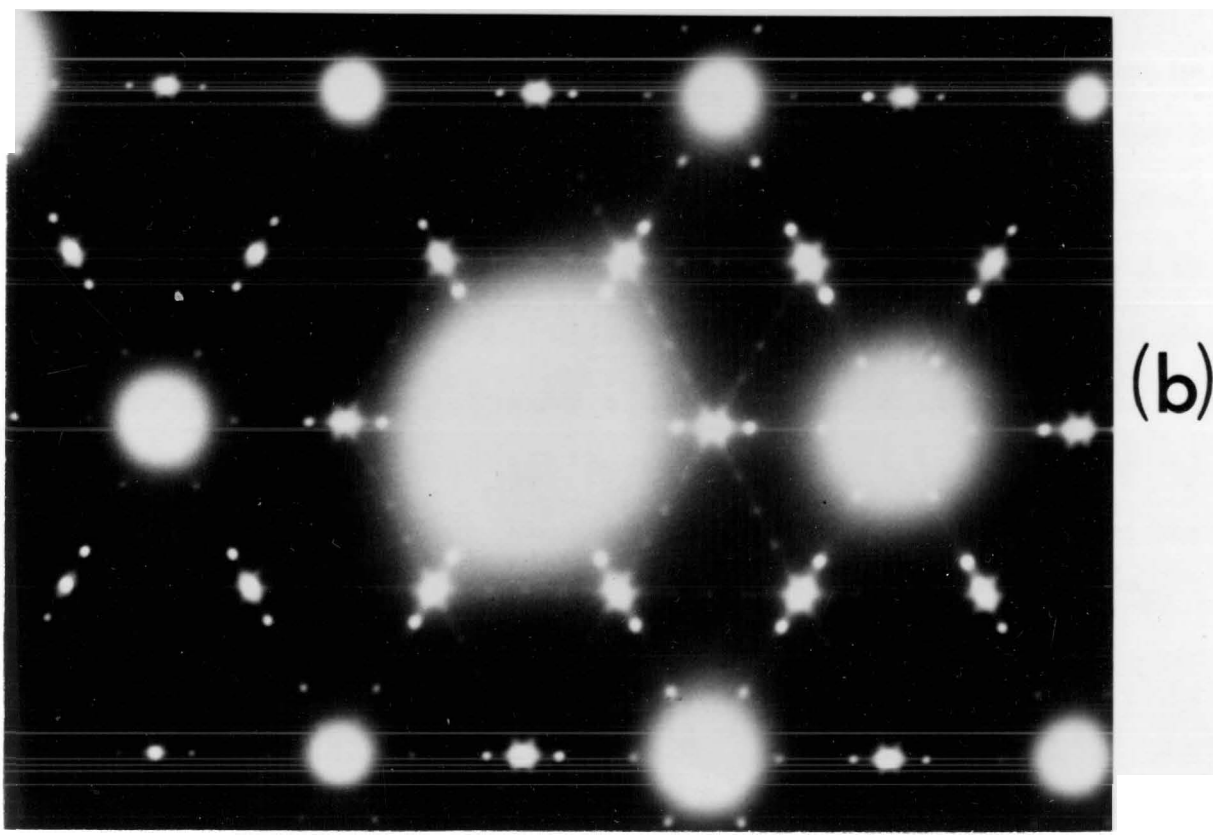

(b)

they always sharpen further on cooling and stay extended so that they appear as streaks pointing radially away from the main spots.

On cooling below about 90K, the streaks almost disappear and are replaced by a new superlattice (Fig. 4.4b) which forms very quickly and reversibly ($\Delta T \lesssim 5K$). This transition has removed essentially all of the diffuse scattering, except for a little near the "$2a_o$" satellites causing them to appear oval, because of overexposure, which they are not. Because these new satellites are again closely spaced and would therefore require a great number of systematic absences if associated with a hexagonal superlattice, they are again likely due to orientational variants as shown in Fig. 4.5a. This superlattice actually appears in two steps. First only the satellites corresponding to a $(1/10 \times \sqrt{3}/2)a_o^*$, that is $(5\sqrt{3} \times 1)a_o$, unit cell are observed along with lines of continuous scattering still partially visible in Fig. 4.4b, half-way between and parallel to the rows of the $(5\sqrt{3} \times 1)a_o$ superlattice satellites of a given orientational variant (Fig. 4.5b). At slightly lower temperatures, the lines of continuous scattering resolve into weak satellites thereby changing the new unit cell to $(1/10 \times \sqrt{3}/4)a_o^*$, which is $(5\sqrt{3} \times 2)a_o$ in real space (Fig. 4.5b). Note that the $(5\sqrt{3} \times 1)a_o$ superlattice satellites are absent whenever h + k = odd, which indicates the presence of a glide plane on (00.ℓ) with glide components $(\vec{a} + \vec{b})/2$.

Fig. 4.5

(a) Diagram of the satellites appearing below about 100K as in Fig. 4.4(b) with the three orientational variants of the $(1/10 \times \sqrt{3}/4)a_o^*$, that is $(5\sqrt{3} \times 2)a_o$ superlattice as indicated. (b) Diagram of one variant of the superlattice in (a) with the unit cell of the $(1/10 \times \sqrt{3}/2)a_o^*$, that is $(5\sqrt{3} \times 1)a_o$ superlattice outlined. Before the satellites spaced $1/10\ a_o^*$ apart appear, continous line-streaking exists in their place.

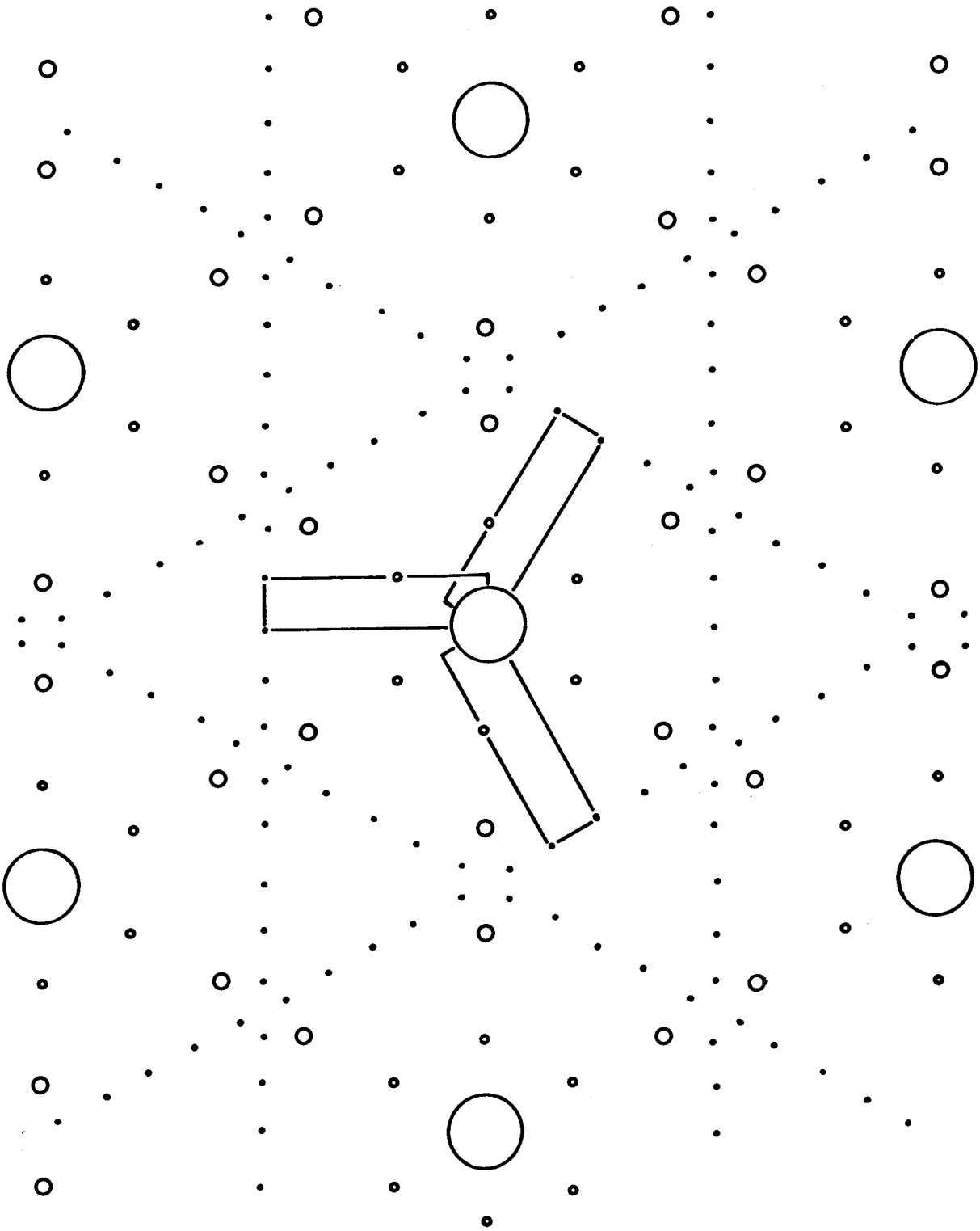

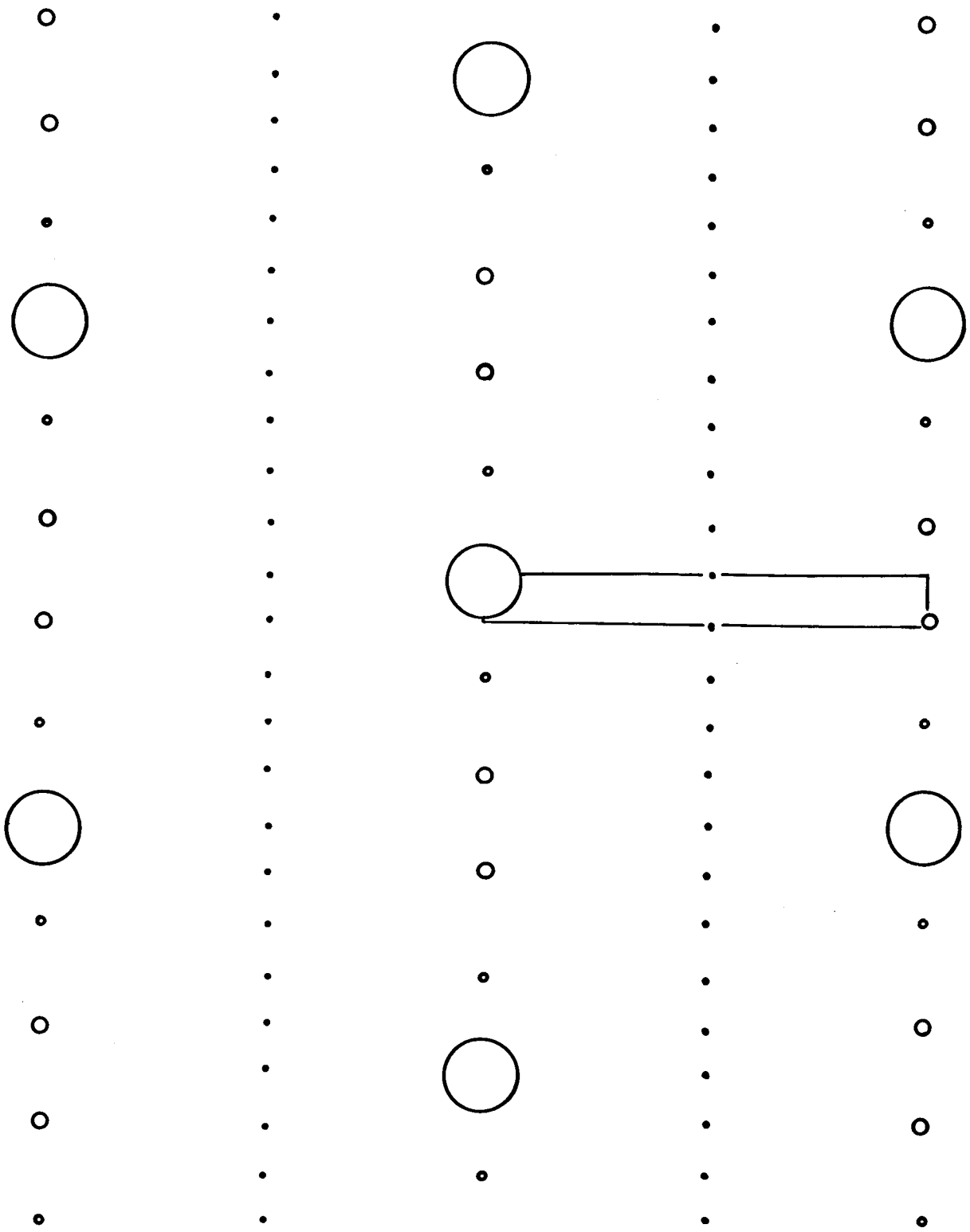

The room temperature electrical resistivity of $Ag_{1/3}TaS_2$ is observed to be 200 × 10^{-4} ± 30% Ω·cm as for $Ag_{2/3}TaS_2$, and the resistance ratio of about 8 is betwen the value for 2H-TaS_2 and $Ag_{2/3}TaS_2$. The ρ(T) behavior is shown in Fig. 4.3 and breaks in the slope are again observed at about 200K and 100K. The overall ρ(T) behaviour is actually quite similar to that of stage 1 and little sample or cycle dependent behavior is observed in the three samples studied. It was found that the resistivity for all samples is "noisy" down to roughly 200K. By "noisy" it is meant that the resistance would instantaneously change by about ± 20% at random. Since a four-probe technique was used, the "noise" is not caused by electrical contact problems. This "noisy" behavior became more prominent for samples that had less than 1/3 mole fraction of silver intercalated. Above about 320K the resistivity is observed to increase sharply, becoming erratic and nonreproducible, as observed in stage 1.

4.3 Discussion of the Low Temperature Superlattices Found in $Ag_{2/3}TaS_2$ and $Ag_{1/3}TaS_2$

Superlattice formation may be caused by intercalate ordering, or a distortion of the host structure which may or may not be associated with CDW formation (see also Tables 5.1 and 10.1). Most of the superlattices (see Fig. 4.1c and Fig. 4.4b) are best explained as three orientational variants which

implies either a rectangular lattice of ordered silver ions or an anisotropic CDW/PLD. Because of the high degree of carrier scattering which is indicated by the small resistance ratio observed, the superlattice satellites are explained as an ordering of the silver ions, but CDW/PLD effects cannot be ruled out.

Since there is less than one mole fraction of silver ions in both intercalation systems, an order-disorder transition with a corresponding superlattice is expected at some temperature. In fact, from concentration considerations alone, a $\sqrt{3}a_o$ superlattice would be expected for both $Ag_{1/3}TaS_2$ and $Ag_{2/3}TaS_2$, but this is not observed.

The low temperature superlattices are explained in terms of rectangular silver superlattices on an hexagonal host lattice allowing the interpretation of seemingly complicated patterns, often implying very large hexagonal unit cells with a high degree of symmetry, in terms of relatively simple rectangular unit cells which, naturally, will have three orientational variants at 120° to each other. However it was impossible to ascertain the presence of domains of orientational variants, even though very simple in principle, via dark field imaging in the electron microscope. The main problem was the very low intensities of the superlattice satellites. Because the low scattered intensity, along with a reasonably large magnification dictates a relatively long exposure time, the real image resolution became quite poor.

This is likely due in part to motion of the sample but more important, probably, is the migration of silver ions away from the area covered by the electron beam because of the local heating which is observed after extended exposure times.

(A) $Ag_{2/3}TaS_2$ Superlattices

At sufficently high temperatures there will be no restrictions placed on the interionic separation of the silver ions and it is only required that they occupy the lattice sites, tetrahedral most likely, provided by the hexagonal host structure. Diffuse scattering would therefore be expected to occur in the diffraction pattern which, just above the order-disorder transition, should acquire well defined intensity contours [26]. This is observed above room temperature and therefore the apparent "$2a_o$" superlattice, that forms near room temperature (Fig. 4.1a), is thought to correspond to an order-disorder transition of some of the silver ions, but not all since some diffuse scattering still remains. The formation of the additional "$4a_o$" satellites below about 200K (Fig. 4.1b), suggests that the silver ions do not order on a "$2a_o$" hexagonal superlattice, but that instead, domains of three orientational variants are present having a $(1/2 \times \sqrt{3}/4)a_o^*$ reciprocal superlattice, with k = odd reflections (the "$4a_o$" satellites) absent above about 200K (Fig. 4.6a). This corresponds to a $(\sqrt{3} \times 2)a_o$

Fig. 4.6

(a) Diagram of Fig. 4.1b, interpreting the "$2a_o$" and "$4a_o$" superlattice satellites from $Ag_{2/3}TaS_2$ as a $(1/2 \times \sqrt{3}/4)a_o^*$, that is $(\sqrt{3} \times 2)a_o$ superlattice of three orientational variants. The "$4a_o$" superlattice satellites are absent at room temperature due to structure factor extinctions. (b) The $(\sqrt{3} \times 2)a_o$ silver superlattice in two successive v.d.W. gaps. Note that the silver ions are not centered with respect to one another and that 1/4 of the "up" and "down" tetrahedral sites are equally occupied so that $x = 1/2$. (c) A $(11\bar{2}0)$ section of stage 1 $Ag_{2/3}TaS_2$ having a $(\sqrt{3} \times 2)a_o$ silver superlattice, satisfying electron and X-ray diffraction data.

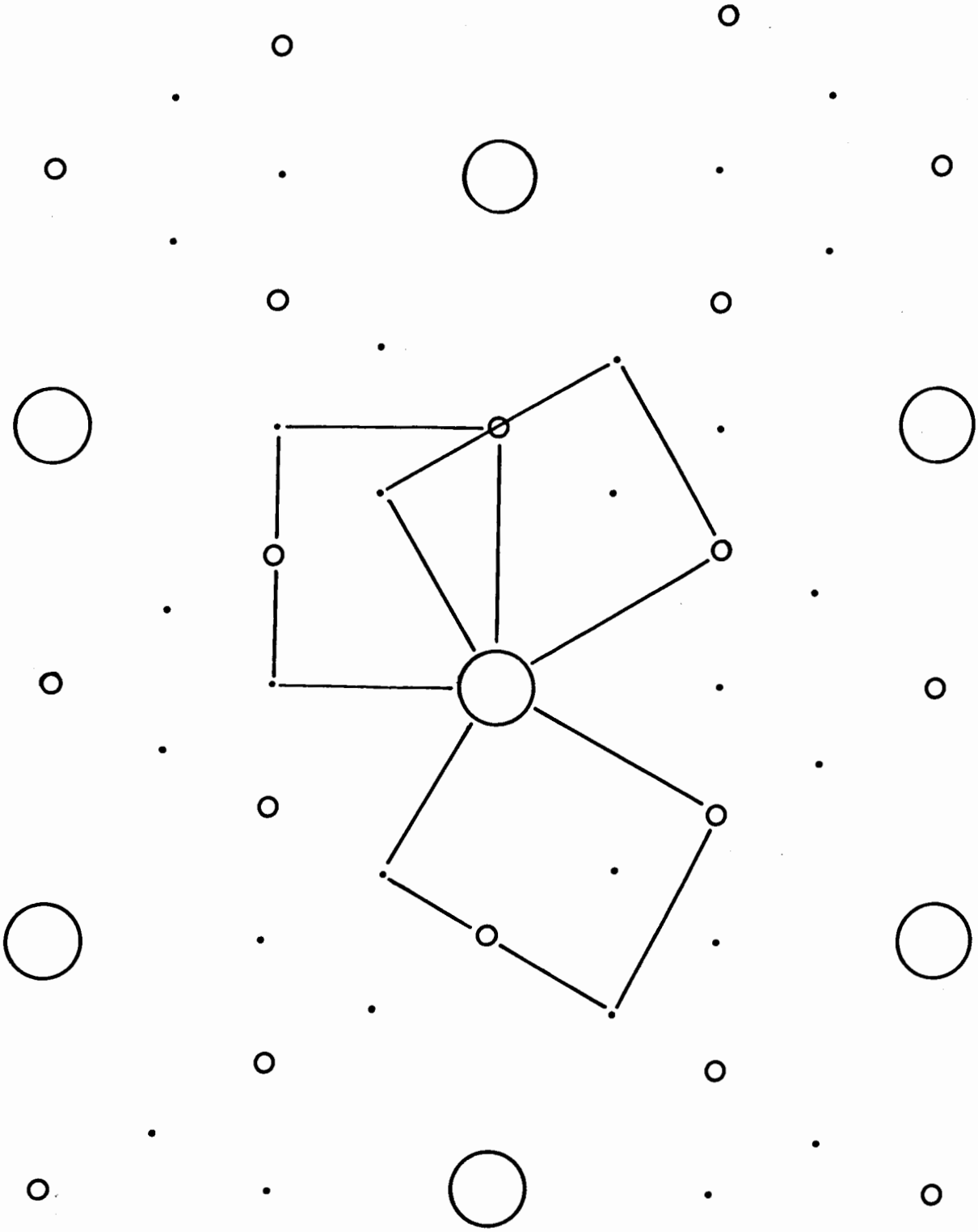

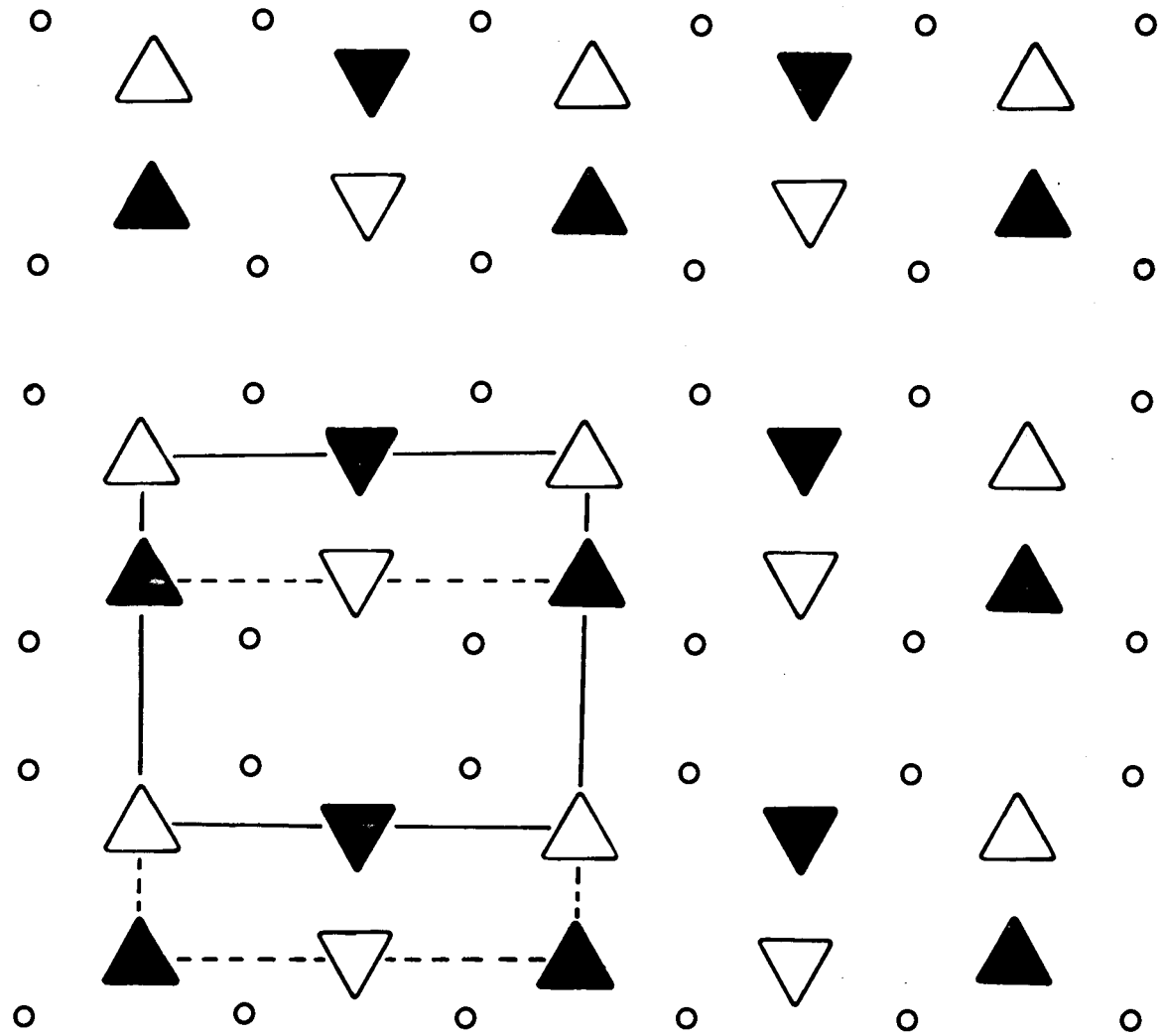
— Ag (u_1, d_1)
— Ag (u_2, d_2)
— tet. sites

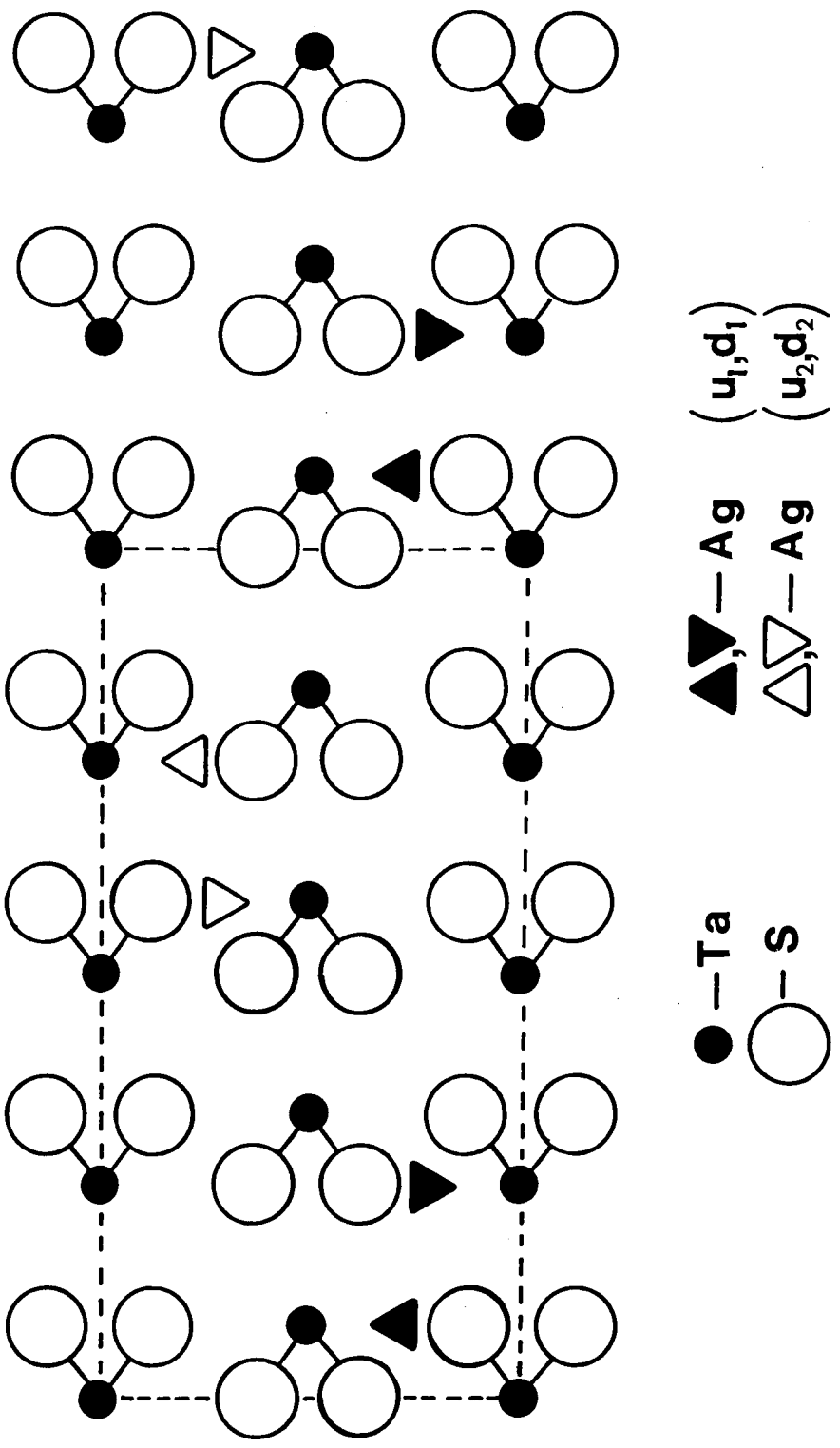
Ta
S
Ag
Ag
(u_1,d_1)
(u_2,d_2)

silver superlattice within a van der Waals gap, as shown in Fig. 4.6b. If the crystal is uniformly intercalated, this structure will ideally require x = 1/2 for an equal occupation of the "up" and "down" tetrahedral sites which is considered to be an important requirement since these sites are energetically equivalent. Therefore, ideally, x = 1/6 mole fractions of silver ions are unaccounted for and are free to distribute themselves in some way. Some are probably randomly distributed throughout the ordered regions and others can be incorporated into a system of nonconservative boundaries, produced by the translational and orientational variants of the ordered regions. This can account for the diffuse scattering observed at and below the order-disorder transition. The geometric orientation of the diffuse scattering contours is in agreement with those found for other disordered tetrahedral intercalation compounds [26] and therefore suggests that these "extra" silver ions are still residing in tetrahedral sites. A detailed discussion of the diffuse scattering will not be presented here since deRidder has already provided a general discussion of this using a cluster approach [26].

Since it is required that all reflections for k = odd be absent above about 200K, the stacking sequence of the silver superlattice can be defined uniquely as shown in Figs. 4.4b and 4.6c. The (hk0) projection of the silver ions, with respect to the upper sites in the first van der Waals gap

(u_1), are therefore

$u_1(0,0)$	$d_1(1/3, 1/2)$
$u_2(1/3, 0)$	$d_2(0, 1/2)$

where u and d refer to up and down tetrahedral sites and the subscripts refer to successive van der Waals gaps respectively, so that

$$F(hkO) = f_{Ag}(1 + e^{i\pi k}) [1 + e^{2i\pi(h/3 + k/2)}]$$

which clearly shows that all reflections with k = odd will be absent. Since the ions at $d_1(1/3, 1/2)$ are not centered with respect to those at $u_1(0,0)$, an intralayer Coulomb interaction can be expected to distort the silver superlattice and therefore also the host lattice. The relaxation of the k = odd extinction condition, imposed by the stacking sequence, can therefore be expected and scattered intensity corresponding to "$4a_o$" reflections should be noticeable at low enough temperatures. Moreover, these satellites should appear without any initial diffuse scattering since it is simply a matter of relaxing the structure factor extinctions. This is exactly what is observed when the sample is cooled below about 200K, the "$4a_o$" satellites do gradually appear without any prior formation of diffuse spots. DeRidder et al. [27] observed a similar pattern for $Cu_{1/3}NbS_2$ and proposed

the same explanation. Boswell et al. [28] also observed this pattern for $Cu_{1/3}NbS_2$ and proposed two order-disorder transitions, generating respectively $2a_o$ and $4a_o$ hexagonal lattices. For this interpretation there is no equal occupation of the "up" and "down" tetrahedral sites within a given van der Waals gap.

The sudden appearance of the $(2\sqrt{3} \times 5)a_o$ superlattice satellites below about 90K (Figs. 4.2a and 4.2b) may well indicate a first order phase transition. The fact that this transition has also removed the diffuse scattering indicates that the "extra" $x \sim 1/6$ silver ions, which have been the cause of the diffuse scattering, have been incorporated in an ordered structure. In fact, it is postulated that these "extra" silver ions have combined with part of the $(\sqrt{3} \times 2)a_o$ superlattice ions to form the $(2\sqrt{3} \times 5)a_o$ superlattice regions having ideally $x = 4/5$. Therfore, a two phase system exists at all times which consists above about 90K of a uniform $(\sqrt{3} \times 2)a_o$ superlattice ($x = 1/2$ ideally) coexisting with randomly incorporated silver ions ($x = 1/6$ ideally), and below about 90K of the $(\sqrt{3} \times 2)a_o$ and $(2\sqrt{3} \times 5)a_o$ superlattice ($x = 4/5$ ideally) coexisting in different regions. The reason for choosing $x = 4/5$ for the $(2\sqrt{3} \times 5)a_o$ superlattice, is simply because $x > 2/3$ is required to absorb the "excess" silver ions and $x = 4/5$ corresponds to the largest packing density which can be achieved if it is required that: (i) nearest neighbor sites are not

Fig. 4.7

Proposed $(2\sqrt{3} \times 5)a_o$ superstructure corresponding to $x = 4/5$ which avoids the simultaneous occupation of nearest neighbor sites and fills an equal number of "up" and "down" sites within a unit cell. The small triangles and circles refer to unoccupied tetrahedral and octahedral sites respectively.

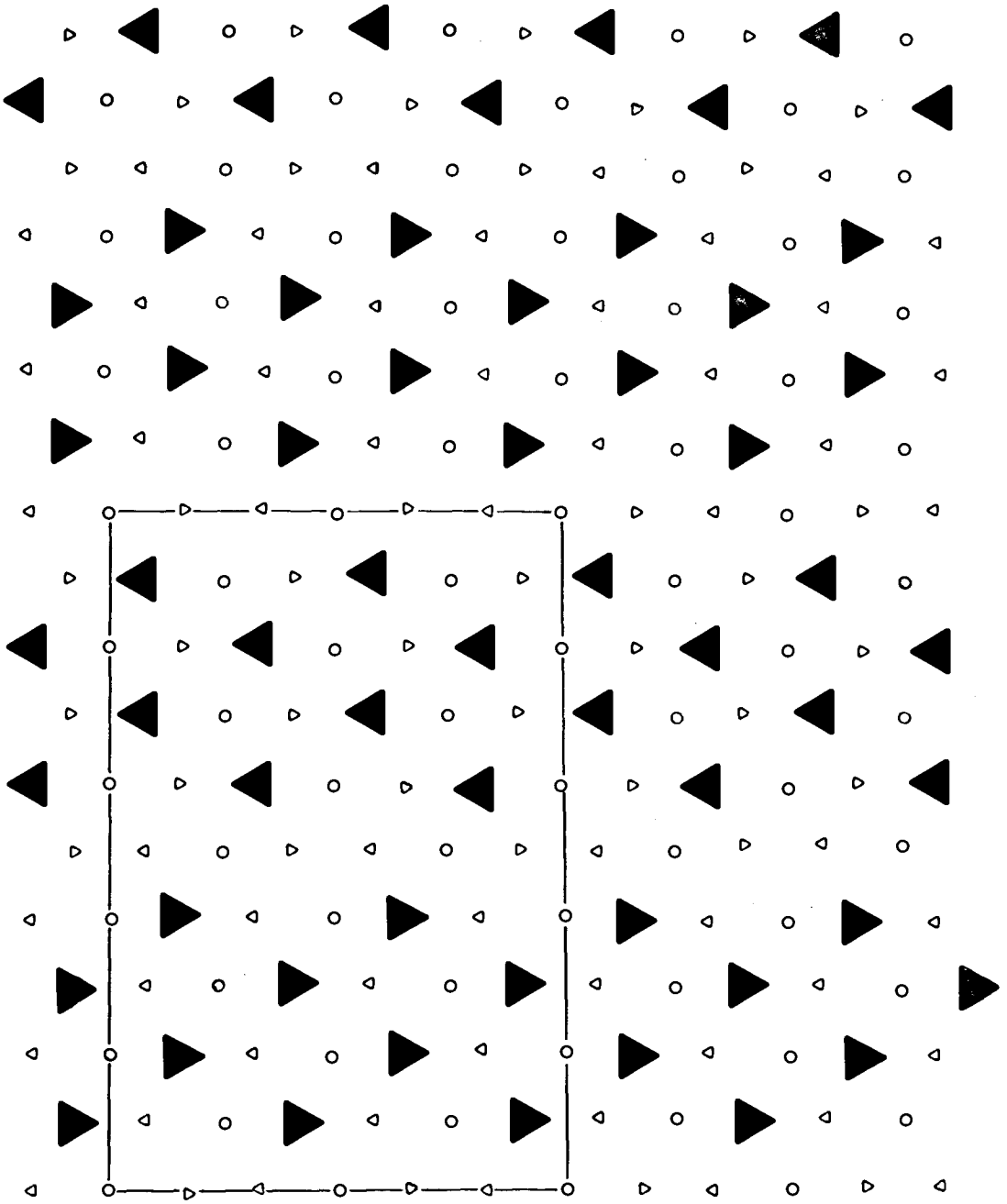

simultaneously occupied and (ii) "up" and "down" tetrahedral sites are equally occupied within the unit cell in a van der Waals gap.

The superlattice shown in Fig. 4.7 satisfies the above conditions. However, it is difficult to confirm since a detailed structural analysis is difficult to carry out because a variety of silver configurations within the unit cell can be generated to explain the observations and it is very difficult to distinguish between them because of uncertain satellite intensities and small, but important, variations in the local silver ion concentration which udoubtedly occur.

When cooling from about 200K to about 100K, the very diffuse satellites which appear hexagonally placed around all main spots (Fig. 4.1b), are typical of sidebands resulting from a periodically deformed host lattice. A deformed host lattice can be expected since the silver ions occupy tetrahedral lattice sites, formed by the sulphur atoms which in turn are tightly bound to the tantalum atoms, so that any silver ion correlations will cause a corresponding modulation of the host lattice. Therefore the intensity of the silver superlattice satellites, particularly those close to the main lattice spots, will always be due in part to the modulated host lattice, in addition to the scattering of the silver ions. Because the host lattice spots are very intense compared to the satellites of the silver $(2\sqrt{3} \times 5)a_o$ superlattice, it is not unreasonable to expect that short

range periodic modulations of the host lattice will result in diffuse side-band reflections even before scattered intensity due to the ordered silver superlattice is observed. By comparing the diffuse spots in Fig. 4.1b with the $(2\ 3 \times 5)\bar{a}_o$ low temperature superlattice in Fig. 4.1c, a correlation between the diffuse side-band reflections and the (110) satellites of the $(2\sqrt{3} \times 5)a_o$ superlattice (remember each of the main spots acts as an origin for the side-bands) can be seen. The fact that the (110) and not the (100) satellites are close to the side-bands implies that the true unit cell of the host lattice modulation may be smaller than the unit cell of a given variant. Inspection of the silver ion distribution in the $(2\sqrt{3} \times 5)a_o$ superlattice (Fig. 4.1c) does actually suggest that the host lattice modulation may have a repeat of $(2\sqrt{3} \times 5/2)a_o$ with a strong modulation having a periodicity of $5a_o/2$, that is $\sqrt{3}a_o^*/5$ along $\langle 11.0 \rangle$ in reciprocal space, which agrees well with the geometric center of the diffuse side-bands as (100) reflections of the suggested smaller unit cell of the host lattice. These side-band satellites therefore appear to signal the onset of the existence of small domains or short range order of silver ions having the $(2\sqrt{3} \times 5)a_o$ superlattice. The reason for the large temperature interval of nearly 100K between the first indications of a $(2\sqrt{3} \times 5)a_o$ superlattice and the final formation of extended domains, in a comparatively sudden transition ($\Delta T \lesssim 5K$), near 90K is not understood.

It is of interest to point out that it is possible to generate a $\sqrt{3}a_o$ hexagonal superlattice which corresponds to $x = 2/3$ and has equal occupation of the "up" and "down" tetrahedral sites (Fig. 4.8). This superlattice requires the simultaneous occupation of nearest neighbor tetrahedral sites and since $\sqrt{3}a_o$ superlattice satellites are not observed, it appears that the Coulombic interaction between these adjacent sites is too large for this superlattice to form.

As already pointed out, the $\rho(T)$ behavior correlates with changes in the electron diffraction pattern. Curves $S_1(a)$ and $S_2(b)$ in Fig. 4.3 suggest that the $(2\sqrt{3} \times 5)a_o$ superlattice forms at 92 ± 3K, and the enhanced decrease in $\rho(T)$ agrees with the idea that disordered scattering sites, that is the "extra" silver ions, within the silver $(\sqrt{3} \times 2)a_o$ superlattice, are removed. The somewhat sample dependent hysteresis in the temperature region above the 92K transition to about 160K may then be due to a hysteresis in the host lattice modulation (Fig. 4.1b) caused by fluctuations in the short range correlations of the silver ions which proceeds superlattice formation. The breaks in the slope at about 200K, consisting of a small drop in $\rho(T)$ just below 210K and then the large decrease centered around 190K, is not understood. However, two things do occur in this temperature range, the "$4a_o$" satellites appear and the diffuse scattering is beginning to coalesce around the main lattice spots signaling the onset of the $(2\sqrt{3} \times 5)a_o$ superlattice .

Fig. 4.8

A possible hexagonal $\sqrt{3}a_o$ superlattice in a v.d.W. gap, having $x' = 2/3$, which is not observed. Note the necessary occupation of nearest neighbor tetrahedral sites if both "up" and "down" sites are to be equally occupied. The small triangles and circles correspond to unoccupied tetrahedral and octahedral sites respectively.

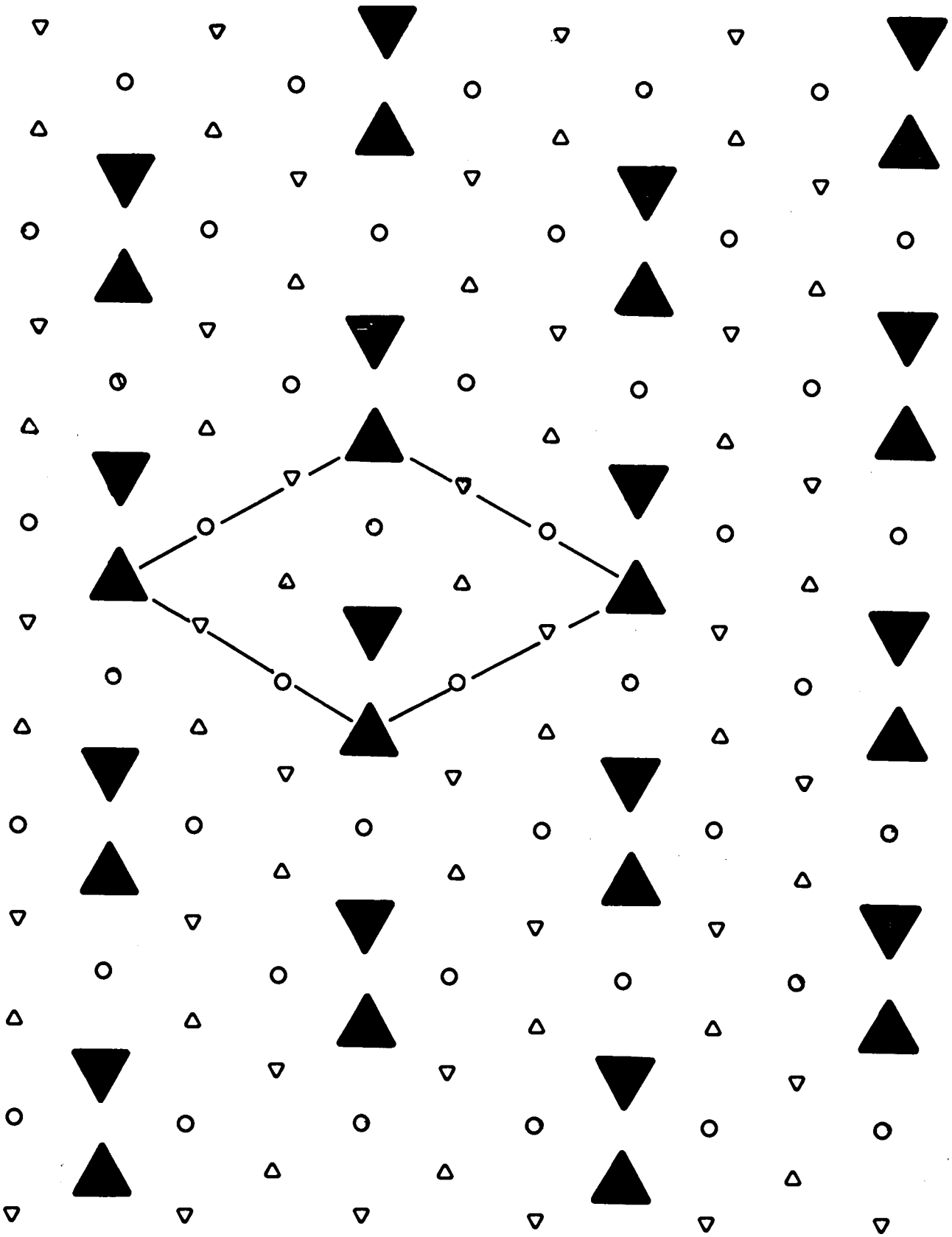

It seems unlikely that the lattice distortion associated with the "$4a_o$" satellites will result in an enhanced decrease of $\rho(T)$, and therefore this decrease might be associated with the onset of the $(2\sqrt{3} \times 5)a_o$ superlattice. The sharp increase in $\rho(T)$ observed above about 320K might be related to the order-disorder transition of the silver ions. However, if so, it is not clear why the resistivity becomes erratic and nonreproducible on temperature cycling.

(B) $Ag_{1/3}TaS_2$ Superlattices

The crystal structure for this stage 2 compound was determined in Chapter 3 and it was found that all reflections for which $2h + k \neq 3n$, are systematically absent. However, for all of the stage 2 electron diffraction patterns, it is found that all (hk.0) reflections are present. This is likely due to "spiking" of reciprocal lattice spots perpendicular to the plane of the sample, since the unit cell is 39.66Å and the sample thicknesses were about 200Å. Another possibility is that the stage 2 stacking sequence may be destroyed in thin crystals, but this is unlikely since the integrity of the $Ag_{1/3}TaS_2$ structure was confirmed down to sample thicknesses of about 700Å using X-ray diffraction.

Again, as for stage 1, the silver ions for $Ag_{1/3}TaS_2$ are ordered near room temperature with some sample to sample

variations. Since the "local" silver ion concentration (x') in a given layer for this stage 2 compound is 2/3 mole fractions (i.e. x' = 2x), it can be expected that the silver ions will order on the same $(\sqrt{3} \times 2)a_o$ superlattice as in stage 1. However, this is probably not the case. Even though we again observe "$2a_o$" satellites and diffuse streaking (Fig. 4.1a) at room temperature, no "$4a_o$" satellites are observed on cooling. Therefore, there is no reason to invoke variants of a $(\sqrt{3} \times 2)a_o$ superlattice, and a $2a_o$ hexagonal superlattice (Fig. 4.9) will explain the observations. The hexagonal superlattice is much more symmetric and therefore presumably energetically more stable than the somewhat asymmetric $(\sqrt{3} \times 2)a_o$ lattice. This suggests that interactions between silver layers are causing the $(\sqrt{3} \times 2)a_o$ lattice in stage 1 and weakened interlayer interactions in stage 2 allows the silver ions to order on the symmetric hexagonal $2a_o$ superlattice. Furthermore, the hexagonal $2a_o$ superlattice is also favoured because the intralayer interactions in stage 2 are expected to be considerably increased over those in stage 1 since we expect the silver ions in stage 2 to be more ionized than those in stage 1 if the net charge transferred to the host layers is fairly constant over the range of x = 1/3 to 2/3. The $2a_o$ hexagonal superlattice is further supported by the fact that

Fig. 4.9

Hexagonal $2a_o$ superlattice for stage 2 $Ag_{1/3}TaS_2$ within a v.d.W. gap having x' = 1/2. The small triangle and circles refer to unoccupied tetrahedral and octahedral sites respectively.

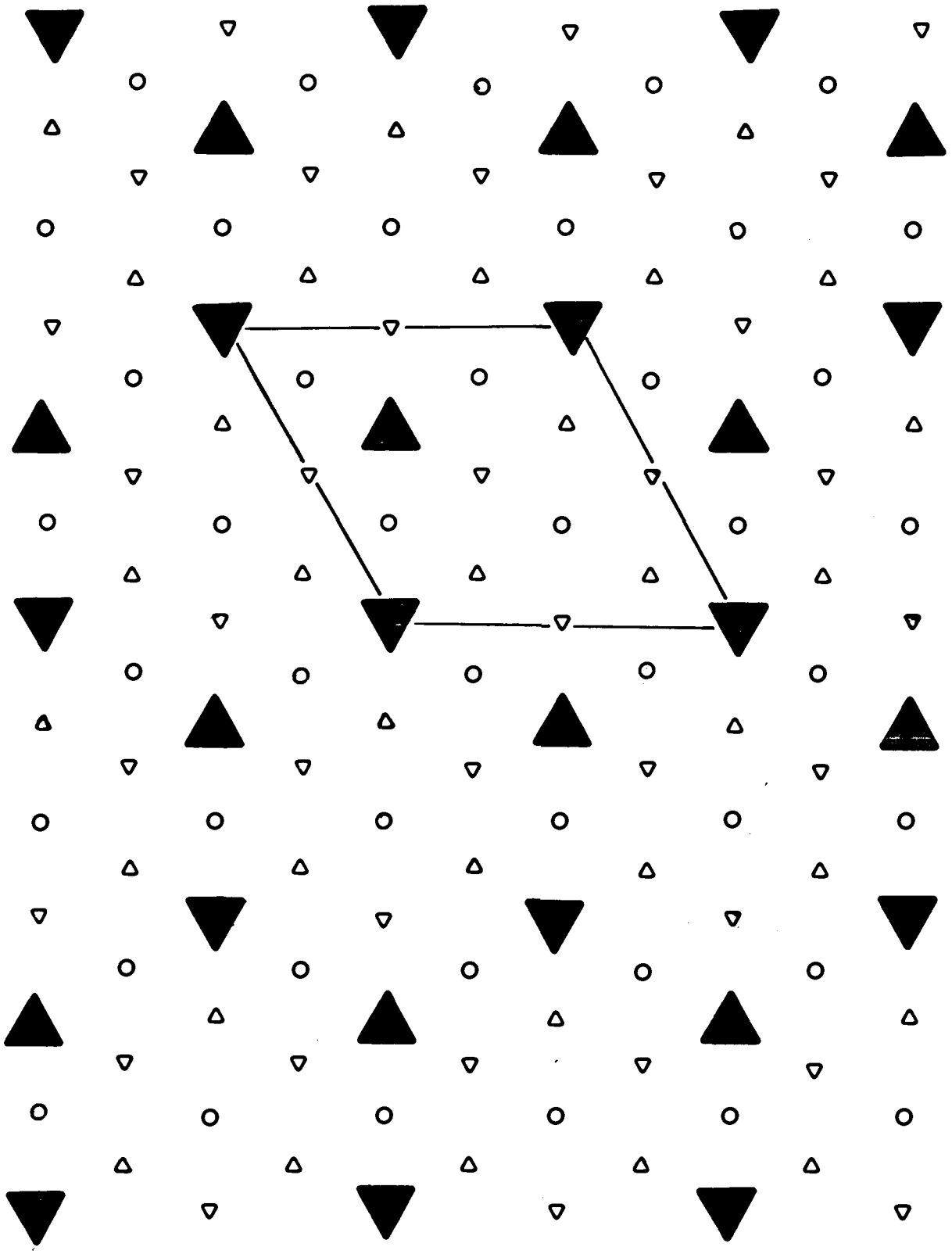

the k = odd absences, required above about 200K for a $(\sqrt{3} \times 2)a_o$ superlattice, cannot be reasonably achieved for the expected 3 layer repeat of the silver superlattice. A 3 layer repeat of the silver superlattice is expected because the $Ag_{1/3}TaS_2$ stage 2 structure has a 6 layer repeat distance in the host stacking sequence as found in Chapter 3. The superlattices are expected to arrange themselves in a staggered configuration along the c axis, but it is impossible to ascertain the exact stacking sequence because several models will produce similar satellite intensities.

Like the $(\sqrt{3} \times 2)a_o$ superlattice observed in stage 1, the hexagonal $2a_o$ superlattice in stage 2 also requires $x' = 1/2$ silver ions ideally. This again leaves $x' \sim 1/6$ to be randomly distributed on tetrahedral sites throughout the intercalated regions and can give rise to the diffuse scattering observed down to about 200K. When cooling from about 200K to about 100K, the diffuse scattering around the main spots disappears and concentrates as streaks through the $2a_o$ superlattice satellites pointing radially away from the main lattice spots (Fig. 4.4a). This is in marked contrst with stage 1 (Fig. 4.1b), where the diffuse scattering concentrates around the main spots on the <11.0> axes and disappears near the "$2a_o$" satellites. Also of interest is that no $(5\sqrt{3} \times 2)a_o$ superlattice satellites, which replaced the diffuse streaking, appear centered where the diffuse streaking was. Instead, the strongest satellites appear at

the points where the diffuse streaking stops (compare Fig. 4.4a and Fig. 4.4b).

Even though the low temperature superlattice for x = 2/3 and 1/3 are different the $(5\sqrt{3} \times 2)a_o$ superlattice in $Ag_{1/3}TaS_2$ likely has a similar origin. Since the satellites are sharp, the superlattice must exist over extended regions and furthermore, because of the sudden formation of the superlattice, the associated phase transition may well be of first order as in stage 1. It is postulated that above about 110K the hexagonal $2a_o$ superlattice x' = 1/2 ideally) coexists with the "extra" silver ions (x'$\sim$ 1/6) which are randomly incorporated throughout the $2a_o$ superlattice on tetrahedral sites, thus giving rise to the diffuse scattering. Furthermore, this also suggests that below about 110K part of the $2a_o$ superlattice plus the "extra" silver ions form the $(5\sqrt{3} \times 2)a_o$ superlattice (probably x' = 4/5 ideally) over extended regions, and coexist with regions still having the hexagonal $2a_o$ superlattice.

A number of structural interpretations are possible for the $(5\sqrt{3} \times 2)a_o$ superlattice (Fig. 4.4b and 4.5a), but again there are some guidelines. First we consider the $(5\sqrt{3} \times 1)a_o$ superlattice which initially appears and again make the assumptions previously made that (i) x' > 2/3 (probably x = 4/5 ideally) so that the "extra' silver ions can be absorbed into this superlattice; (ii) nearest neighbor

sites are not simultaneously occupied, and; (iii) "up" and "down" tetrahedral sites are equally occupied within the unit cell in a van der Waals gap. This leads to the structure shown in Fig. 4.10. The half-filled nearest neighbor tetrahedral sites on the corners and center of the unit cell forming pseudo one-dimensional "chains" of lattice sites which have either one or the other of the sites completely filled (never both simultaneously) at random, thus forming "chains" of silver ions having no intra- or interchain correlations. A superstructure having an even larger silver ion concentration of $x = 9/10$ could have been proposed, but then the $(\vec{a} + \vec{b})/2$ glide plane within the van der Waals gap would have to be sacrificed and the more unlikely assumption made that this glide plane exits between alternate van der Waals gaps. As already discussed for stage 1, this superlattice should also modulate the host lattice so that one should again expect side-bands to contribute additional scattered intensity to the satellites close to the main spots. The (110) type satellites around the main spots, which are the first allowed reflections, are the most intense and this suggests that if these correspond to (100) side-band satellites, the host lattice has a strong modulation with a periodicity of $2a_o^*/5$, that is $5\sqrt{3}a_o/4$ in real space along the <11.0> direction.

When the temperature of the sample displaying a ($\times$ 1)a_o superlattice is further lowered slightly,

Fig. 4.10

Proposed $(5\sqrt{3} \times 1)a_o$ superstructure corresponding to $x' = 4/5$ which has a glide plane $(\vec{a} + \vec{b})/2$ so that extinctions for $h + k$ = odd exist. The half filled triangles joined with a double ended arrow indicate sites which are randomly occupied with the restriction that they are never occupied simultaneously. The small triangles and circles refer to unoccupied tetrahedral and octahedral sites respectively.

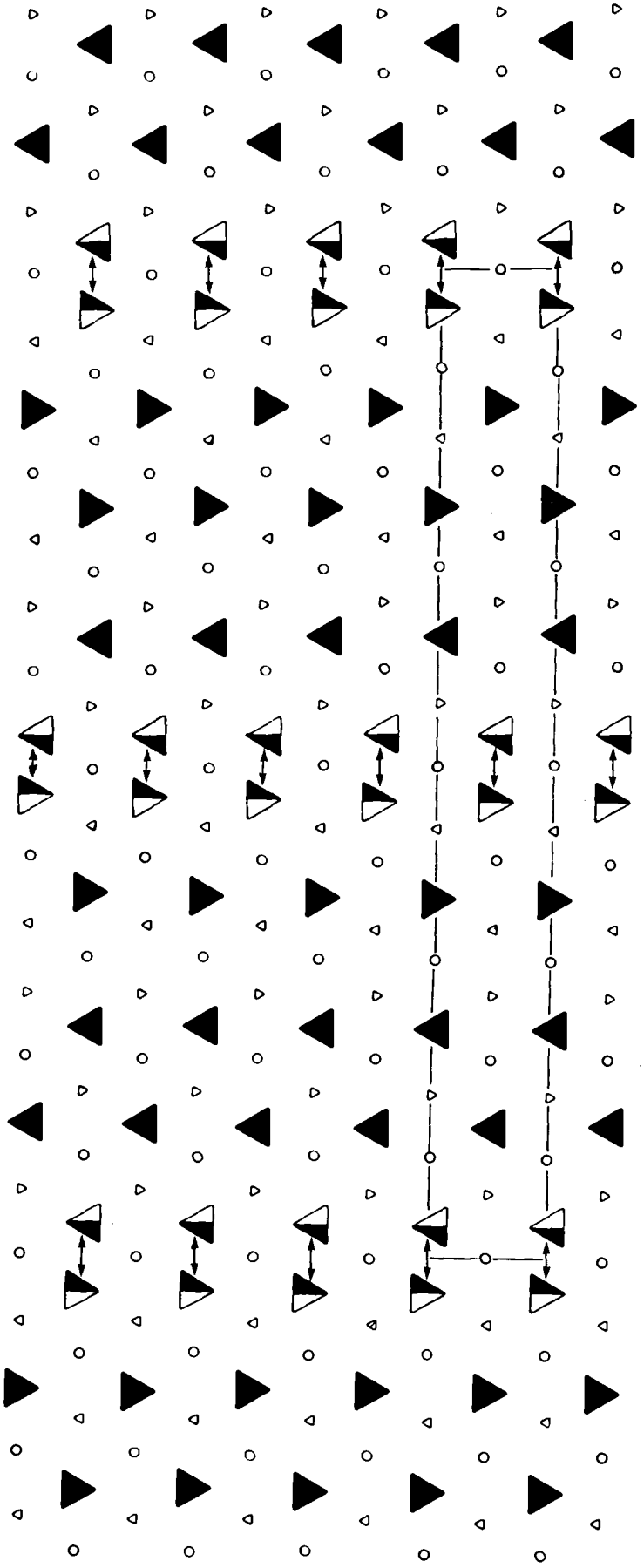

continuous line streaking first appears between and parallel to the rows of the $(5\sqrt{3} \times 1)a_o$ superlattice satellites, still partially visible in Fig. 4.4b, which quickly resolves into further satellites, thus forming the patterns associated with the $(5\sqrt{3} \times 2)a_o$ superlattice shown in Figs. 4.5a and 4.5b. This sequence of events can easily be explained with the superlattice proposed in Fig. 4.10. The continuous lines at $\sqrt{3}a_o^*/4$ correspond to the silver ions becoming equidistance within the pseudo one-dimensional "chains" with a repeat distance of $2a_o$, but no correlation between chains. Keeping in mind that both "up" and "down" sites must be equally occupied, implies that the maximum x can be achieved by alternately occupying these sites along the "chains", thus generating a $2a_o$ repeat distance. Finally, these lines of continuous scattering coalesce into further satellites, thus forming the $(5\sqrt{3} \times 2)a_o$ superlattice, when ordering occurs between the silver ions in the adjacent "chains".

The streaking observed through the $2a_o$ superlattice satellites (Fig. 4.4a) is again likely related to short range order existing prior to the actual formation of an extended $(5\sqrt{3} \times 1)a_o$ superlattice. The geometry and orientations of the streaks suggest that these short range correlations correspond to a $(\sim 1/2 \times \sqrt{3}/2)a_o^*$, that is a $(\sim \sqrt{3} \times 1)a_o$ superlattice which seems a reasonable precursor for the $(5\sqrt{3} \times 1)a_o$ superlattice. However, the large temperature interval of nearly 100K over which this short range order

exists is again puzzling and no explanation will be attempted here.

As in stage 1, $\rho(T)$ for stage 2 shows a break in the slope at about 100K which now corresponds to the formation of the $(5\sqrt{3} \times 2)a_o$ superlattice. Therefore, this decrease in the resistivity, as for stage 1, can be associated with the removal of the random scattering centers within the silver $2a_o$ superlattice. A broad change in the slope is again observed near 200K and since no "$4a_o$" satellites are observed, it can now be associated with the change in the diffuse scattering, which is signalling the onset of the $(5\sqrt{3} \times 2)a_o$ superlattice. Therefore a similar association suggests itself for stage 1. The sharp increase in $\rho(T)$ above room temperature may again be associated with an order-disorder transition of the silver ions, but much more work is needed here. The "noisy" behavior observed in the resistivity above about 200K is also puzzling, but it may be associated with the motion of the domains of intercalated silver ions within the host crystal.

4.4 Conclusions Regarding the Low Temperature Superlattices Found in $Ag_{2/3}TaS_2$ and $Ag_{1/3}TaS_2$

Since the silver ions intercalated into 2H-TaS_2 residing in "up" and "down" tetrahedral sites which are energetically equivalent, the requirement that they be equally filled within

a unit cell in a van der Waals gap is assumed. This, along with minimizing the intra- and interlayer repulsive interactions of the silver ions, favours the formation of $2a_o$ and $(\sqrt{3} \times 2)a_o$ superlattices at room temperature for $x = 1/3$ and $x = 2/3$ respectively rather than a $\sqrt{3}a_o$ superlattice which might be expected on concentration arguments alone. However, since both of these superlattices only require $x' = 1/2$ to be complete, some of the silver ions are unaccounted for and are presumed to be incorporated randomly on tetrahedral sites throughout the $2a_o$ or $(\sqrt{3} \times 2)a_o$ superlattices. Finally, when either of the stage 1 or 2 samples are cooled below about 90K, the entropy term due to these randomly intercalated silver ions becomes sufficiently small to allow the formation of two coexisting ordered phases which are $2a_o$ plus $(5\sqrt{3} \times 2)a_o$ for stage 2, and $(\sqrt{3} \times 2)a_o$ plus $(2\sqrt{3} \times 5)a_o$ for stage 1. The diffuse scattering is likely related to the short range fluctuations toward these ordered phases, noticeable below about 200K, but it is not clear why this condition exists over a temperature interval of about 100K. An alternative explanation of the diffuse scattering in this temperature interval (200K to 90K) may be that it is not indicative of short range order preceeding the low temperature superlattice, but that it instead corresponds to changes inthe types and number of silver ion clusters [5] from those that occurred above about 200K. Further work, including intensity

measurements is required to provide a definitive interpretation of this diffuse scattering.

The general $\rho(T)$ behavior is similar for $Ag_{2/3}TaS_2$ and $Ag_{1/3}TaS_2$ and in both cases features in $\rho(T)$ correlate with the diffraction results. The decrease in the resistivity at about 200K and about 90K can therefore be viewed as a consequence of the reduction in the random scattering.

CHAPTER 5

SUPERLATTICES, CHARGE DENSITY WAVES AND ELECTRICAL RESISTIVITY IN MIXED PHASES OF Ag_xTaS_2

5.1 Experimental Arrangement and Procedure

The crystals were prepared electrochemically as described in Chapter 2. However, in contrast to Chapter 4, now the crystals consisting of mixtures of stage 1, 2 and dilute stage 1 (see Chapter 3) are of interest. In particular, samples were prepared containing nominally x = 0.10, 0.13, 0.26, 0.30, 0.39, 0.42 and 0.50 mole fraction of silver ions as determined by weighing. However, even though very small, thin (about 10μm) 2H-TaS_2 crystals were used for intercalation, the values for x' (x' = nx; n = stage) are difficult to ascertain because the relative amount of one phase over another is difficult to determine. The presence of a mix of phases was determined by taking X-ray diffraction powder patterns obtained from a part of the respective Ag_xTaS_2 crystal. The crystal was then further divided for electron diffraction and electrical resistivity studies. The resistivity measurements were carried out in the basal plane, using a four-probe technique, down to liquid helium temperature. The diffraction patterns were all taken at 100kV with the beam of a Phillips E.M. 300 electron microscope perpendicular to the basal plane of the sample which could be cooled to about 25K [24]. The

electron beam size was typically about 1μm.

5.2 Results of Low Temperature Superlattice and Charge Density Wave Formation in Ag_xTaS_2

A brief overview of some significant observations is presented first (see also Tables 5.1 and 10.1). When the intercalated silver content is reduced only slightly below x = 1/3, one observes at room temperature the presence of $a_o^*/\sqrt{3}$ satellites, corresponding to an apparent $\sqrt{3}a_o$ superlattice, and $2a_o$ superlattice satellites, as shown in Fig. 5.1a for x = 0.30. When x is further decreased, a dramatic decrease in the room temperature intensity of the $2a_o$ superlattice satellites is observed, along with an increase in the intensity of the $a_o^*/\sqrt{3}$ satellites, until for $x \lesssim 1/4$ the $2a_o$ superlattice satellites are no longer observed at room temperature (Fig. 5.2a).

One could assume that the $2a_o$ and $\sqrt{3}a_o$ superlattice satellites originate from the same silver ion superlattice which would then have to consist of three orientational variants each of which is $(1/2 \times \sqrt{3}/6)a_o^*$, that is $(\sqrt{3} \times 3)a_o$ in real space and must have systematic absences that vary with x to produce the observed changes in the superlattice satellites. However, when any of the specimens were tilted, no additional satellites ever appeared. Therefore it can be concluded that at room temperature for

Fig. 5.1

Electron diffraction patterns of stage 2 $Ag_{0.30}TaS_2$:
(a) at room temperature; showing a hexagonal $2a_o$ and $\sqrt{3}a_o$
superlattice which develop respectively in shifted and unshifted regions of the host. (b) near 25K; a $(5\sqrt{3} \times 2)a_o$ superlattice appeared below about 100K and the intensity of the $\sqrt{3}a_o$ superlattice satellites have considerably decreased compared to the $2a_o$ superlattice satellites.

(Photographs kindly taken by Mr. M. Smith and Dr. A.E. Curzon.)

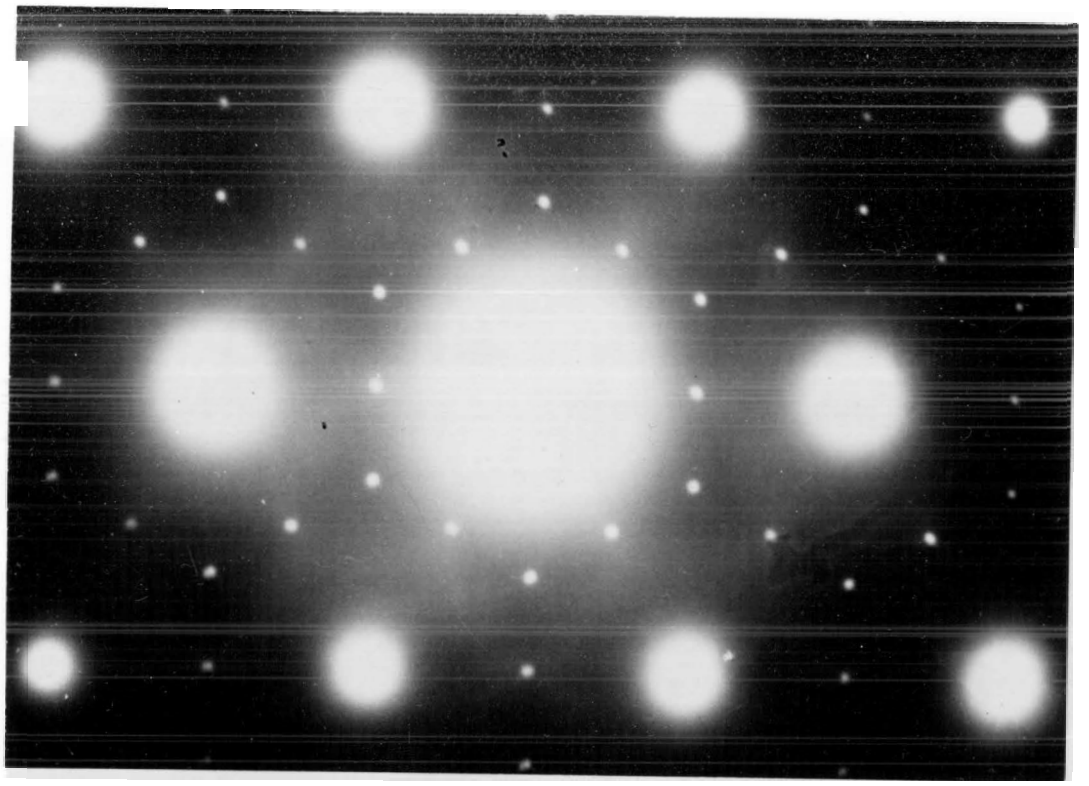

(a)

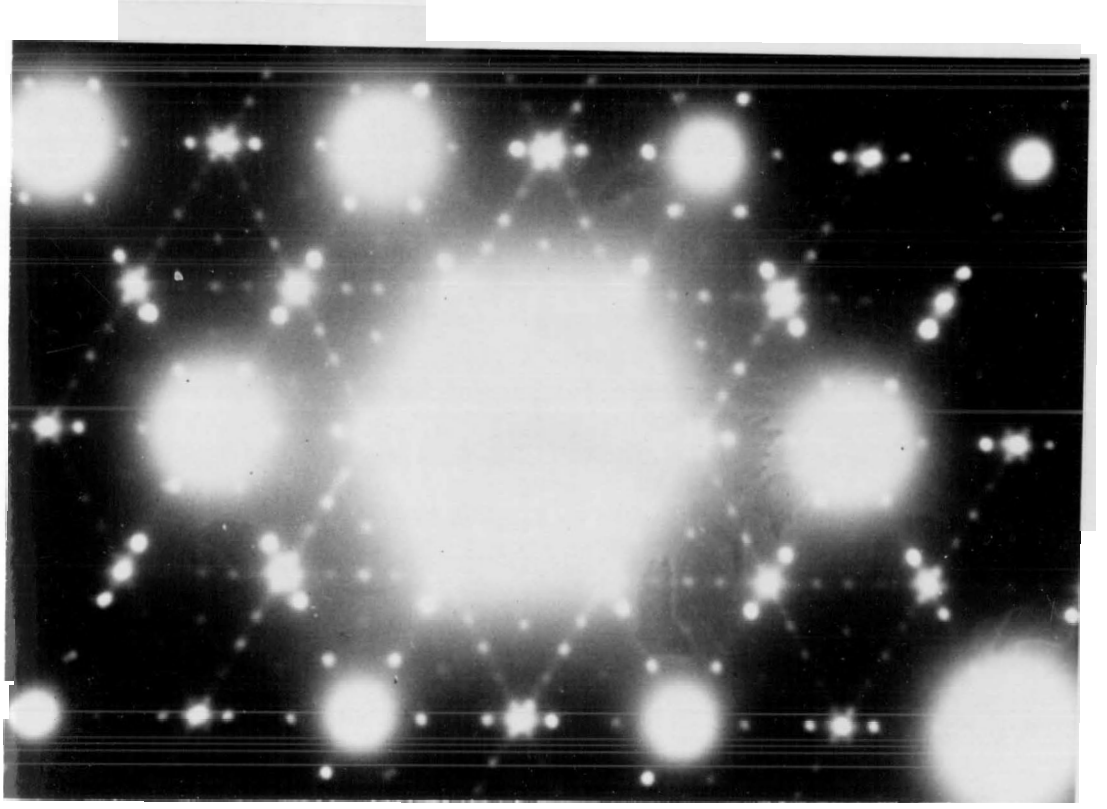

(b)

$x \lesssim 1/4$ only $\sqrt{3}a_o$ superlattice regions exist and that as x is increased ($1/4 \lesssim x \lesssim 1/3$) the $\sqrt{3}a_o$ superlattice regions decrease in area and begin to coexist with the $Ag_{1/3}TaS_2$ stage 2 phase ($2a_o$ superlattice satellites), already described in Chapter 4, until for $x = 1/3$ the $\sqrt{3}a_o$ superlattice regions have disappeared completely. Detailed observations for various x values are presented below.

(A) $Ag_{0.30}TaS_2$

For $x = 0.30$ at room temperature, the $\sqrt{3}a_o$ and $2a_o$ superlattice satellites have about equal intensity and both are sharp (Fig. 5.1a). In addition to these satellites, diffuse scattering is present which is identical to that observed for the $x = 1/3$ and 2/3 samples at room temperature (Fig. 4.1a) in that it hexagonally surrounds the main lattice spots with the corners of the hexagons pointing along <10.0> with a distance between opposite corners of less than a_o^* (again about $0.85a_o^*$). Further diffuse scattering joins the corners of adjacent hexagons and passes through the $2a_o$ superlattice satellites. When the sample is heated, the $2a_o$ and $\sqrt{3}a_o$ superlattice satellites do not disappear simultaneously and the latter satellites can still be observed near 400K as diffuse spots.

Cooling the sample results in the $2a_o$ superlattice satellites gaining in intensity relative to the $\sqrt{3}a_o$

Fig. 5.2

Electron diffraction pattern of stage 2 $Ag_{0.26}TaS_2$: (a) at room temperature; only a $\sqrt{3}a_o$ superlattice is present along with some diffuse intensity directed radially along <10.0> directions. (b) near 400K; showing the $\sqrt{3}a_o$ superlattice satellites becoming very diffuse. (c) near 25K; the $2a_o$ superlattice satellites appear near 230K and the very weak satellites at $(0.347 \pm 0.002)a_o^*$ near 28K initially appear below 100K.

(Photographs kindly taken by Mr. M. Smith and Dr. A.E. Curzon.)

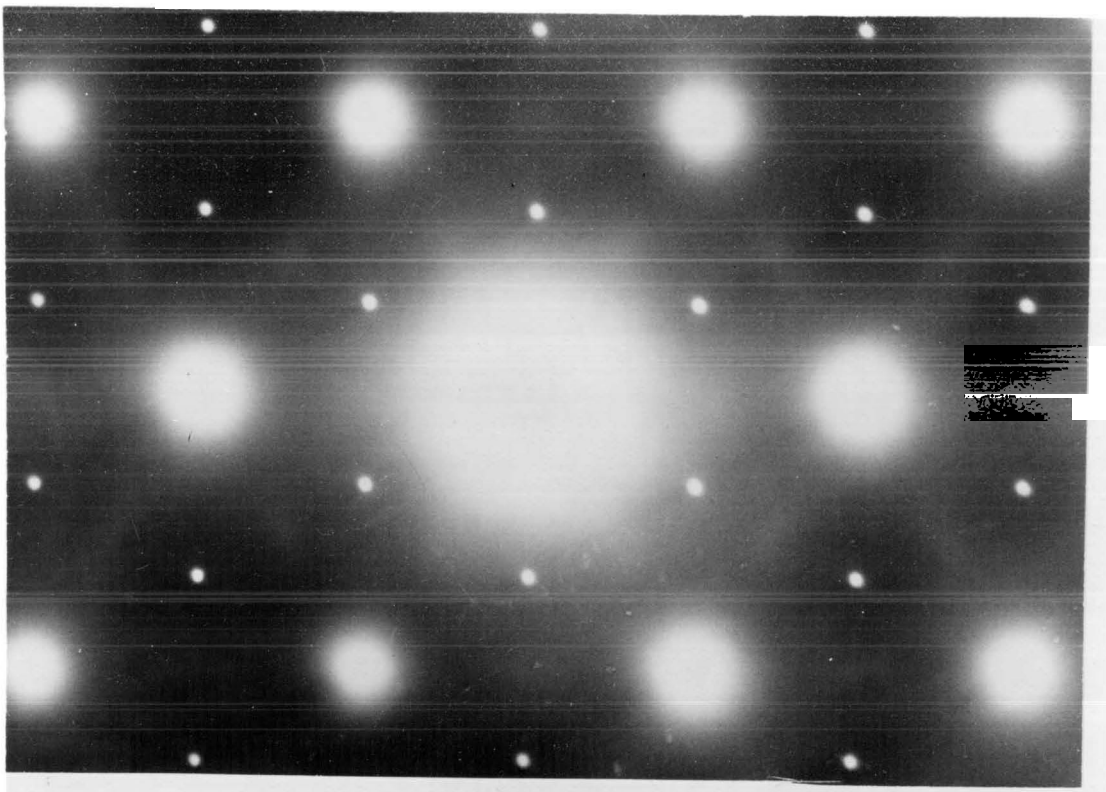

(a)

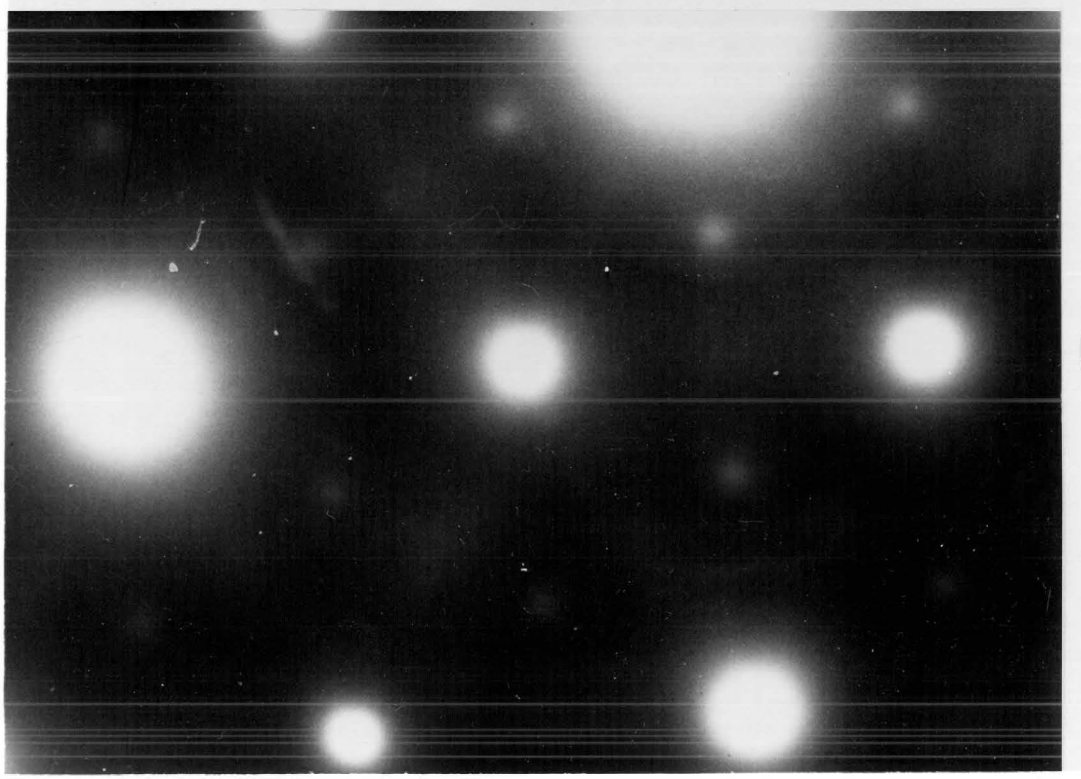

(b)

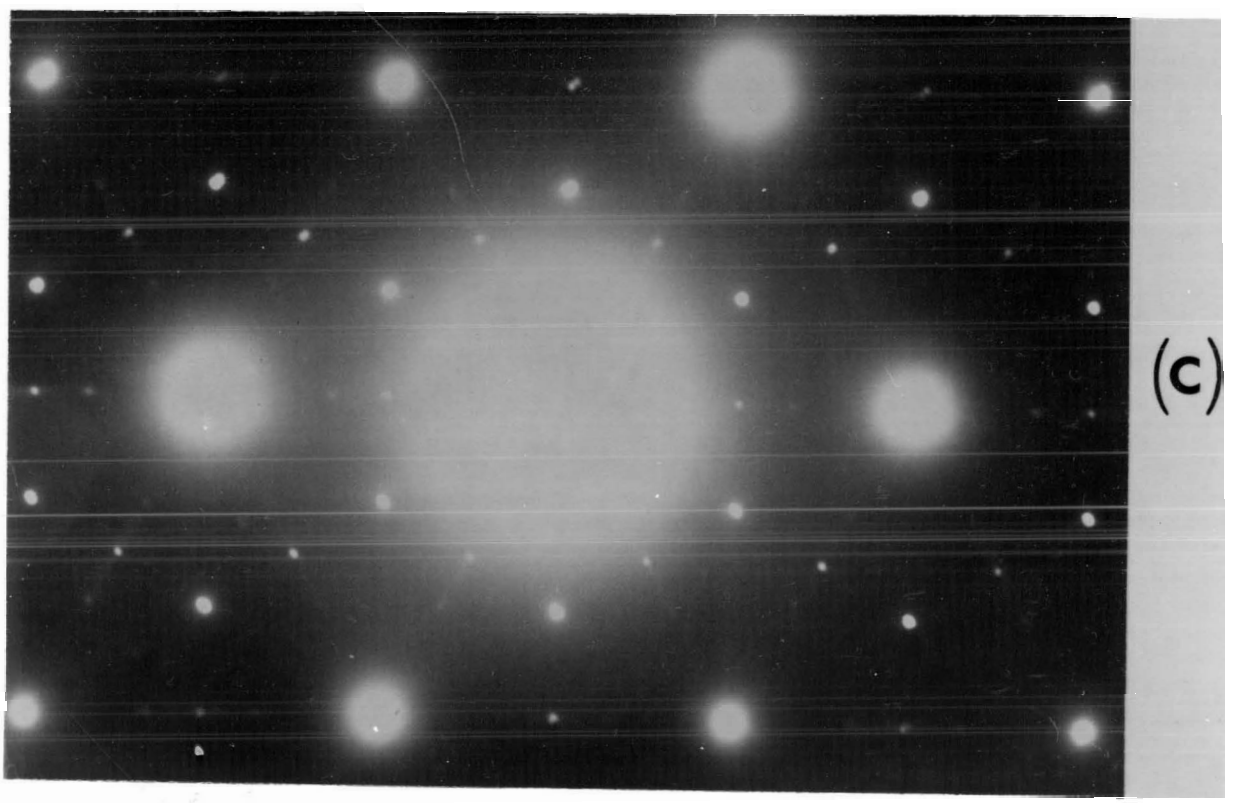
(c)

superlattice satellites. The diffuse scattering behaves as it did in the $Ag_{1/3}TaS_2$ samples in that it concentrates below about 200K as streaks through the $2a_o$ superlattice satellites and then disappears below about 110K where it is simultaneously replaced by new superlattice satellites. Initially, as for $Ag_{1/3}TaS_2$, these new satellites correspond to three orientational variants of a $(5\sqrt{3} \times 1)a_o$ superlattice plus continuous line-streaking halfway between the rows of the $(5\sqrt{3} \times 1)a_o$ superlattice satellites. After cooling a few degrees further, the line-streaking resolves into yet further satellites so that one finally observes the $(1/10 \times \sqrt{3}/4)a_o^*$, that is $(5\sqrt{3} \times 2)a_o$ superlattice (Fig. 5.1b). Note that at these low temperatures the $\sqrt{3}a_o$ superlattice satellite intensities have considerably weakened when compared to the $2a_o$ or even the $(5\sqrt{3} \times 1)a_o$ superlattice satellites.

(B) $Ag_{0.26}TaS_2$ Superlattices

At room temperature for $x = 0.26$ only a $\sqrt{3}a_o$ superlattice is observed whose satellites are relatively intense (Fig. 5.2a). Some diffuse scattering is also present but it is not geometrically oriented as observed for $x \gtrsim 0.30$, instead it points radially away from the main lattice reflections along $\langle 10.0 \rangle$ and intensifies somewhat near $a_o^*/2$. When heating, the $\sqrt{3}a_o$ superlattice satellites do

not disappear just above room temperature and are still noticeable near 400K (Fig. 5.2b) although the satellites have become fuzzy. Even though it is difficult to be quantitative, it is apparent that the disappearance of the $\sqrt{3}a_o$ superlattice occurs over a larger temperature interval than that for the $2a_o$ superlattice observed for larger x.

Cooling the sample below about 230K does cause weak $2a_o$ superlattice satellites to appear in addition to the relatively strong $\sqrt{3}a_o$ superlattice satellites. Diffuse streaks through the $2a_o$ superlattice satellites are again evident, however they are longer, sharper and much weaker than those observed when x is closer to 1/3 mole fraction (compare Fig. 5.2c with Fig. 4.4a). Continuing to cool the sample, further new satellites can be observed below about 100K which are $(0.347 \pm 0.002)a_o^*$ from the main spots, along the <10.0> directions, at either end of the streaks which are still visible at 25K (Fig. 5.2c).

(C) 2H-TaS_2, $Ag_{0.10}TaS_2$ and $Ag_{0.13}TaS_2$ Superlattices

The x = 0.10 and 0.13 samples are quite similar in that at room temperature they both show intercalated regions having a $\sqrt{3}a_o$ superlattice (Fig. 5.3a) in addition to apparently unintercalated regions where no superlattices are observed. It should be pointed out again that the beam size is about 1μm. No hint of a $2a_o$ superlattice is observed in either

Fig. 5.3

Diffraction patterns of intercalated regions in x = 0.10 or 0.13 samples: (a) at room temperature; only a $\sqrt{3}a_o$ superlattice is present. (b) near 130K; the $2a_o$ superlattice satellites appeared near 180K. (c) near 25K; the incommensurate satellites appeared below about 100K and are at $(0.337 \pm 0.002)a_o^*$ near 25K.

(Photographs kindly taken by Mr. M. Smith and Dr. A.E. Curzon.)

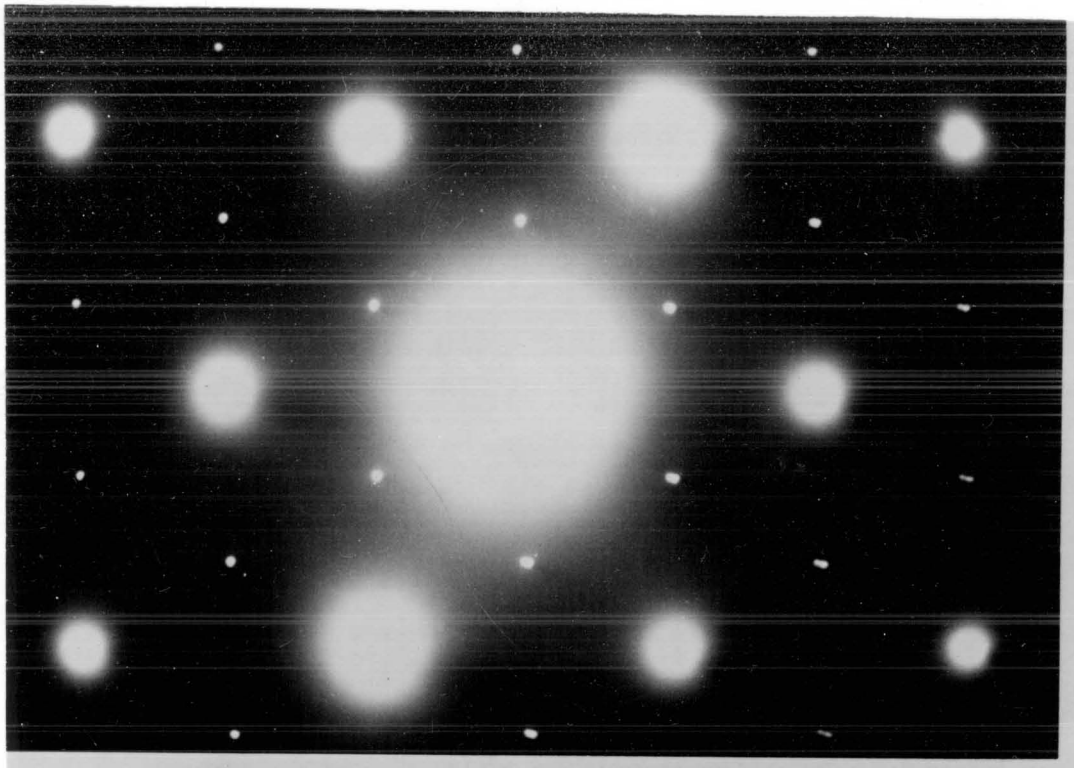

(a)

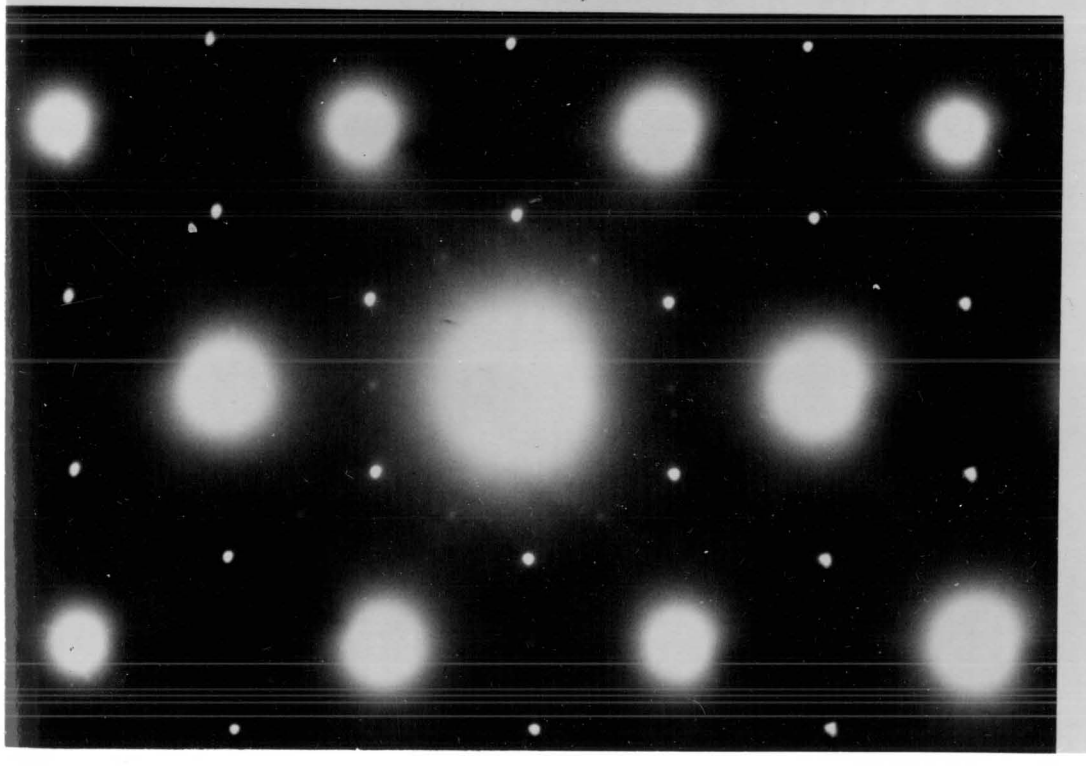

(b)

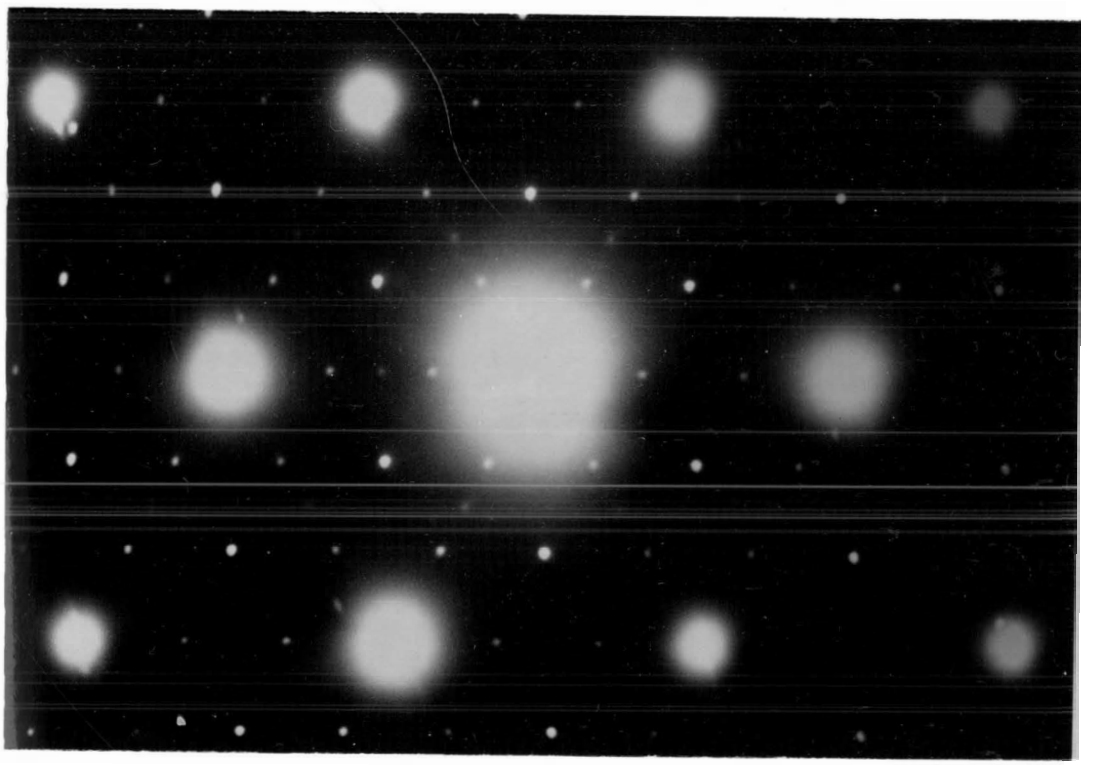

(c)

sample, and the only difference between the two samples is that for x = 0.10 there are more apparently unintercalated regions.

When heating these samples, the $\sqrt{3}a_o$ superlattice satellites again persist to well above room temperature and as for x = 0.26 (Fig. 5.2b) are fuzzy at 400K. Observing these intercalated regions while cooling, very weak $2a_o$ superlattice satellites will form below about 180K, which will become stronger on further cooling (Fig. 5.3a). Below 100K and above 70K, further satellites are observed which are at $(0.337 \pm 0.002)a_o^*$ along the <10.0> axes from the main spots near 25K (Fig. 5.3c).

Observing the apparently unintercalated regions while cooling, one finds that very fuzzy $2a_o$ and "$3a_o$" superlattice satellites appear below about 200K. The latter become sharper and stronger on cooling (Figs. 5.4a, 5.4b), but the $2a_o$ satellites disappear again below 100K. The exact position for the "$3a_o$" superlattice satellites at 25K is again $(0.337 \pm 0.002)a_o^*$ from the main spots. Very little hysteresis is noticed for any of these superlattice satellites when the samples are temperature cycled.

For completeness, a pure 2H-TaS_2 sample was cooled and no other superlattices aside from the "$3a_o$" CDW/PLD as previously reported [25] is observed near 76K. It is of interest that these satellites do not appear at $a_o^*/3$ along <10.0>, as reported by Tidman et al.[25], but instead are

Fig. 5.4

Diffraction patterns of apparently unintercalated regions in x = 0.10 or 0.13 samples; (a) near 130K; very diffuse $2a_o$ and "$3a_o$" superlattice satellites have appeared near 180K. (b) near 25K; the diffuse "$3a_o$" superlattice satellites have sharpened below about 100K and are incommensurate at $(0.337 \pm 0.002)a_o^*$ near 25K. The $2a_o$ superlattice satellites have disappeared again.

(Photographs kindly taken by Mr. M. Smith and Dr. A.E. Curzon.)

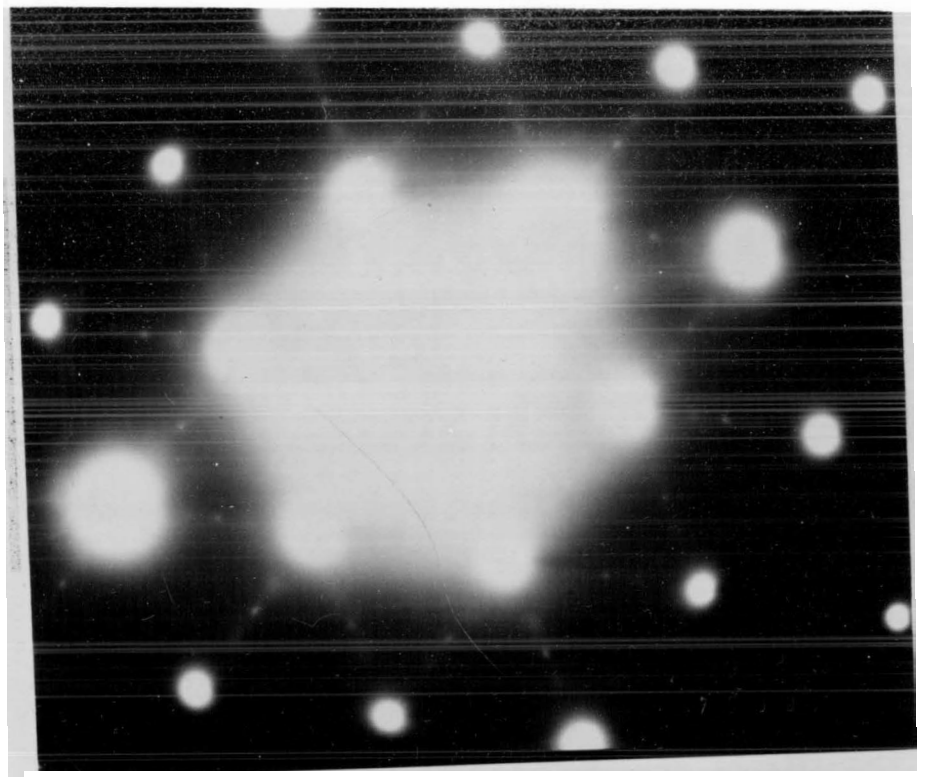

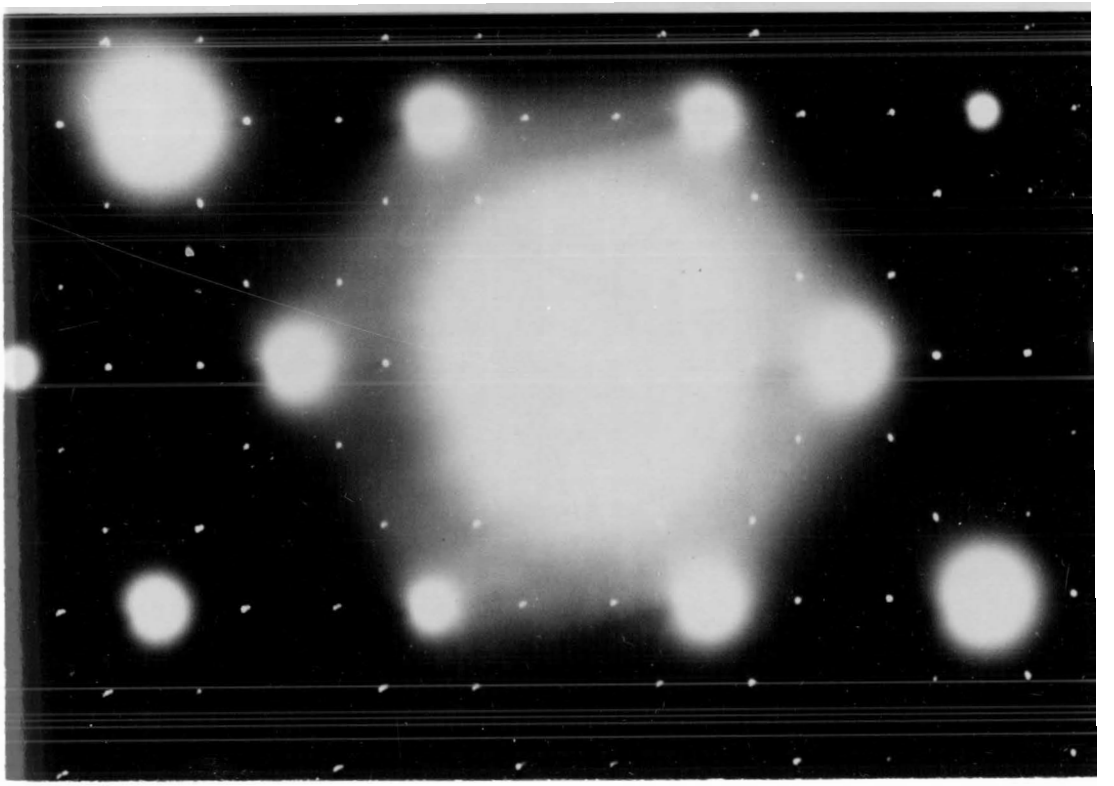

observed at $(0.338 \pm 0.002)a_o^*$ at 25K [66] and are therefore incommensurate with the host lattice.

(D) $Ag_{0.39}TaS_2$ Superlattices

For x = 0.39, with the exception of the presence of very weak $\sqrt{3}a_o$ superlattice satellites, the diffraction patterns observed on cooling to 25K are identical to those observed for x = 1/3 (Chapter 4). However, when cycling above 100K, whereas for x = 1/3, the $(5\sqrt{3} \times 2)a_o$ superlattice satellites disappear completely, for x = 0.39 they only disappear in part and "$4a_o$" satellites, discussed in Chapter 4, remain to much higher temperatures (Fig. 5.5) (even to room temperature if the sample is heated quickly), but will then always completely disappear within a few hours. On repeated cooling, the "$4a_o$" satellites will not reappear unless the sample is first cooled to below about 100K, so that the $(5\sqrt{3} \times 2)a_o$ superlattice is re-established.

(E) $Ag_{0.42}TaS_2$ Superlattices

Intercalating to x = 0.42 results in essentially the same diffraction patterns observed for x = 0.39 (i.e. like those for x = 1/3 plus weak $\sqrt{3}a_o$ superlattice satellites) down to about 100K. However, when cooling below about 100K, the continuous line-streaking does not disappear for x = 0.42 (as

Fig. 5.5

Electron diffraction pattern of $Ag_{0.39}TaS_2$, near 150K. The sample was first cooled below 100K so that the "$4a_o$" satellites have appeared. These "$4a_o$" satellites disappear if the specimen is held for a few hours at 150K.

Fig. 5.6

Electron diffraction pattern of an $Ag_{0.42}TaS_2$ sample near 25K. Below about 100K a $(5\sqrt{3} \times 1)a_o$ superlattice appears along with continuous line-streaking which does not resolve into the further satellites generating the $(5\sqrt{3} \times 2)a_o$ superlattice.

(Photographs kindly taken by Mr. M. Smith and Dr. A.E. Curzon.)

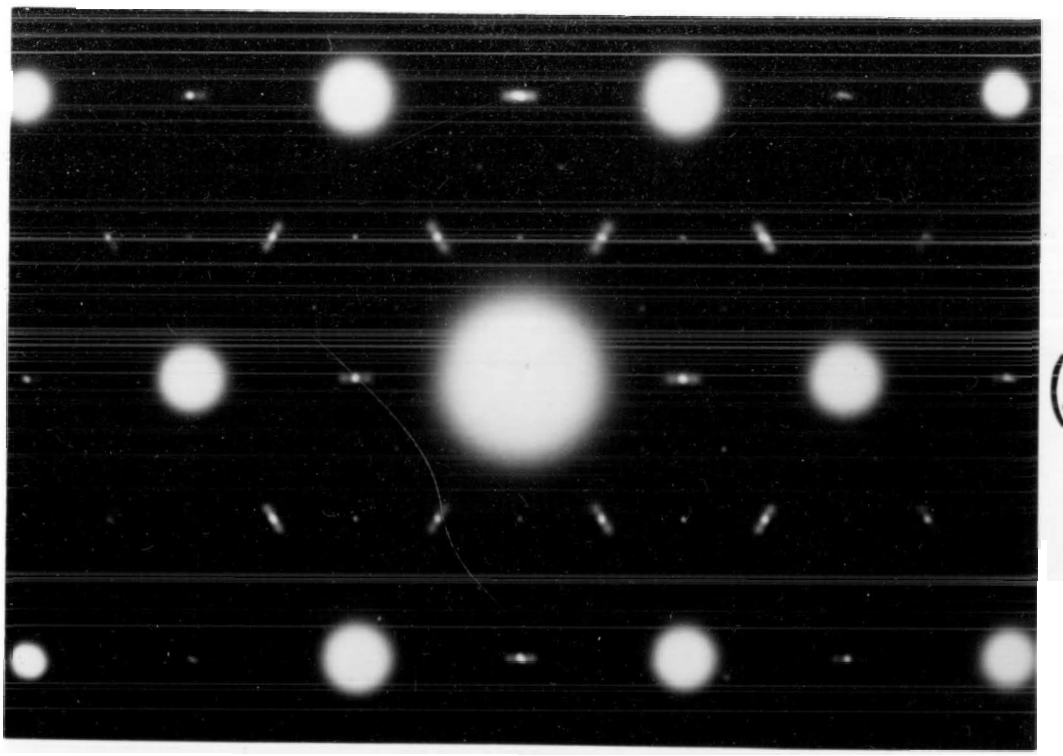

(5.5)

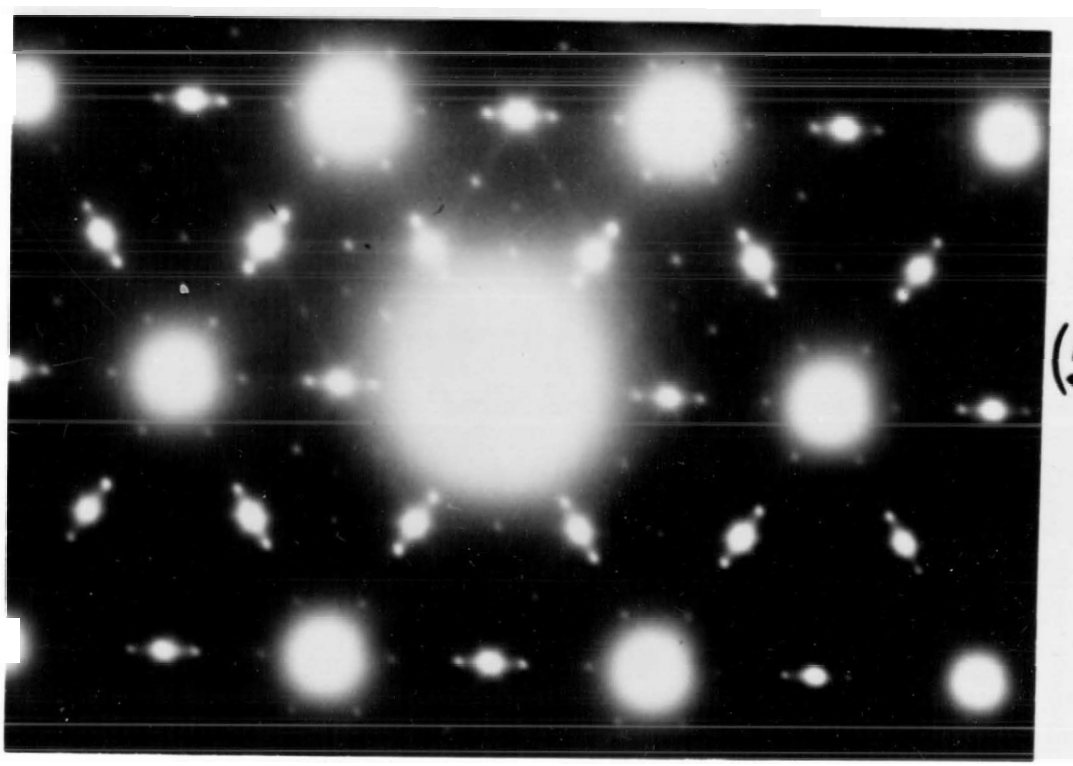

(5.6)

it does when x is closer to 1/3) and is still present at 25K (Fig. 5.6; compare with Fig. 4.3b). Consequently the $(5\sqrt{3} \times 2)a_o$ superlattice does not appear and the $(5\sqrt{3} \times 1)a_o$ superlattice is retained. As for x = 0.39, the "$4a_o$" satellites again do not exist above 100K unless the sample is first cooled to below about 100K (Fig. 5.6), after which they will again persist to higher temperatures on heating and disappear within a few hours.

(F) $Ag_{0.50}TaS_2$ Superlattices

As for the other x values at or above 1/3 mole fraction, one again observes only a $2a_o$ superlattice at room temperature along with diffuse scattering when cooling below about 200K the appearance of "$4a_o$" satellites (Fig. 5.7a) can be observed and they will immediately disappear again on heating above 200K, as for x = 2/3 (Chapter 4). However, it can be seen that there are additional very weak satellites present below 200K, four of which are rectangularly grouped around all $2a_o$ superlattice satellites. These satellites are at first glance very reminiscent of the (220) reflections from the $(2\sqrt{3} \times 5)a_o$ low temperature superlattice observed for x = 2/3 (Fig. 4.1d) which, however, is incorrect. Again, to avoid a large number of systematic absences, they are best indexed as (110) reflections of three orientational variants of a $(1/4 \times \sqrt{3}/6)a_o^*$, that is $(2\sqrt{3} \times 3)a_o$ superlattice reflections for higher (hkℓ) are too weak to be observed, or

Fig. 5.7

Diffraction patterns of an x = 0.50 sample: (a) near 170K; the "$4a_o$" satellites appear and disappear reversibly near 200K. In addition, (110) satellites from three orientational variants of a $(2\sqrt{3} \times 6)a_o$ superlattice can be seen. (b) near 25K; the (100) satellites of $(2\sqrt{3} \times 6)a_o$ superlattice are now also observed in addition to the $(5\sqrt{3} \times 2)a_o$ superlattice and line-streaking which appear below 100K.

(Photographs kindly taken by Mr. M. Smith and Dr. A.E. Curzon.)

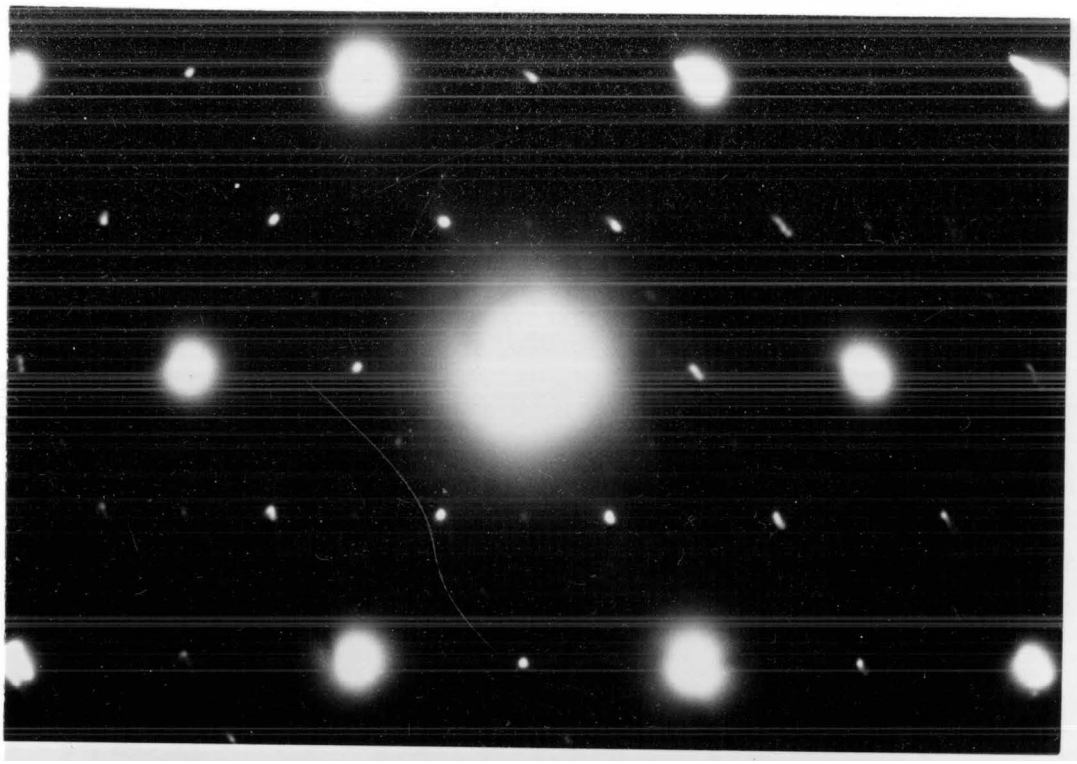

(a)

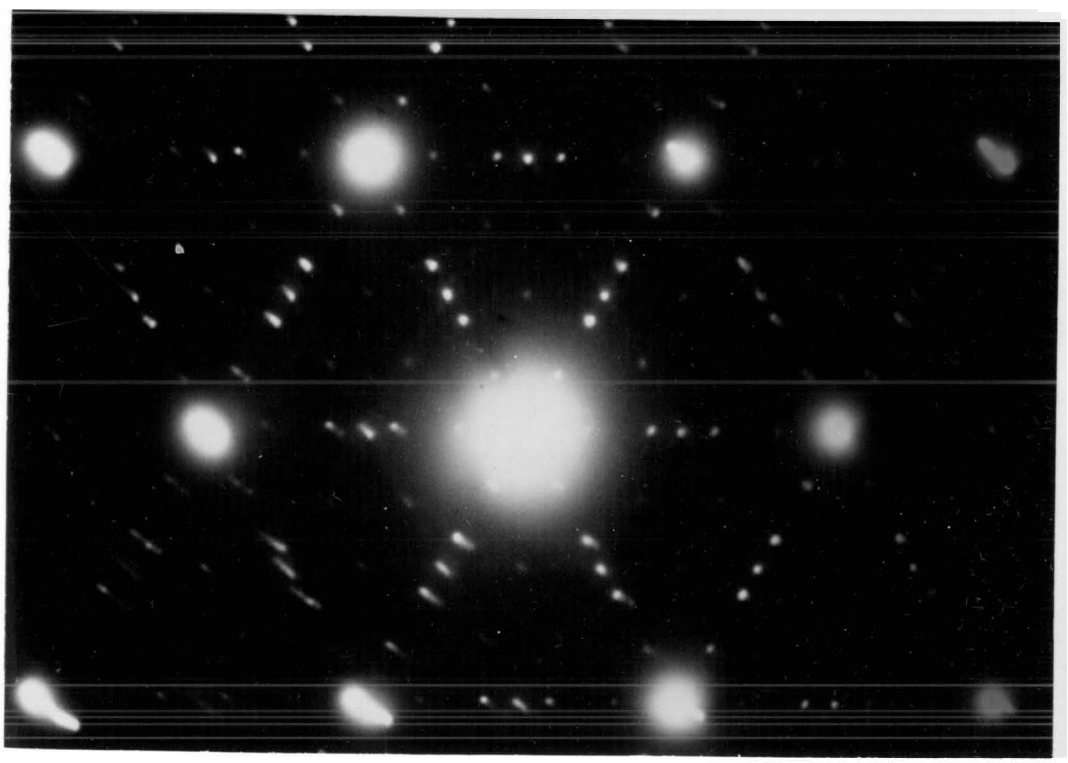

(b)

are absent. Cooling below about 100K (Fig. 5.7b) results in $(5\sqrt{3} \times 2)a_o$ superlattice satellites, as for x = 1/3, with the line streaking only partially resolved though; at $\sqrt{3}a_o^*/6$ along <11.0> faint satellites also appear and correspond to (100) reflections of the $(2\sqrt{3} \times 3)a_o$ superlattice; and finally, very faint $\sqrt{3}a_o$ superlattice satellites are also present. If the sample is temperature cycled, these superlattice satellites show no noticeable hysteresis.

5.3 Results of the Temperature Dependence of the Electrical Resistivity for Ag_xTaS_2

The change in the electrical resistivity versus temperature was measured for samples containing x = 0.10, 0.13, 0.26, 0.30, 0.39, 0.42 and 0.50 mole fraction of intercalated silver ions and it is found that the variations in $\rho(T)$ are continuous with increasing x (Fig. 5.8). In particular,as x is increased above 1/3, $\rho(T)$ develops more pronounced breaks in the slope near 200K and 100K and the resistance ratio ($R_{300}/R_{4.2}$) decreases from about 8 for x = 1/3 to the characteristic value of about 4 for x = 2/3. As x is decreased below 1/3 mole fraction to x = 0.26, the break in the slope near 200K washes out and the break at about 100K vanishes completely, as is shown in Fig. 5.8 S_2(b), while simultaneously the resistance ratio improves to about 18.

Fig. 5.8

The electrical resistivity versus temperature dependence for selected x values of Ag_xTaS_2. S_1 corresponds to stage 1 with x = 0.66; $S_2(a)$ and $S_2(b)$ represent stage 2 with x = 0.33 and x = 0.26 respectively; S_n corresponds to x = 0.10 and the sharp break in $\rho(T)$ at 75 ± 1K, as in pure 2H-TaS_2; 2H-TaS_2 represents $\rho(T)$ of the unintercalated host material showing the discontinuity at 75.3K due to a CDW/PLD [5].

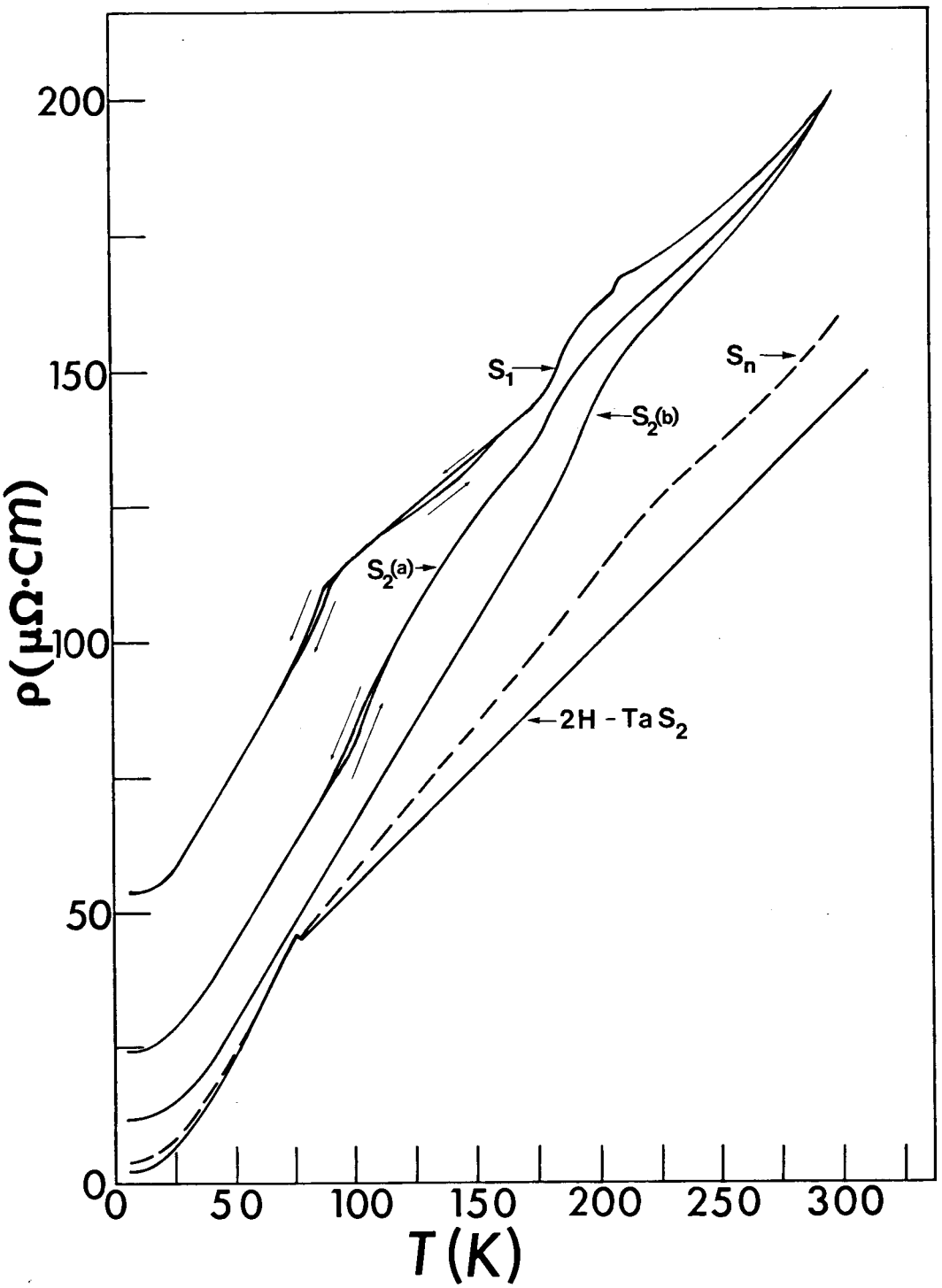
200
150
100
50
0
ρ(μΩ·cm)
0
50
100
150
200
250
300
T(K)
S1
Sn
S2(b)
S2(a)
2H - Ta S2

Decreasing x still further results in the appearance of a sharp break in the slope at 76 ± 2 K as shown for x = 0.10 in Fig. 5.8 S_n but also observed for x = 0.13. Note that the resistance ratio for x = 0.10 has now increased to at least 30 and the broad shoulder near 200K is still visible.

Even though absolute values of the resistivity are used in Fig. 5.8, with the exception of that for 2H-TaS_2, they are only intended to be indicative of the samples' absolute resistivity values and were arrived at by measuring several samples. The uncertainty in ρ arises because of the difficulty in measuring the sample thickness accurately. However, it is certain that the absolute values of the resistivities at room temperature are greater than the 150$\mu\Omega\cdot$cm for 2H-TaS_2 and less than 400 $\mu\Omega\cdot$cm.

5.4 Discussion of the Low Temperature Superlattices, Charge Density Waves and Electrical Resistivity Results for Ag_xTaS_2

Throughout this discussion it may be of help to refer to the summary presented in Table 5.1 and 10.1. The presence of a stage 2 $\sqrt{3}a_o$ superlattice at silver concentrations below x = 1/3 was unexpected since a $\sqrt{3}a_o$ superlattice was not observed for the more ideal concentrations of x = 1/3 and 2/3. Even more surprising is that for x = 0.26 and below, the $\sqrt{3}a_o$ superlattice is the only superlattice observed at room

Fig. 5.9

$\sqrt{3}a_o$ silver ion superlattice within a given van der Waals gap. Whereas the circules correspond to octahedral sites and the triangles to "up" and "down" tetrahedral sites, the large filled-in symbols correspond to those sites occupied by silver ions.

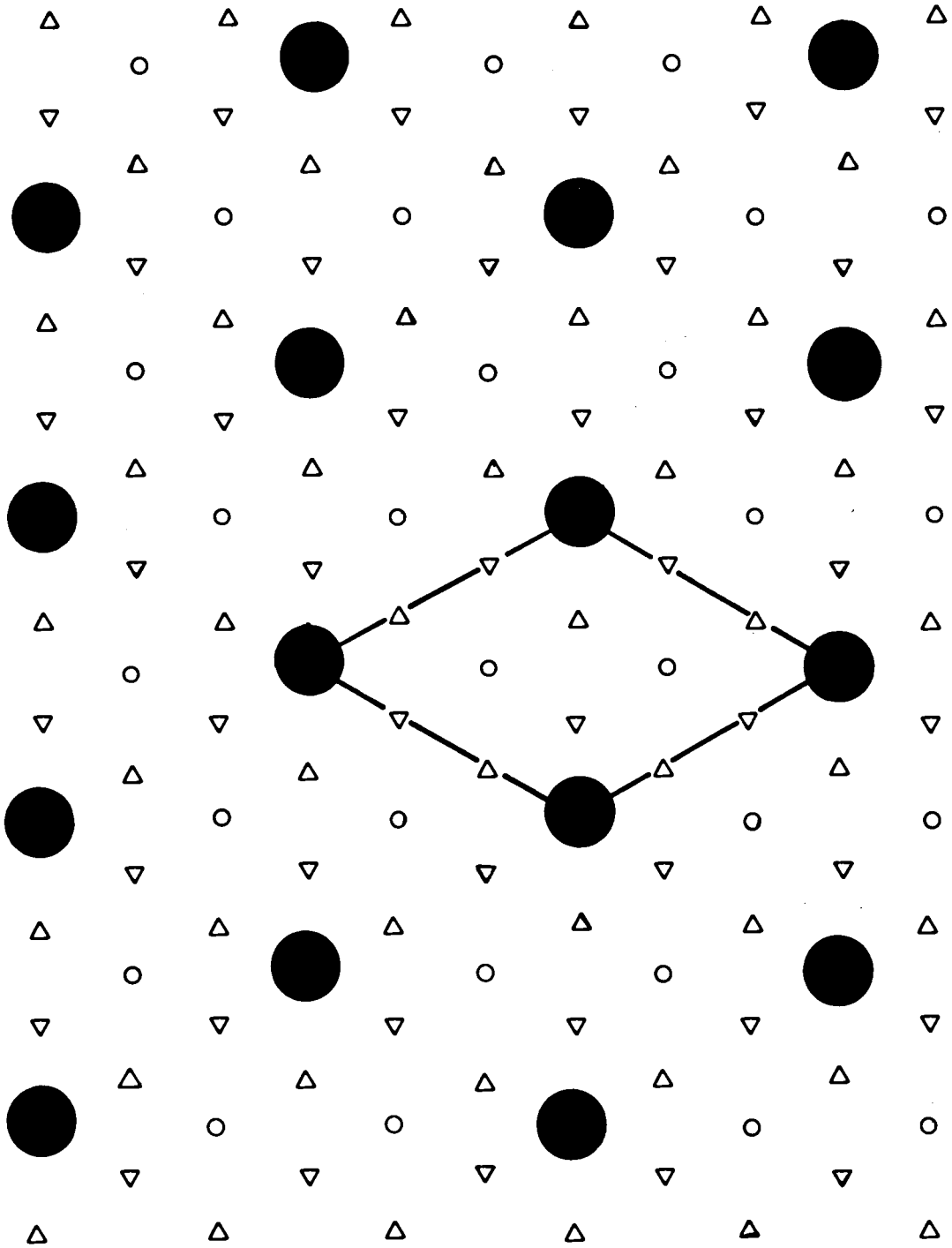

temperature (Fig. 5.2a, 5.3a). This can only mean that the silver ions causing the $\sqrt{3}a_o$ superlattice are residing in octahedral and not tetrahedral lattice sites. This conclusion is made because if the silver ions occupied tetrahedral sites, it would be essential that both the "up" and "down" tetrahedral sites be equally filled within a unit cell in the van der Waals gap, as already discussed in Chapter 4, so that the $\sqrt{3}a_o$ superlattice in Fig. 4.8 would be required. However, such a tetrahedral site superlattice is very unlikely because it requires that the silver ions occupy nearest neighbor sites and that $x' = 2/3$, Note that exactly for this x' concentration (attained with $x = 1/3$ or $2/3$), no $\sqrt{3}a_o$ superlattice satellites are observed (see Chapter 4) and the explanation based on Fig. 4.8 would therefore require that as x decreases below 1/3 mole fraction, x' will increase toward 2/3 which is very unlikely. An alternative explanation to the $\sqrt{3}a_o$ superlattice in Fig. 4.8 is that the silver ions reside in octahedral sites (Fig. 5.9) rather than tetrahedral lattice sites. The $\sqrt{3}a_o$ superlattice in Fig. 5.9 ideally requires $x = 1/6$ for stage 2 and this would therefore also explain why the $\sqrt{3}a_o$ superlattice satellites become dominant for $x \lesssim 1/4$.

X-ray powder patterns have indicated that tetrahedral sites are occupied in $Ag_{1/3}TaS_2$ and $Ag_{2/3}TaS_2$ (Chapter 3), but no such conclusions were made for other concentrations. In fact, since intercalation occurs because of charge transfer

from the intercalant to the tantalum "d_{z2} orbitals", the silver ions can be expected to reside initially in octahedral sites which are directly above and below the "d_{z2} orbitals", before shifting of the host layers has occurred (Chapter 3). Therefore it is assumed that "suitable" intercalation sites are those that have tantalum atoms above and/or below directing their "d_{z2} orbitals" into them. This situation is quite commonly also observed in other intercalation systems and is further discussed in Chapter 10.

A change in the host structure of $Ag_{1/3}TaS_2$ was observed by X-ray powder patterns (Chapter 3), if x is not within about ±0.005 of 1/3 mole fraction. Outside this limit it was found that although the (hk.0) and (00.ℓ) lines remain sharp, the (hk.ℓ) lines become fuzzy. This suggests that even though the host layers are intact and a stage 2 structure exists for $x \gtrsim 1/10$, the three-dimensional correlation of the host planes becomes vague and therefore implies that a stacking re-arrangement occurs. The changes in the stage 2 stacking sequence of the host layers might therefore be important to the existence of the $\sqrt{3}a_o$ superlattice satellites, since both show a similar dependence on x. This suggests that even though silver ion concentrations of, say, x = 1/6 andx = 1/3 correspond to stage 2 compounds, we might well expect that for x = 1/6, the host layers have not yet shifted relative to one another so that the silver ions are still residing in octahedral sites (Fig. 5.10a) and since x' = 1/3, the right concentration also exists for the simple $\sqrt{3}a_o$ superlattice in Fig. 5.9 . Another indication that a structural change

occurs when $1/6 < x < 1/3$ is from the relatively rapid increase in the lattice parameters observed near $x \simeq 1/4$ (Chapter 3). Because the lattice parameter remains relatively constant when a given phase is filled (Chapter 3) one can conclude that their pronounced increase reflects the additional space required by the silver ions when their intercalation site changes from the larger octahedral to the smaller tetrahedral sites.

As x is increased above 1/6, the "extra" silver ions will randomly occupy further octahedral sites until for some x value the host layers will shift (1/3, 2/3) relative to one another (Fig. 5.10). This shifting, to put it simply, is likely the consequence of the increasing Coulomb repulsion between opposing "d_{z2} orbitals" counteracting the attractive nature of an exchange interaction provided by their overlap, as they are increasingly filled with electrons donated by the intercalating silver atoms. What is loosely meant by Coulomb repulsion between "d_{z2} orbitals" is that since that part of the conduction band occupied by the electrons is quite narrow ($\sim$1 e.V.[29]) and essentially made up of "d_{z2} orbitals" [29], the spatial distribution of the electrons in the conduction band will be somewhat localized like the "d_{z2} orbitals". Therefore a staggered arrangement of the "d_{z2} orbitals" along $\hat{c}$ would correspond to a smaller Coulomb interaction energy. A more detailed discussion of the Coulomb and exchange energies, as it relates to stacking sequences observed here and in other intercalation systems, is given in Chapter 10.

Fig. 5.10

Two models of a stage 2 Ag_xTaS_2 structure: (a) x' = 1/3 and the silver ions are occuping 1/6 of the available octahedral sites. The units cell corresponds to 2 host layers which have not shifted with respect to one another. (b) x' = 2/3 and the silver ions are occupying 1/6 of the available tetrahedral sites. The host layers have shifted so that there are 6 layers per unit cell (see Chapter 3).

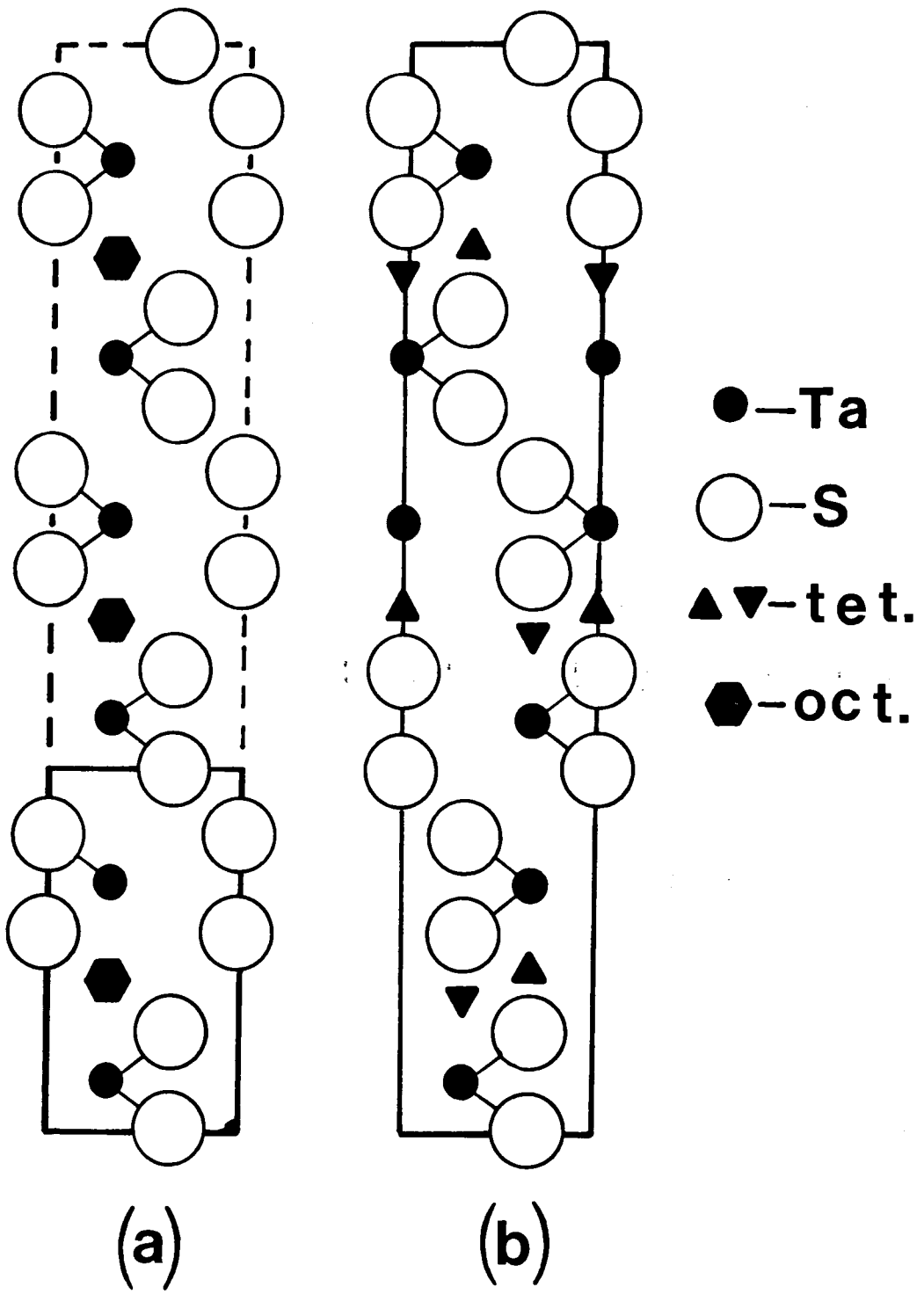
●—Ta
○—S
▲▼-tet.
⬢-oct.
(a)
(b)

Two immediate results of a stacking rearrangement of the host layers (Fig. 5.10) are that the tetrahedral sites have become suitable for intercalation and moreover, the total number of these suitable sites has doubled. Immediately after the shifting of the host layers has occurred, the ordered silver ions will reside in one particular tetrahedral site so that, since there are "up" and "down" sites present which are energetically equivalent, a redistribution of the silver ions will occur to a new superlattice. The new superlattice will have the two tetrahedral sites equally occupied while still minimizing the Coulomb interaction energies between the ions,and this results in the hexagonal $2a_o$ superlattice plus some randomly distributed silver ions at room temperature for $Ag_{1/3}TaS_2$ as found in Chapter 4. An estimate of x' required to produce host layer shifting is difficult. However, considering that for the x = 0.26 sample no $2a_o$ superlattice satellites are visible at room temperature (Fig. 5.2a) and that for x = 0.30 the $2a_o$ and $\sqrt{3}a_o$ superlattice satellites have comparable intensities, it follows that shifting of the host layers occurs for a silver ion concentration (x') of a little above 1/2 mole fraction.

Although both staging and the shifting of the host layers are related to the degree of intercalation, it should be realized that they can and will occur independently of each other in general. Furthermore, it is the existence of octahedral sites which are "suitable" for intercalation,which exist below x = 1/3, that are thought to be the cause of the $\sqrt{3}a_o$ superlattices. Preliminary confirming evidence for the

stage 2 structure in Fig. 5.10a has come from X-ray powder patterns of a thermally prepared $Ag_{1/6}TaS_2$ sample. The pattern is best indexed as a stage 2 compound having $a_o = 3.322 \pm 0.005$Å with the silver ions occupying octahedral sites as shown in Fig. 5.10a [30].

When the samples with $1/4 < x < 1/3$ are cooled it is found that the $2a_o$ superlattice satellites gain dramatically in intensity if they were already present at room temperature and if not, they will then develop at some temperature above 100K. This indicates that there is a conversion to the $Ag_{1/3}TaS_2$ stage 2 structure (Fig. 5.10b) on cooling. To understand the reason for the greater stability of the $2a_o$ superlattice at lower temperatures requires a detailed free energy calculation. It may well be that the larger entropy associated with the disordered silver ions, because of the more numerous sites (tetrahedral) "suitable" for occupation, may be the significant factor. Of course, for silver mole fractions near or below $x \simeq 1/6$, $2a_o$ superlattice satellites may also be the result of a simple hexagonal $2a_o$ superlattice with silver ions in octahedral sites because this superlattice should ideally exist for $x = 1/8$ if the host is uniformly stage 2.

Another interesting feature of the regions supporting a $\sqrt{3}a_o$ superlattice is that they do not support further silver superlattices at lower temperatures, in contrast to $x = 1/3$ and 2/3 samples which support two silver superlattices below

100K (Chapter 4). Furthermore, when heating a sample having a $\sqrt{3}a_o$ superlattice, the satellite reflections remain sharp to temperatures well above room temperature, where $2a_o$ superlattice satellites for all samples are already completely diffuse or absent. Eventually, at about 400K, as can be seen in Fig. 5.2b for x = 0.26 but also observed in the x = 0.10, 0.13 and 0.30 samples, the $\sqrt{3}a_o$ superlattice satellites are also diffuse. Furthermore, the temperature interval during which the satellites change from sharp to diffuse is observed in these samples to occur over a much broader temperature region for the $\sqrt{3}a_o$ compared to the $2a_o$ or $(\sqrt{3} \times 2)a_o$ superlattice satellites. Although further work is required, so far these results suggest that the order-disorder transition for the silver ions is 50K to 100K higher when they are occupying octahedral ($\sqrt{3}a_o$ superlattice) compared to tetrahedral ($2a_o$ or $(\sqrt{3} \times 2)a_o$ superlattice) sites.

The existence of a CDW/PLD below 75K, having $q^* = (1 + \delta)a_o^*/3$ with $\delta = (0.011 \pm 0.005)$ at 25K, for x = 0.10 and x = 0.13 samples appears certain. Of interest are the following two observations. The $\rho(T)$ dependence (Fig. 5.8S_n) shows that a CDW/PLD transition occurs at 76 ± 2K for the x = 0.10, 0.13 and the pure 2H-TaS_2 sample which, within experimental error, is the same temperature as reported by others for pure 2H-TaS_2 [25,31]. However, in addition, for the two intercalated samples $\rho(T)$ also has a shoulder near

200K, about the same temperature at which the "$3a_o$" CDW/PLD is first observed, using electron diffraction, in the apparently unintercalated regions of these samples (Fig. 5.4a). The temperature dependence of the electrical resistivity, along with the difference in the superlattice onset temperature, confirms that the CDW/PLD is indeed present in intercalated regions. Therefore, the explanation that q* is constant because of the presence of pure 2H-TaS_2 regions to $x \sim 1/8$, even though very tempting, can be discounted. Very much of interest is that the spanning vector in the intercalated (Fig. 5.3c) and apparently unintercalated (Fig. 5.4b) regions is identical, within experimental error, to $q^* = (0.338 \pm 0.002)a_o^*$ observed in pure 2H-TaS_2.

The apparently unintercalated regions where no superlattices develop above 200K likely correspond to dilute stage 1 regions. Interestingly, the dilute stage 1 phase, which exists near $x \sim 0.10$ for thermally intercalated samples (Chapter 3), apparently does not exist to these concentrations when the samples are electrochemically intercalated at room temperature. Instead, stage 2 coexists with presumably dilute stage 1 to lower concentrations, with the former regions eventually disappearing as x decreases further. This again points to the importance of the prevailing conditions under which intercalation is carried out, and agrees with the decreased range of x predicted for the dilute stage 1 phase,

if the sample is prepared at lower temperatures [23].

When the x = 0.26 sample is cooled below about 100K(Fig. 5.2c) the very weak satellites at (0.347 ± 0.004)a_o* from the main spots along <10.0> are again likely due to a CDW/PLD. This is not unreasonable, even though there is no break in the slope of ρ(T) (Fig. 5.8), because the intensity of the superlattice satellites at 25K (Fig. 5.2c) do indicate that the CDW/PLD is very weak. Furthermore, the resistance ratio of the x = 0.26 sample is about 18 so that impurity scattering is also not excessive.

Whereas the x = 0.26 and the intercalated regions of the x = 0.10 and 0.13 samples do not show a CDW/PLD above 100K (Fig. 5.4b), surprisingly the unintercalated regions in the latter samples do (Fig. 5.3b). In fact, very fuzzy "3_o" CDW/PLD and $2a_o$ superlattice satellites can already be observed near 180K ($\sim 5T_o/2$), which will then sharpen on cooling, indicating second-order behaviour. The cause of the weak and initially fuzzy $2a_o$ superlattice satellites in the presumably unintercalated regions of the sample is unclear, but they are often observed in non-stoichiometric unintercalated compounds and various explanations, including a CDW/PLD, have been proposed [32].

The minor variations in q* tend to lend support to the saddle-point nesting model [33] (Γ - K points coupled through a CDW distortion with a spanning vector q* = "$2/3a_o$*") as a cause for the CDW/PLD because it can explain why no apparent

change in q* is observed for intercalated samples (x = 0.13) even though the Fermi surface is likely to be modified by intercalation. The suppression of the CDW observed for x = 0.26 could then be a direct result of burying the saddle-points below the Fermi sea which is increasing because of charge transfer, and the 1.5% decrease in q* (i.e from $0.663a_o^*$ to $0.653a_o^*$) may be explained by a change in the location of the saddle-points which is expected to be a second-order effect. On the other hand, an alternative model where a coupling vector q* = "$a^*_o/3$" connects pieces of Fermi surface [34] can certainly not be ruled out and the increase in q* would be the direct consequence of a small change in the Fermi sea. For x = 0.30 it is tempting to interpret the $(5\sqrt{3} \times 1)a_o$ superlattice satellites appearing below about 100K (Fig. 5.1b) as a CDW/PLD having q* = $0.400a_o^*$. However, this is highly unlikely because these satellites are relatively strong and are observed to concentrations of at least x = 0.50 (Fig. 5.7b), where considerable impurity scattering exists because the samples resistance ratio (Fig. 5.8) is low (~ 6). Furthermore, for the higher x values, the saddle-points must surely be buried deep below the Fermi surface. These satellites were previously explained as a silver superlattice (Chapter 4).

The sample with x = 0.30 is stage 2 but, as indicated by Fig. 5.1a at room temperature, has regions corresponding to the nominally $Ag_{1/6}TaS_2$ and $Ag_{1/3}TaS_2$ (Fig. 5.10)

structures present. As previously discussed (Chapter 4) the latter regions incorporate some randomly distributed silver ions which can therefore be expected to order on a $(5\sqrt{3} \times 2)a_o$ superlattice near 100K, whereas the former regions, in contrast, should not produce further superlattices when cooled. Inspection of Fig. 5.1b reveals that these coclusions do appear to be correct at least to 25K.

For x = 0.39, 0.42 and 0.50, the $2a_o$ (or$(\sqrt{3} \times 2)a_o$ with k = odd absent) superlattice satellites are again observed at room temperature as expected. However, in addition to these, very weak $\sqrt{3}a_o$ superlattice satellites are also observed at all temperatures (Figs. 5.5, 5.6, 5.7). The fact that they are very weak suggests that only a small number of silver ions are involved. It is reasonable to expect some silver ions to occupy the octahedral sites in the unintercalated van der Waals gaps of stage 2, before the host layers shift to the stage 1structure (Chapter3), and be the cause of the weak $\sqrt{3}a_o$ superlattice satellites. These satellites will not be considered in any further discussion because some local variations in x will always exist for one reason or another and can cause these very weak $\sqrt{3}a_o$ (and $2a_o$ for low x) superlattice satellites when ideally they should not exist.

Keeping the above in mind, the x = 0.39 sample behaves very similar to the x = 1/3 sample (Chapter 4) at all temperatures. However, for x = 0.42 the $(5\sqrt{3} \times 2)a_o$

superlattice does not develop below 100K and instead the $(5\sqrt{3} \times 1)a_o$ superlattice and line-streaking persists to 25K along with "$4a_o$" satellites (Chapter 4) (Fig. 5.6). Therefore, although the silver ions develop a $2a_o$ spacing within "chains" (Chapter 4) to produce the line-streaking in reciprocal space, inappreciable interchain correlations develop for this ($x = 0.42$) concentration to produce the $(5\sqrt{3} \times 2)a_o$ superlattice. When the $x = 0.39$ and 0.42 samples are warmed again above about 100K, the "$4a_o$" satellites do not disappear reversibly and remain to higher temperatures (Fig. 5.5), thus indicating the presence of regions having the stage 1 $(\sqrt{3} \times 2)a_o$ superlattice (Chapter 4). This is in agree ment with x-ray diffraction results (Chapter 3) which indicate the presence of a mixed stage 1 and 2 phase for $1/3 < x < 2/3$. The hysteresis in the appearance and disappearance of the "$4a_o$" satellites indicates that stage 1 is more stable than stage 2 at lower temperatures, but once formed, will only slowly revert back to stage 2 at temperatures above 100K.

As $x = 2/3$ is approached, it is expected that at some point the "$4a_o$" satellites will appear reversibly below about 200K (Chapter 4). This is observed for $x = 0.50$ (Fig. 5.7a), however, in addition, one can also observe satellites corresponding to (110) reflections from three orientational variants of a $(2\sqrt{3} \times 3)$ superlattice which can be tentatively associated with the ordering of the "excess"

silver ions in the stage 1 regions. The strong $(5\sqrt{3} \times 2)a_o$ superlattice satellites along with considerable line-streaking (Chapter 4) to 25K, forming below 100K, indicates that the sample is still predominantly stage 2. However, the "$4a_o$" satellites in addition to the $(2\sqrt{3} \times 3)a_o$ superlattice do indicate a significant amount of stage 1 regions. For x = 2/3 the "excess" silver ions order on a $(2\sqrt{3} \times 5)a_o$ superlattice below 100K and it would be difficult to predict why the $(2\sqrt{3} \times 3)a_o$ and not the $(2\sqrt{3} \times 5)a_o$ superlattice is more stable for x = 0.50. However, it certainly is not unreasonable for these variations in superlattice size to occur since the superlattices are governed by the particular number of silver ions available and the details of their interaction.

5.5 Conclusions Regarding the Low Temperature Superlattices and Charge Density Waves Observed in Ag_xTaS_2

By combining information obtained from single crystal electron diffraction, X-ray powder diffraction patterns and electrical transport measurements, the various structures of the Ag_xTaS_2 system have been interpreted. A summary is presented in Table 5.1 which applies to samples that are uniformly electrochemically intercalated at room temperature. It should be remembered that if the samples are prepared thermally, the intercalation temperature, rate of cooling, etc., can cause

Table 5.1

Summary of the oberved superlattices for Ag_xTaS_2 and the temperature regions in which they are observed, for selected mole fractions of intercalated silver ions.

x	x'	stage	interc. site	Superlattices Observed: about 400K to 300K	about 300K to 200K	about 200K to 100K	about 100K to 25K
zero	zero	-	-	-	-	-	"$3a_o$" CDW/PLD $(0.338\ 0.002)a_o^*$ (66)
zero to ∿1/6	Properties correspond to a mix of those for x = zero and x = 1/6. No observable change in q^* of the CDW/PLD. Sometimes very weak $2a_o$ superlattice satellites are observed.						
1/6 (ideal behaviour)	1/3	2	octahedral	$\sqrt{3}a_o$	$\sqrt{3}a_o$	$\sqrt{3}a_o$	$\sqrt{3}a_o$; "$3a_o$" CDW/PLD $(0.337\ 0.002)a_o^*$
∿1/6 to ∿1/3	Properties are a mix of those for x = 1/6 and x = 1/3, with those of the latter becoming more apparent at lower temperatures. The "$3a_o$" CDW/PLD superlattice is lost just above x=1/4 where it is $(0.347 \pm 0.002)a_o^*$.						
1/3	2/3	2	tetrahedral	-	$2a_o$	$2a_o$	$2a_o$; $(5\sqrt{3}\times 2)a_o$
∿1/3 to ∿2/3	Properties are a mix of those for x = 1/3 and 2/3, with those of the latter predominating at lower temperatures. For $x \approx \frac{1}{2}$ in the stage 1 regions, the low temperature superlattice is $(2\sqrt{3}\times 3)a_o$ and not $(2\sqrt{3}\times 5)a_o$ as expected.						
2/3	2/3	1	tetrahedral	-	$(\sqrt{3}\times 2)a_o$ and absences k = odd	$(\sqrt{3}\times 2)a_o$	$(\sqrt{3}\times 2)a_o$; $(2\sqrt{3}\times 5)a_o$

considerable variations in the observed phases, and will therefore also effect the silver superlattices observed.

The existence of CDW/PLD in Ag_xTaS_2 intercalation compounds has been observed. The spanning vector in pure 2H-TaS_2 is $(0.338 \pm 0.002)a_o^*$ and therefore incommensurate with respect to the host lattice. For x near 1/8 the spanning vector remains unchanged, but increases to $(0.347 \pm 0.002)a_o^*$ for x near 1/4, therefore giving support to the saddle-point nesting model [33] because of the small changes in q*. Above $x \sim 1/4$, when the resistance ratio of the samples rapidly decreases below about 18, the CDW/PLD appear to be suppressed either because of excessive "impurity" scattering or buried saddle-points.

Even though both staging and the stacking arrangement of the TaS_2 layers are dependent on the degree of intercalation, they are independent of each other. In particular, it is suggested that on intercalation the stacking sequence of TaS_2 layers is altered because the Coulomb interaction between the "d_{z^2} orbitals" exceeds their exchange interaction. On the other hand, as is further discussed in Chapter 10, staging is likely due to a balance between the Coulombic repulsion of the silver ions in a van der Waals gap and the work required to separate and bend successive TaS_2 layers and insert silver ions between them (rather than the work done in compressing the TaS_2 planes, between intercalated layers, parallel to $\hat{c}$, as discussed by

Safran and Hamann for graphite [35]).

The shifting of the host layers to the $Ag_{1/3}TaS_2$ structure seems to occur for values of x' somewhat above 1/2 and results in a change of the "suitable" intercalation sites from octahedral to tetrahedral, so that in both cases the silver ions will be situated close to a tantalum "d_{z^2} orbital".

CHAPTER 6

SUPERLATTICES IN Ag_xTiS_2

6.1 Experimental Arrangement and Procedure

Using 1T-TiS_2, single crystals of Ag_xTiS_2 were prepared containing various amounts of silver, ($0 < x \lesssim 0.42$) corresponding to pure stage 1 and stage 2, and mixed phases. The samples were electrochemically prepared as already described in Chapters 2 and 3. The degree of intercalation was determined by weighing, and X-ray powder patterns of part of the crystals, were taken to confirm the phase formed as inferred by the mole fraction intercalated.

The electron diffraction patterns were obtained with a 100kV beam perpendicular to the basal plane of the sample, from about 400K to 25K [24], using a Phillips E.M. 300 electron microscope. The temperature dependence of the electrical resistivity was not determined for any of the Ag_xTiS_2 samples.

6.2 Results of the Low Temperature Superlattice Formation in Ag_xTiS_2

The Ag_xTiS_2 system was not pursued in any great detail, but some observations follow. When the intercalated mole fraction of silver is below about x = 1/15, no superlattice satellites are observed down to 25K. For

greater mole fractions of intercalated silver ions, up to the maximum of about $x \simeq 0.42$, only superlattice satellites corresponding to a $\sqrt{3}a_o$ superlattice were observed (Fig. 6.1). The temperature at which the $\sqrt{3}a_o$ superlattice satellites change from fuzzy to sharp is, however, found to be dependent on the degree of intercalation In particular, whereas for $Ag_{0.20}TiS_2$ (stage 2) the $\sqrt{3}a_o$ superlattice satellites appear sharp below about 290K, for $Ag_{0.40}TiS_2$ (stage 1) the $\sqrt{3}a_o$ superlattice satellites does not become sharp until about 250K and moreover, for a $Ag_{0.50}TiS_2$ sample (stage 2; for a discussion of the stage see Chapter 10) the $\sqrt{3}a_o$ superlattice satellites do not become sharp until about 210 K. For all samples the $\sqrt{3}a_o$ superlattice satellites will become more intense on cooling and eventually, for the samples containing larger mole fractions of silver, the $\sqrt{3}a_o$ superlattice satellites will become almost as intense as the main lattice reflections. Diffuse scattering, appearing as streaks in the <11.0> directions, joining the $\sqrt{3}a_o$ superlattice satellites is also observed for most samples.

6.3 Discussion of the Low Temperature Superlattice Observed in Ag_xTiS_2

The absence of superlattice satellites, other than those corresponding to a $\sqrt{3}a_o$ superlattice, for all mole fractions

of silver investigated ($0 < x \lesssim 0.42$) is very surprising indeed. It implies that for some intercalate concentrations a significant mole fraction of silver ions are not incorporated into the $\sqrt{3}a_o$ superlattice and must therefore be randomly distributed. It is these randomly distributed silver ions which will then, presumably, be the source of the diffuse streaking observed (note that for the Ag_xTaS_2 samples, above about 100K, randomly intercalated silver ions are also observed in addition to a silver ion superlattice (Chapters 4 and 5)). Since a $\sqrt{3}a_o$ superlattice will ideally exist for $x = 1/3$ and $x = 2/3$ mole fraction, one could argue that randomly intercalated silver ions are not actually present and that instead regions containing $x = 1/3$ and $x = 2/3$ mole fraction of silver ions exist in various proportions within the sample. Even though this explanation is possible in principle, it is thought to be extremely unlikely because it is completely unclear why these two phases, of widely differing concentrations and interionic interactions, should coexist.

In Chapter 3 it was determined that the silver ions in Ag_xTiS_2 ($0 < x \lesssim 0.42$) reside in octahedral intercalation sites and the dichalcogen sandwich stacking arrangement does not change, so that the titanium atoms remain in-line along $\hat{c}$. Interestingly, for $x \lesssim 1/4$, the Ag_xTaS_2 samples too only develop a $\sqrt{3}a_o$ silver superlattice, down to about 25K, and what might be quite significant is that in this

Fig. 6.1

The $\sqrt{3}a_o$ superlattice statellites observed for $0 < x \lesssim 0.42$ below room temperature.

(Photographs kindly taken by Mr. M. Smith and Dr. A.E. Curzon.)

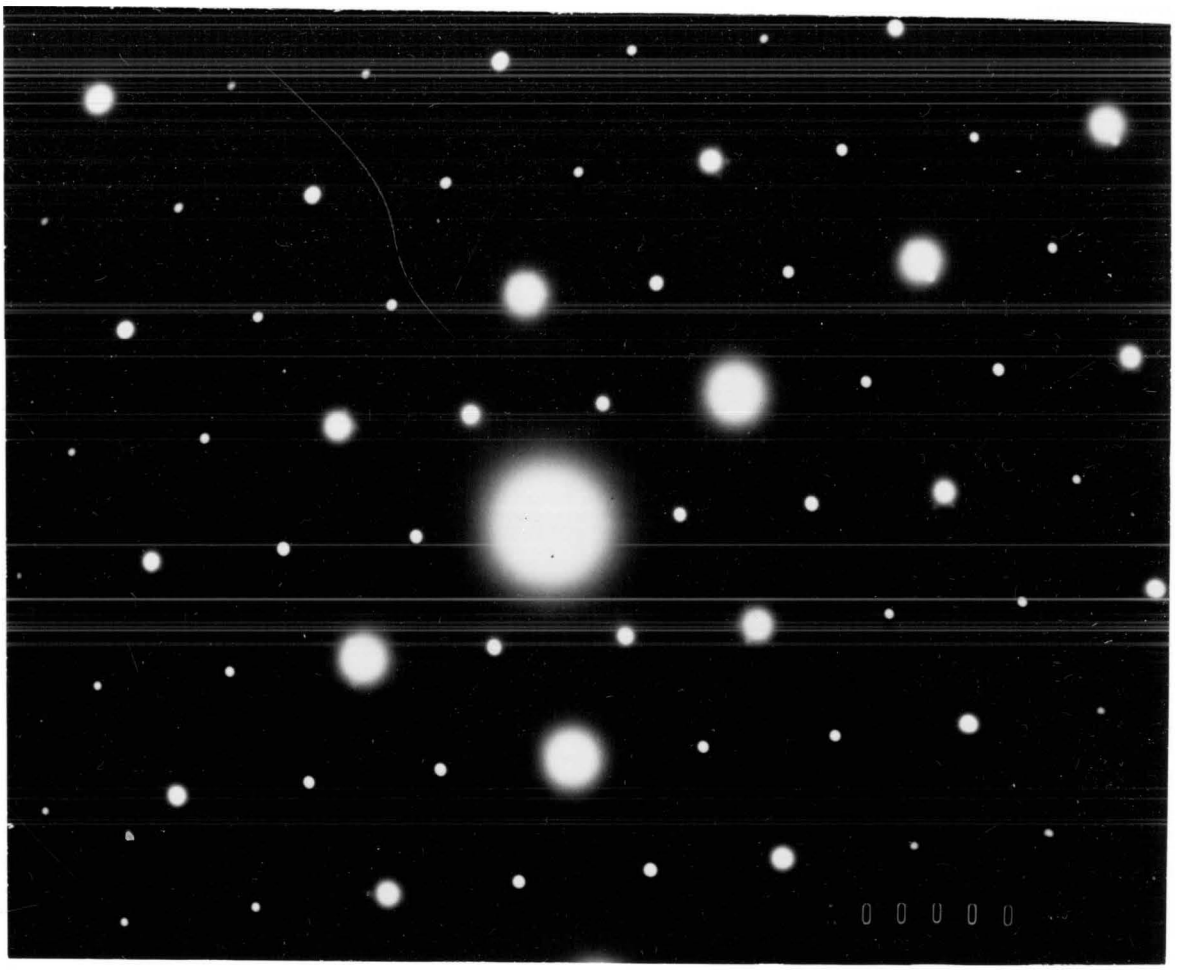

concentration range the silver ions also reside in octahedral intercalation sites and the tantalum atoms are also arranged in an in-line configuration along $\hat{c}$. This fits in well with the ideas presented in Chapters 5 and 10 on the relationship between intercalation sites, octahedral versus tetrahedral, and the eclipsed versus staggered arrangement of the transition metal atoms along $\hat{c}$. In particular, because the non-bonding orbitals (t_{2g}) of titanium in Ag_xTiS_2 are ideally empty when x = 0, Coulomb repulsion should only occur for much higher x compared to Ag_xTaS_2, where one of the t_{2g} orbitals of tantalum ("d_{z^2}") is ideally already one-half filled for x = 0. This is indeed the case and whereas for Ag_xTaS_2 a conversion from an eclipsed to a staggered arrangement of the tantalum atoms occurs above x $\simeq$ 1/4, for Ag_xTiS_2 the titanium atoms remain in-line at least to x $\simeq$ 0.42. However, it would appear that in stage 2 Ag_xTiS_2 and Ag_xTaS_2 compounds, above x $\simeq$ 1/4 the stress caused by the excess mole fraction of silver ions (x $\simeq$ 1/12), above the x = 1/6 ideally required for a $\sqrt{3}a_o$ superlattice, will cause changes in their structures because the former develops a stage 1 phase (Chapter 3) andthe latter experiences a layer stacking rearrangement (Chapter 5). For a further discussion of staging and stacking sequences refer to Chapter 10.

The reason for the decrease in the order-disorder transition temperature as the mole fraction of silver in

Ag_xTiS_2 increases is not clear. One explanation may be that as the degree of intercalation increases the net charge transfer to the host lattice may well decrease so that the ordering of the silver ions, largely dependent on their Coulombic interactions, will occur at lower temperatures.

CHAPTER 7

E.M.F. MEASUREMENTS

7.1 Introduction to Electrostatic and Chemical Potentials

When an ion is intercalated, it will encounter electrochemical potentials and it becomes important to clearly define exactly what is meant by the various terms involved (see also Bockris [36]). As a starting point assume a homogeneous medium α, in a vacuum. The work, W, done in moving a test charge, q_T, from $r = \infty$ to some point, o, inside the medium, defines the net potential, $\bar{\mu}$, as a state function.

$$^{\alpha}\bar{\mu}_T = 1/q_T \, (^{\alpha}W_T) = 1/q_T \int_{\infty}^{o} {}^{\alpha}F_T \cdot dl \qquad (7.1)$$

This net potential is usually referred to as the electrochemical potential of the test charge q_T in the phase α and is a function of temperature. At OK, $^{\alpha}\bar{\mu}_T$ is alternatively called the Fermi energy, but because it usually only varies slowly with temperature it is similar (within less than 1%) to the Fermi energy at room temperature. Therefore the two terms, electrochemical potential and Fermi energy, are often used interchangeably depending on whether electrons or other chemical species are referred to.

Fig. 7.1

Schematic illustration of the various potentials an ion encounters at an interface.

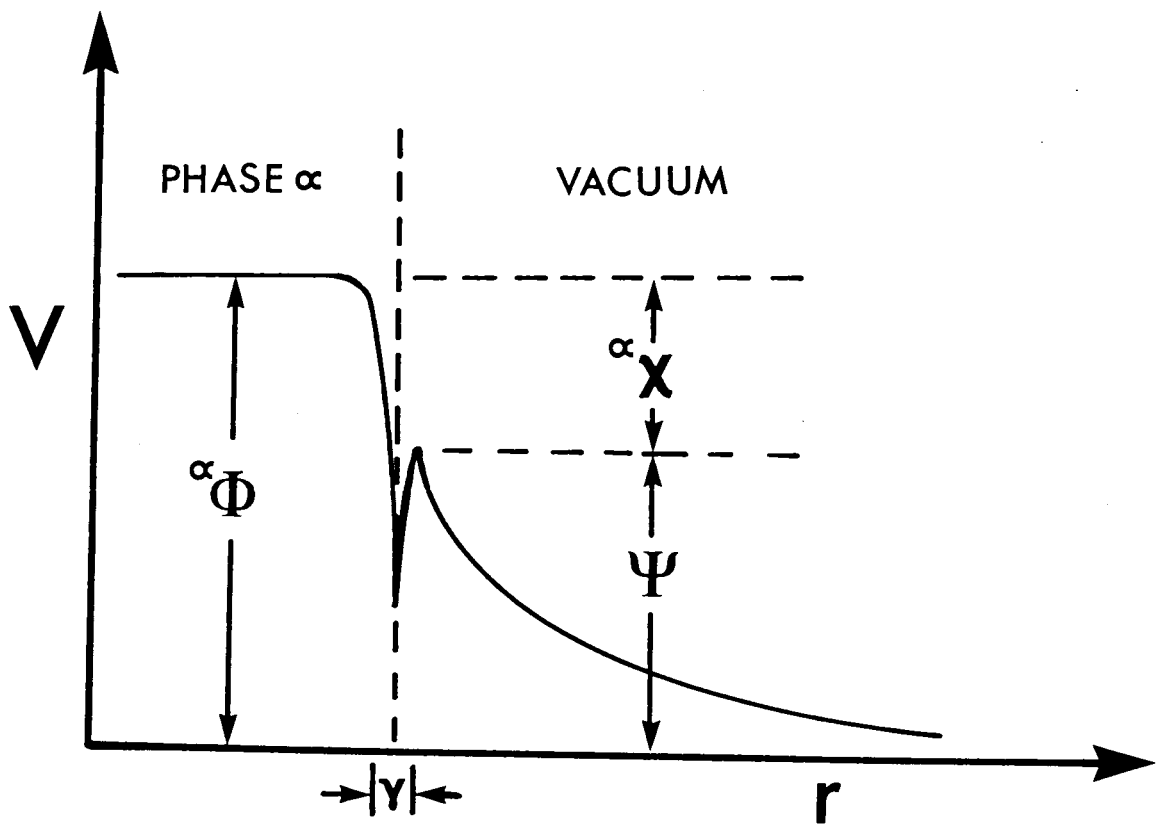
PHASE α
VACUUM
V
$^{\alpha}\chi$
$^{\alpha}\Phi$
Ψ
γ
r

Since external fields (electrostatic) can usually be accounted for, the electrochemical potential can be separated into a "purely" chemical work term, and a "purely" electrostatic work term.

$$\overline{{}^{\alpha}\mu_i} = {}^{\alpha}\mu_i + z_i F {}^{\alpha}\Phi \tag{7.2}$$

where ${}^{\alpha}\Phi$ is the Galvani potential, z_i the charge number, F the faraday constant and ${}^{\alpha}\mu_i$ is the chemical potential within phase α. It proves helpful to further separate the Galvani potential into a Volta (Ψ) and a Surface potential (χ)

$$\Phi = \Psi + \chi \tag{7.3}$$

as illustrated in Fig. 7.1.

The Volta potential (Ψ) is measurable since it is defined within one phase only. On the other hand, the Surface potential (χ) is not measurable since, if a test charge were brought into the medium, a rearrangement of electronic structures would occur thus making chemical and electrostatic work indistinguishable. Note that the Galvani potential is therefore also not measurable. The Surface potential is thought to occur typically over distances, γ, which are of order 100Å and is caused by a double (or dipole) layer on the surface of α which in turn is caused by electrons spreading

beyond the surface of α.

Since we can (in principle) measure both ${}^{\alpha}\mu_i$ and Ψ, it becomes convenient to define another potential which is called the Work function, ${}^{\alpha}\nabla_i$, of the test charge in α.

$$ {}^{\alpha}\nabla_i = {}^{\alpha}\mu_i - z_i F\Psi = {}^{\alpha}\mu_i + z_i F\chi \qquad (7.4) $$

The Work function is measured via photoelectric or thermionic emission and is a useful parameter in characterizing changes on a surface due to adsorption since, presumably, χ will be predominantly influenced.

On considering an electrochemical cell such as in Fig. 2.2, at equilibrium an ideal electrometer will measure a potential $\Delta\Phi$. The electromotive force (E.M.F.) of the cell is defined as the limiting value of $\Delta\Phi$ as the current through the cell goes to zero.

$$ E = \Delta\Phi \ (i \to 0) \qquad (7.5) $$

Therefore the E.M.F. of the cell in Fig. 2.1 can be written as

$$ E = \{\Phi_{Cu} - \Phi_{Ag}\} + \{\Phi_{Ag} - \Phi_{Ag^+}\} + \{\Phi_{Ag^+} - \Phi_{Ag_xMCh_2}\} + \{\Phi_{Ag_xMCh_2} - \Phi'_{Cu}\} \qquad (7.6) $$

where Φ'_{Cu} refers to the copper lead attached to the MCh_2 electrode. Therefore in an isothermal environment

$$E = \Phi_{Cu} - \Phi'_{Cu} = \Delta\Phi(Ag/Ag^+) + \Delta\Phi(Ag^+/Ag_xMCh_2) \qquad (7.7)$$

and each half-cell E.M.F., $\Delta\Phi$, contributes to the net cell E.M.F. but can never be measured individually. Therefore, to simplify comparisons between cells, the hydrogen half-cell

$$H_2 \leftrightharpoons 2H^+ + 2e^- \qquad (7.8)$$

is arbitrarily defined as having an E.M.F. of zero volts at all temperatures, and all other half-cells have an E.M.F. expressed relative to this hydrogen half-cell.

7.2 Experimental Arrangements, Procedure and Electrode Preparation

It turns out that the H_2/H^+ half-cell is not a very useful reference potential and a much better choice is the calomel electrode which has a potential of 0.245V with respect to H_2/H^+. Therefore the calomel electrode was used as a reference electrode, and silver as the working electrode when determining the E.M.F. of reaction 2.3 as a function of the intercalated mole fraction (x) of silver (Fig. 7.2). Of

Fig. 7.2

Experimental arrangement for measuring the open circuit voltage of the intercalated crystals using a calomel electrode for a reference voltage. The salt bridge is required to prevent AgCl precipitate, which will form from a reaction between KCl in the calomel electrode and the $AgNO_3$ in the electrolyte, from clogging the sintered glass opening in the calomel electrode.

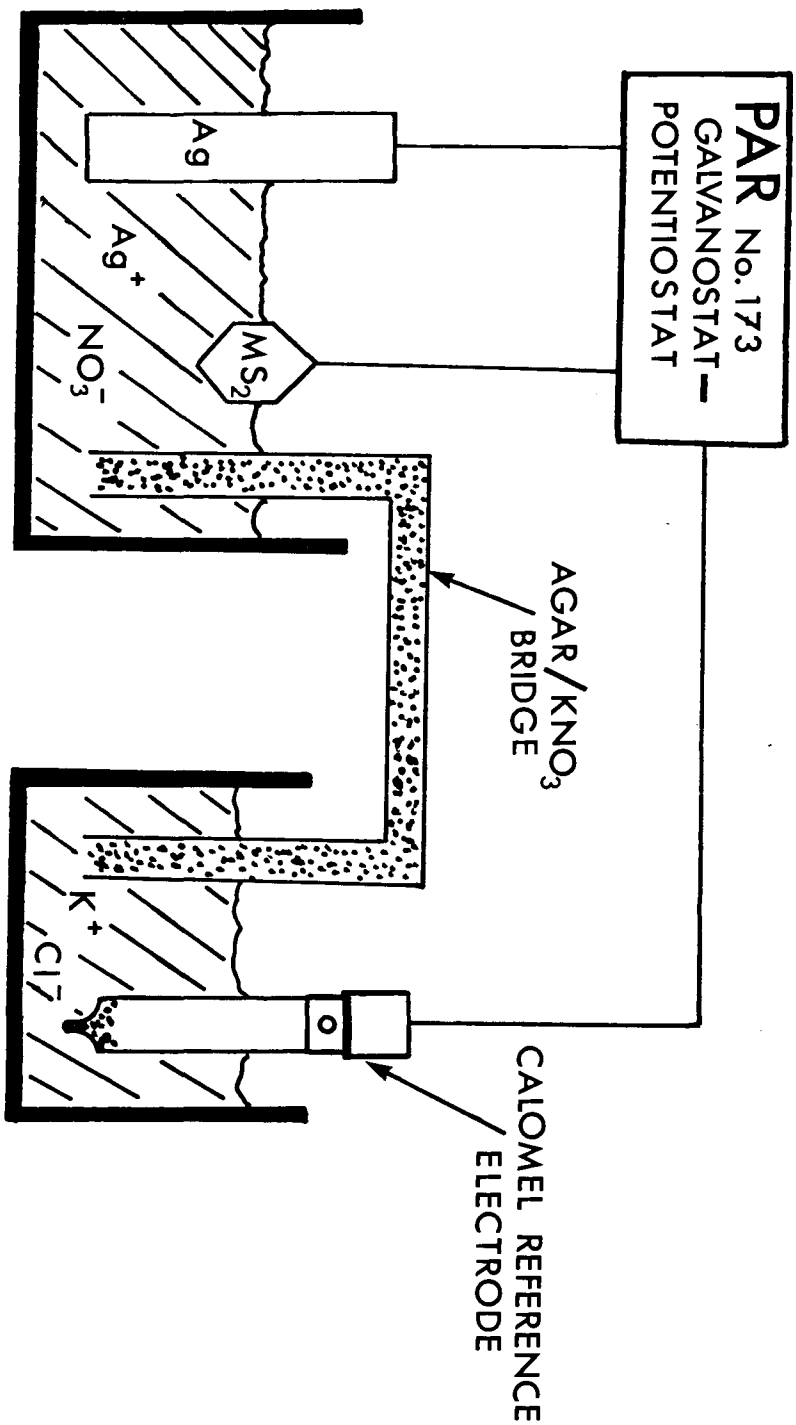
PAR No. 173
GALVANOSTAT—
POTENTIOSTAT
Ag
Ag+
NO3−
MS2
AGAR/KNO3
BRIDGE
K+
Cl−
CALOMEL REFERENCE
ELECTRODE

course, glycerol was used as the solvent for $AgNO_3$ to avoid the parasitic reactions with water. To further minimize the parasitic side reaction problem and for reasons of convenience and standardization an electrolyte concentration of 0.1N was consistently used for all E.M.F. measurements.

The E.M.F. of Ag_xTaS_2 samples was determined by using thermally prepared powder samples of known composition and by intercalating 2H-TaS_2 crystals electrochemically. Both methods have drawbacks, but do tend to be somewhat complementary. The Ag_xTiS_2 samples were only electrochemically prepared since the chemical side reactions (Eq. 2.4 and 2.5) are not of any significance.

The problem with the thermally prepared Ag_xTaS_2 or Ag_xTiS_2 samples is that the surfaces of the crystallites are usually "dirty" with iodine, sulphur, etc. Therefore, under the zero net current condition at which E.M.F.'s are measured, various other equilibrium reactions can exist and will contribute to the measured net E.M.F. The degree to which the E.M.F.'s of the other equilibrium reactions are important is determined by the magnitude of their respective exchange currents, compared to the exchange current for the equilibrium intercalation reaction. For thermally prepared Ag_xTaS_2 samples with $x < 1/3$, it is found from experience that the exchange currents of competing equilibrium reactions are usually not very significant. However, for samples with $x > 1/3$ it was sometimes, not always, found that not all the

Fig. 7.3

Electrode construction for measuring the open circuit potential of thermally prepared Ag_xTaS_2 and Ag_xTiS_2 crystallites.

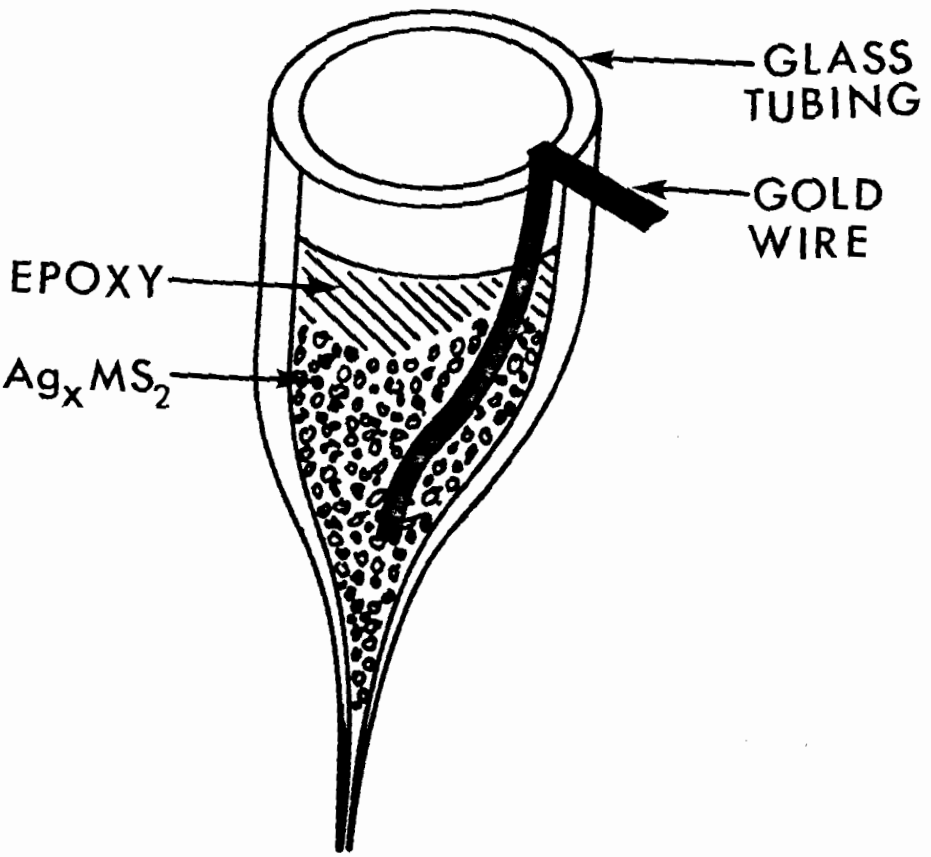
GLASS
TUBING
GOLD
WIRE
EPOXY
Ag_xMS_2

silver had intercalated and that traces of silver could be found on the crystal surfaces. The exchange current of the resulting Ag/Ag^+ equilibrium reactions turned out to be significant because spuriously low E.M.F.'s, close to the Ag/Ag^+ potential, were measured for these samples. Therefore, the most reliable E.M.F.'s for thermally prepared Ag_xTaS_2 samples were those intercalated with small mole fractions of silver.

The detailed electrode construction for thermally prepared powder samples is shown in Fig. 7.3. Quartz tubing was drawn until it had a very fine capillary at one end. Intercalated dichalcogenide powder, along with a gold wire, was then inserted, tapped tight until good electrical contact was obtained, and the whole assembly epoxied at the top for mechanical rigidity.

Electrochemically intercalated samples, for E.M.F. measurements, were prepared in two ways. Either the 2H-TaS_2 or 1T-TiS_2 crystals were soaked in aqueous $AgNO_3$ electrolytes of different concentrations thus achieving different degrees of intercalation which were then determined by weighing, or a 0.1N $AgNO_3$/glycerol electrolyte was used and the dichalcogenide electrode intercalated in-situ with the degree of intercalation determined via coulometry. As already mentioned, the problem with both of these methods is that there is usually more intercalate at the crystal edges, to which the E.M.F. is sensitive, than in the bulk of the

Fig. 7.4

Crystal mounting for intercalating 2H-TaS_2 or 1T-TiS_2 electrochemically.

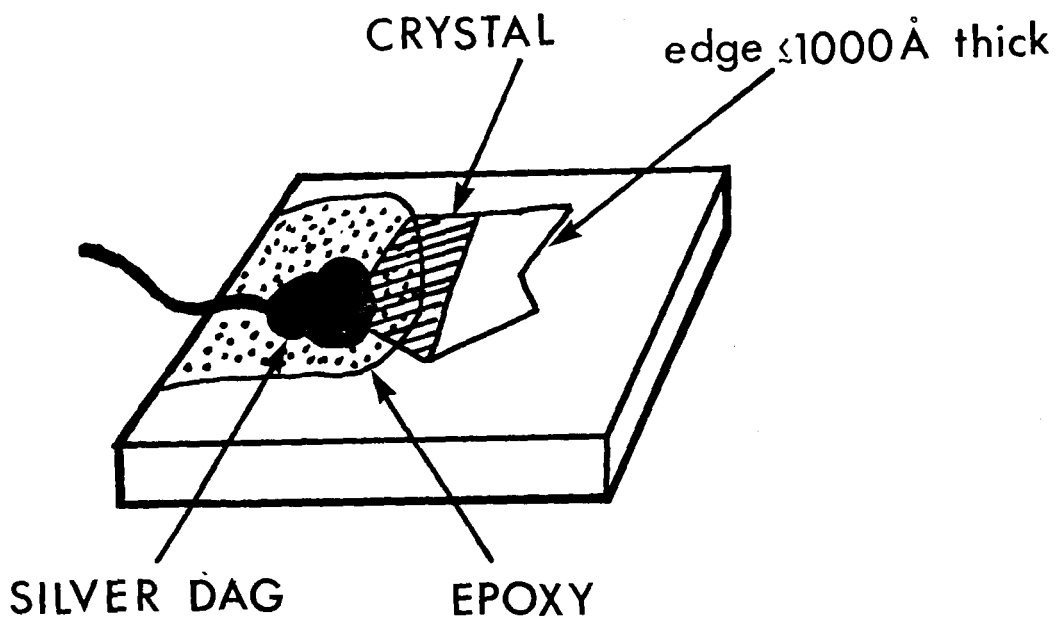
CRYSTAL
edge ≤1000 Å thick
SILVER DAG
EPOXY

sample. This means that the correlation established between the total mole fractions of silver intercalated (x) and the E.M.F. measured can easily be misleading. This problem can be considerably minimized by using dichlcogenide crystals which are as thin as possible (also see results in Chapter 9). Extremely thin crystals were used as electrodes when intercalating in-situ because, since the electrodes need not be handled, they could be made of thicknesses which were less than about 1000Å (Fig. 7.4). For such electrodes the equilibriation time, at room temperature, following some degree of fractional intercalation, was reduced from days or even months to a few hours. The fractionally intercalated samples were judged to be essentially in equilibrium if the drift in the cell open circuit voltage was less than about 1mV/hr.

7.3 Results of the E.M.F. Measurements for Ag_xTaS_2 and Ag_xTiS_2

(A) Ag_xTaS_2 E.M.F. Dependence

The experimental result for the open circuit voltage or free energy dependence of the Ag_xTaS_2/0.1N $AgNO_3$,glycerol/Ag cell as a function of the degree of intercalation is given in Fig. 7.5. Each data point corresponds to a sample prepared with a specific mole fraction

Fig. 7.5

The measured open circuit potential of a Ag_xTaS_2/0.1N$AgNO_3$, glycerol/Ag electrochemical cell, plotted against x. Also indicated above the curve are the stages as determined by X-ray diffraction studies. The indicated error bars are typical of all data points. Specifically these error bars are drawn on all thermally intercalated samples.

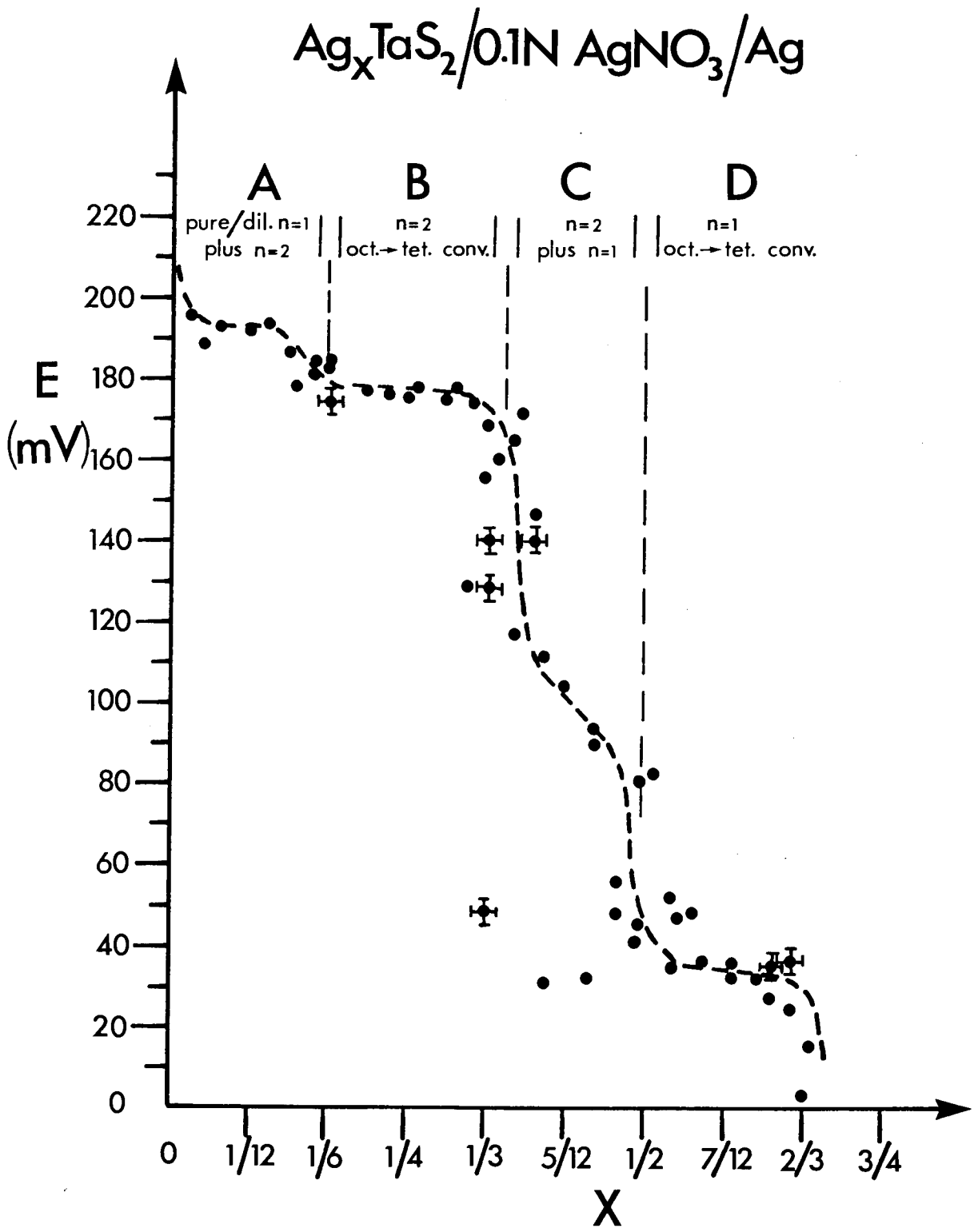
Ag_xTaS_2/0.1N $AgNO_3$/Ag
A
pure/dil. n=1
plus n=2
B
n=2
oct.→tet. conv.
C
n=2
plus n=1
D
n=1
oct.→tet. conv.
E
(mV)
220
200
180
160
140
120
100
80
60
40
20
0
0
1/12
1/6
1/4
1/3
5/12
1/2
7/12
2/3
3/4
X

of silver. Even though there is some scatter in the data points, the line indicating the functional dependence of the free energy is probably fairly realistic. When some of the samples, having apparently radically different voltages, were checked for uniformity of intercalation (e.g using X-ray diffraction and X-ray fluorescence), they inevitably proved to be of a poor quality. This was particularly the case in region C ($1/3 \lesssim x \lesssim 1/2$) and therefore a series of five samples were extremely carefully prepared within this concentration range and their open circuit potentials monitored over a period of about one year. The open circuit potentials were all initially near+40mV, but then gradually rose to those indicated (i.e. from about +80mV to +120mV) and are thought to be good values.

To determine the reversibility of the electrochemical cell, a single crystal less than 1000Å thick was used as an electrode. The open circuit voltage was measured after resting the cell after each fractional intercalation or deintercalation step and it became quickly apparent that the cell can be reversibly used galvanically or electrolytically.

(B) Ag_xTiS_2 E.M.F. Dependence

In Fig. 7.6 the open circuit voltage or free energy dependence of the Ag_xTiS_2/0.1N$AgNO_3$,glycerol/Ag electrochemical cell is shown as a function of x, the degree

Fig. 7.6

The open circuit potential of an $Ag_xTiS_2/0.1NAgNO_3$, glycerol/Ag electrochemical cell, plotted against x. Also indicated above the curve are the stages as determined from X-ray diffraction studies.

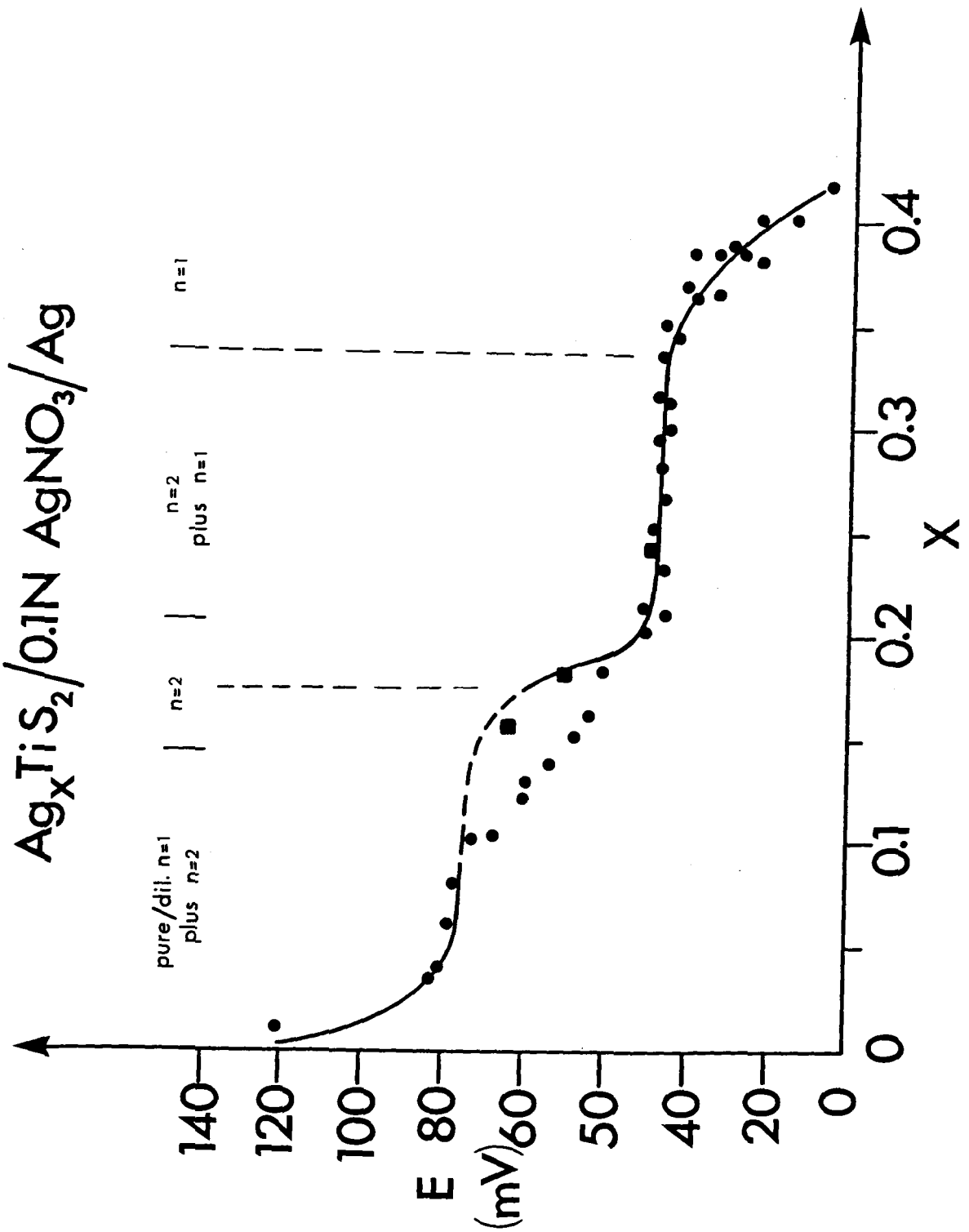
Ag_xTiS_2/0.1N $AgNO_3$/Ag
pure/dil. n=1
plus n=2
n=2
n=2
plus n=1
n=1
E (mV)
140
120
100
80
60
50
40
20
0
0
0.1
0.2
0.3
0.4
X

of intercalation. The data points were obtained using in-situ intercalation of 1T-TiS_2 anodes which were typically about 500Å thick. There is very little random scatter in the data points compared to the results for Ag_xTaS_2 and this is undoubtedly a consequence of the greatly decreased rate at which the parasitic side reactions (Eqs.2.4 and 2.5) occur. For $0.08 \lesssim x \lesssim 0.18$ mole fractions of silver the functional dependence of the free energy is indicated with a dashed line because, even though it does not follow the data points, it is thought to be closer to the correct dependence. The reason for this belief is that the data points drawn as squares were taken after waiting in excess of 8 hours for the cell to come to equilibrium and thus correspond to the best open circuit voltages. The reason for this exceptionally slow approach to an equilibrium potential will become clear below.

When it was attempted to cycle the Ag_xTiS_2 electrochemical cells it became immediately apparent that they were partially irreversible at room temperature because it was impossible to regain an open circuit voltage above about +50mV. Therefore, in contrast to the Ag_xTaS_2 cells, the Ag_xTiS_2 cells will only cycle reversibly for mole fractions above about $x = 0.20$, that is, for stage 1. However, when the electrochemical cell was heated to above about 150C, the Ag_xTiS_2 anode was found to be more reversible and it was possible to obtain an open circuit voltage above about 70mV, which corresponds to deintercalating the Ag_xTiS_2 cathode to mole fractions below $x \sim 1/5$. However, this heating caused

the electrolyte to decompose and in particular, silver precipitated thus causing a short-circuit reaction. The cell reaction at elevated temperatures was therefore not pursued in any greater detail, except in noting that deintercalation to lower mole fractions was possible.

7.4 Discussion of the E.M.F. Measurements for Ag_xTaS_2 and Ag_xTiS_2

The presence of plateaus and relatively sharp decreases to the open circuit voltage for both the Ag_xTaS_2 and Ag_xTiS_2 was to be expected, on the basis of the structural variations as discussed in the previous chapters, and their observation was gratifying. The occurence of the drops in the potentials can be understood if one considers that whenever a stable phase has formed, for a certain intercalate concentration, the free energy of that phase will then necessarily be at a minimum. Further intercalation of the host crystal will initially cause the additional silver ions to occupy energetically unfavourable sites, requiring larger energies per intercalated anion, and eventually cause the growth of an entirely new phase having a comparatively smaller free energy. Therefore, an activation energy can be expected with an associated drop in the open circuit potential, indicating that a stable phase has been completed. Once a new phase has

formed and begins to coexist with the previous phase, the open circuit voltage, although expected to decrease still further, should do so comparatively slowly. If a crystal is intercalated at a constant current and the voltage monitored, the features in the open circuit voltage will become much more pronounced because the intercalate right at the edges, which determines the voltage, has a well-defined, although non-equilibrium distribution.

The various phases of an intercalated dichalcogenide can come about for various reasons. For instance, a stable phase may result for a particular degree of intercalation so that the intercalate can order on a superlattice which will minimize Coulomb interactions [37]. Another way of producing a different phase is if the host structure changes in some way such as by staging or just shifting, because of the intercalate, as is found for Ag_xTaS_2 and Ag_xTiS_2 (Chapters 3, 5 and 6). Of these three examples of possible phase changes, a structural change in the host lattice will undoubtedly have a much larger effect on the open circuit potential than that produced by a order-disorder transition of the intercalate, simply because in the former case the Brillouin zone and consequently the Fermi level may change. However, order-disorder transitions have been associated with variations in the open circuit voltage of Li_xTiS_2 [37,38]. It will not be clear whether this interpretation is correct until a careful measurement of the lattice parameters,

as a function of x, has been carried out as assurance that the fairly subtle changes in the open circuit potential are not caused by changes in the lattice parameters. Small changes in the c_o lattice parameters, for example, may well occur because of changing Coulomb and exchange interactions between the "d_{z^2} orbitals" (see Chapter 10).

(A) Ag_xTaS_2 E.M.F.

Inspection of the open circuit potential variations for Ag_xTaS_2 in Fig. 7.5, reveals four pronounced drops preceding each of the mole fraction intervals A through D. These drops in the open circuit potential should therefore indicate the beginning of a new phase in each case, or four distinct phases in all. Using the information provided by the X-ray powder patterns in Chapter 3 and the electron diffraction patterns of Chapters 4 and 5, it becomes relatively straightforward to identify these four phases.

Region A (Fig. 7.5): The initial drop in the voltage corresponds to the formation of the stage 2 structure illustrated in Fig. 5.10a, where the silver ions are occupying octahedral sites. Stage 2 then grows at the expense of pure 2H-TaS_2 as x is increased and this transformation ideally comes to completion for x = 1/6 mole fraction. As already pointed out in Chapter 5, the dilute stage 1 phase which

exists for thermally intercalated samples only exists to very small concentrations for those prepared electrolytically, if at all.

Region B (Fig. 7.5): Here the initial drop in the voltage indicates that some of the host layers are beginning to shift with respect to one another, as described in Chapter 5, placing the silver ions into tetrahedral sites and eventually producing the $Ag_{1/3}TaS_2$ stage 2 structure shown in Fig. 5.10b. This stacking rearrangement, which allows a larger local silver ion concentration (x'), will finally come to completion near x = 1/3. In this concentration region a change in the silver superlattice also occurs from $\sqrt{3}a_o$ to $2a_o$ plus random sites, and may or may not contribute to the exceptionally level voltage plateau observed.

Region C (Fig. 7.5): Just above x = 1/3 mole fractions the voltage decreases rapidly because of the activation energy involved in the formation of stage 1. However, as was the case for stage 2, the first silver ions causing stage 1 to form will again likely reside in octahedral sites initially and thus for x = 1/2 mole fraction the idealized stage 1 structure shown in Fig. 7.7 should exist. The electron diffraction pictures in this concentration range do show some $\sqrt{3}a_o$ superlattice satellites (characteristic of octahedral site occupation in stage 2) but they are very weak. As can be

Fig. 7.7

Anticipated structure for $Ag_{1/2}TaS_2$, with x = 1/3 of the silver ions in tetrahedral sites and x = 1/6 of the silver ions in octahedral sites.

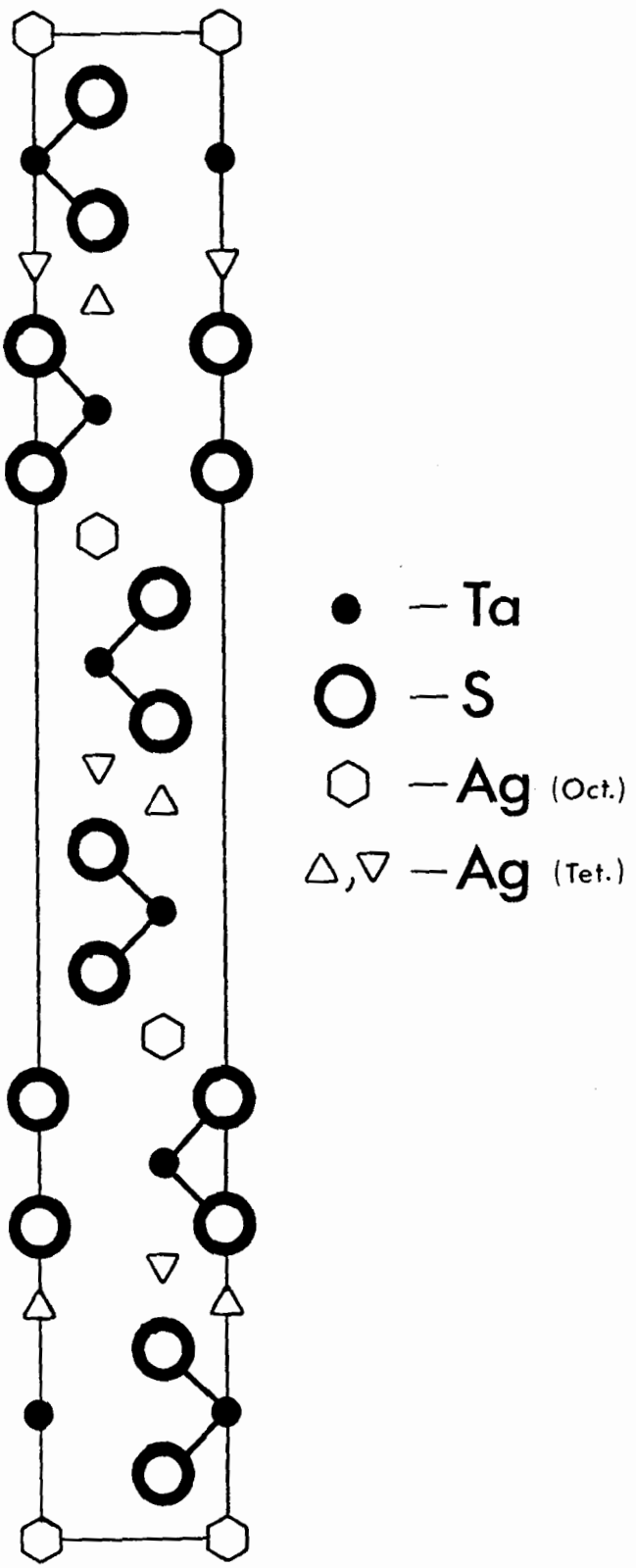
● — Ta
○ — S
⬡ — Ag (Oct.)
△,▽ — Ag (Tet.)

seen from the E.M.F. measurements, within this intercalate concentration range a great amount of scatter exists in the observed open circuit potentials with maximum variations from about +170mV (the previous plateau) to about +35mV (the next plateau). Furthermore, in Chapter 3 it was found that $Ag_{5/12}TaS_2$ could be thermally prepared either as pure stage 2 or as a mix of stage 2 and 1, depending on the rate of cooling. Therefore, it would appear that the cause of the large variations in the observed voltages is the variety of phases that are especially easy to create within this concentration range, their structure depending on the methods and conditions of sample preparation.

Region D (Fig. 7.5): The 2H-TaS_2 host is now completely stage 1 and the initial drop in the open circuit voltage, as in region B for stage 2, marks the shifting of those parts of the host layers still containing silver ions in octahedral sites. When this rearrangement is finally complete, near $x = 2/3$, the host crystal structure is that of MoS_2 (Fig. 3.3). Finally, if x begins to exceed about 2/3 mole fraction the voltage will rapidly drop to zero volts because of the energetically unfavourable sites that the additional silver ions have to occupy.

Considering all the structural changes involved during the discharge of a Ag_xTaS_2/Ag galvanic cell it was very surprising to discover that the intercalation reaction is

apparently reversible, that is, the cell can be recharged to about 200mV. To verify the structural reversibility of these cells more completely, X-ray powder patterns were taken of parts of the Ag_xTaS_2 electrode after it was recharged to about x = 1/3, 1/6 and zero mole fractions following complete intercalation to x = 2/3. The powder patterns confirmed that the structural changes are indeed reversible.

Interestingly enough, even though the occupation of octahedral and tetrahedral sites by the silver ions results in distinctly different phases as judged by the open circuit voltage variations. This is not apparent in the variation of the lattice parameters (Fig. 3.5). For instance, c_o only changes marginally near x = 1/2 and there certainly is no suggestion that a phase change is occuring. However, there is good agreement for the onset of the stage 2 to stage 1 transitions as indicated by the variations in the lattice parameters (Fig. 3.5) and the changes in the open circuit voltage.

(B) Ag_xTiS_2 E.M.F.

As can be seen in Fig. 7.6, for the Ag_xTiS_2 electrochemical cell, the variations in the open circuit potential with x are much simpler than those of the Ag_xTaS_2 cell. This is in agreement with the simpler structural changes that occur for Ag_xTiS_2 on intercalation, as discussed in Chapter

3. There are two drops in the open circuit voltage which signals the formation of a new phase in each case, and therefore agrees with the X-ray results (Chapter 3) where two phases (stage n = 2 and n = 1) were discovered (the stacking rearrangements doubled the number of phases for Ag_xTaS_2).

Region A (Fig. 7.6): As for Ag_xTaS_2, the dilute stage 1 phase, found when the Ag_xTiS_2 samples are thermally prepared, must only occur for very small x since it is not observed if the samples are electrochemically prepared. Instead, as found with electron diffraction of electrochemically prepared Ag_xTaS samples (Chapter 5), stage 2 (Fig. 3.9) forms immediately and coexists with pure 1T-TiS_2. Then, as x is further increased, the relative amount of stage 2 increases until, judging from Fig. 7.6, near x = 0.18 the sample appears to be completely stage 2. This limit of $x \simeq 0.18$, for the intercalated mole fractions, also agrees with the electron diffraction results because the $\sqrt{3}a_o$ superlattice observed suggests that x = 1/6 for the ideal stage 2 structure.

Region B (Fig. 7.6): The drop in the open circuit potential near x = 0.18 in signals the appearance of stage 1 (Fig. 3.7), even though the a_o and c_o lattice parameters (Fig. 3.10) indicate that stage 1 is not present at or near x = 0.20 for the thermally prepared samples. The explanation for this

contradiction may be linked to the difference in sample preparation or, more likely, to the irreversible stage 2 formation as discussed below.

The irreversible intercalation of silver into the Ag_xTiS_2 electrode above about +50 mV was surprising because no structural changes, except for an expansion of the van der Waals gap in the intercalated regions, occur on intercalation. Structural changes could inhibit the reversibility of the intercalation reaction because the large activation energies which may be associated with them will reduce the reaction rate to such a degree that the system will appear irreversible. However, structural changes do not prevent the Ag_xTaS_2 system from being reversible and are obviously not the cause in the Ag_xTiS_2 system. Thus it would appear that the cause for the irreversibility is likely electronic in nature and that the electron density donated into the titanium t_{2g} orbitals, by the intercalate, somehow makes stage 2 Ag_xTiS_2 a particularly stable compound. Indeed, one would expect an enhanced exhange interaction, which lowers the free energy of Ag_xTiS_2 for small x. It is this irreversible behaviour which will also explain why it is difficult to achieve an equilibrium open circuit potential for intercalate concentrations of $0.08 \lesssim x \lesssim 0.18$ mole fractions (Fig. 7.6). The reason is that once the silver ions enter a crystal edge, thereby forming stage 2 regions, which correspond to a very stable phase, any further diffusion into the unintercalated

regions becomes severely inhibited. Meanwhile, however, intercalation at the edges will proceed to stage 1 with the corresponding drop in the open circuit potential. Therefore, the extremely slow recovery rate of the open circuit potentials for $0.08 \lesssim x \lesssim 0.18$ is controlled by the rate at which the stage 2 regions diffuse into the bulk of the crystal and, in fact, there is actually no guarantee that the apparent onset of stage 1 regions near $x = 0.20$ might be spuriously low because of incomplete intercalation of the interior crystal regions. However, as previously noted, there is an alternative explanation for the inconsistency between changes in voltage and structure which is due to sample preparation. As in Chapter 3, by referring to Safran's staging phase diagram [23] one can see that if T/U_o is increased, the appearance of the stage 1 phase should be delayed to higher x values. Therefore, for the thermally prepared samples, the delayed onset of stage 1 until large mole fractions of silver are intercalated (Fig. 3.10) could actually be expected, and taken as further support of Safran's staging phase diagram.

Above about 0.34 mole fraction in Fig. 7.6, the open circuit voltage begins to drop toward zero, which corresponds to the $\sqrt{3}a_o$ superlattice formation that is observed for stage 1 (Chapter 6). Stage 1, because of the $\sqrt{3}a_o$ superlattice, should ideally be complete for $x = 1/3$ and, consequently, intercalating above 1/3 mole fraction should require the occupation of energetically less favourable sites

so that a corresponding decrease in the open circuit voltage should occur, because of the "overfilling", in agreement with observation.

7.5 Conclusions Regarding the E.M.F. Measurements for Ag_xTaS_2 and Ag_xTiS_2

There is good agreement in the Ag_xTaS_2 and Ag_xTiS_2 systems between their stage number, and the drops in their open circuit potentials. In the Ag_xTaS_2 system further phase changes occur, in addition to the changes in the stage number, because of the stacking rearrangements. Although these stacking rearrangements do not have a pronounced effect on the lattice parameters, they nevertheless cause drops inthe open circuit potential. Therefore, it is clear that the equilibrium open circuit potential of an intercalation system is a good parameter with which to monitor phase changes.

It is not clear why in Ag_xTiS_2 the silver ions will not reversibly deintercalate completely at room temperature, especially considering that the silver ions do deintercalate reversibly at room temperature in Ag_xTaS_2 where structural changes do occur. One might argue that the structural damage which undoubtedly occurs to a greater extent in Ag_xTaS_2 because of the structural changes it experiences, will enhance the ability of the silver ions to deintercalate to a greater extent. However, as will be shown in Chapter 9, the optical

transmission characteristics of thin ($\lesssim$1000Å) single crystals of Ag_xTaS_2 and Ag_xTiS_2, which do not suffer structural damage on intercalation, also indicate that whereas the former is reversible the latter again is not.

It was noted that by heating the Ag_xTiS_2/Ag cell to above about 150C, the reversibility of the Ag_xTiS_2 electrode could be enhanced, in agreement with the optical results of Chapter 9. This irreversibility at low x values of silver is not understood, but as further discussed in Chapter 10, may well be due to the enhanced metallic bonding experienced by the TiS_2 layers.

CHAPTER 8

OPTICAL TRANSMISSION

8.1 Introduction to the Transmission Characteristics of Layer Compounds

The optical transmission characteristics of thin films of the dichalcogenides before and after intercalation can give useful information about changes in the Fermi surface or even the band structure itself. Band structure calculations by Matheiss [39] have shown that the orientation of the bands in k-space is well established by a single transition metal dichalcogenide sandwich and that the introduction of interlayer coupling has no significant effect on the shape or position of the bands. Of course, this is not completely unexpected because of the pseudo two-dimensional character which these dichalcogenides exhibit. The band structure of 2H-TaS_2 and 2H-MoS_2 for example is very similar and the differences in their optical transmission spectra can be primarily ascribed to the difference in the degree of filling of their non-bonding conduction band as illustrated in Fig. 1.4. Therefore, to a first order approximation, a rigid band structure model will be assumed and consequently during intercalation the only effect of the charge tranfer, from intercalate to host, is that the Fermi level in the non-bonding conduction band increases.

Fig. 8.1

Density of states schematic proposed by Wilson and Yoffe from valence bond arguments (Fig. 1.4). Between the bonding (σ) and antibonding (σ^*) levels are the t_{2g} non-bonding orbitals which form a conduction band. Schematic shown in (a) is proposed for 2H-TaS_2 and that in (b) is proposed for 1T-TiS_2.

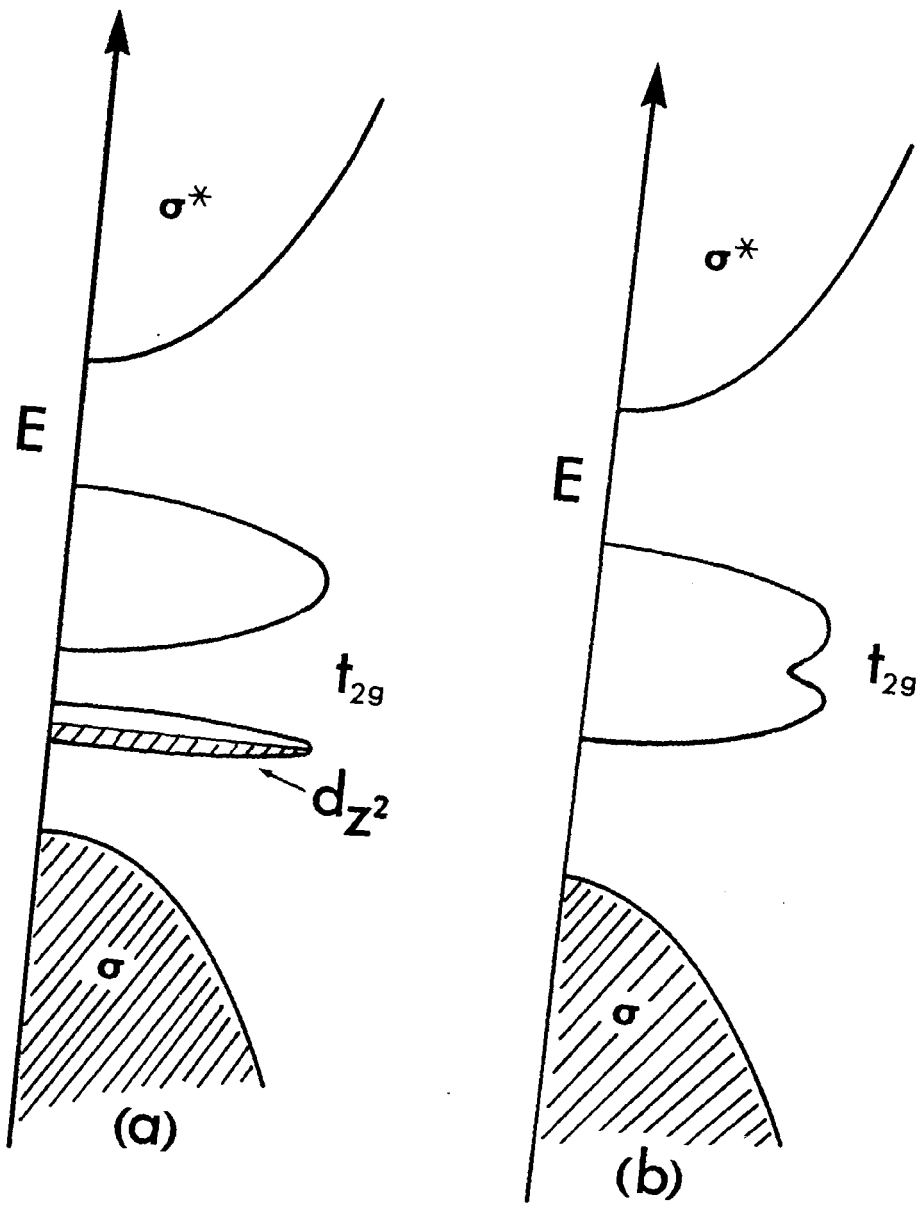
σ*
E
t2g
dz²
σ
(a)
σ*
E
t2g
σ
(b)

The gradual filling of the conduction band, because of intercalation, should therefore affect the degree of free carrier absorption in addition to the inter-band transitions. Consequently, the optical transmission results are usually evaluated with the above two effects in mind, by using the schematic density-of-states for 2H-TaS_2 and 1T-TiS_2 (Fig. 8.1) as determined by Wilson and Yoffe [7] via valence bond and ligand field arguments.

8.2 Apparatus and Experimental Arrangement for Measuring the Transmission Spectrum

Obtaining a transmission spectra of intercalated and unintercalated dichalcogenide crystals has one major difficulty, the extremely small size of the sample area that can transmit light. Films must be at least less than about 2000Å thick if they are to pass a significant amount of light and typical sample areas that can be prepared and which will meet this requirement are in the order of 10^{-1}mm across. Typical commercial apparatus, like the Carey 14 for instance, is clearly unsuitable and in order to deal with the extremely small effective sample area, an experimental arrangement as depicted in Fig. 8.2 was assembled. The basic distinguishing features of this assembly, compared to standard arrangements, are the inclusion of a microscope objective and screen. The screen has two apertures, one of which is used to select

Fig. 8.2

Apparatus and experimental arrangement for measuring the transmission spectra of small ($\lesssim$ 1mm diameter) crystals which can be intercalated *in situ*.

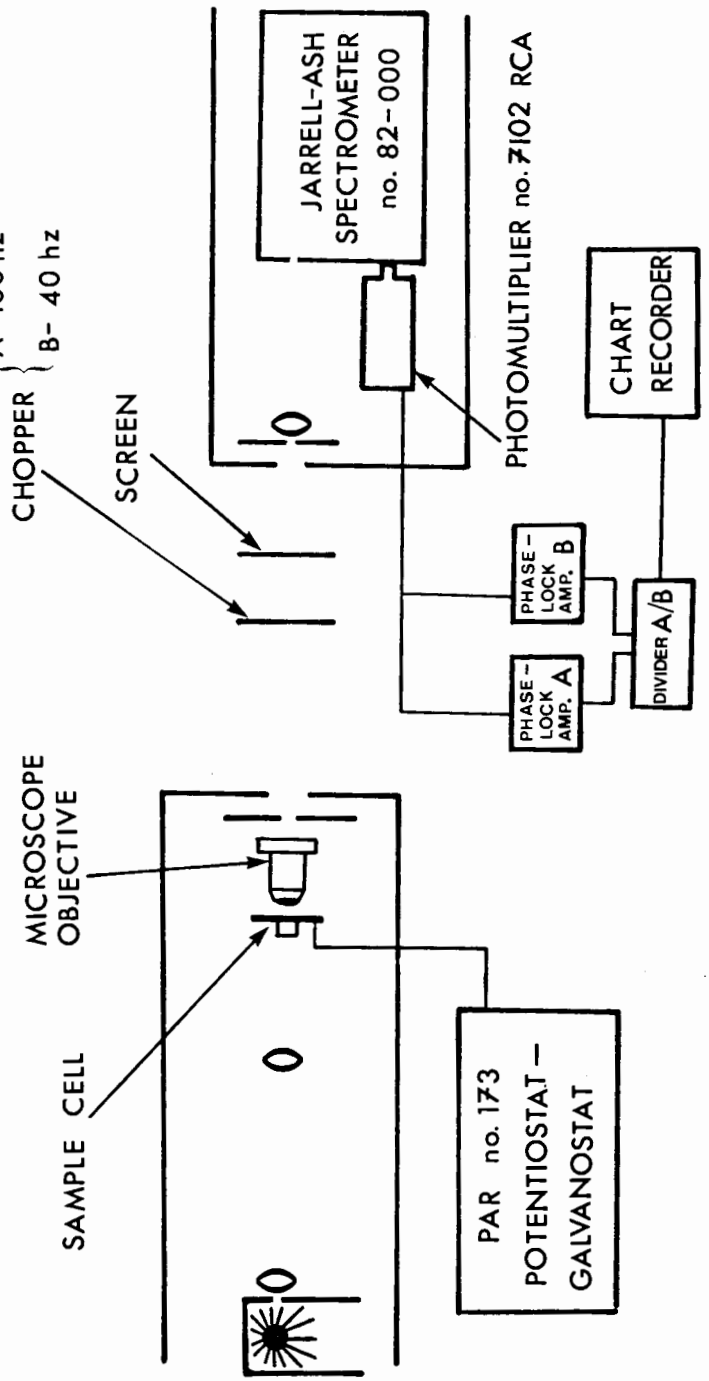
A- 100 hz
B- 40 hz
CHOPPER
SCREEN
JARRELL-ASH SPECTROMETER no. 82-000
PHOTOMULTIPLIER no. 7102 RCA
CHART RECORDER
PHASE-LOCK AMP. B
PHASE-LOCK AMP. A
DIVIDER A/B
MICROSCOPE OBJECTIVE
SAMPLE CELL
PAR no. 173 POTENTIOSTAT-GALVANOSTAT

the part of the sample image of interest and the other provides for a reference beam which parallels the optical path of the sample beam, except that it does not pass through the sample itself. Needless to say, the screen has to be custom-made for the particular sample under study. The sample and reference beam are then chopped at different frequencies and focussed onto the entrance slit of the Jarrell-Ash No. 82-000 spectrometer. The photon energy range which could be investigated with this apparatus ranged from about 1.2 eV to 2.8 eV using a photomultiplier tube with a S1 response. Some care was taken in the choice of lenses to prevent the two beams from being overly divergent, since otherwise the data quality was found to suffer. The reasons for this are varied and include, among other factors, the incomplete coverage of the spectrometer grating and a varying sensitivity across the electrode area of the photomultiplier tube.

The sample holder is actually an electrochemical cell which allows the 2H-TaS_2 or 1T-TiS_2 electrodes to be intercalated or de-intercalated in situ (Fig. 8.3). Contact to the dichalcogen crystal is made with silver dag which, to prevent a short circuit reaction (Eq. 2.3), is in turn covered with R.T.V. (room temperature vulcanizing) silicon rubber. The electrolyte, as usual, is a 0.1N $AgNO_3$ glycerol solution which is kept water free by completely sealing the electrochemical cell. Finally, intercalation and de-intercalation is controlled via a P.A.R. model 173 Potentiostat/Galvanostat.

Fig. 8.3

Top view of sample cell (Fig. 8.2). The electrolyte is 0.1N $AgNO_3$ in glycerol. The various glass pieces are attached to each other with silicon RTV. Silicon RTV is also used to isolate the Ag dag, making electrical contact to the sample, from the electrolyte in order to prevent a short circuit.

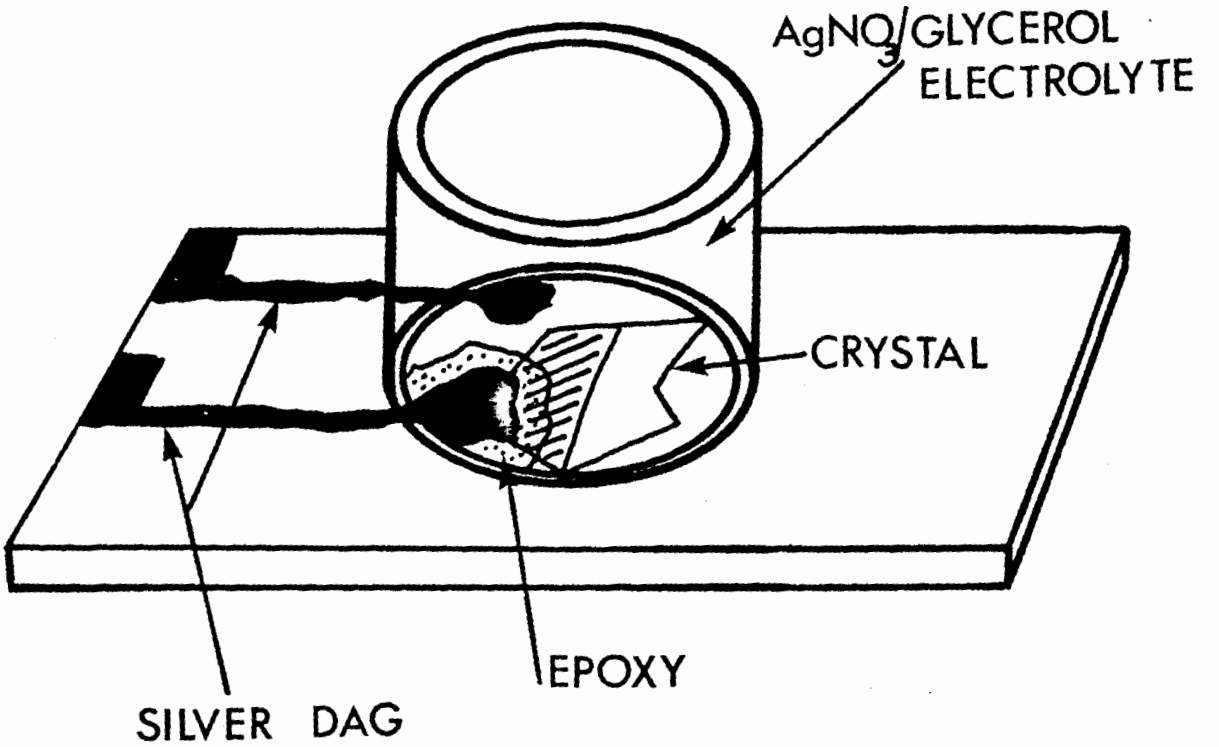
AgNO3/GLYCEROL
ELECTROLYTE
CRYSTAL
EPOXY
SILVER DAG

8.3 Procedure Used for Measuring the Transmission Spectrum of Ag_xTaS_2 and Ag_xTiS_2

Typical sample thicknesses used for the transmission experiments were from about 500Å to 1000Å. Care was exercised that the sample area under analysis was of a uniform colour, that is thickness, so that unnecessary complications, such as interference effects, are minimized. These very thin films also have the decidedly positive characteristic of allowing the intercalate to come to equilibrium relatively quickly after some intercalation or de-intercalation has been allowed. The degree of intercalation was determined somewhat indirectly, but all the same it is still thought to be quite accurate. The procedure was to use a coulometer, incorporated into the P.A.R. Potentiostat/Galvanostat, to keep track of the net coulombs passed, which could later be calibrated into mole fractions of silver, after the maximum possible number of coulombs that can be passed is established. It was assumed that this maximum number of coulombs will correspond to x = 2/3 and 0.42 mole fractions of silver for 2H-TaS_2 and 1T-TiS_2 respectively, as has already been repeatedly determined, during sample preparation in the previous chapters. The second easy way of determining the mole fraction intercalated is via the open circuit potential, which can be compared to the open circuit potentials (Fig. 7.5 and 7.6) established in Chapter 7. Good agreement was usually found

between these two methods of determining x, however, if some doubt did exist, the latter method was preferred in determining the intercalated mole fractions.

Intercalation was carried out by decreasing the voltage below the equilibrium value for a short time and then returning the intercalation cell to an open circuit condition. Equilibrium was assumed to be achieved when the open circuit voltage varied less than about 1mV/hr. During de-intercalation the voltage of the dichalcogenide electrode was kept below 1.10V with repsect to H_2/H^+ since this voltage should be sufficient to completely deintercalate the dichalcogen electrodes and should also avoid possible oxidation problems which are encountered if significantly larger voltages are used.

8.4 Results and Discussion of the Optical Transmission Measurements of Ag_xTaS_2 and Ag_xTiS_2

(A) Ag_xTaS_2 Transmission

Depending on the sample thickness, 2H-TaS_2 will appear anywhere from a beige-yellow to orange-brown or a dark brown in colour, and this corresponds to sample thicknesses from less than 500Å to about 2000Å. When the samples are intercalated by completing the external circuit it is possible to see a dark front advance into the interior of the crystal

and samples which are greater than about 800Å in thickness will appear to become opaque after intercalation. The rate and other details of this dark optical front, caused by the intercalating silver ions, will be further discussed in Chapter 9.

The essentially reversible room temperature transmission spectra for selected Ag_xTaS_2 mole fractions, so chosen to effectively illustrate the effects of intercalation on the transmission spectrum, are shown in Fig. 8.4. The particular sample, whose unintercalated and intercalated spectra is given in Fig. 8.4, is about 1500Å thick as determined via the Nomarski technique. Its spectrum, with one exception, was very representative of the ten or so other samples investigated. The one exception concerns a shoulder which is often observed between about 1.7 eV and 2.4 eV where the absorption is still quite low. It was found that the exact position and magnitude of this shoulder is thickness dependent so it appears that it is most likely due to an interference effect between the parallel-sided samples. Recent work by Beal et al. agrees with this interpretation, however, Wilson and Yoffe [7] interpret this shoulder as a screened exciton . For the thicker samples this shoulder is not very noticeable and that is why the relatively thick (~1500Å) sample was chosen for Fig. 8.4. To keep with usual

Fig. 8.4

The reversible room temperature absorption spectrum (A = 1-T) for a Ag_xTaS_2 about 1500Å thick, which is electrochemically intercalated in situ.

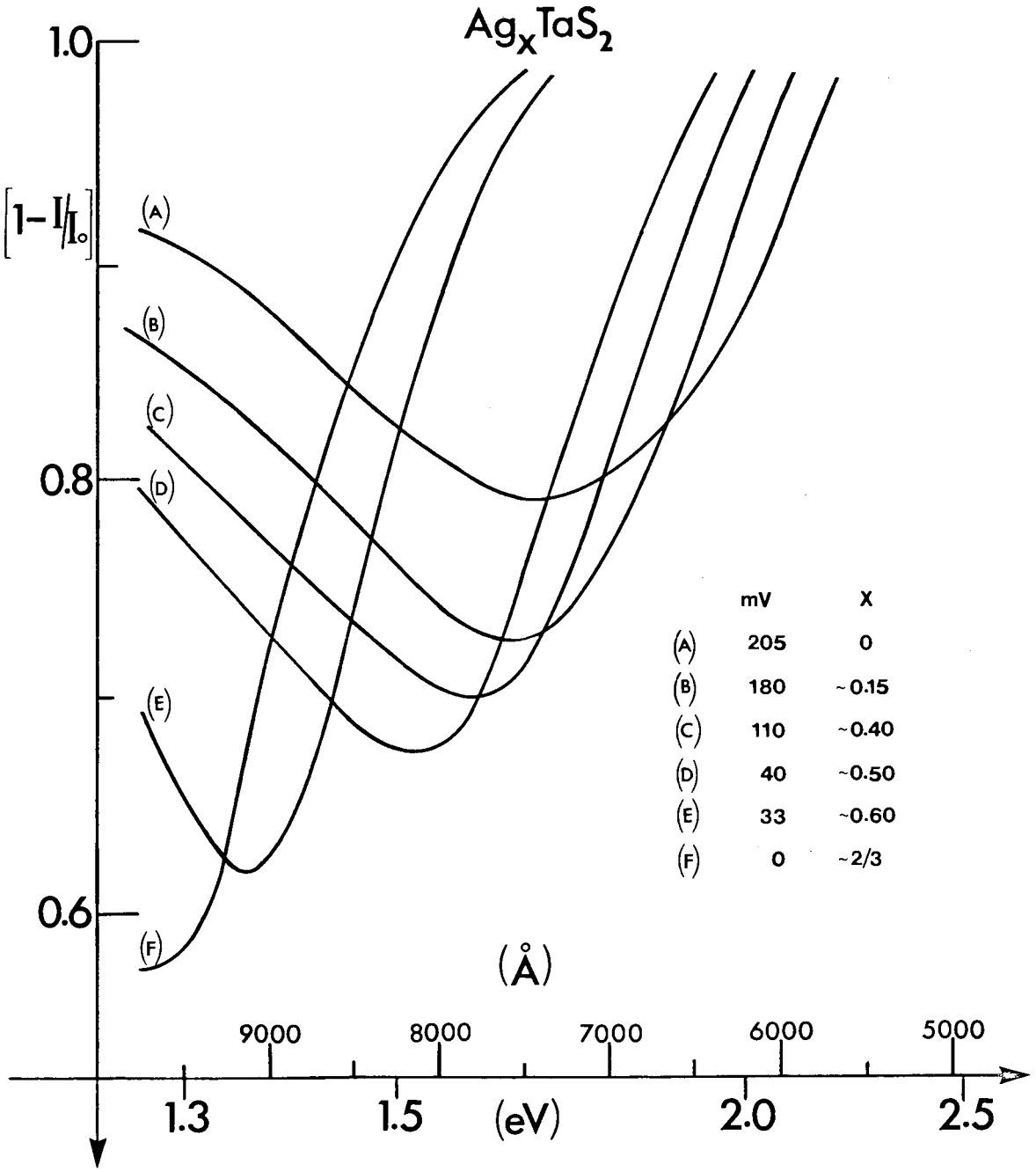
Ag_xTaS_2
1.0
0.8
0.6
$[1-I/I_o]$
(A)
(B)
(C)
(D)
(E)
(F)
mV X
(A) 205 0
(B) 180 ~0.15
(C) 110 ~0.40
(D) 40 ~0.50
(E) 33 ~0.60
(F) 0 ~2/3
(Å)
9000
8000
7000
6000
5000
1.3
1.5
(eV)
2.0
2.5

practice, not the transmission (T), but rather (1-T) which is similar to the absorption is plotted. Immediately noticeable and surprising is that the optical absorption of the sample actually decreases considerably at lower energies, and does not decrease overall as it appeared to do to the naked eye. The reason, of course, is that the eye's maximum sensitivity is near 2.0eV and the transmission in this energy range very quickly approaches zero on intercalation.

By comparing the spectra for pure 2H-TaS_2 in Fig. 8.4 with, for example, that determined most recently by Beal et al. [41], good overall agreement is found and, in particular, the absolute transmission intensities are in excellent agreement. The 2H-TaS_2 spectrum (Fig. 8.4) has a minimum absorption region centered near 1.5 eV and Wilson and Yoffe [7] cite free carrier absorption and interband transitions as responsible for the rise in the absorption at lower and higher energies respectively and, of course, near 1.5 eV the net absorption is the sum of these two absorption mechanisms. Wilson and Yoffe speculate that the "d_z2 conduction band" does not overlap the p/d valence band (Fig. 8.1) and that therefore the predominant interband transitions observed above about 1.5 eV are from the high density of states regions in the p/d valence band to those in the d/p conduction band. However, in deference to more recent data from photo-emission measurements [42,43] and electron energy loss measurements [44], it would apear that the "d_{z2} conduction band"

partially overlaps the p/d valence band. These experimental results have been further substantiated by Wexler and Woolley's [40] band structure calculation for the 2H family which, although they are very similar to the older calculations by Mattheis [39], do differ significantly from them by predicting, among other things, essentially no gap between the "d_{z^2}" and p/d bands. Joint density of states calculations for 2H-$NbSe_2$ by Doran [45], based on the band structure calculations by Wexler and Woolley [40], indicate a narrow peak in the joint density of states at about 2.5 eV arising from "d_{z^2}" to d/p band transitions and a broad peak at about 5.5 eV due to p/d to d/p band transitions. The band structure of 2H-TaS_2 is very similar to that of 2H-$NbSe_2$, in fact all 2H dichalcogenides share this similarity [39,40] but of course, the specific energies at which, for example, the peaks occur in the joint density of states depends on the particular dichalcogenide. By inspecting Fig. 8.4 it is clear that the joint density of states for the "d_{z^2}" to d/p transition is centered well above the 2.5 eV calculated for 2H-$NbSe_2$ and from the data of Beal et al. [41] it is clear that this joint density of states is actually centered close to about 3.3 eV.

Because of the above observations and calculations, the density of states distribution obtained by Wexler and Wooley, schematically drawn in Fig. 8.5, will be used to interpret the optical transmission results presented in Fig. 8.4. The

Fig. 8.5

Density of states schematic for 2H-TaS_2 according to Wexler and Wooley [40].

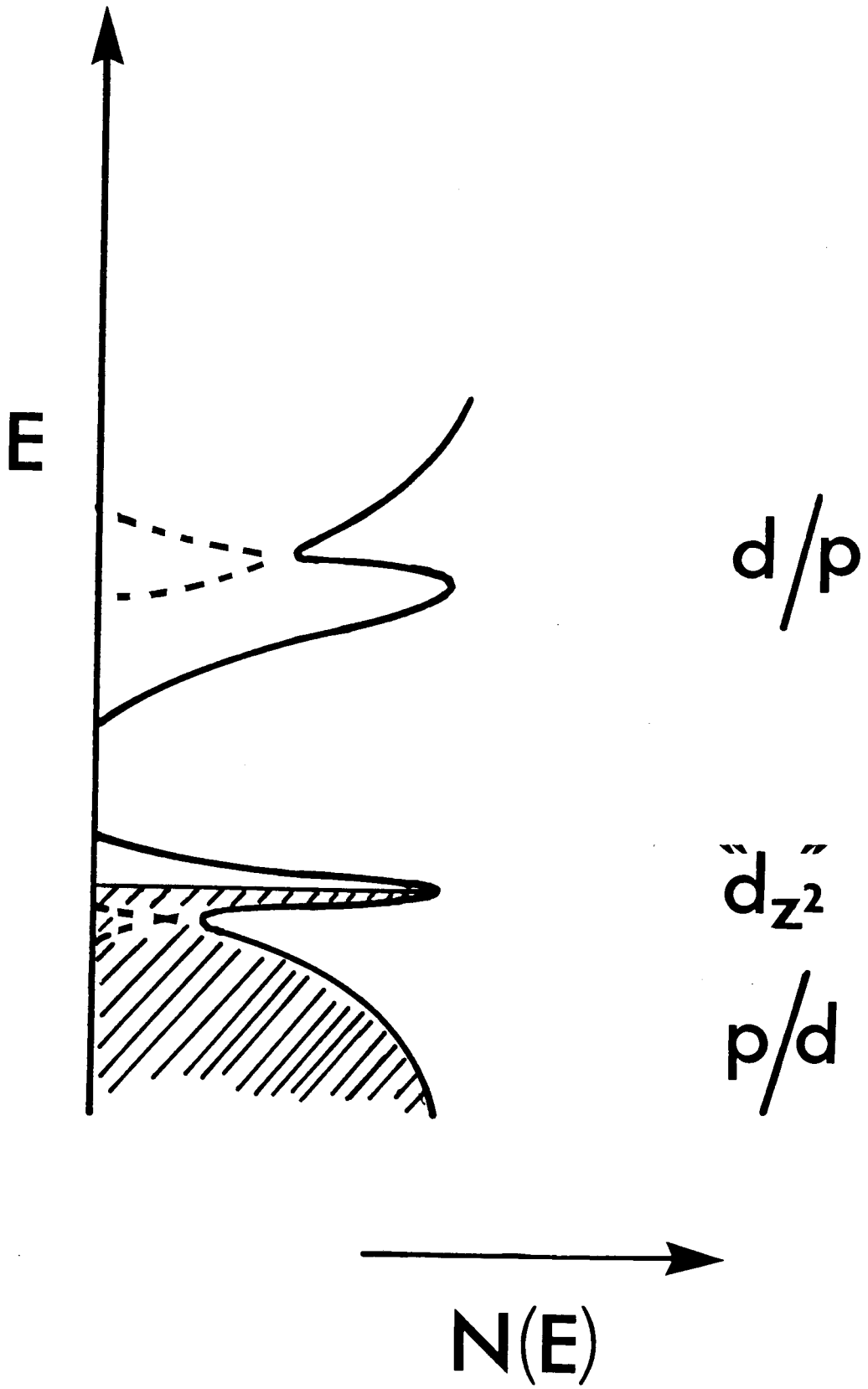
E
d/p
"d_{z^2}"
p/d
N(E)

interband band transitions observed above about 1.5 eV for 2H-TaS_2 will therefore be predominantly caused by "d_{z2}"to d/p transitions with, of course, some contribution also from the p/d to "d_{z2}" and maybe even the p/d to d/p transitions. Below about 1.5 eV strong free carrier absorption [7,41] is evident in Fig. 8.4 for 2H-TaS_2 but, because of the incomplete data, a quantatative fit of the absorption edge to a Drude model was not attempted.

As the intercalation of silver ions into 2H-TaS_2 proceeds, at least three major consequences can be observed in the transmission spectrum (Fig. 8.4):

(i) the absorption at lower energies generally decreases;

(ii) the minimum in the absorption decreases further and simultaneously moves to lower energies;

(iii) the edge of the interband transitions moves to lower energies, by about 0.75eV when $x \simeq 2/3$.

If these changes are interpreted in terms of a relatively rigid band strcture model, they confirm that charge transfer from the intercalate to the host, where the charge can delocalize and form a dichalcogen macro-anion, does occur. However, when trying to link a particular observation to a particular mechanism, as will be attempted below, problems do arise because of the interplay that exists between

several absorption mechanisms.

As the electron density in the previously half-filled "d_{z^2} conduction band" increases because of intercalation, the band becomes more than one-half full and, because the density of states of the "d_{z^2} band" is cusp-like [40], the density of states at the Fermi level will decrease considerably. Consequently, since the number of conduction electrons decreases, the free carrier absorption in the relaxation region ($1/\tau \ll \omega \ll \omega_p$ [46]) will also decrease. This decrease in the plasma frequency, as intercalation proceeds, will therefore explain, to a large part, observations (i) and (ii) and the latter observations in particular will result from the decreasing overlap of the plasma edge with the absorption band caused by the "d_{z^2}" to d/p transitions. Because of the filling of the cusp-like "d_{z^2} band", the joint density of states for the p/d to "d_{z^2}" transitions will also significantly decrease and this should therefore further enhance the transmission, again in agreement with observation (ii). Furthermore, because the Fermi level will increase with x, the absorption edge of the "d_{z^2}" to d/p interband transitions will occur for lower energies in agreement with observation (iii). In fact, from photo-emission evidence, on the "d_{z^2}" half-band width of $LiNbSe_2$ [43], a lowering of about 0.7 eV to 1.0 eV was found and is therefore in surprising agreement with the 0.75eV observed for $Ag_{2/3}TaS_2$. For the thinner samples, the

absorption for the fully or nearly fully intercalated samples can actually be observed to decrease again above about 2.4 eV and this suggests therefore that a maximum in the absorption occurs near 2.0 eV. Clearly this is yet another consequence of shifting the peak in the joint density of states of the "d_{z2}" to d/p transitions to lower energies and, judging by the shift of the interband absorption edge (Fig. 8.4), the shift in the absorption peak should also decrease in the order of 1 eV. Therefore, the shift in the absorption peak from its previous value of about 3.3 eV in 2H-TaS_2 [41] to about 2.0 eV in thin $Ag_{2/3}TaS_2$ samples is in good agreement. From the appearance of the transmission spectra of the $x \simeq 0.60$ and $x \simeq 2/3$ samples in Fig. 8.4, a maximum in the absorption near 2.0 eV again seems reasonable. However, because this particular sample was too thick, not enough light was transmitted above about 2.0 eV to ascertain whether or not the absorption does in fact decrease in this region as it did for the thin samples.

It is interesting to note that staging and, therefore, changes in the stacking sequence do not appear to have a particularly obvious influence on the transmission spectra of Ag_xTaS_2. Instead, the changes in the spectra simply seem to progress in a "monotonic" fashion with increasing x from 2H-TaS_2 to $Ag_{2/3}TaS_2$ (Fig. 8.6) with the possible exception perhaps in the mole fraction interval of about $0.50 \lesssim x \lesssim 0.60$ where a relatively large shift in the "d_{z2}" to d/p

Fig. 8.6

Room temperature optical transmission data for a thin Ag_xTaS_2 crystal at 5461Å versus the intercalated mole fractions as determined via Fig. 7.5.

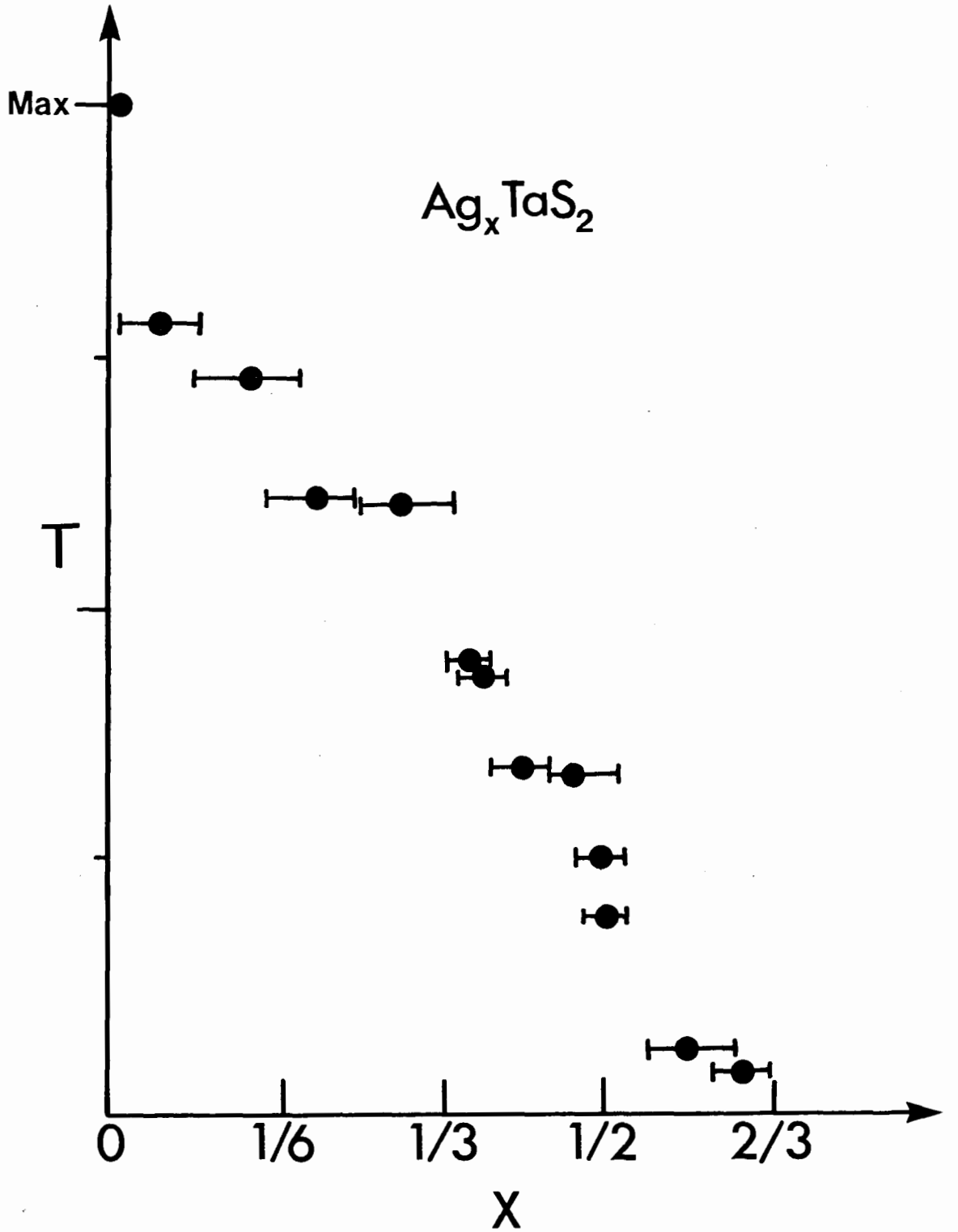
Max
Ag_xTaS_2
T
0
1/6
1/3
1/2
2/3
X

transition joint density of states occurs for a relatively small change of($\sim$0.10 mole fraction) of silver intercalated. What may be relevant to this observation is that, according to Fig. 7.7, in this mole fraction interval the sample experiences a shifting of about one-half of its intercalated layers to finally achieve the 2H-MoS_2 structure (Fig. 3.3) from the predicted structure, not yet experimentally proven, shown in (Fig. 7.7). However, if this is indeed relevant, it is then difficult to understand why a similar rapid shift in the joint density of states of the "d_{z2}" to d/p transitions is also not observed in the mole fraction interval of $1/6 \lesssim x \lesssim 1/3$ where a similar structural change occurs.

(B) Ag_xTiS_2 Transmission

Sufficiently thin samples of 1T-TiS_2 appear varying shades of blue in transmitted light, depending on the samples thickness, and samples much greater than about 1000Å thick will appear opaque to the eye. When the samples are intercalated with silver, two distinct fronts can be seen to move from the edge to the center of the crystal. The area behind the first front is a lighter blue in colour and the area behind the second front is almost colourless. Another aspect of intercalating 1T-TiS_2 with silver that becomes immediately apparent is that it proceeds at a very much slower rate compared to the rate at which silver intercalates into

Fig. 8.7

The room temperature absorption spectrum (A = 1-T) for a Ag_xTiS_2 sample about 800Å thick, which is electrochemically prepared in situ. The spectra are not reversible above about 50mV, corresponding to mole fractions below about $x = 0.20$.

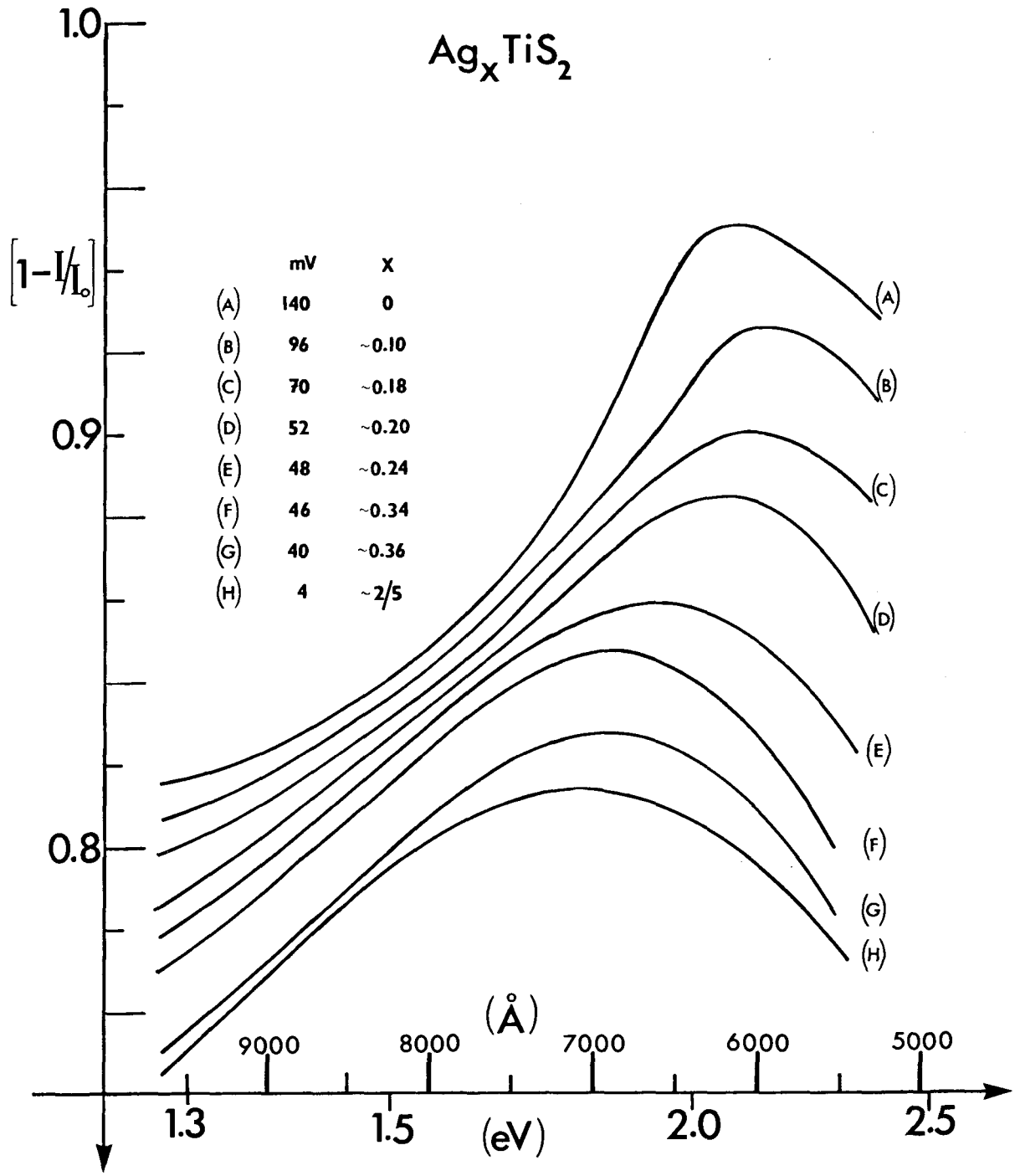
Ag_xTiS_2
1.0
0.9
0.8
$[1-I/I_o]$
mV X
(A) 140 0
(B) 96 ~0.10
(C) 70 ~0.18
(D) 52 ~0.20
(E) 48 ~0.24
(F) 46 ~0.34
(G) 40 ~0.36
(H) 4 ~2/5
(A)
(B)
(C)
(D)
(E)
(F)
(G)
(H)
(Å)
9000
8000
7000
6000
5000
1.3
1.5
(eV)
2.0
2.5

2H-TaS_2. In parallel with the differences in the intercalation rates, the diffusion rate for the silver ions is also very much slower in Ag_xTiS_2 when compared to Ag_xTaS_2. In Chapter 9 the rate and other aspects of the optical fronts will be further discussed.

In contrast with Ag_xTaS_2, the room temperature transmission spectrum for Ag_xTiS_2 was found to be only partially reversible with x, in agreement with the only partially reversible behaviour of the open circuit voltage observed in Chapter 7. Again, as in Chapter 7, there is good evidence that intercalation can be made reversible by heating the sample above 150C when deintercalating. However, at these elevated temperatures problems developed with the electrolyte in that silver had a tendency to precipitate and short-circuit the cell.

The 1T-TiS_2 sample whose unintercalated and intercalated transmission spectra are shown in Fig. 8.7, has a thickness of about 400Å, as measured using the Nomarski technique. Comparison of this spectrum for 1T-TiS_2 with the most recent data obtained by Beal et al. [47], indicates that there is excellent overall agreement, including the absolute transmission intensity.

A generally accepted density of states for 1T-TiS_2 is schematically shown in Fig. 8.8 according to recent band structure calculations [48,49], with the latter calculation estimating an indirect gap (p to "d_{z2}") of about 0.25eV

Fig. 8.8

Density of states schematic for 1T-TiS_2 according to Fong et al. [48].

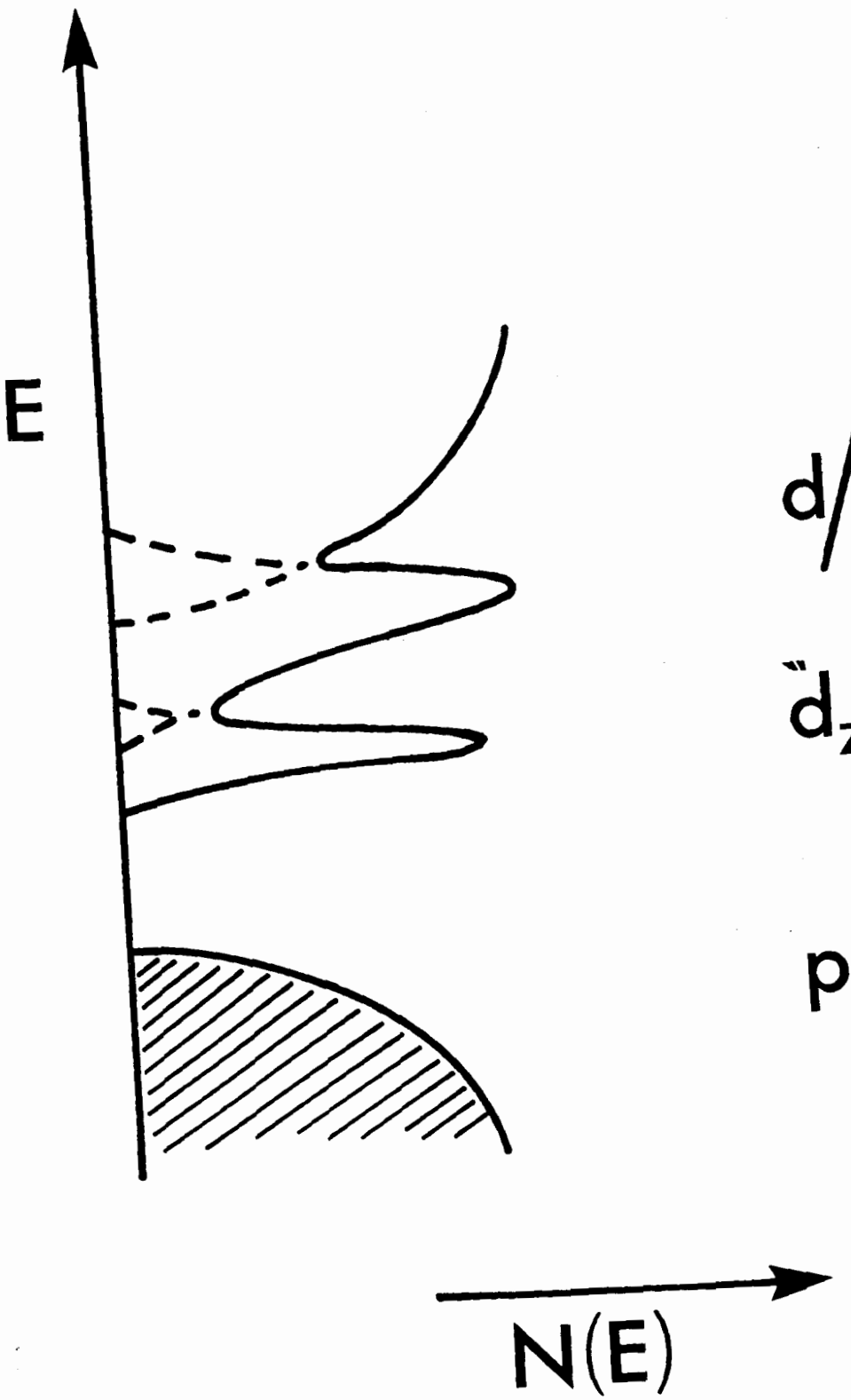
E
d/p
"d$_{z^2}$"
p
N(E)

for stoichiometric 1T-TiS_2. However, in practice 1T-TiS_2 is generally found to be an extrinsic semiconductor with n-type character due to poor sample stoichiometry and it is claimed that this is caused by excess titanium ions which are intercalated in the van der Waals gap [50].

In agreement with the density of states model in Fig. 8.8, no free carrier absorption is observed for 1T-TiS_2 (Fig. 8.7). However, even after intercalation, when charge transfer to the non-bonding bands should have provided for some free carriers, no noticeable rise in absorption due to a plasma edge is observed and moreover, the transmission is still increasing. Therefore, the plasma edge, almost certain to exist for the intercalated samples, is well below 1.25 eV. For comparison, in $LiTiS_2$ [47], the onset of the plasma edge occurs near 1.0 eV.

Again, as was the case for the Ag_xTaS_2 spectra, it is difficult to restrict changes wrought in the transmission spectra after intercalation to a specific cause and instead, cause and effect relationships are usually rather intertwined. However, the predominant cause for the absorption peak near 2.0 eV in pure 1T-TiS_2 (Fig. 8.7) is, according to the density of states model in Fig. 8.8, likely caused by transitions from the valence p-band to the "d_{z2}" peak in the density of states of the non-bonding (t_{2g}) d-bands. Then, as intercalation proceeds, the "d_{z2} band" becomes progressively more occupied, because of the

charge transferred to the host from the silver ions, and a subsequent reduction in the joint density of states should occur for these transitions. This is in agreement with the observations (Fig. 8.7) which do show a considerable decrease in the absorption in the range near 2.0eV. The peak remaining near 2.0eV for $x \simeq 0.40$ is likely due to a "d_{z2}" to d/p transition. Consequently, if the changes due to intercalation are interpreted using a relatively rigid band structure model, it would appear that charge transfer to the non-bonding d-bands is confirmed, however, the indications are not as convincing as they are for Ag_xTaS_2.

The changes in the transmission spectrum on intercalation are, as for Ag_xTaS_2, not dependent on staging in an obvious way. Instead, the transmission again varies "monotonically" with increasing degree of intercalation, x.

8.5 Conclusions Regarding the Room Temperature Optical Transmission Measurements of Ag_xTaS_2 and Ag_xTiS_2

The energy window from about 1.2 eV to 2.8 eV was accessible for studying the transmission spectra of silver intercalated 2H-TaS_2 and 1T-TiS_2. For Ag_xTaS_2 this window is extremely well placed, a fortuitous circumstance which allows the observation of changes in both the free electron plasma resonance and the interband transitions caused by intercalation. On the other hand, the transmission spectra

for the Ag_xTiS_2 intercalation compounds are not quite as informative in this energy range, but a change in an interband transition is observed. Another major observation of interest and common to both Ag_xTaS_2 and Ag_xTiS_2 systems is that the changes in the transmission spectrum on intercalation are directly proportional to the degree of intercalation and that staging and host layer rearrangements, have apparently no noticeable effects. Therefore, changes in the optical transmission spectrum is a useful means by which the silver ion concentration can be monitored (see Chapter 9).

The transmission spectra of the silver intercalated 2H-TaS_2 and 1T-TiS_2 on the whole are consistent with a relatively rigid band structure model, wherein the intercalate ionizes to some degree and transfers its charge to the predominantly "$d_{Z}2$ band", the lowest lying of the non-bonding (t_{2g}) d-bands of the dichalcogen host, which thereby effectively becomes a macro-anion. Comparing these results with those of Beal et al. for lithium intercalated 2H-TaS_2 and 1T-TiS_2 [41,47] one finds that silver and lithium intercalates have very similar effects on the transmission spectra of the dichalcogenide in the energy range of about 1.2 eV to 2.8 eV investigated for silver. This correspondence is quite significant because it does suggest that silver behaves similar to lithium when intercalated and that therefore, since lithium is surely essentially completely ionized (see Chapter 2), the silver atoms must also be highly ionized.

Whereas the transmission spectra for Ag_xTaS_2 is essentially reversible at room temperature, that of Ag_xTiS_2 is only partially reversible, and it is impossible to re-establish stage 2 unless the sample is heated well above about 150C. The irreversibility of Ag_xTiS_2 below about $x = 0.20$ is further discussed in Chapter 10.

CHAPTER 9

INTERCALATION AND DIFFUSION RATES

9.1 Introduction

A number of methods have been used to study the motion of mobile ions in intercalation systems, including ionic conductivity, radioactive tracers, electrochemical techniques, and NMR. However, as observed in Chapter 8, the changes observed in the transmission spectra on intercalation can also be used to directly monitor intercalation kinetics, diffusion rates and staging. Here are some of the results of studies on the motion of optical fronts observed in thin crystals of 1T-TiS_2 and 2H-TaS_2 electro-intercalated with silver. In the Ag_xTaS_2 system these optical fronts correspond to a shift in the interband transition edge ("d_{z2}" to d/p essentially) to lower energies (Fig. 8.4) which in turn causes a large increase in the absorption near 2.3 eV in the visible region, proportional to the increase in x. In the Ag_xTiS_2 system the joint density of states of the interband transitions decreases with increasing x near 2.3 eV so that the absorption, in contrast to the Ag_xTaS_2 system, decreases with increasing x (Fig. 8.7).

9.2 Apparatus and Experimental Arrangement for Observing the Motion of Optical Fronts

Thin, transparent samples of the dichalcogenides were

mounted in an identical manner to that used when their transmission spectrum was determined (Fig. 8.3) and the electrolyte was 0.1N $AgNO_3$/glycerol or at times 0.1N $AgNO_3$/water. The optical fronts were generated by simply short-circuiting the dichalcogen anode to the silver cathode. Sample thicknesses were determined via interference fringe techniques and a typical interference photograph of a partially intercalated Ag_xTiS_2 crystal is shown in Fig. 9.1. The sample was observed through a Reichert model MeF2 microscope which is provided with camera bellows fitted with a ground glass projection screen. The ends of a pair of light pipes, separated by either 60 μm or 100 μm depending on the objective, are mounted on the projection screen and the other ends are fitted to a photo-multiplier tube so that, as the intercalation fronts pass, the changes in the optical density can be recorded. A convenient light source often used was the mercury green light at about 2.3 eV. In Figure 9.2 a schematic of the experimental apparatus is presented.

9.3 Results of the Intercalation and Diffusion Rates Observed in 2H-TaS_2 and 1T-TiS_2

The interference fringes in Fig. 9.1, using a Ag_xTiS_2 sample, show three distinct regions and X-ray studies on material removed from each of such regions clearly shows that the material is, starting from the edge, stage 1, stage 2 and

Fig. 9.1

An interference fringe photograph (λ = 5461Å) of the basal surface of a 24μm thick 1T-TiS_2 crystal partially intercalated with silver, showing empty (x = 0 or possibly dil. stage 1), stage 2 and stage 1 regions.

(G.A. Scholz et al.[53]; photographs kindly taken by Mr. P. Joensen.)

Fig. 9.2

Experimental arrangement and apparatus used for determining the intercalation and diffusion rates.

Fig. 9.4

Transmission photograph of a 300Å thick 1T-TiS_2 crystal partially intercalated with silver, showing from the edge, stage 1, stage 2 and empty (dil. stage 1) crystal.

(G.A. Scholz et al. [53]; photograph kindly taken by Mr. P. Joensen.)

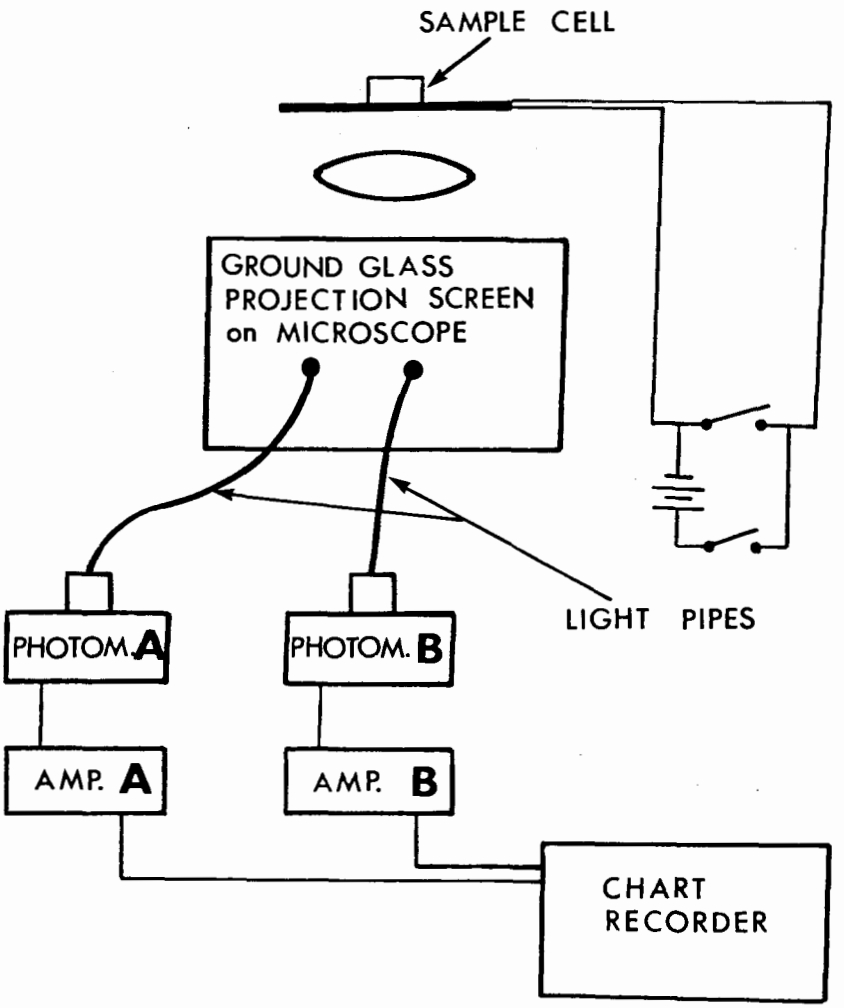
SAMPLE CELL
GROUND GLASS
PROJECTION SCREEN
on MICROSCOPE
LIGHT PIPES
PHOTOM. A
PHOTOM. B
AMP. A
AMP. B
CHART
RECORDER

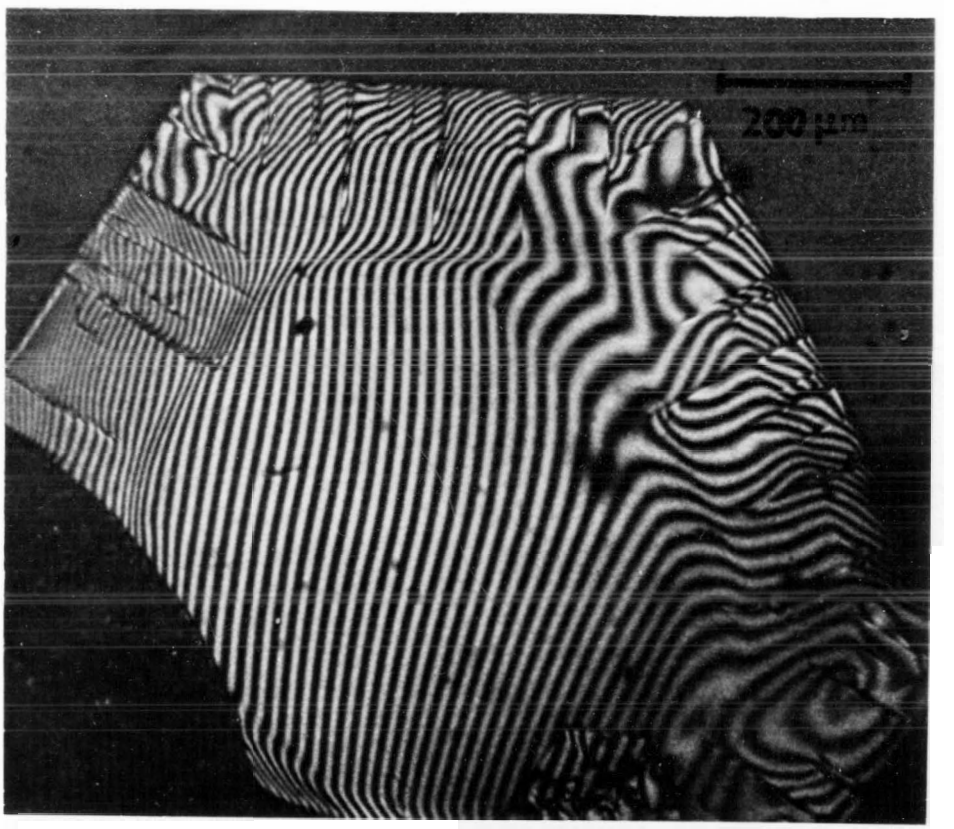

(9.1)

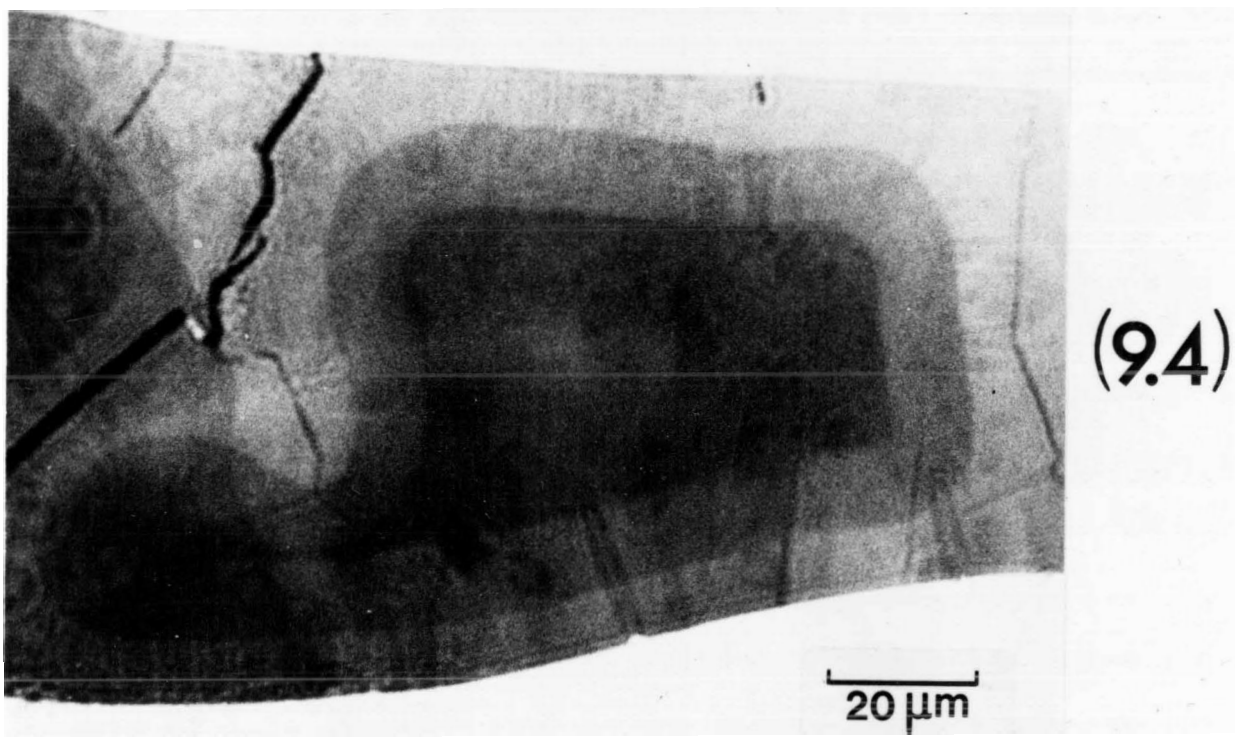

(9.4)

essentially empty (maybe dilute stage 1 though) crystal. The fringe shifts indicate an increase in the crystals thickness of 1.5 μm between the empty and stage 2 regions (assuming the same change in height at both basal surfaces). This corresponds to an increase in thickness of 6%, in good agreement with the 6.3% expansion for stage 2 Ag_xTiS_2 expected on the basis of the X-ray data of Chapter 3. It was also possible to identify the intercalation stages from changes in the optical reflectivity of the crystal and by cracks, if the crystals were relatively thick.

X-ray fluorescence, with a scanning electron microscope, can also be used to study the relative amounts of silver in the three regions of partially intercalated Ag_xTiS_2 and Fig. 9.3, where a composite of data from two crystals is used, shows the relative silver content, determined by a series of point measurements taken in a line perpendicular to the crystal edge. The results dramatically illustrate staging and unambiguously verify that the optical fronts are rather sharp discontinuities in the silver concentration. The electron beam size used to generate Fig.9.3 was about 1μm and the beam energy was 20 keV. Crystals in the thickness range from 1μm to 50 μm gave essentially the same results. It was determined in Chapter 8 that when thin 1T-TiS_2 crystals are interclated with silver, the optical transmission increases more or less proportional to the silver content and can therefore be used as an effective way of illustrating

Fig. 9.3

Relative silver content for partially intercalated 1T-TiS_2 for positions in from the crystal edge determined using an XRF microprobe. The stage 2 and stage 1 region fronts as observed optically are indicated by the vertical lines.

(G.A. Scholz *et al.* [53]; data kindly taken by Mr. P. Joensen.)

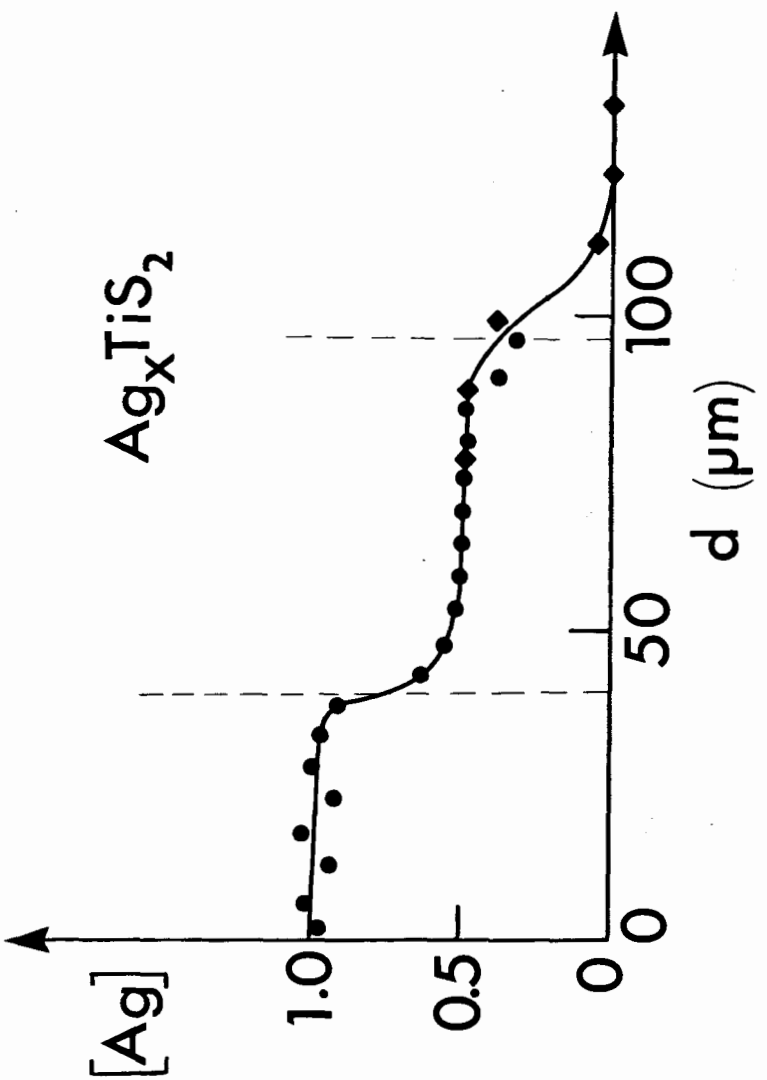
Ag_xTiS_2
[Ag]
1.0
0.5
0
0
50
100
d (μm)

staging. In Fig. 9.4 for example, two intercalalated regions are observed which clearly correspond to stage 1 at the edge of a thin 1T-TiS_2 crystal and to stage 2, adjacent to stage 1, toward the crystal interior.

Intercalation and diffusion rates for silver were determined by monitoring the optical density simultaneously at two positions in the crystal via the ground glass screen of the microscope. A typical trace of the transmitted light intensity at the two positions is shown in Fig. 9.5. If a crystal was partially intercalated and then the electrical circuit opened, the fronts were observed to become diffuse. Observation of the diffuse fronts, following an open circuit, allows the thermal diffusion rate of the silver ions to be determined.

Observations on thin crystals of 2H-TaS_2 and 1T-TiS_2 show that deintercalation, like intercalation, also occurs in stages, starting at the edge of the crystal. For example, a stage 1 crystal deintercalates by the propagation of first, a stage 2 and then an empty region in from the edge of the crystal. Therefore, intercalation and deintercalation are not time reversible events.

It may be of interest to point out here that 1T-TiS_2 crystals less than about 1/2 μm thick, unlike thicker samples, were never observed to crack or breakup, because of intercalation, even after much cycling. A comparison between the intercalation of thin 2H-TaS_2 and 1T-TiS_2 show two major

Fig. 9.5

The transmitted light intensity for λ = 5461Å as a function of time at two positions about 100μm apart at room temperature for a short circuited cell. Note that a decrease in the transmitted intensity can be observed simultaneously, within the 10^{-1} sec. experimental error, at both locations.

(Data kindly taken by Mr. P. Joensen.)

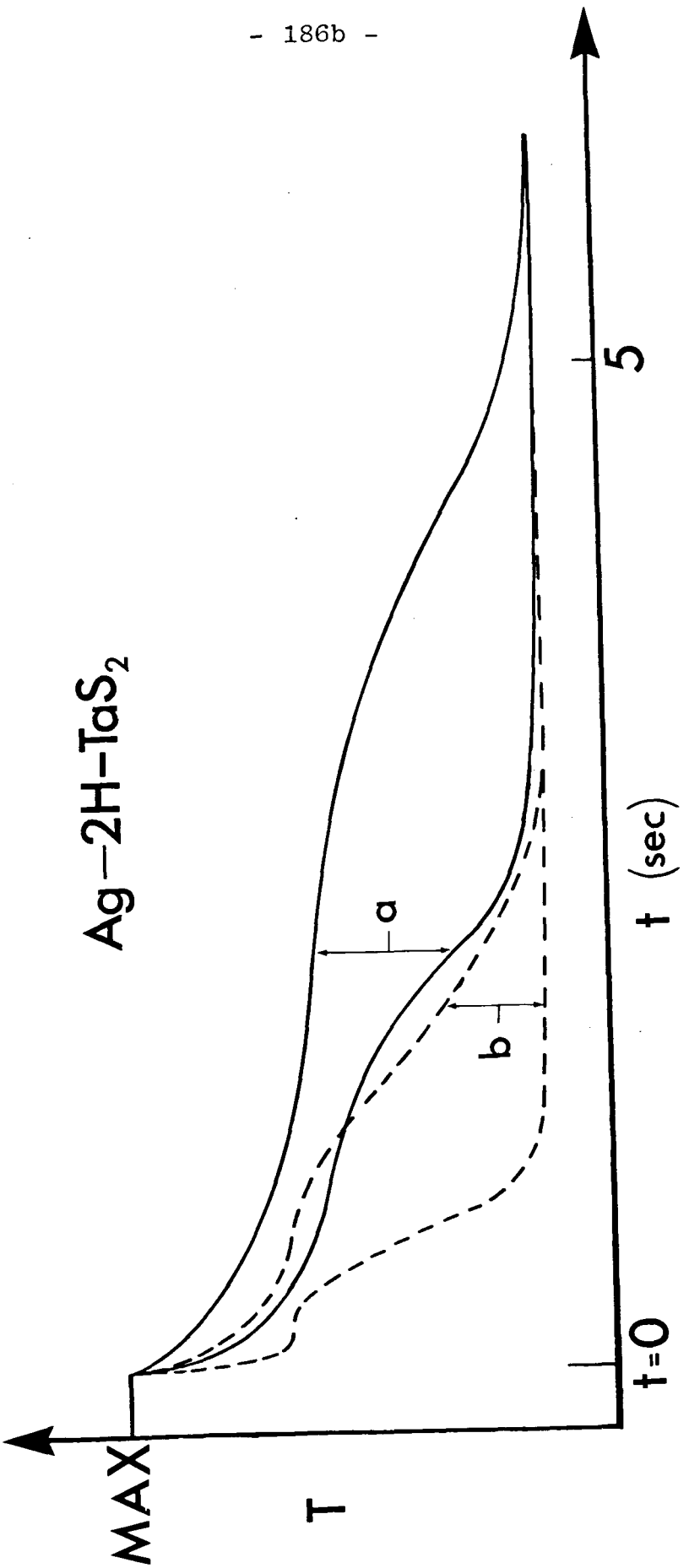
Ag—2H-TaS2
MAX
T
t=0
5
t (sec)
a
b

differences: the latter's intercalation rate is very much faster than the former, and that the intercalation front in 2H-TaS_2 is not as sharp as in 1T-TiS_2.

In Fig. 9.6 the speed at which the stage 2/1 optical front advances at room temperature, for a short-circuited 2H-TaS_2/Ag cell, is plotted as a function of crystal thickness using the 25% transmission points. A pronounced rate increase can be noticed below a thickness of about 500Å. The intercalation rate in Fig. 9.6 decreases approximately as $t^{-3/2}$, where t is the crystal thickness. Fig. 9.7 shows the room temperature thickness dependence for the advancement rate of the stage 2/1 optical front again using the 25% transmission points, for a short-circuited 1T-TiS_2/Ag cell, plotted on a log-log scale. Here the rate drops off approximately as $t^{-1/2}$. At 80°C, the intercalation rates for silver in thin 2H-TaS_2 and 1T-TiS_2 crystals were, respectively, a factor of 3 and a factor of 10 times faster than at room temperature.

From open circuit observations of the stage 2/1 optical front in partially intercalated crystals, the thermal diffusion coefficient for silver in Ag_xTiS_2 is estimated about $10^{-10}cm^2/s$ at 80C. This was calculated by using the Einstein-Smoluchowski equation:

$$\langle x^2 \rangle = 2Dt \qquad (9.1)$$

where $\langle x^2 \rangle$ is the mean square distance traversed by the

Fig. 9.6

Room temperature intercalation rate for the stage 2/1 optical front in 2H-TaS_2 versus crystal thickness using the 25% transmission points.

(G.A. Scholz et al. [53]; data kindly taken by Mr. P. Joensen.)

Fig. 9.7

Room temperature intercalation rate for the stage dil. n = 1/2 optical front in 1T-TiS_2 versus crystal thickness using the 25% transmission points.

(G.A. Scholz et al. [53]; data kindly taken by Mr. P. Joensen.)

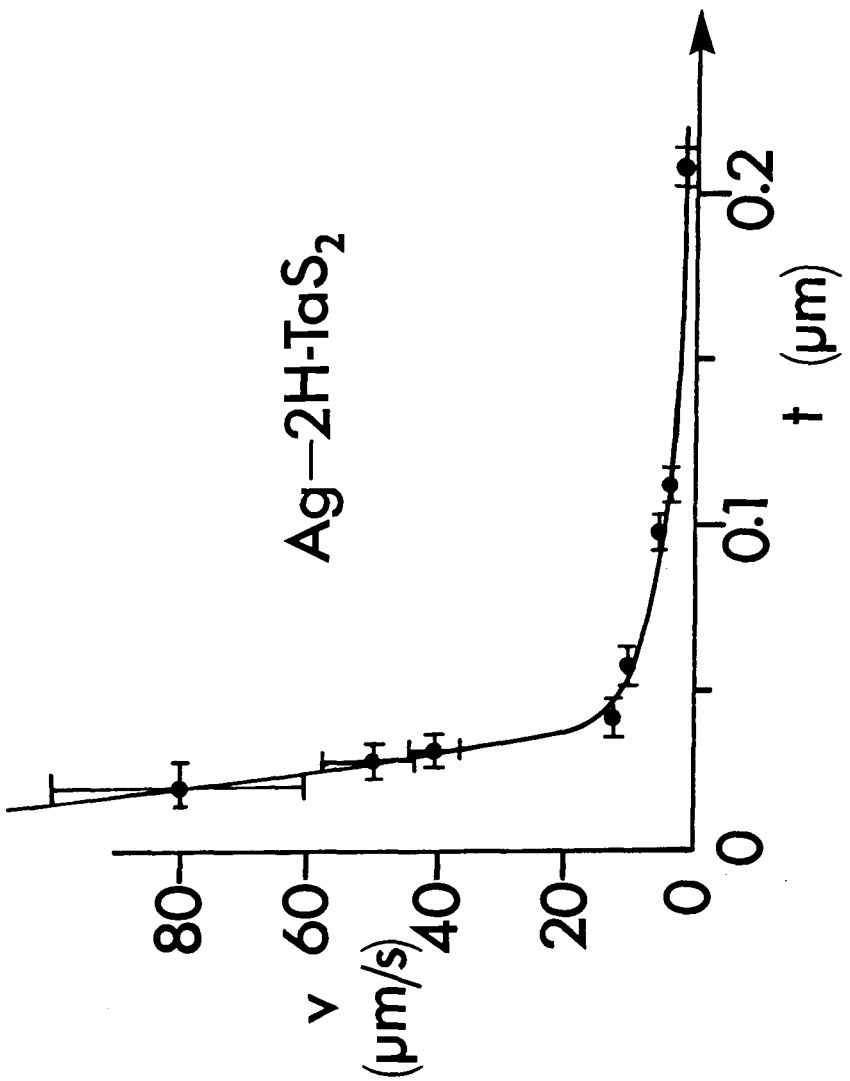

(9.6)

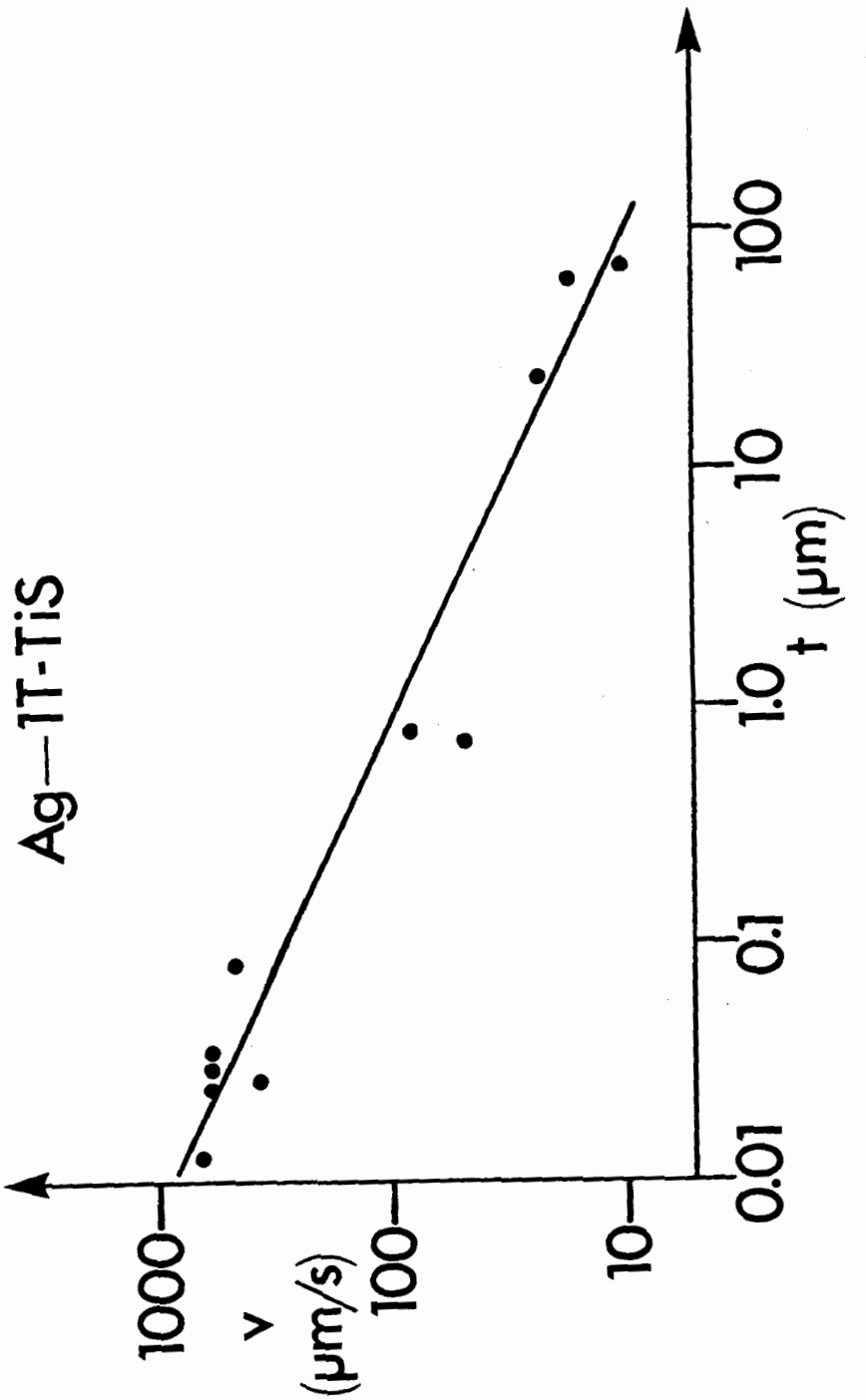

(9.7)

majority of the silver ions, that is the optical front, and D is the diffusion coefficient. For the silver ions in Ag_xTaS_2 the diffusion coefficient is much larger, about $10^{-8}cm^2/s$ at room temperature and about $10^{-7}cm^2/s$ at 80°C. This can be compared with typical diffusion coefficients of ions in solution which are about $10^{-5}cm^2/s$.

If the dichalcogenides are intercalated at a constant current, it was found that the main voltage drop and the optically observed onset of stage 1 at the crystal edge correlated well with the drop in voltage observed in the open circuit potential of these materials in Fig. 7.5 and Fig. 7.6.

Realizing the tremendous enhancement of the intercalation rate into very thin dichalcogenide crystals, it was of interest to see how some extremely fine and, in particular, thin 2H-TaS_2 powder would react with a concentrated aqueous $AgNO_3$ solution, as already discussed in Chapter 2. The result of adding this concentrated electrolyte to the fine 2H-TaS_2 powder was immediate and quite spectacular in that the glass vial became very hot and the mixture began to effervesce. The black 2H-TaS_2 powder changed colour and became bright yellow and the electrolyte became very acidic. In addition, when observing the powder under a microscope, although the characteristic platelet shape of the crystallites was retained, their metallic lustre had vanished and instead they became almost translucent in appearance. X-ray powder diffraction

patterns of this yellow material contained no sharp lines whatsoever and the material appears to be amorphous.

At first glance the effervescence appeared to be caused by the liberation of a gas which, because the solution is acidic, could only be oxygen. In an attempt to trap the evolving gas it was found that in fact no gas was actually produced at all. This could actually have been expected, when one realizes that for the oxidation of water a half-cell potential well in excess of the thermodynamic value of about 1.2 V would be required. Therefore, it became clear that the effervescence is nothing more than the boiling of the electrolyte caused by the extremely exothermic nature of the chemical reaction.

9.4 Discussion of the Optical Fronts Observed in Silver Intercalated Thin 2H-TaS_2 and 1T-TiS_2 at Room Temperature

Optical studies on intercalating, transparent dichalcogen crystals have provided much direct data on the kinetics of intercalation and 2-D diffusion. What made those observations possible is that the optical properties of the transparent crystals in the visible appear to be more or less directly proportional to the local concentration of silver, as shown in Fig. 8.6 for Ag_xTaS_2.

As can be seen in Fig. 9.5, a decrease in the transmitted light intensity due to intercalation occurs at both monitoring positions, which are separated by 100μm, with no apparent time

lag. Therefore, depending on the exact intensity between which the advancing fronts are measured, varying intercalation rates will be calculated. If the initial decrease in the transmitted intensity is used, where the time lag between the two positions is limited to the instrumental resolution which is about 10^{-1} sec.,an extremely large intercalation rate of about $10^{3}\mu m/s$ can be calculated for both dichalcogenides. The explanation for this apparent anomalous rate lies in the fact that the front of the intercalating silver ions is not a step function, and instead the ions will distribute themselves in some type of bell-shaped concentration profile so that a few of the silver ions within a given basal plane will intercalate into the interior of the crystal to much greater distances than the bulk of the ions. Because 2H-TaS_2 and 1T-TiS_2 are metals, $\rho \sim 10^{-4}\Omega\cdot cm$ at room temperature, there can be no large scale electric fields in the interior of these crystals. Therefore, intercalation should correspond to a diffusion process which stems from the concentration gradient of silver ions. These differences in the intercalation rate, or equivalently the diffusion rate D, are therefore similar to those encountered between bulk and tracer diffusion coefficients. Bockris [36] shows that the chemical diffusion coefficient, of interest here, corresponds to the net movement of about 60% of the diffusing material and threfore the use of the 25%, rather than the 40% transmission points in determining the intercalation rate, i.e. D, will

actually be a conservative approximation of the chemical diffusion coefficient of the silver ions in the dichalcogenides. The room temperature diffusion coefficients for silver in Ag_xTaS_2 and Ag_xTiS_2 are fairly typical of other intercalation systems, for example, $D \sim 10^{-9}cm^2/s$ for lithium in Li_xTiS_2 [51], and in superionic conductors, for AgRbI for example, $D \sim 10^{-5}cm^2/s$[52].

The fastest intercalation rate ever observed was about 80μm/s in a very thin ($\sim$ 200Å) Ag_xTaS_2 crystal and if this intercalation rate were interpreted in terms of a diffusion model [Eqn. 9.1], a diffusion constant of $D \sim 10^{-5}cm^2/s$ would result. This order of magnitude in D is typically observed for ionic diffusion in liquid electrolytes and it is very surprising to find that silver ions can diffuse at a comparable rate in a metallic solid. In fact, such large diffusion rates are of the same order of magnitude encountered for some of the best superionic conductors [52]. Since the silver ions in 2H-TaS_2 and in some of the superionic conductors move at comparable rates, one could conclude that intercalation and deintercalation is a conduction process, that is, they might be driven by electric fields at the edge and within the Ag_xTaS_2 crystal, as is the case in the superionic conductors. However, whereas the dichalcogenides are fairly good metals, the host materials of the superionic conductors are insulators and therefore are capable of supporting strong electric fields in their interior.

Nevertheless, it appears that the rapid intercalation rates are not limited by thermal diffusion and must therefore be related in some way to significant electric fields within (and perhaps across) the layers. More work is required here. Thickness effects have also been observed for Li in thin 1T-TiS_2 by Scholz et al. [53] and also for graphite by Hooley [54].

Some qualitative indication of why thick crystals intercalate more slowly may be provided by Fig. 9.8 which shows a schematic diagram of a partially intercalated crystal. Because an elastic energy (say E_k) is required to bend a host layer on intercalation, it seems clear that a perfect crystal will always start to intercalate first at the basal surfaces (observed first by Hooley with graphite [54]). Intercalation should proceed in subsequent layers below the basal surfaces. The Nth intercalating layer below the surface will introduce NE_k bends in that host crystal layer so that an increasing elastic energy must be overcome with every new intercalated layer. One would thus expect a slower intercalation rate as N increases, and eventually, intercalation might well cease altogether. Note that Fig. 9.8 should apply to any intercalating crystal, with or without islands or staging.

The observation that electrointerclation proceeds at an enhanced rate for very thin crystals, with the maximum rates observed below a thickness of about 500Å, has obvious

Fig. 9.8

Schematic diagram of intercalation starting at the basal surface. An elastic energy E_k is required for one bend in a host layer.

(G.A. Scholz *et al.* [53].)

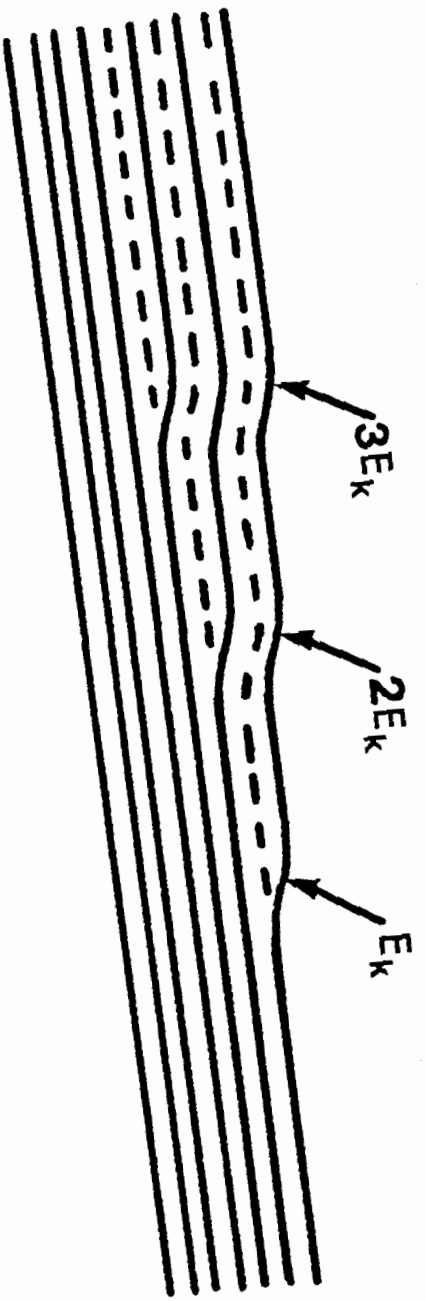
$3E_k$
$2E_k$
E_k

applications in batteries where high power capacities are required. Patent submissions on this have been made in both Canada and the U.S.A. [67].

The violent, effervescent exothermic reaction of the fine 2H-TaS_2 powder with the concentrated aqueous $AgNO_3$ solution would appear to be a natural consequence of enhancing the chemical reactions already discussed in Chaper 2 by providing very thin 2H-TaS_2 crystallites. Clearly this reaction is irreversible and does not correspond to an intercalation reaction. Although this chemical reaction because of its very exothermic nature is very intriguing, it was not pursued any further.

CHAPTER 10

CONCLUSIONS, THEORIES AND PREDICTIONS GOVERNING STAGING, HOST LAYER STACKING AND PREFERRED INTERCALATION SITES

10.1 Introduction

When transition metal dichalcogenides are intercalated the Ch-M-Ch sandwiches remain intact but structural phase changes, reflected in changes in the stage number, the host layer stacking sequence or the preferred intercalation sites, may occur. An extensive data base has been compiled for the Ag_xTaS_2 and Ag_xTiS_2 intercalation systems which, when combined with additional information of other group IV, V and VI transition metal dichalcogenides published by other workers, indicates that definite trends exist between the mole fraction intercalated and the phase changes observed in the intercalated material. These trends will now be used as the basis for a qualitative discussion which will endeavour to explain and predict some of the changes in phase observed as x varies.

10.2 Host Layer Stacking in the Transition Metal Dichalcogenides

For convenience a summary of the phase changes observed and deduced in the Ag_xTaS_2 and Ag_xTiS_2 intercalation systems (Chapters 3, 4, 5, 6 and 7) is presented in

Table 10.1

Summary of the structural phase changes observed in the Ag_xTaS_2 and Ag_xTiS_2 intercalation systems.

Ag_xTaS_2	Thermally prepared at 750C and then quenched			Electrochemically interc. at room temp. in 0.1N $AgNO_3$/glyc.		
	stage	site occup.	(*) stacking	stage	site occup.	(*) stacking
0	-	-		-	-	
$0 < x \lesssim 1/12$	1'			1'&2		
$1/12 \lesssim x \lesssim 1/6$	1'&2	Oct.	Eclipsed		Oct.	Eclipsed
$x \simeq 1/6$				2		
$1/6 \lesssim x \lesssim 1/4$	2	Oct. & Tet.	Eclipsed & Staggered		Oct&Tet	Eclip.&Stagg.
$1/4 \lesssim x \lesssim 1/3$						
$x \simeq 1/3$		Tet.	Staggered		Tet.	Staggered
$1/3 \lesssim x \lesssim 5/12$	2&1	Tet. & Oct.	Staggered & Eclipsed	2&1	Tet. & Oct.	Staggered & Eclipsed
$5/12 \lesssim x \lesssim 1/2$						
$x \simeq 1/2$				1	Tet.	Staggered
$1/2 \lesssim x \lesssim 2/3$	1	Tet.	Staggered			
$x \simeq 2/3$						
Ag_xTiS_2						
0	-	Oct.	Eclipsed	-	Oct.	Eclipsed
$0 < x \lesssim 1/8$	1'			1'&2		
$1/8 \lesssim x \lesssim 1/5$	1'&2			2		
$x \simeq 1/5$	2					
$1/5 \lesssim x \lesssim 2/5$	2&1			2&1		
$x \simeq 2/5$	1			1		
	Further predicted changes in the Ag_xTiS_2 System					
$2/5 \lesssim x \lesssim 1/2$	1&2	Oct&Tet	Eclip.&Stagg.	1&2	Oct&Tet.	Eclip.&Stagg.
$x \simeq 1/2$	2	Tet.	Staggered	2	Tet.	Staggered
$1/2 \lesssim x \lesssim 3/5$	2&1	Tet&Oct	Stagg.&Eclip.	2&1	Tet&Oct.	Stagg.&Eclip.
$x \simeq 3/5$	1	Tet.	Staggered	1	Tet.	Staggered

Note: 1' is dilute stage 1;

(*) refers to the stacking sequence of the transition metal atoms at the intercalation sites.

Table 10.1. Immediately noticeable is that whenever the transition metals are eclipsed or staggered with respect to each other, the silver intercalate will reside in octahedral or tetrahedral intercalation sites respectively. Furthermore, whereas both eclipsed and staggered configurations occur in Ag_xTaS_2, only the former occurs in Ag_xTiS_2. To facilitate this discussion, a few introductory remarks are in order.

The optical transmission results in Chapter 8 gave clear evidence that a charge transfer occurs from the intercalate to the host. This charge transfer will be to the lowest lying empty states, which correspond to the t_{2g} level associated with the $d_{x^2-y^2}$, d_{xy} and d_{z^2} non-bonding orbitals (Fig. 1.4). Because of crystal field effects, the lower peak in the density of states of the t_{2g} level is predominantly d_{z^2} in character for 2H-TaS_2, 1T-TiS_2 and other transition metal dichalcogenides. In fact, as already pointed out in Chapter 1, for the 2H-compounds the degeneracy in the t_{2g} states is considerably reduced and a gap develops between the lower peak in the density of states, predominantly d_{z^2} in character, and the upper states which are predominantly $d_{x^2-y^2}$ and d_{xy} in character. This lower lying peak is relatively narrow, about 1eV wide or less [29], and forms the conduction band in these dichalcogenides. For 1T-TiS_2 it is ideally empty and for 2H-TaS_2 it is ideally half full. Therefore, for simplicity, charge transfer from the

intercalate to the host will be discussed as occuring into these "d_{z2} orbitals". Because this "d_{z2}" level is relatively narrow, considerable localization of the electron density should exist in a manner not unlike that of a d_{z2} orbital.

Therefore, keeping the above in mind, it is suggested that the Coulomb and Exchange interactions between the "d_{z2} orbitals" in adjacent layers are the primary considerations when determining whether or not the adjacent (along $\hat{c}$) transition metal atom, in the various transition metal dichalcogenides and their intercalation compound, will arrange themselves in an eclipsed or staggered manner. The localization of the conduction electron density similar to that of the d_{z2} atomic orbital, although undoubtedly a small effect, will favour a staggered arrangement of the transition metal atoms because of a Coulomb repulsion between the "d_{z2} orbitals" in adjacent layers. But on the other hand, an overlap of the "d_{z2} orbitals" results in an overlap (exchange) integral which, although again probably quite small, will provide an exchange energy which reduces the overall interaction energy and therefore favours an eclipsed configuration of the "d_{z2} orbitals" and therefore also of the transition metal atoms. Whether the eclipsed or staggered arrangement exists should therefore depend critically on the transition metal atom, Group IV, V or VI, and the degree of intercalation, that is, charge transfer.

The Ag_xTaS_2 intercalation system, among others, is particularly suitable for demonstrating this delicate balance which can exist between the Coulomb and exchange energies, for two reasons. First, tantalum is a group V metal, so that the "d_{z^2} band" is ideally about half filled when $x = 0$ and second, the various Ag_xTaS_2 structures have been well characterized in the previous chapters. As can be noted in Table 10.1, as long as $x \lesssim 1/4$ mole fraction the tantalum atoms remain eclipsed as in pure 2H-TaS_2 (Fig. 5.10) and therefore the exchange interactions between the "d_{z^2} orbitals" dominates. However, when $x' \approx 2x \gtrsim 1/2$ mole fraction, sufficient charge transfer has occured so that the stabilizing influence of the exchange interaction is exceeded by the Coulombic interaction between the "d_{z^2} orbitals". Therefore for $x' \simeq 2/3$ the tantalum atoms, wherever the silver ions have intercalated, rearrange themselves into a staggered configuration (Fig. 5.10) which will minimize the Coulomb interaction. But note that staggering only occurs in the layers that are intercalated and not in the unintercalated layers. This suggests that the charge transferred from the silver ions to the host, instead of delocalizing uniformly, remains closely associated with the silver ions.Finally, when $x \simeq 2/3$, all host layers are uniformly intercalated and the transferred charge density has caused all tantalum atoms to arrange themselves in a staggered configuration (Fig. 3.3).

In the Ag_xTiS_2 intercalation system, a conversion from

the eclipsed to a staggered configuration of the titanium atoms is not observed up to $x \simeq 0.42$ (Table 10.1) and indicates that the coulombic interaction, between the "d_{z^2} orbitals",does not exceed the energy decrease associated with the exchange interaction. This result is now not entirely unexpected when one takes into account that the "d_{z^2} conduction band" in 1T-TiS_2 is ideally empty so that the charge density in the conduction band for Ag_xTiS_2, even if $x \simeq 2/5$, will probably be less than that found even in unintercalated 2H-TaS_2. On the other hand, if the degree of intercalation could be substantially increased, a shifting of the host layers should eventually occur. In agreement with this hypothesis, a shifting of the host layers is observed in Cu_xTiS_x ($0.70 \lesssim x \lesssim 1.0$) [55] . Note that copper and silver behave similarly when intercalated as can be seen when comparing, for example, Ag_xTaS_2 and Cu_xTaS_2 [20] or Ag_xNbSe_2 and Cu_xNbSe_2 [56] structures. Another way one should be able to precipitate a shift in the Ag_xTiS_2 host layers, to a staggered configuration of the titanium atoms along c, should be the application of hydrostatic pressure. A compound like $Ag_{0.42}TiS_2$ should be particularly suitable for this type of a pressure experiment because a considerable amount of silver is intercalated so that the Coulomb interactions should already be significant.

For pure 2H-MoS_2 the "d_{z^2} band" is completely full

and the Coulomb repulsion between the "d_{z^2} orbitals" should immediately be the dominant interaction. Indeed, in pure 2H-MoS_2 the Mo atoms are staggered. The staggered host structure obtained for $Ag_{2/3}TaS_2$, $Cu_{2/3}TaS_2$, $Ag_{2/3}NbSe_2$, $Cu_{2/3}NbSe_2$, etc., is actually commonly referred to as the MoS_2 structure. Note that a 1T-type structure is not stable at room temperature for the group VI dichalcogens. A change in the stacking sequence is by no means observed exclusively with silver or copper intercalates, but is also observed with almost all other intercalates, such as the post transition elements [57], alkali metals [58] and amines [59] among others. To sum up, whether the Coulomb or the exchange interaction will predominate, favouring either a staggered or an eclipsed configuration respectively, will therefore depend on the particular transition metal dichalcogenide and the net charge density transferred to the "d_{z^2} orbitals", which in turn will depend on the particular intercalate chosen and the amount of it intercalated.

10.3 Preferred Intercalation Sites in the Transition Metal Dichalcogenides

Whenever a stacking change, from eclipsed to staggered, occurs in the group IV or V transition metals, a change in the site occupied by the intercalate also inevitably occurs. For the pure materials, the transition metal will naturally be in

an eclipsed configuration for all of the 1T-dichalcogenides, but also in the commonly observed polymorphs (2H and 4Hb) of the group V dichalcogenides. The intercalate, when initially introduced, will then almost always reside in the trigonal antiprismatic (octahedral) intercalation sites which are located directly above and below the transition metal atoms (Figs.3.7, 5.10). If thereafter sufficient intercalate is introduced to produce the staggered configuration of the transition metal atoms, the intercalate will then almost always still be found directly above or below the transition metal atom which can correspond to either trigonal prismatic or tetrahedral intercalation sites. Note though that it is not necessary for the intercalate to move and change the site it occupies, but rather, it is the relative translation by ± (1/3, 2/3, 0) of the adjacent dichalcogen sandwiches which, while the intercalant actually remains stationary either above or below the transition metal, effectively moves the intercalant into the tetrahedral or trigonal prismatic site (see also discussion in Chapter 5). This close association between intercalant and transition metal is not only always observed for the silver and copper intercalates, but is in fact generally observed in a surprisingly large number of intercalation compounds unless, of course, some sort of steric constraints exist. The likely criteria that the intercalate has for choosing an intercalation site directly above and/or below the transiton metal atom is the "d_{z2} orbital" of the

transition metal which is directed into the intercalation site and can therefore make metallic bonding between host and intercalate possible because of, for example, the overlap of the silver 5s and the transition metal "d_{z^2}" orbitals. Furthermore, since the intercalate is partially ionic, it will certainly also receive maximum electrostatic screening if it is situated directly above or below the "d_{z^2} orbital".

There are however, as always, some systems which appear to partially violate the above generalizations. However, this only indicates that there are still other parameters to consider which can also be of importance in certain situations. For example, when higher concentrations of intercalate ($x \sim 1$) are present in the host one often observes that the intercalate and the transition metal atom are no longer directly above or below each other. This is observed with a number of post-transition element intercalation compounds (In, Tl, Sn, Pb, Bi in the group V dichalcogenides [60]) and in a few alkali metal intercalation compounds (Li, Na, K) in ZrS_2 along with Na_xTiS_2 ($x \gtrsim 0.80$) [58]). In the latter series of compounds, although Zr and Ti are in fact staggered in agreement with the first part of the hypothesis, the alkali atoms are found in octahedral sites which are staggered with respect to the transition metal atoms (Fig. 10.1a). The structure of the group V dichalcogenides intercalated with the post-transition elements is even more surprising in that the intercalate appears to occupy neither

Fig. 10.1

(a) The type 1(b) structure found by Dannot et al. [58] for some of the alkali intercalated group IV dichalcogenides.

(b) Intercalate position sometimes observed when the group V dichalcogenides are intercalated with post-transition elements. Note that the intercalate does not occupy sterically favourable intercalation sites and therefore strongly suggests the presence of a strong intercalate-sulphur bond.

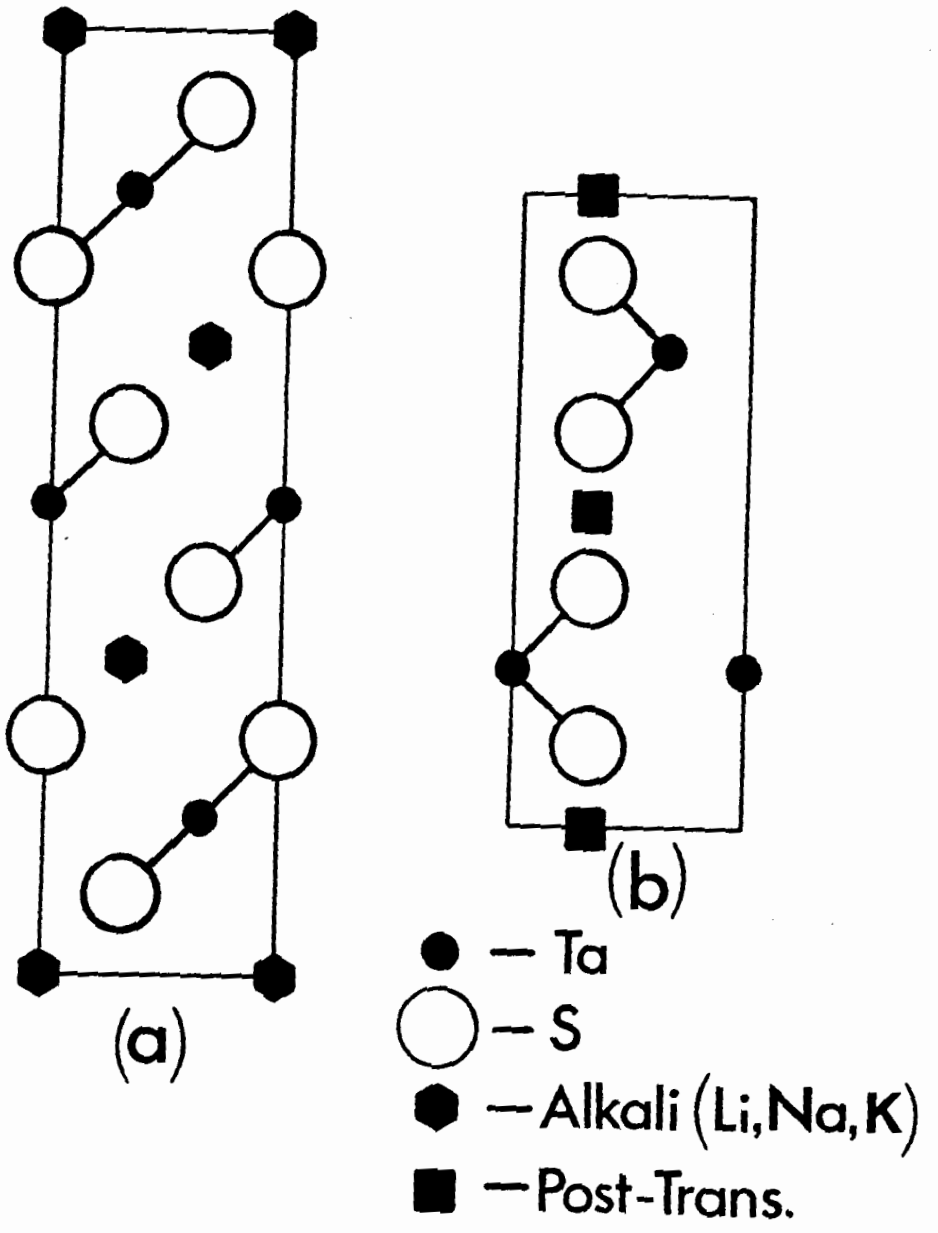
(a)
(b)
● — Ta
○ — S
⬢ — Alkali (Li,Na,K)
■ — Post-Trans.

octahedral nor tetrahedral intercalation sites and instead is positioned in-line with the chalcogen atoms (Fig. 10.1b) [60].

In the Na_xTiS_2 system the transition to the "anomalous" structure, the staggered configuration of the Na and Ti atoms, occurs for $x \simeq 0.80$ and the $\hat{a}$ and $\hat{c}$ axis lattice parameters are also observed to mirror this transition [58]. Whereas c_o, initially near 7.00Å, had been decreasing slightly to above 6.92Å as x increased to $\simeq 0.70$, above $x \simeq 0.80$ c_o decreases drastically to about 6.75Å and thereafter even on further intercalation remains below 6.85Å. This strongly indicates that if the intercalated mole fraction is sufficiently large, the intercalate-chalcogen bond will become an important factor, as is beautifully illustrated above in the Na_xTiS_2 system and should be true generally, whether the intercalate is a post-transition or alkali atom. The intercalate-chalcogen bond will therefore serve to bond the adjacent host layers in a much stronger fashion than the previous van der Waals type bond had and will result in; a "stiffening" of the host structure, pronounced effects on the dispersion relation of the phonons and a expected reduction in the layer spacing along the $\hat{c}$ axis.

Another consequence of intercalating to large mole fractions is that metallic bonding between the intercalates may become increasingly important and one would eventually expect a conduction band, composed essentially from

intercalate orbitals (sp^2 or sd^2 likely), to form. Therefore, even though one might ideally expect that the charge transferred by the intercalating ions should eventually fill up the host conduction band, that is the "d_{z2} orbitals", and thereby transform the intercalated material into an insulator, this will not occur because of the likely formation of an "impurity" conduction band at these large intercalate concentrations.

Pursuing some of the preceding ideas, some predictions can be made about intercalate structures as yet unknown. When an attempt is made to intercalate the Mo and W dichalcogenides with alkali metals, difficulties are often encountered, however, they can be successfully intercalated [9,61]. In these intercalation compounds the alkali ions can be expected to be in the tetrahedral intercalation sites, directly above or below the transition metal, for concentrations below $x \sim 1$. Then for larger values of x, a variety of structural changes may occur in which the alkali ions will likely be staggered with respect to the transition metal and may not even be residing in lattice sites by being in-line with the chalcogen atoms (Eqn.10.1b) as is observed in some of the post transition intercalates [60]. In any case, a phase change should be expected for $x \gtrsim 1$, including possibly a reduction in the interlayer spacing along $\hat{c}$. For higher concentrations still ($x \sim 2$) we might even expect that the chalcogen-transition metal bond will be disturbed as the

chalcogen-alkali bonding becomes increasingly important and relatively unusual structures like 1H [60] may appear. Of course, even though Mo and W dichalcogenides are ideally semiconductors, their high-x intercalation compounds will still be metallic because a "alkali metal conduction band" will likely form.

Another way of disrupting the close association of the intercalate with the "d_{z2} orbitals" might be accomplished by applying hydrostatic pressure. For example, using a $Ag_{2/3}TaS_2$ crystal a change in the silver ion occupation site, from tetrahedral to octahedral, can be expected for sufficiently high pressures. The reason for this expected change is the anticipated excessive overlap experienced between the silver orbitals and the "d_{z2} orbitals" of the host.

10.4 Staging in the Transition Metal Dichalcogenides

The term staging [9,10,35] has already been described in Chapter 1 and now an effort will be made to discuss the factors important to staging. As already pointed out in Chapter 1, whether or not intercalation will occur at all is the result of a number of factors. Whereas on the positive side, the delocalization of the intercalate's valence electrons and the host's electron affinity are important, on the negative side, the elastic properties of the host, the interlayer bond and Coulombic interactions are important.

Obviously, since intercalation is observed, the positive aspects can be dominant. Nevertheless, the intercalating system will still attempt to minimize its free energy by minimizing the negative aspects of the intercalation reaction as much as possible.

Staging is therefore considered to be the direct result of minimizing these latter interactions, of which the most important are thought to be:

(1) The work required to separate the host layers (E_s), first pointed out by Setton [62].

(2) The work required to introduce bends, or pleats, (E_k) into the host layers.

(3) The Coulomb interaction (Eq) between the intercalated ions.

When the first few guest ions enter a van der Waals gap, forming the dilute stage 1 phase (Chapter 3), the elastic nature of the pseudo 2-D host layers will allow them to buckle somewhat and thereby provide some room for the guest ions. In order to minimize the Coulomb interaction between the intercalated ions and to reduce the strain induced into the host lattice, the intercalated "impurities" will remain apart as much as possible. One of the marked features of this dilute stage 1 phase is that the unit cell parameters remain essentially unchanged from that of the pure dichalcogenide and is oberved in Ag_xTaS_2 and Ag_xTiS_2 for $x \lesssim 1/8$ and $\lesssim$ 1/12 respectively. If N ions are intercalated, as illustrated

Fig. 10.2

Schematic illustration of the elastic strains which are introduced in the host layers when a few ions are randomly intercalated to form the dilute stage 1 phase. Further intercalation will eventually make the existence of a large number of bends in the host layers energetically unfavourable, causing the intercalate to coalesce into islands.

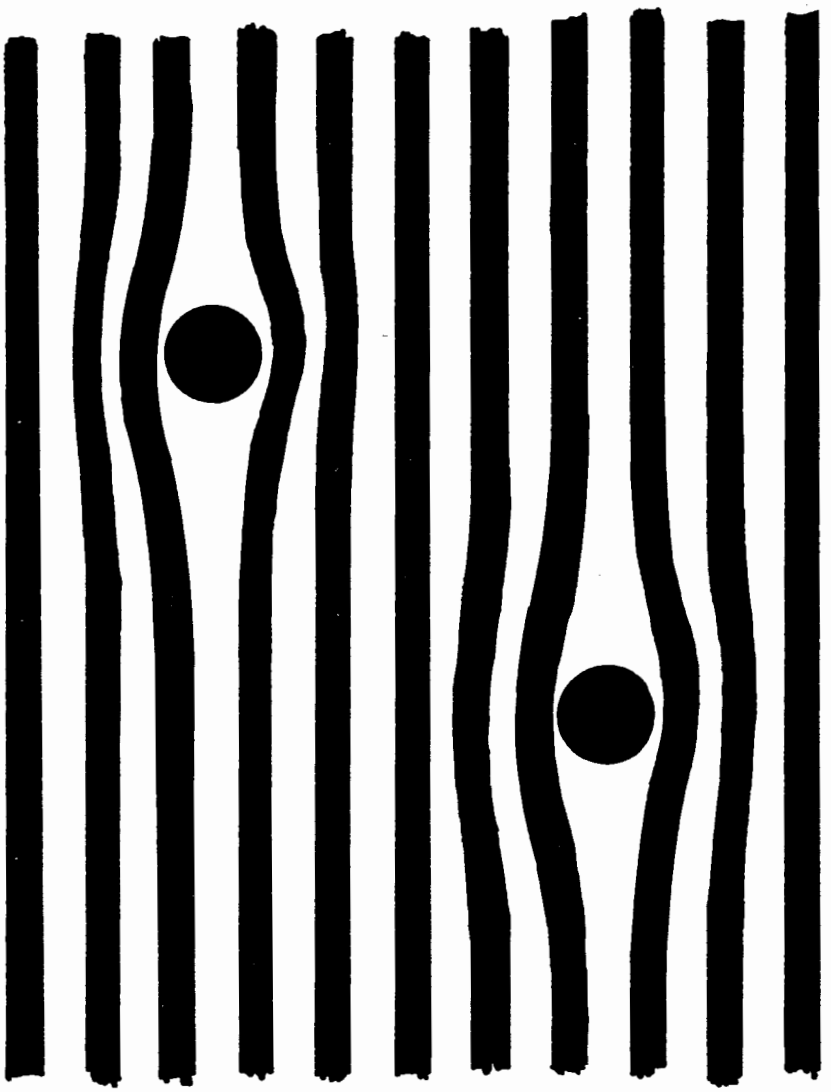

in 2-D in Fig. 10.2, we can expect that the elastic energy of the host layers will increase by an amount $4N_O x E_k$, where N_O is the total number of transition metal atoms and $x = N/N_O$. The Coulomb interaction (Eq) will be minimal because, if $x \simeq 1/20$ the intercalated ions are separated by about $\sqrt{20}a_O$, that is in the order of 15Å, and are therefore expected to be well screened by the conduction electrons. The work done to separate the layers (E_S) will also be minimal because there is essentially no change in c_O for the dilute stage 1 phase compared to pure 2H-TaS_2 (Chapter 3). A change in c_O is assumed to be a good gauge for determining E_S.

It should be pointed out that it is exactly for this dilute stage 1 phase that the staging arguments presented by Safran and Hamann [35] are correctly applied since their theory is essentially an impurity or defect theory. For larger intercalate concentrations, stage 2 for example, the crystal is free to expand parallel to $\hat{c}$ so that the crystal's outer basal planes are not "pinned" with respect to each other. However, it is just this "pinning" which is an essential ingredient in an impurity or defect theory of staging and any conclusions based on this type of model should therefore be evaluated with a great deal of care. Clearly, in order to minimize elastic strains, any impurities or "impurity islands" will order themselves along $\hat{c}$ so that they are staggered with respect to each other and will therefore appear to stage for the appropriate concentrations.

If the mole fraction of intercalate continues to increase, the lattice strain energy (E_k) will eventually become more severe than the work required to separate the layers (E_S) and the Coulomb interaction between the intercalated ions (Eq) combined. As a consequence, in each layer the intercalated ions will coalesce into islands which will grow in size and in numbers as the mole fraction of intercalate is further increased. The particular stage, or if staging occurs at all, will then, as already pointed out, depend primarily on the work required to separate the host layers (i.e. E_S). Some hosts have very loosely bound layers and consequently their intercalation compounds can show very large stage numbers. In the graphite intercalation compounds for example, which can be considered to have loosely bound layers when compared to the dichalcogenides, stages as high as 10 have been reported and stage 6 is commonly observed [10]. In contrast, for dichalcogenide intercalation compounds stage 4 is the largest reported [63] and stage 2 is commonly observed. If staging does occur, the "pleated layer model" described by Daumas and Herold [64] is intuitively correct, although no direct evidence to its correctness has ever been presented. The great appeal of this model is in that it can explain in a very straightforward manner how a stage 2 to stage 1 conversion can occur (or stage 3 to stage 2, etc.) without requiring the intercalate to migrate from one van der Waals gap to another. The stage 1 to 2 conversion, observed in Chapter 3 when a

x = 5/12 sample was heated, can therefore be easily visualized physically. When the stage 1 material is heated its layers will "soften", thus decreasing E_k, and it becomes energetically more favourable for stage 2 to exist, even though the lattice strain energy (E_k) along with the Coulomb interaction energy (Eq) of the intercalate (with increased density x') will increase somewhat, because the increase in E_k and E_q will be more than balanced by the energy decrease (E_s) acquired because stage 2 only requires that one half of the layers are separated.

If a stage n compound has successfully formed, then on further intercalation the island density will increase and thus yield a progressive reduction in the stage number. Ideally, if x is doubled the stage number will be halved until stage 1 is finally achieved. Of course, this assumes that all other pertinent parameters like charge transfer, orbital overlap, host structure, etc., remain essentially unchanged which, however, may not necessarily be the case. In the above sense for example, there are fewer changes in the Ag_xTiS_2 system than in the Ag_xTaS_2 system as is illustrated below.

In the Ag_xTiS_2 compounds when $0 < x \lesssim 0.42$, no changes are observed in the host structure (ignoring the simple expansion of the unit cell paramters noted in Chapter 3) and the silver ions always reside in octahedral sites and order on a $\sqrt{3}a_o$ superlattice on cooling (Chapters 3 and 6). Consequently, a stage 2 structure exists ideally for x = 1/6

which, however, can be overfilled to x ≃ 1/5 before stage 1 begins to form (Chapter 7). Stage 1 in turn exists ideally for x = 2/6, but again overfills to x ≃ 2/5. The simple repetitive relationship that exists between the stage number and the intercalated mole fraction is therefore clearly illustrated.

In the Ag_xTaS_2 systems on the other hand, changes are observed in the host structure with increasing silver content. The silver ions will initially occupy octahedral and later tetrahedral lattice sites to produce different superlattices on cooling. Consequently, a stage 2 structure again exists ideally for x = 1/6 having a $\sqrt{3}a_o$ superlattice, which will overfill by ≃ 1/12 mole fraction to x ≃ 1/4. But then, instead of precipitating stage 1 when intercalating slightly further, a stacking rearrangement of the host layers occurs which places the silver ions into tetrahedral sites (Fig. 5.10), and stage 2 is observed to persist. Because the new superlattice is $2a_o$ (Fig. 4.3) this stage 2 structure should exist ideally to x = 1/4, but is actually observed to overfill and persist to x ≃ 1/3 before stage 1 does begin to form (Chapters 3, 5 and 7). The persistence of stage 2 must be related to the larger packing density of the silver ions which has increased from ideally x' = 1/3 (octahedral sites) to x' = 1/2 (tetrahedral sites), judging by the superlattices, after the stacking rearrangement forces the silver ions to occupy tetrahedral rather than octahedral intercalation

sites. Although one could think of several reasons why stage 2 will persist after the stacking rearrangement occurs, there are two causes that suggest themselves immediately. The first is that when the intercalate occupies the tetrahedral sites there are first, second and third nearest neighbor sites available which are separated by $a_o/\sqrt{3}$, $2a_o/\sqrt{3}$ and $3a_o/\sqrt{3}$ respectively (Fig.4.8), but when the octahedral sites are occupied, sites are only available at $a_o/\sqrt{3}$ and $3a_o/\sqrt{3}$ (Fig. 5.9). Clearly, in both cases the nearest neighbor sites are not occupied, because of the large Coulomb interaction, as already pointed out in Chapter 5, but the sites at $2a_o/\sqrt{3}$ can be occupied and will therefore allow a higher packing density when the silver ions occupy tetrahedral sites. Further help to an increased packing density might also come from a decrease in the charge transfer to the host lattice because, for example, whereas in the octahedral sites the silver ions are associated with the "d_{z2} orbitals" in both adjacent layers, in the tetrahedral sites they are only associated with one of the "d_{z2} orbitals" (Fig. 5.10).

Stage 1 Ag_xTaS_2, which begins to form for $x > 1/3$, will undergo structural transformations similar to stage 2. First the silver ions, in the previously unintercalated regions, will again reside in octahedral sites (Fig. 7.7), possibly to $x = 1/6$ again ideally, before the final structural change to the 2H-MoS_2 structure (Fig. 3.3) occurs for $x = 1/2$ (i.e. 1/3 + 1/6) ideally. After this structural change the

latter silver ions will now also reside in tetrahedral sites and will again be able to increase their packing density. The superlattice observed is $(\sqrt{3} \times 2)a_o$ (Chapter 5), which again requires $x' = 1/2$ ideally, so that the structure should be ideally complete for $x = 0.58$ (i.e. 1/3 + 1/4) but will again overfill by 1/12 mole fraction to $x \simeq 2/3$. Therfore, even though more complicated, the repetitive relationship between the intercalated mole fraction and the stage number is again clearly illustrated.

The above series of observations on stacking and staging in the Ag_xTiS_2 and Ag_xTaS_2 intercalation systems allows for an interesting prediction to be made for the Ag_xTiS_2 system. If it were possible to increase the intercalated mole fraction to above $x \simeq 0.42$, a stacking change in the titanium atoms should eventually occur to a staggered configuration, as discussed in 10.2, which will place the silver ions into tetrahedral, or possibly trigonally prismatic sites. However, once this change in lattice sites occurs, a larger packing density (x') will again likely be possible, either because of the extra sites available or a decrease in the charge transfer to the host lattice (the latter cause is necessary if the silver ions occupy trigonally prismatic sites). If the packing density does increase, it will then become very likely that stage 2 will be regained simply because, as previously explained, the system's free energy can still be lowered overall, even though lattice strains (E_k) and increased

Coulomb interactions (Eq) are introduced, because the work required to separate the layers (E_S) will be halved. On further intercalation, stage 1 should again reform and be complete for about twice the mole fraction at which stage 2, with the silver ions in tetrahedral or trigonally prismatic sites, is complete. Furthermore, if the arguments about the Coulomb and exchange interactions of the "d_{z2} orbitals" are correct, it will be possible to change the titanium atoms stacking sequence from an eclipsed to a staggered configuration by simply applying hydrostatic pressure, but in addition to this, we might also observe that the host will change from, say, stage 1 to stage 2. The change of stage, by the application of hydrostatic pressure, can be expected by realizing that if the host layer stacking sequence changes (probably even if it doesn't change) the parameters important in determining the stage number, as for example x', E_k, Eq, etc., will also be affected and may consequently change the stage number observed from that before hydrostatic pressure was applied. This sequence of events can in principle occur in a variety of ways, depending on the host and intercalate, to produce a variety of seemingly complex changes of phase.

Although not yet conclusively confirmed, it appears that by using a $Ni/0.1NAgNO_3/TiS_2$ galvanic cell, intercalation to larger mole fractions of silver is possible and the existence of pure stage 2 has been inferred, via Raman scattering, for a $Ag_{1/2}TiS_2$ sample [65]. Here the titanium stacking sequence

should be staggered along $\hat{c}$, wherever intercalation occurs, as observed for some of the alkali metal intercalates (Fig. 10.1a). This in turn suggests that the silver ions will likely reside in the tetrahedral, or possibly the octahedral, intercalation sites. Furthermore, it should also be possible to prepare a stage 1 Ag_1TiS_2 sample where all titanium atoms are staggered along $\hat{c}$.

REFERENCES

1. R.F. Frindt and D.J. Huntley, Optical and Electrical Properties , Physics and Chemistry of Materials with Layered Structures, Vol. 4, D. Reidel Pub. Co., 385 (1976).

2. J.A. Wilson, F.J. DiSalvo and S. Mahajan, Adv. Phys. 24, 117 (1975).

3. Proc. of the Int. Conf. on Ordering in Two Dimensions , Lake Geneva, U.S.A., Elsevier N. Holland Inc. (1980).

4. D.W. Murphy and F.A. Trumbore, J. Cryst. Growth,, 39, 185 (1977).

5. W.J. Wattamaniuk, J.P. Tidman and R.F. Frindt, Phys. Rev. Lett. 35, 62 (1975).

6. J.P. Tidman and R.F. Frindt, Can. J. Phys. 54, 2306 (1976).

7. J.A. Wilson and A.D. Yoffe, Adv. Phys. 18, 193 (1969).

8. R. Huisman, R. de Jonge, C. Haas and F. Jellinek, J. Solid State Chem. 3, 56 (1971).

9. W. Rüdorff, Chimica 19, 489 (1965).

10. A. Herold, Intercalated Layer Materials , Physics and Chemistry of Layered Structures, Vol. 6, D. Reidel Pub. Co., 323 (1979).

11. M.S. Whittingham, Prog. Solid St. Chem. 12, 41 (1978).

12. H. Schäfer, Chemical Transport Reactions , Academic Press Inc. (1964).

13. K. Kaluarachchi (personal communications, March 1982).

14. J. Bernard and Y. Jeannin, Adv. in Chem. 'Non-stoichiometric Compounds', 191 (1962).

15. F. Jellinek, J. Less-Common Metals 4, 9 (1962).

16. G.S. Parry, C.B. Scruby and P.M. Williams, Phil. Mag. 29, 601 (1974).

17. J.R. Dahn, W.R. McKinnon, R.R. Haering, W.Y.L. Buyers and B.M. Powell, Can. J. Phys. 58, 207 (1980).

18. W.K. Unger, J.M. Reyes, O. Singh, A.E. Curzon, J.C. Irwin and R.F. Frindt, Solid State Commun. 28, 109 (1978).

19. J.A. Wilson, Phys. Stat. Sol. (b) 86, 11 (1978).

20. A.E. Van Arkel et C. Crevecour, J. Less-Common Metals 5, 177 (1963).

21. M.S. Wittingham, Chem. Commun., 328 (1974).

22. R. Schöllhorn and H. Meyer, Mat. Res. Bull. 9, 1237 (1974).

23. S.A. Safran, Phys. Rev. Lett. 44, 937 (1980).

24. A.E. Curzon, G.A. Scholz and O. Singh, J. Phys. (E) 15, 629 (1982).

25. J.P. Tidman, O. Singh, A.E. Curzon and R.F. Frindt, Phil. Mag. 30, 1191 (1974).

26. R. De Ridder, Proc. Int. Conf. on Layered Materials and Intercalates , Univ. of Nijmegen, The Netherlands, 39 (1979).

27. R. De Ridder, G. van Tendeloo, J van Landuyt, D. van Dyck and S. Amelinckx, Phys. Stat. Sol. (a) 37, 591 (1976).

28. F.W. Boswell, A. Prodan and J.M. Corbett, Phys. Stat. Sol. (a) 35, 591 (1976).

29. G. Wexler and A.M. Woolley, J. Phys. C 9, 1185 (1976).

30. G.A. Scholz (unpublished results).

31. T. Butz, A. Hübler, A. Lerf, and W. Biberacher, Mat. Res. Bull. 16, 541 (1981).

32. J.A. Wilson, F.J. DiSalvo and S. Mahajan, Adv. Phys. 24, 117 (1975).

33. T.M. Rice and G.K. Scott, Phys. Rev. Lett. 35, 120 (1975).

34. J.A. Wilson, Phys. Rev. B 15, 5748 (1977).

35. S.A. Safran and D.R. Haman, Physica 99B, 469 (1980).

36. J. O'M. Bockris and A.K.N. Reddy, Modern Electrochemistry , Vol. 1, Plenum Pub. Corp. (1973).

37. A.H. Thompson, J. Electrochem. Soc. 126, 608 (1979).

38. A.J. Berlinsky, W.G. Unruh, W.R. McKinnon and R.R. Haering, Solid State Comm. 31, 135 (1979).

39. L.F. Mattheiss, Phys. Rev. B 8, 3719 (1973).

40. G. Wexler and A.M. Woolley, J. Phys. C 9, 1185 (1976).

41. A.R. Beal and S. Nulsen, Phil. Mag. B 43, 985 (1981).

42. N.V. Smith and M.M. Traum, Phys. Rev. B 11, 2087 (1975).

43. P.M. Williams and F.R. Shepherd, J. Phys. C 6, L36 (1973). F.R. Shepherd and P.M. Williams, J. Phys. C 7, 4427 (1974).

44. M.G. Bell and W.Y. Liang, Adv. Phys. 25, 53 (1976).

45. N.J. Doran and A.M. Woolley, J. Phys. C 14, 4257 (1981).

46. J.M. Ziman, Principles of the Theory of Solids , Cambridge Univ. Press (1979).

47. A.R. Beal and S. Nulsen, Phil. Mag. B 43, 965 (1981).

48. C.Y. Fong, J. Camassel, S. Kohn and Y.R. Shen, Phys. Rev. B 13, 5442 (1976).

49. A. Zunger and A.J. Freeman, Phys. Rev. B 16, 906 (1977); ibid 17, 1839 (1978).

50. R.H. Friend, D. Jerome, W.Y. Liang, J.C. Mikkelsen and A.D. Yoffe, J. Phys. C 10, L705 (1977).

51. S. Basu and W. Worrell, Proc. Int. Conf. on Fast Ion Transport in Solids, Electrodes and Electrolytes , Lake Geneva, U.S.A., 149 (1979).

52. J.N. Mundy, Proc. Int. Conf. on "Fast Ion Transport in Solids, Electrodes and Electrolytes", Lake Geneva, U.S.A., 159 (1979).

53. G.A. Scholz, P. Joensen, J.M. Reyes and R.F. Frindt, Physica 105B, 214 (1981).

54. J.G. Hooley, Carbon 18, 82 (1980).

55. N. Le Nagard, O. Gorochov and G. Collin, Mat. Res. Bull. 10, 1287 (1975).

56. K. Koerts, Acta Cryst. 16, 432 (1963).

57. F.J. DiSalvo, G.W. Hull, Jr., L.H. Schwartz, J.M. Voorhoeve and J.V. Waszczak, J. Chem. Phys. 59, 1922 (1973).

58. A. LeBlanc, M. Danot, L. Trichet and J. Rouxel, Mat. Res. Bull 9, 191 (1974).

59. R.R. Chianelli, J.C. Scanlon, M.S. Wittingham and F.R. Gamble, Inorg. Chem. 14, 1693 (1975).

60. R. Eppinga and G.A. Wiegers, Proc. Int. Conf. on Layered Materials and Intercalates , Univ. of Nijmegen, The Netherlands, 121 (1979).

61. V. Schmidt, Dissertation Tübingen (1971).

62. R. Setton, Bull. Soc. Chim. Fr. 2, 521 (1972).

63. J. Rouxel, Intercalated Layer Materials , Physics and Chemistry of Layered Structures, Vol. 6, D. Reidel Pub. Co., 201 (1979).

64. N. Daumas and A. Herold, C.R. Acad. Sci. C268, 373 (1969).

65. K.K. Bardhan, R. Leonelli and J.C. Irwin, Bulletin of the American Physical Society, Program of the 1982 March Meeting in Dallas 27, 314 (1982).

66. G.A. Scholz, O. Singh, R.F. Frindt and A.E. Curzon (to be published).

67. R.F. Frindt, P. Joensen, J.M. Reyes and G.A. Scholz, U.S. application No. 360, 363 (March 1982 by C.P.D.L.).

68. R. Leonelli, M.Sc. Dissertation Simon Fraser University (1980).